Pacific Cell Annual Meeting

October 24-26, 2025

Searles Valley, CA

Organizers: Steve Bacon & Ian Pierce

Contributions from: James Dolan, Maggie Duncan, Ken Hudnut, Özgür “Oz” Kozacı, Victoria Langenheim, Chris Madugo, Sydney Maguire, Sally McGill, Devin McPhillips, Chris Milliner, Silvio Pezzopane, Fred Phillips, Kathleen Rodrigues, Zachary Smith, and Mindy Zuckerman

Trip Overview

The last time the Friends of the Pleistocene visited Searles Valley was in 1967, which was the 2nd Pacific Cell (formerly the Pacific Coast Section) field trip.

We will be visiting fragile surface ruptures. Please avoid trampling these. We will also be in a pristine desert environment. Please pack out all your trash and leave no trace. Watch for desert tortoise particularly on roads and under vehicles before driving, avoid damaging cacti, and stay on existing road tracks. Bring plenty of water, a good hat (and possibly sun umbrella) as the sun can be intense even in late October and there is no shade. We will not have restrooms available at the stops, so plan accordingly. There are pit toilets at the Trona Pinnacles. Nights will likely be cold, so dress warm, bring a warm sleeping bag, and please help bring some firewood if you have the ability. Cell service is spotty, we recommend having satellite maps cached (The Strabo spot and Caltopo apps have great options for this). Preloading/saving the stop locations is a good idea. Ian may have a functioning Starlink network broadcast from his rig, the network name is SunriseTavern and password SunsetTavern, please avoid streaming as the bandwidth is limited. Particularly on Day 1, please take care crossing Highway 178 (several turns onto/off of this highway) as there can be very high-speed traffic. Also take care crossing uncontrolled railroad crossings along the Pinnacle Rd. On dirt roads there may be OHV traffic (motorcycles, side by sides, ATVs, etc.), watch for these as they may be traveling at high speed. The closest fuel stations, groceries, ice, medical services, and other facilities are in Ridgecrest. Trona has limited services, but should have gas.

Ridgecrest Regional Hospital: (760)446-3551
1081 N China Lake Blvd, Ridgecrest, CA 93555

Camp Location

35.4868, -117.6022

Camp is an undeveloped dry campground. We will provide portable restrooms. Pack out everything you pack in. No water is available on site.

From Trona Rd turn west onto Searles Station Rd (dirt). Drive 0.75 miles, camp will be on the right.

Alternatively, if heading northeast on Searles Station Cutoff (immediately after intersection with railroad tracks/ map labeled ‘Searles’), turn right onto Searles Station Rd. Main dirt road initially heads southeast, then broad left turn to head east-northeast. Follow this main dirt road for 2.0 miles, camp will be on the left.

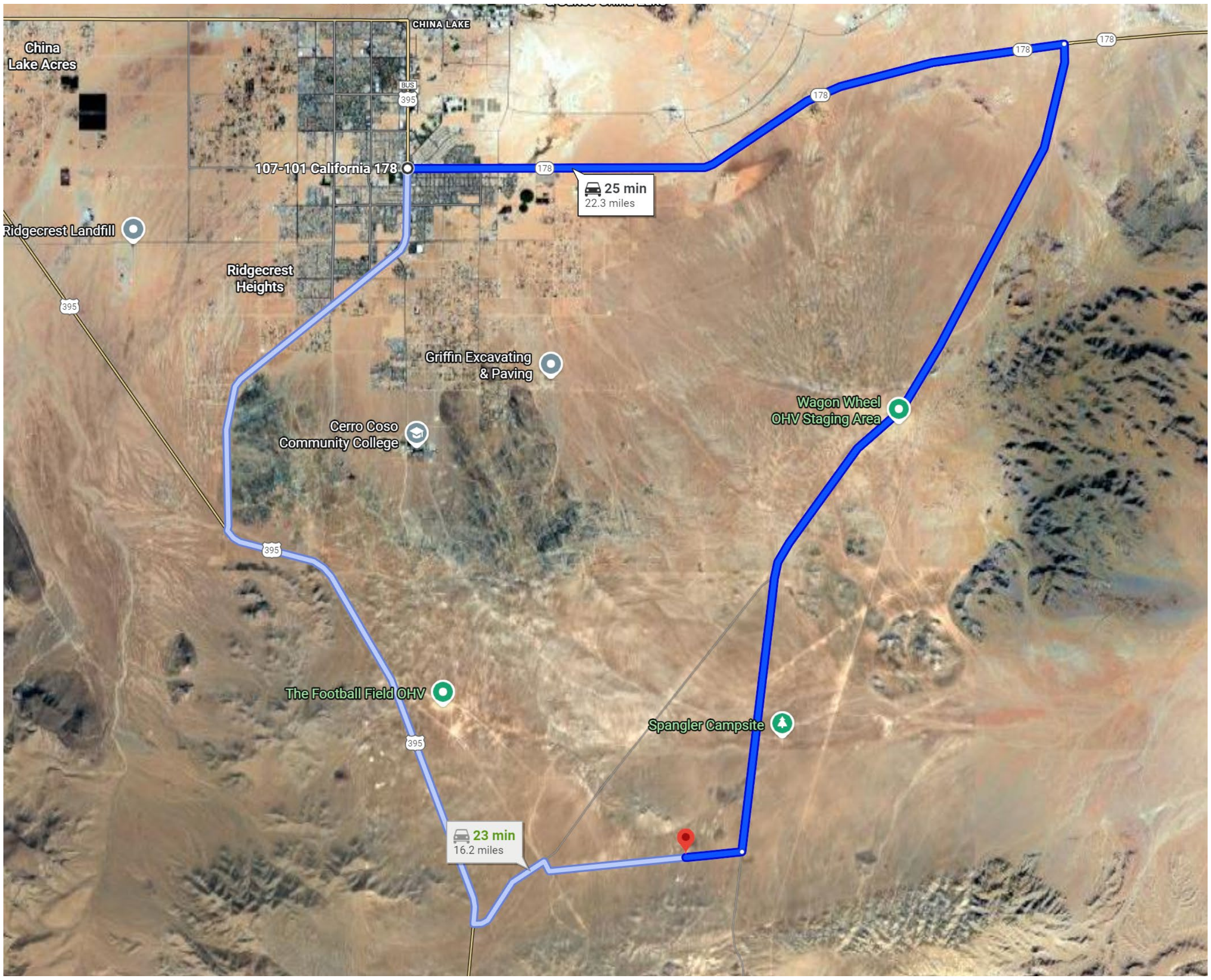

Camp Location

Stop Locations

Day	Stop	GPS Coordinates (Parking)	GPS Coordinates (Hike)	Google Map Link	Name
		35.4868, -117.6022		https://maps.app.goo.gl/9nBBaPRaJNsrUnF19	CAMP
1	1	35.8467, -117.3172	N/A	https://maps.app.goo.gl/PuYHUfpaZF9HdRxp9	Searles Valley Overview
	2	35.6256, -117.3789	N/A	https://maps.app.goo.gl/MEfpPNxSD6ndjvtz9	Pinnacles Shorelines
	3	35.6228, -117.5659	35.6274, -117.5623	https://maps.app.goo.gl/7RX2X2LkzQSz8Zoz8	M6.4 Trench Sites
	4	35.6467, -117.4801	N/A	https://maps.app.goo.gl/sgqAAYYMU9doLCt16	M7.1 & Highway 178
2	1	35.5901, -117.4163		https://maps.app.goo.gl/aX1YKCFnFXUG1r2j6	M7.1 Splay Fault Outcrop
	2	35.61705, -117.3688	N/A	https://maps.app.goo.gl/C1FcRUpWnKJMZXUW8	Trona Pinnacles
	3	35.5965, -117.4021	35.5823, -117.3845	https://maps.app.goo.gl/gt2HL9XCTWr9rAku7	M7.1 Basin Trench
3	1	35.4790, -117.5603		https://maps.app.goo.gl/YwKQtZ4pKnurUL8H8	
	2	35.4440, -117.6817		https://maps.app.goo.gl/5RfJ5SChPZVBtxmL9	

Road Logs & Detailed Directions

Day 1 Road Log

Day 1 Road Log

Day 1 - Camp to Stop 1

Direction	Coordinates	Miles	Cumulative Miles	Approximate Time to Stop (min)
Zero odometer before turning out of the campsite.	(35.486830, -117.602297)	0	0	
LEFT out of campsite and head east along Searles Station Rd., following fiber optic cable markers.		0.7	0.7	
LEFT on Trona Rd.		11.8	12.5	
RIGHT on Hwy 178.		20	32.5	
RIGHT on unnamed dirt road.	(35.845064, -117.336196)	1.1	33.6	
Stop 1. Drive across the drainage and park at the turnaround.	(35.846755, -117.316234)			40

Day 1 - Stop 1 to Stop 2

Direction	Coordinates	Miles	Cumulative Miles	Approximate Time to Stop (min)
Head west from Stop 1 back out to Hwy 178.		1.1	34.7	
LEFT on Hwy 178.		12.8	47.5	
LEFT on Pinnacle Road/RM 143 to "Trona Pinnacles Entrance" - proceed straight.		0.5	48	
VEER RIGHT at Y junction towards Trona Pinnacles		3.7	51.7	
Stop 2. Pull off to the left of the road into the open space and park as directed by FOP organizers. We will then walk approximately 0.1 mile along the road to the spring site.	(35.6256, -117.3789)			35

Day 1 - Stop 2 to Stop 3

Direction	Coordinates	Miles	Cumulative Miles	Approximate Time to Stop (min)
Head north back on Pinnacles Rd.		3.7	55.4	
Keep LEFT (straight) to continue on Pinnacles Rd.		0.5	55.9	
LEFT on Hwy 178.		7.4	63.3	
LEFT on Trona Road. Watch for cross traffic.		0.3	66	
RIGHT onto Randsburg Wash Rd.		1.6	67.6	
RIGHT onto unpaved OHV road (RM 4132) with orange pipeline marker at the entrance.	(35.615507, -117.556134)	0.9	68.5	
Stop 3. Turn around at the teardrop and park. We will walk approximately 0.5 miles to the stop.	(35.624096, -117.567546)			25

Day 1 - Stop 3 to Stop 4

Direction	Coordinates	Miles	Cumulative Miles	Approximate Time to Stop (min)
Drive back along RM 4132 to return to junction with Randsburg Wash Rd.		0.9	69.4	
LEFT onto Randsburg Wash Rd. Watch for cross traffic.		1.6	71	
LEFT onto Trona Rd. Watch for cross traffic.		2.7	73.7	
RIGHT onto CA 178.		2.1	75.8	
RIGHT on RM 4137. This road is unmarked but follows the powerline.	(35.649251, -117.474981)	0.3	76.1	
Stop 4. We will park and walk approximately 250 feet further along the road to reach the scarp.	(35.646585, -117.480129)			20

Day 1 - Stop 4 to Camp

Direction	Coordinates	Miles	Cumulative Miles	Approximate Time to Stop (min)
Continue driving southwest along RM 4137/powerline road.		2.2	78.3	
RIGHT onto RM 4136		0.1	78.4	
LEFT onto Trona Rd.		10.5	88.9	
RIGHT onto Searles Station Rd. (watch for the BLM sign and fiber optic cable marker at the turn).		0.7	89.6	
Back at the campsite.				20

Camp to Stop 1-1

Note: We used walking directions because we couldn't update the directions due to road closures affecting google maps at time of writing.

Stop 1-1 to 1-2


Argus Peak
Great Falls Basin
Valley Wells
Trona, CA 93592
Trona
PIONEER POINT
Trona Rd
Searles Valley
TRONA
33 min
18.5 miles
ARGUS
Borosolvay
Searles Lake
South Trona
Westend
Trona Rd
Pinnacles Entrance
Fish Rocks
178
Trona Pinnacles National Natural Landmark

Stop 1-2 to 1-3

Note: We used walking directions because we couldn't update the directions due to road closures affecting google maps at time of writing. The red pin is the turnoff of Randsburg Wash Road onto unnamed dirt road heading NW to the site. Continue up this unnamed dirt road, past intersection with Bowman Rd to stop parking area.

Stop 1-3 & hike: We will have discussions near the parking area and then go on a short hike to view 6.4 rupture morphology and trench sites. The hike is about ½ mile and follows an unnamed dirt road. Those with higher clearance 4x4 can drive to the trench site, though parking is limited. *Please take care not to trample fragile surface ruptures.*

Hiking route:

Stop 1-3 to 1-4

Note that this is *REVERSED* we couldn't update the guidebook due to road closures affecting google maps at the time of writing. The red pin is stop 3 and white is stop 4.

Optional after-stop drive or ½ mile hike to visit Milliner site.

Day 2 Directions

Day 2 Road Log

Day 2 - Camp to Stop 1

Direction	Coordinates	Miles	Cumulative Miles	Approximate Time to Stop (min)
Zero odometer before turning out of the campsite.	(35.486830, -117.602297)	0	0	
LEFT out of campsite and head east along Searles Station Rd., following fiber optic cable markers.		0.7	0.7	
LEFT on Trona Rd.		9.2	9.9	
RIGHT on Randsburg Wash Rd.		5.6	15.5	
LEFT on BLM RM 143/Pinnacles Rd.		2	17.5	
Stop 1. We will walk approximately 0.2 miles to the train tracks for stop 1.	(35.589968, -117.416482)			35

Day 2 - Stop 1 to Stop 2

Direction	Coordinates	Miles	Cumulative Miles	Approximate Time to Stop (min)
Continue driving northeast along RM 143/Pinnacle Rd.		2.8	20.3	
VEER RIGHT at junction and head towards the pinnacles (do not continue on RM 143).		0.1	20.4	
Continue straight, then keep right at the fork in the road and continue northeast along the well-traveled road.		0.4	20.8	
Stop 2. look for RM 9245 sign at the base of the big pinnacle.	(35.616782, -117.368720)			30

Day 2 - Stop 2 to Stop 3

Direction	Coordinates	Miles	Cumulative Miles	Approximate Time to Stop (min)
Continue along the main road through the pinnacles.		0.1	20.9	
VEER LEFT at the Y junction (there is a restroom along the way if needed).		0.2	21.1	
Proceed past restroom, following the main road. Do not veer left into the pinnacles.		0.1	21.2	
Keep RIGHT at the Y junction and follow the road NOT lined with rocks.		0.3	21.5	
Continue straight to get back onto RM 143/Pinnacle Rd.		1.9	23.4	
Stop 3. The site is an approximate 1.5 mile walk southeast of our parking spot.	(35.596503, -117.402118)			25

Day 2 - Stop 3 to Camp

Direction	Coordinates	Miles	Cumulative Miles	Approximate Time to Stop (min)
Continue southwest along RM 143/Pinnacle Rd.		2.8	26.2	
RIGHT onto Randsburg Wash Rd.		5.6	31.8	
LEFT onto Trona Rd.		9.2	41	
RIGHT onto Searles Station Rd.		0.7	41.7	
Back at the campsite.	(35.486830, -117.602297)			40

Camp to Stop 2-1

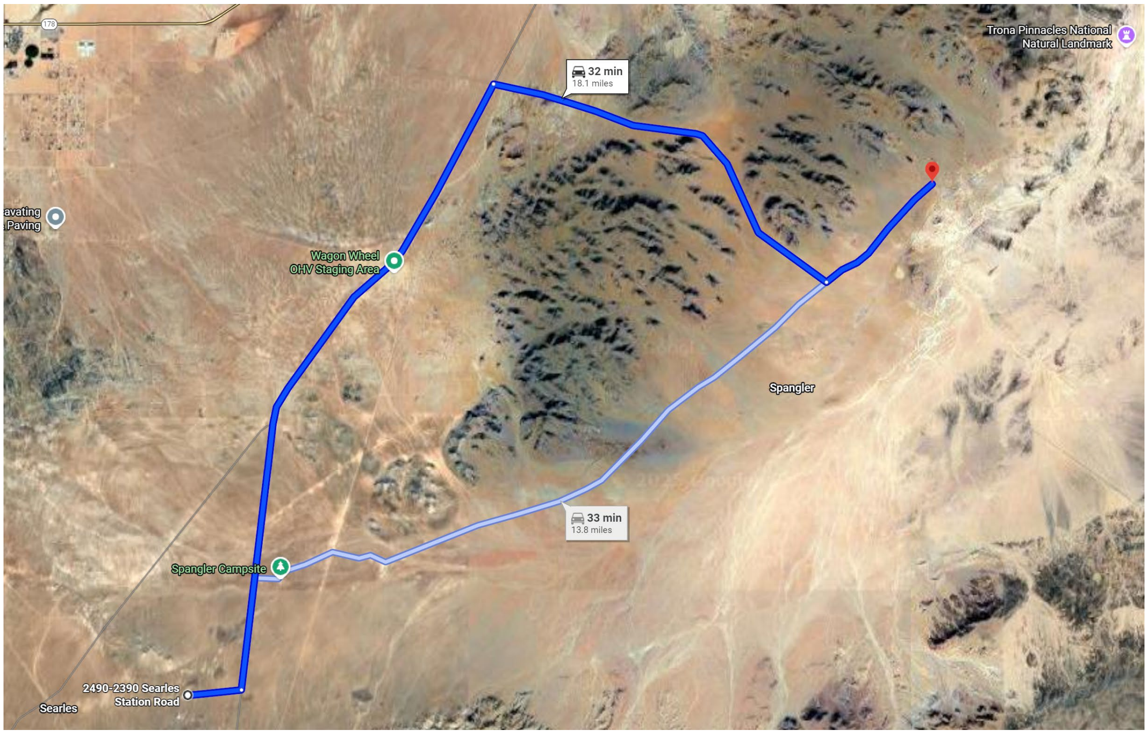

Stop 2-1 to 2-2

Stop 2-2 to 2-3

Stop 2-3. We will park at this location, discuss the stop from the road, and then hike along the rupture to Stop 2-3 followed by more discussion. Alternative access to drive into stop 2-3 is described below.

Stop 2-3- Following discussion at the parking area on the Pinnacle rd, hike southeast (1.4 miles) with the group following the surface rupture. Return via the same route. *Please take care not to trample fragile surface ruptures.*

Stop 2-3 – *alternative (drive)* return to Trona Pinnacles (following discussion from main road area before hike begins). From 35.6164, -117.3685 is a small dirt road heading south that is visible in Google Satellite maps (it is not a labeled road in Google maps). This road is passable with moderate clearance 4x4 (Subaru should be OK, 2WD might be OK if you stay out of sand). Follow this road south. There are several turn offs. Unless you have high confidence in your navigation skills and a cached satellite map, follow someone who knows where they are going as there are multiple forks you will need to take (generally you will want to take the right forks, but the directions are from memory). You will be able to drive to the hike-in destination: 35.5823, -117.3845. Total drive distance is approximately 3.5 miles from the start of the road at the Pinnacles to the destination.

Hiking route:

Measure distance

Click on the map to add to your path

Total distance: 1.38 mi (2.23 km)

Day 3 Directions

Day 3 Road Log

Day 3 - Camp to Stop 1

Direction	**Coordinates**	**Miles**	**Cumulative Miles**	**Approximate Time to Stop (min)**
Zero odometer before turning out of the campsite.	(35.4868, -117.6022)	0	0	
LEFT out of campsite and head east along Searles Station Rd., following fiber optic cable markers.		0.7	0.7	
RIGHT on Trona Rd.		0.8	1.5	
LEFT on RM 284 (you will see a sign for Spangler Hills OHV Area).		0.5	2	
Continue straight on RM 284, do not turn onto RM 1555.		0.5	2.5	
Continue straight on RM 284, do not turn onto RM 259.		0.7	3.2	
Stop 1. We will turn around and park, then walk approximately 200 feet to our stop.	(35.4785, -117.5602)			20

Day 3 - Stop 1 to Stop 2

Direction	**Coordinates**	**Miles**	**Cumulative Miles**	**Approximate Time to Stop (min)**
Return along RM 284 to junction with Trona Rd.		1.7	4.9	
RIGHT on Trona Rd.		0.8	5.7	
LEFT on Searles Station Rd., back in direction of campsite. Continue past campsite.		2.6	8.3	
RIGHT at dirt road along train tracks.		0.1	8.4	
LEFT on Searles Station Ctf. Cross the train tracks and continue.		1.2	9.6	
LEFT onto Hwy 395.		3	12.6	
RIGHT on Garlock Rd.		0.4	13	
RIGHT on EP 21/Iron-Canyon. Note the BLM sign marking the entrance. This road comes up fast.		1.2	14.2	
Continue straight on EP 21.		0.1	14.3	
LEFT on EP 253.		0.1	14.4	45
Stop 2. We will park at the turnaround.	(35.4441, -117.6816)			

Camp to Stop 3-1

Note: Google Maps does not have the dirt road to access this site, but continue along the indicated road to access the stop.

Stop 3-1 to 3-2

Note: The map is completely incorrect due to road closures at time of writing this guidebook. It is included for visual reference of where stops 3-1 and 3-2 are. Follow the road log.

Contents

Acknowledgements

Huge thanks to Jay Patton for keeping the FOP Pacific Cell email list going and holding the friends together. Thanks to everyone in the community who came together to help collect data and study the 2019 Ridgecrest earthquake. Thanks to SCEC & USGS for providing funding for research to Pierce, Koehler, Williams, and Arrowsmith. Thanks to everyone who contributed to help cover the costs of tires, hotel rooms, and gas for Pierce & Koehler's initial field reconnaissance. Thanks to Steve Wesnousky for teaching us about faults and letting us use his truck for the initial post-earthquake field reconnaissance.

Acknowledgement of G.I. Smith and colleagues' work beginning in the 1950s also needs to be made for first establishing the stratigraphic framework and geochronology of the hydrology of the paleo-Owens River system. A heartfelt thanks to Bud Burke and Silvio Pezzopane for being instrumental in guiding Steve Bacon in the early days of his master's thesis research of Owens Lake at Humboldt State University beginning in January 1999. Also want to acknowledge the many Humboldt State University students, friends, and colleagues that provided field assistance during these early days, including R. Bowers, A. Jayko, P. Hancock, T. Leroy, J. Macey, J. Patton, J. Redwine, J. Stallman, and D. Sutherland. Steve Bacon also acknowledges the National Science Foundation for research funding, as well as Matt Boggs and the U.S. Navy for research support and access to Naval Air Weapons Station China Lake.

And always, want to thank our families for simply putting up with us!

In Memoriam: Jim Macey

We honor the memory of Jim Macey (RIP), who has been a big part of Humboldt geology on the east side for decades. From field camps, to field trips, to the Keeler debris flow, to being a safe refuge for field trippers and field mappers, he will be greatly missed.

Though not a geologist himself, Jim was a true friend of the Pleistocene.

Introduction and Geologic Background

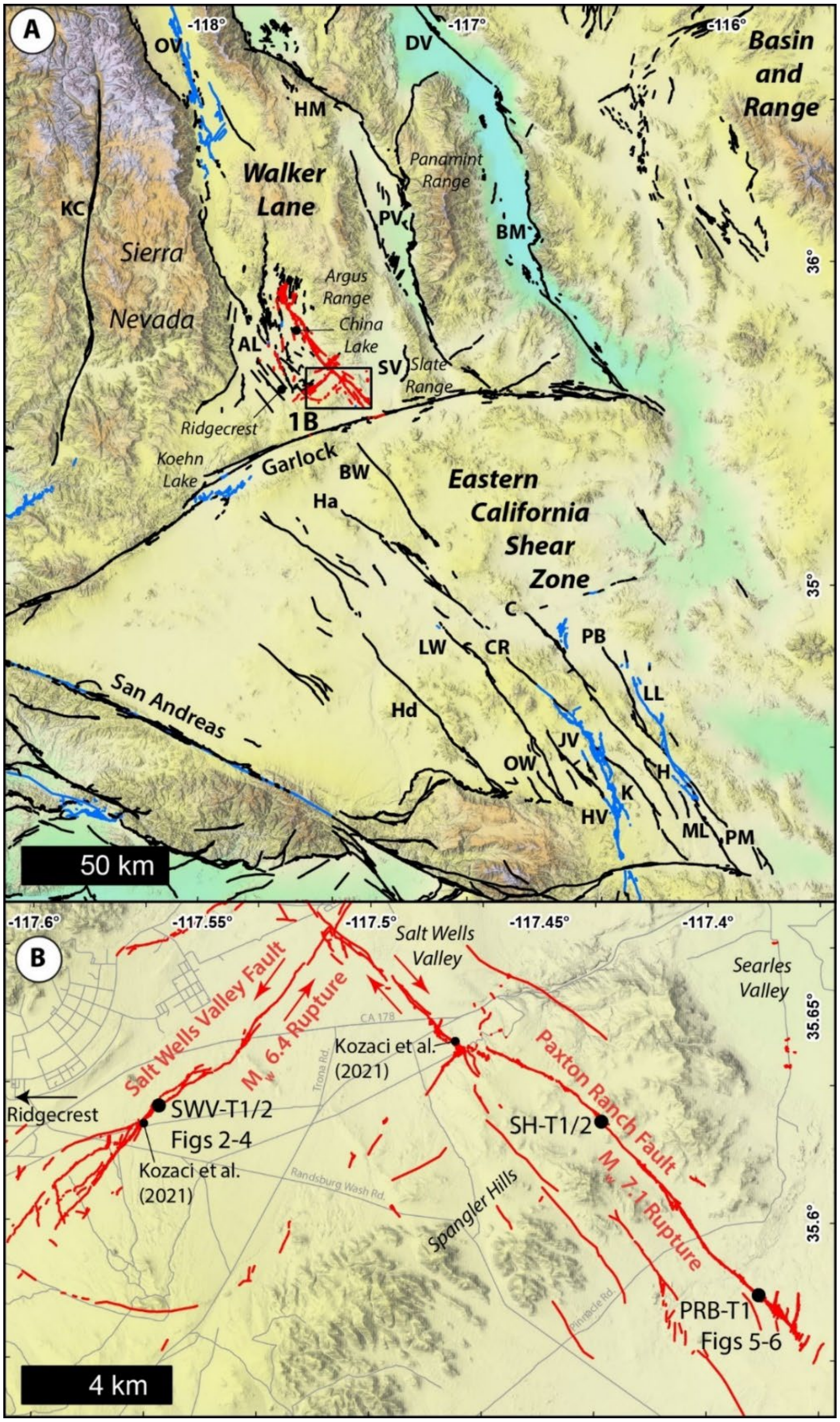

Figure I-1. *Upper: Quaternary faults of southeastern California plotted on a 10-m elevation colored hillshade. Black are Late Quaternary and blue are historical ruptures from the USGS Quaternary Fault and Fold Database. Red are the 2019 Ridgecrest surface ruptures (Ponti et al. 2020). The Garlock fault divides the Southern Walker Lane belt from the Eastern California Shear Zone. Lower: Location map of the southern portion of the Ridgecrest ruptures showing the 3 trench sites. Fault labels: OV: Owens Valley, KC: Kern Canyon, HM: Hunter Mountain, PV: Panamint Valley, DV: Death Valley-Fish Lake Valley, BM: Black Mountains, AL: Airport Lake, SV: Searles Valley-Tank Canyon, BW: Blackwater, Ha: Harper, Hd: Helendale-South Lockhart, LW: Lenwood-Lockhart, CR: Camp Rock-Emerson-Copper Mountain, C: Calico-Hidalgo, PB: Pisgah-Bullion LL: Lavic Lake, HV: Homestead Valley, JV: Johnson Valley, OW: Old Woman Springs, ML: Mesquite Lake, PM: Pinto Mountain, K: Kickapoo, H: Hidalgo.*

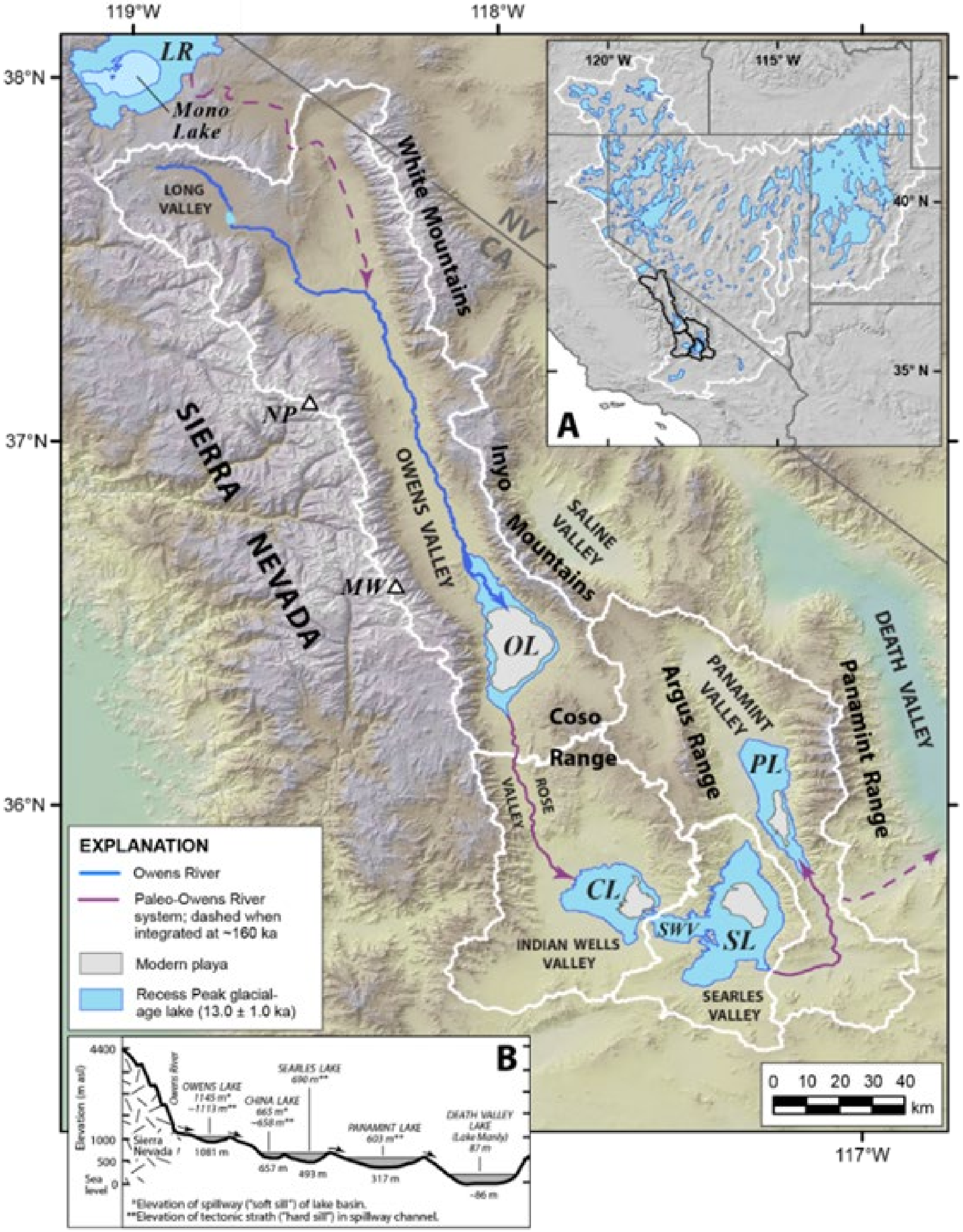

Figure I-2. *Major physiographic features on the southeastern Sierra Nevada in relation to modern playas and pluvial lakes of the paleo-Owens River-Lake system (ORLS). Inset A is map of distribution of pluvial lakes in Great Basin and inset B is profile of the chain of lakes of the ORLS. Watershed boundaries of lake basins are shown (white line) for: CL – China Lake; OL – Owens Lake; PL – Panamint Lake; SL – Searles Lake; and SWV – Salt Wells Valley. (Bacon et al., 2020).*

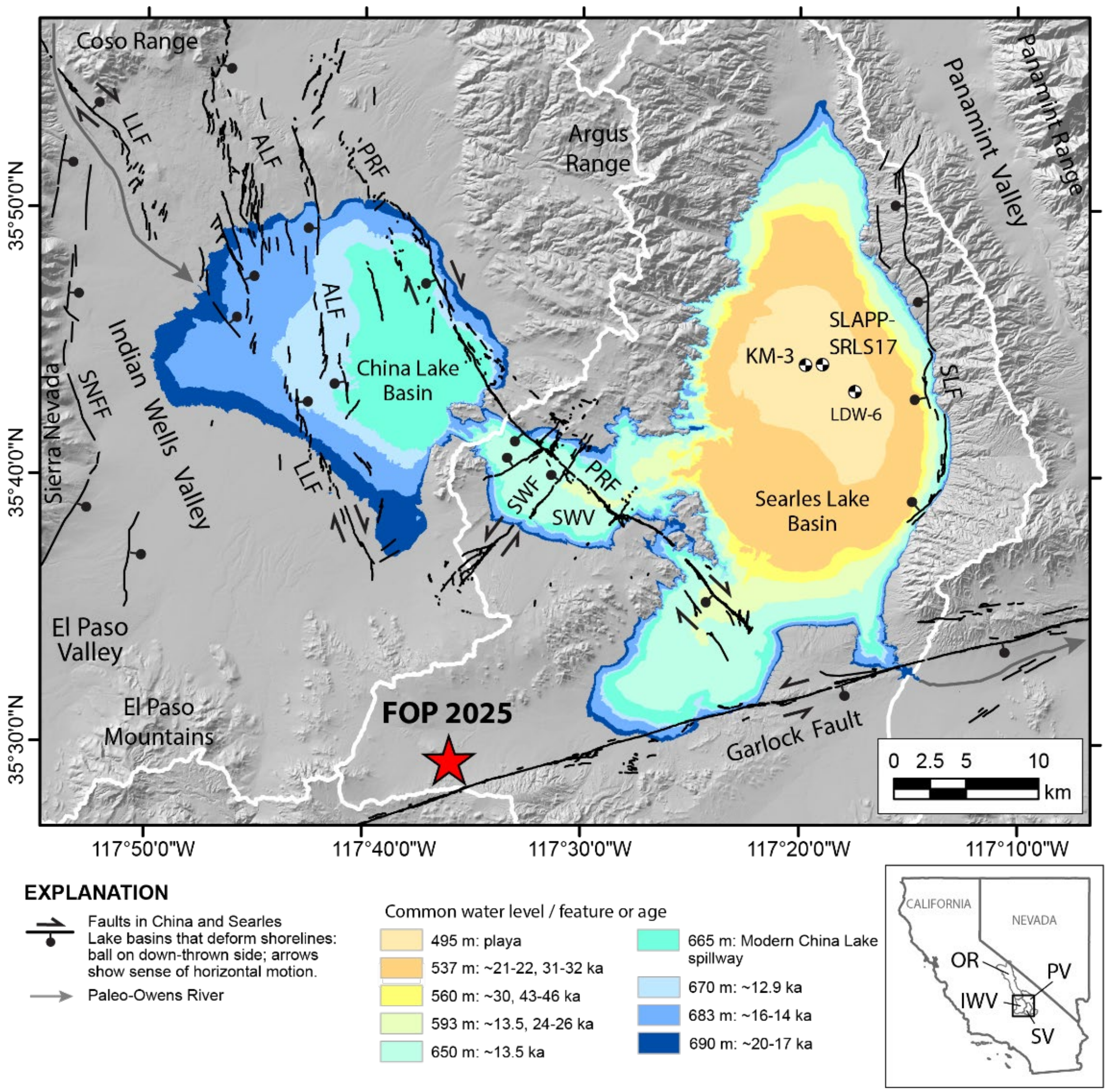

Figure I-3. *Major physiographic features within China and Searles Lakes basins and Salt Wells Valley (SWV). Unpublished water-level map showing inferred ages from the compilation of previously published outcrop evidence and lake core data (KM-3; SLAPP-SRLS17; LDW-6). Location of the primary active faults in the lake basins are also shown. Faults from USGS fault and fold database: ALF – Airport Lake fault; LLF – Little Lake fault; SLF – Searles Lake fault; SNFF – Sierra Nevada Frontal fault; and 2019 Ridgecrest earthquake surface ruptures: PRF – Paxton Ranch fault and SWF – Salt Wells fault. Red star shows FOP 2025 campsite location.*

Paleoclimate Setting and Lake-Level History

Paleo-Owens River-Lake system

The Sierra Nevada forms one of the principal rain shadows in the western U.S. with its highest crest elevations of 3400–4300 m occurring in Owens Valley, eastern California (Fig. I-2). The entire range was extensively glaciated during the Pleistocene, and many small glaciers and perennial snowfields persist in sheltered cirques at high elevations (Moore and Moring, 2013), where the last two glacial advances occurred during the Recess Peak (~14,000–12,000 yr BP) and Little Ice Age – Matthes (~250–170 cal yr BP) glaciations (Burbank, 1991; Clark and Gillespie, 1997; Bowerman and Clark, 2011; Phillips, 2016; 2017). The Owens River watershed is an ideal area for paleoclimate research because it is optimally located to record long-term atmospheric circulation patterns that modulate streamflow and lake-level variations in the western U.S. (e.g., Enzel et al., 1989; Redmond and Koch, 1991; Fig. I-2). The watershed is also sensitive to arid to semi-arid hydroclimate variability (Li et al., 2000). It is the single largest watershed draining the eastern Sierra Nevada and contains over 230 km of range crest spanning the highest elevations.

The paleo-Owens River-Lake system (ORLS) contains a robust record of climate change that is preserved in lacustrine sediment deposited by a chain of intermittently connected Pleistocene pluvial lakes in Owens Valley and progressively downstream in Indian Wells, Searles, Panamint, and Death Valleys (e.g., Smith and Pratt, 1957; Smith and Street-Perrott, 1983; Smith and Bischoff, 1997; Phillips, 2008; Fig. I-2).

Latest hydrologic connections between Owens and China-Searles Lakes basins

Pluvial Owens Lake had significant lake-level fluctuations during the Pleistocene-Holocene transition (16,000–12,000 cal yr B.P.) in response to extreme hydroclimatic variability that produced intermittent overflowing lake conditions and hydrologic connections with downstream China and Searles Lakes based on geomorphic and outcrop data (e.g., Bacon et al., 2006; Orme and Orme, 2008; Reheis et al., 2014; Rosenthal et al., 2017) and sediment-core records (e.g., Benson et al., 1997; Smith and Bischoff, 1997; Phillips, 2008).

Recent studies of past Owens Lake water-level fluctuations demonstrate that the watershed-lake system is a sensitive recorder of Holocene droughts and pluvials (Bacon et al., 2018), as well as established the first spatiotemporal connections between latest Pleistocene and early Holocene water and overflow levels by dating shoreline features and sediment in the overflow channel of Owens Lake, thereby demonstrating a far more recent hydrologic connection between Owens Lake and downstream China and Searles Lakes than previously understood. The last two overflow episodes of Owens Lake occurred during the early Holocene from ~11,000 to 10,500 cal yr BP and from ~8700 to 6500 yr BP (Bacon et al., 2020). Spill was characterized by relatively low energy surface flows, based on the type of fluvial stratigraphy and paleoenvironmental conditions documented downstream in Rose and Indian Wells Valleys (Rosenthal et al., 2017; Fig. I-2).

Motivation of current paleohydrologic research to be discussed during FOP 2025

Geomorphic features in the form of beach ridges and wave-cut platforms with corresponding elevations provide the best datums to estimate lake stage and in turn lake depth. When these types of geomorphic features are directly dated, a well constrained lake-level curve can be constructed and used in paleohydrologic modeling to infer hydroclimate change. All prominent beach ridges in Owens Lake basin have been directly dated (e.g., Bacon et al., 2020), however, there is a lack of published ages for all beach ridges in China and Searles Lake basins. Although the late Pleistocene paleohydrology of China Lake (e.g., Rosenthal et al., 2017) and Searles Lake (Smith, 2009) has previously been characterized based on a robust record of ^{14}C dating of gastropod shells and carbonate deposits in outcrops, none of the beach ridges in the basins were directly dated (Fig. I-3). Therefore, there is a large data gap in the absolute elevation and corresponding ages of late Pleistocene to Holocene water-level fluctuations downstream of Owens Lake.

Geologic mapping encompassing the playa margins of Searles Lake basin (Smith, 2009) and China Lake basin (Bacon et al., 2019) provide geomorphic evidence for latest Pleistocene to early Holocene lakes in the China-Searles Lake system. Stratigraphic evidence that supports the existence of Holocene lakes as far downstream as Searles Valley is from early sediment lake-core studies of the sedimentology and ^{14}C and ^{230}Th dating of carbonates and salt layers in cores KM-3 and LDW-6 (Peng et al., 1978; Liddicoat et al., 1980; Smith, 1979; 2009; Fig. I-3). More recent sediment lake-core studies of the mineralogy and U/Th dating in cores SLAPP-SLRS17 also provide a revised chronology since 200 ka and returned modeled salt ages of 8.5 ± 0.9 and 12.1 ± 0.8 ka for shallow lakes in the basin (Olson and Lowenstein, 2021; Olson et al., 2023; Stroup et al., 2023). The uncertainties of the new sediment core ages of shallow lakes in Searles Valley and the last two periods of overflow from Owens Lake overlap. This is compelling evidence that Owens Lake and Searles Lake may have been hydrologically connected as recently as during the early Holocene. If so, when and how deep of a lake?

The new geomorphic and stratigraphic descriptions and ^{14}C and luminescence dating presented during the fieldtrip (Day 1) are preliminary and part of an ongoing NSF project that began in August 2024. The overarching goal of the NSF project is aimed at addressing the geomorphic and stratigraphic data gaps in the ORLS by directly dating the late Pleistocene to Holocene (if any) beach ridges and associated sediment to refine previous shoreline chronologies of China and Searles Lake. These shoreline chronologies will ultimately be used as control points in another component of the NSF project involving watershed-lake paleohydrologic modeling of the ORLS to estimate changes in past precipitation and snowpack extent during the Holocene relative to historical baselines.

The 2019 Ridgecrest Earthquakes

The sequence began on July 4, 2019, when a Mw 6.4 earthquake ruptured ~14 km of the northeast-striking, left-lateral Salt Wells Valley fault (Figure I-1). One day later, a Mw 7.1 event broke ~45 km of the nearly orthogonal, northwest-striking right-lateral Paxton Ranch fault (DuRoss et al., 2020; Ponti et al., 2020; Pierce et al., 2020; Thompson Jobe et al., 2020; Rodriguez Padilla et al., 2021; Gold et al., 2021). Seismologic and geodetic studies (Barnhart et al., 2019; Ross et al., 2019; Xu et al., 2020; Magen et al., 2020) demonstrated that the two faults are kinematically linked, forming a conjugate fault system accommodating complex rupture processes. Geomorphically, the Salt Wells Valley fault is expressed as a sinuous, low-relief lineament through granitic bedrock hills and pediments, whereas the Paxton Ranch fault trends across the western part of Searles Valley, the Spangler Hills, and into the China Lake basin (Figure I-1). The 2019 Ridgecrest earthquakes emphasize the potential for multi-fault ruptures in the Walker Lane and Eastern California Shear Zone, echoing previous and subsequent large events like the 1932 Ms7.3 Cedar Mountain, 1992 Mw7.3 Landers, 1999 Mw7.1 Hector Mine, and 2020 Mw6.5 Monte Cristo Range earthquakes (Sieh et al., 1993; Bell et al., 1999; Fialko et al., 2001; Dee et al., 2021) (Figure I-1).

The 2019 Ridgecrest earthquake sequence occurred within the southern portion of the Walker Lane, an approximately 100–150 km wide zone of discontinuous and distributed faulting that accommodates 10−12 mm/yr of northwest-directed dextral shear (Dixon et al., 2000; Unruh et al., 2003; Wesnousky, 2005a; Pierce et al., 2021) (Figure I-1). The Walker Lane merges with the Eastern California Shear Zone (ECSZ) to the south, here divided across the Garlock fault, and roughly follows the California–Nevada border northward beyond the Lake Tahoe region. This broad domain absorbs approximately 15–25% of the total northwest directed shear of the Pacific–North America plate boundary, while the San Andreas system carries the remainder (Wesnousky, 2005b). Throughout the Walker Lane/ECSZ corridor, multiple fault systems display a mix of right-lateral, left-lateral, and normal to oblique slip, reflecting the complex kinematics of transtensional shear (Dokka and Travis, 1990; Wesnousky et al., 2012; Pierce et al., 2021). Conjugate fault systems are common throughout the Walker Lane (e.g., Hatch et al., 2019; Pierce and Koehler, 2023).

The southern Walker Lane is characterized by a series of major north-northwest trending basins including Owens, Searles, Panamint, and Death Valleys. Each of these basins contains both north-striking normal faults (primarily west dipping aside from the eastern margin of the Sierra Nevada) and northwest-striking strike-slip faults. Collectively, these major fault systems—Owens Valley, Panamint Valley, Searles Valley, and others—accommodate the transtensional motion between the Sierra Nevada microplate, the Garlock fault, and the southern Basin and Range province.

Major nearby faults:

1. Garlock Fault

The Garlock fault divides the southern Walker Lane from the Eastern California Shear Zone (ECSZ) and is one of the most prominent left-lateral strike-slip faults in California. Extending for over 250 km from near the San Andreas fault in the west to the southern Basin and Range in the east, it generally strikes east–west, although local bends and stepovers occur (Dawson et al., 2003; Rittase et al., 2014). Slip-rate estimates vary along strike, and have dramatically varied in time through the Holocene from ~3-13 mm/yr (Dolan et al., 2016; Fougere et al., 2024). Paleoseismic trenching studies have documented multiple Holocene surface-rupturing earthquakes, but the Garlock fault has not produced a major historical event (Dawson et al., 2003). Static and dynamic triggering of small earthquakes along the Garlock fault by nearby large ECSZ events, including the 1992 Landers and 2019 Ridgecrest sequences (Hill et al., 1993; Ramos et al., 2020).

2. Owens Valley Fault

North of Ridgecrest, the Owens Valley fault system trends roughly north–south along the eastern side of the Sierra Nevada. This zone famously ruptured in 1872 during the M7.4–7.9 Owens Valley earthquake (Beanland and Clark, 1994). The fault is predominantly right-lateral strike-slip, though it also exhibits local normal or oblique components in places, with a late Quaternary slip rate of 0.6-1.6 mm/yr (Haddon et al., 2016). Paleoseismic and historical investigations indicate multiple late Pleistocene to Holocene events, including the 1872 rupture that formed prominent scarps visible along much of the valley (Bacon and Pezzopane, 2007; Kirby et al., 2008; Amos et al., 2013; Haddon et al., 2016).

3. Panamint Valley Fault

The Panamint Valley fault is a major range-bounding normal and oblique-slip fault that defines the eastern margin of the Panamint Range and the western margin of Panamint Valley. It trends broadly NW–SE, parallel to other Walker Lane structures. Although large historical events on the Panamint Valley fault are not documented, geomorphic and paleoseismic evidence indicates multiple late Quaternary fault scarps and associated earthquake activity with a slip rate of 1.75-2 mm/yr (Hoffman, 2009; McAuliffe et al., 2013; Choi, 2016).

4. Searles Valley-Tank Canyon Fault

Immediately east of the Paxton Ranch fault lies Searles Valley, bounded by the southern Slate Range to the east, and the Argus Mountains and the Spangler Hills to the west and southwest, respectively (Figure I-1). The Searles Valley-Tank Canyon fault system includes a set of subparallel and oblique-slip faults that cut across the eastern margin of the basin and exhibit both strike-slip and normal displacement at a rate of 0.2-0.3 mm/yr (Numelin et al., 2007).

Relationship of the 2019 Ruptures to Regional Structures

The two faults that ruptured during the 2019 Ridgecrest sequence—the NE-striking Salt Wells Valley fault and the NW-striking Paxton Ranch fault—are immediately north of the Garlock fault (Figure I-1). Notably, the Paxton Ranch fault trends toward the broader Walker Lane and Eastern California Shear Zone (including the Airport Lake, Blackwater, Lenwood, and Helendale faults), whereas the Salt Wells Valley fault aligns more closely with the western part of the Garlock fault, prior to its more eastward bend near Koehn Lake (Dawson et al., 2003). In contrast with the other major faults in this part of the Southern Walker Lane, the Paxton Ranch fault is not associated with a major fault-bounded mountain range. The conjugate geometry of the Salt Wells Valley and Paxton Ranch faults highlights the complex stress regime that persists in the region, influenced by the oblique plate boundary motion and the interaction of multiple fault systems with varying orientations.

Day 1 Stop 1

Field Stop Leaders: Fred Phillips[1], Steven Bacon[2], Maggie Duncan[2], and Kathleen Rodrigues[2], and ([1]New Mexico Institute of Mining and Technology; [2]Desert Research Institute, Reno, Nevada;)

LOGISTICS

After turning right onto Stockwell Mine Road, continue another 1.2 miles on a well-graded dirt road to our destination. The dirt road traverses the central portion of the Valley Wells beach ridge complex that will be the primary focus of one of the presentations at the stop. Park on the shoulder of the dirt road. Bring a chair to enhance your level of comfort at Stop 1 because we plan to give three presentations for you to enjoy.

The goals of Stop 1 are to: (1a) introduce the history and broad perspective of paleoclimate research in Searles Valley and the paleo-Owens River system (Phillips); (1b) present preliminary lake-level reconstructions of China and Searles Lakes in relation to the overflow history of Owens Lake (Bacon); and (1c) present new stratigraphic descriptions and preliminary luminescence ages of the Valley Wells beach ridge complex, northern Searles basin (Duncan, Bacon, Rodrigues).

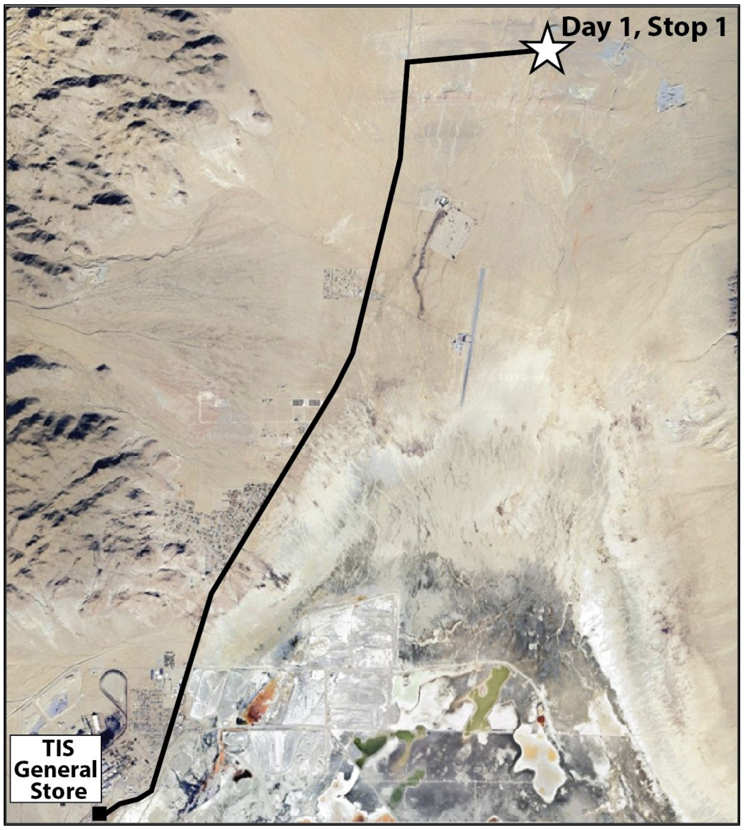

Route to Day 1, Stop 1 from the TIS General Store and Gas Station in Trona.

Discussion (A) Searles Lake, California: A paleoclimatic archive

Field Stop Leader: Fred Phillips (New Mexico Institute of Mining and Technology, Socorro, NM)

Introduction

The first stop on the 2025 Friends of the Pleistocene, Pacific Cell, Annual Field Trip is on a high beach ridge of Pleistocene Searles Lake. The main presentation at that location, by Steve Bacon, will highlight recent work on shorelines and outcrops that elucidate the lake-level history of this basin and associated ones in the ancient Owens River system. The purpose of this short note is to remind readers that Searles and associated basins contain an exceptional record of paleoclimatic history, much of it in the subsurface, and to give a brief overview of the findings of numerous studies.

One aspect of the paleo-Owens River system that enhances the paleoclimatic record is that the vast majority of the runoff supplying the system comes from the eastern slope of the Sierra Nevada. Runoff first flowed into Owens Lake, from there into China Lake, and then Searles Valley, Panamint Valley, and finally Death Valley (Figure 1-1a-1). These basins are successively more arid in the downstream direction. This means that the basins downstream of China Lake contributed very small amounts of runoff compared to the Sierra Nevada, greatly simplifying the paleohydrology of the system.

For lakes forming essentially a single bowl, like the Great Salt Lake, the most recent high lake cycle typically wipes out the shorelines formed during earlier cycles. Paleoclimatologists must therefore rely on subsurface proxy data from drill cores. Cores have the advantage that they provide a much more continuous record than shorelines, but they require that ancient lake levels be inferred from proxy information rather than measured directly on outcrops and this adds a great deal of uncertainty. Lake Lahontan, the other very large late Pleistocene lake of the Great Basin, was formed of numerous sub-basins that all received significant runoff and that overflowed into one another in a complex fashion, adding significantly to the difficulty of paleoclimatic reconstruction.

Long and reasonably continuous sediment cores have been recovered from most of the basins in the paleo-Owens system, but in this lake system the proxy data from cores can be compared with shoreline positions older than the last lake cycle because downstream basins preserve a shoreline record of the intervals of exceptional wetness prior to the most recent lake cycle. This combination of availability of sediment cores, an exceptionally long shoreline record that highlights times of unusual wetness, and the simplicity of interpreting the climatic significance of the lake-level history make the paleo-

Owens system, and Searles Lake in particular, an exceptionally fruitful locality for paleoclimatology.

Historical background

Although several short notes were published on the saline deposits of the Searles basin around the turn of the 20th Century, the real starting point is the work of H.S. Gale (1914a; 1914b). In two remarkably prescient reports, Gale recognized the interconnectedness of the entire paleo-Owens system, the particular significance of Searles Valley, and the linkage between ‘ice ages’ in the Sierra Nevada and the expansion of the desert lakes.

Elliot Blackwelder had previously laid the foundations for understanding the glacial record of the Sierra Nevada. He (Blackwelder, 1941; Blackwelder, 1954) attempted to relate the lacustrine and glacial histories. He inferred that Searles basin contained a series of lower shorelines that were correlative with the most recent (Tioga) glaciation and that a shoreline at the overflow level correlated to the penultimate (Tahoe) glaciation. Subsequent, far more detailed, research has corroborated his early inference.

U. S. GEOLOGICAL SURVEY BULLETIN 580 PLATE V

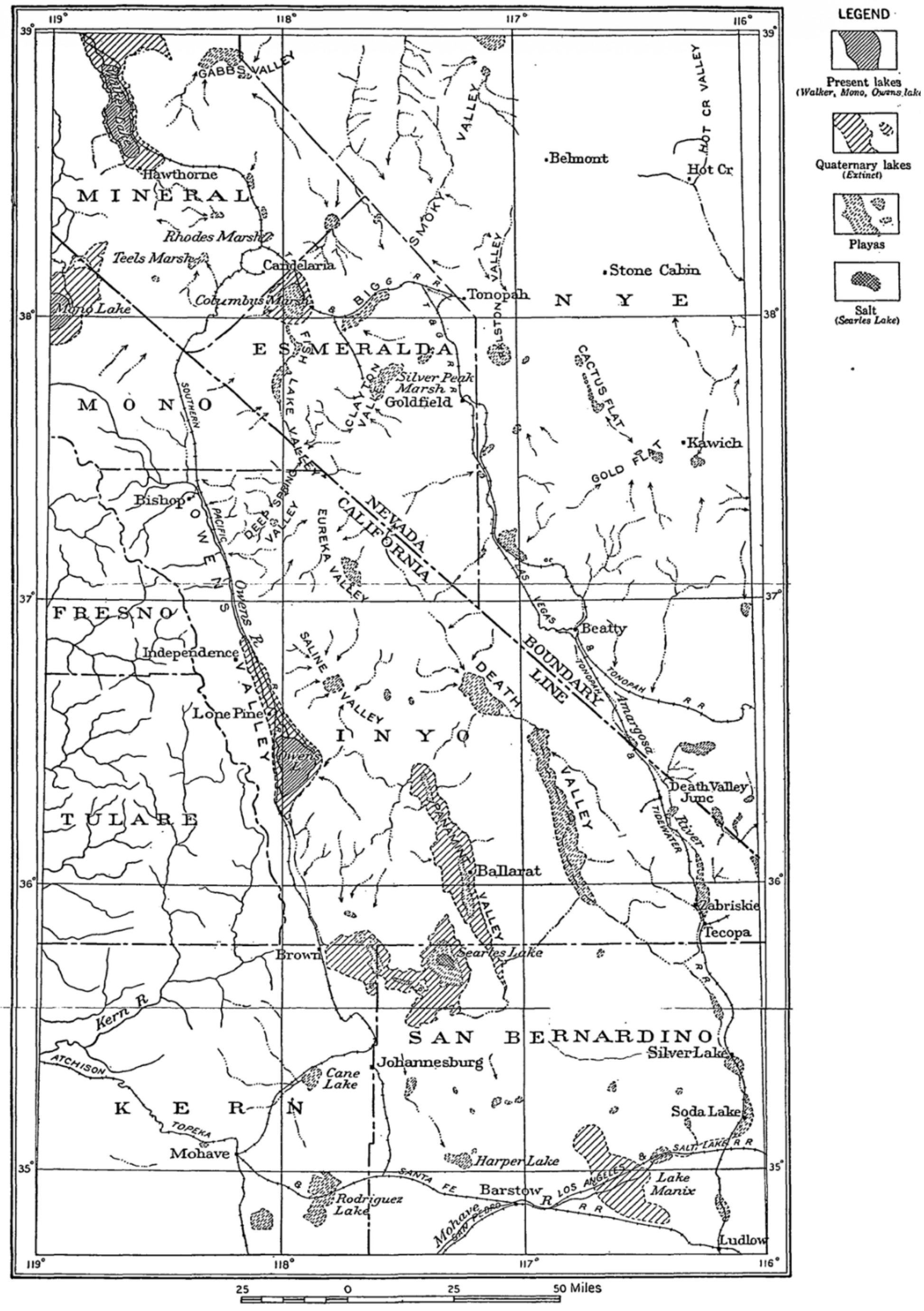

INDEX MAP SHOWING THE GENERAL POSITION OF THE OWENS-SEARLES-PANAMINT LAKE SYSTEM, CALIFORNIA.

Figure 1-1a-1. Plate V from Gale (1914b), showing both the extent of the modern lakes and playas and the reconstructed extent of Pleistocene pluvial lakes.

George I. Smith of the US Geological Survey began working on drill cores from Searles Lake in the late 1950's. The work was motivated by the search for lithium deposits, not related to batteries but rather to the use of lithium in nuclear reactors and nuclear weapons. Smith, however, recognized the great paleoclimatic value of drill cores from the paleo-Owens River system. He discovered that, in order to better understand its mineral reserves, Kerr-McGee Corporation had drilled a large-diameter core from the surface to bedrock and had performed exhaustive chemical analyses of the core. The company was amenable to using the core for scientific investigations and publication of results from the core. He laid the foundations for interpretation of the geochemical record of the Searles evaporites and clastic sediments in a USGS Professional Paper in 1979 (Smith, 1979). In Smith et al. (1983) he published the geochemical data and an interpretation of its paleoclimatic significance. The difficulty of dating of this core, and other cores from the various lakes in the system, has long been a major impediment to paleoclimatic utilization. That same year I co-published with him a first attempt at using 36Cl to date the core (Phillips et al., 1983). This was followed up by Jannik et al. (1991) that combined ^{36}Cl with several other dating methods to obtain a chronology for the lake sediments and a lake-level history back to 2 Ma. Two critically important dating methods were paleomagnetic correlation (Liddicoat et al., 1980) and U/Th (Bischoff et al., 1985). That history indicated that Searles Lake had been the usual terminal lake for the Owens River, with only possibly six relatively brief intervals of overflow from Searles to Panamint Valley in the past 1 Myr. Phillips et al. (1992) measured stable isotopes on carbonate-containing minerals in the KM-3 core and related a lake-level history generated by modeling the isotopes to the global marine oxygen-18 record of sea level and glaciation.

Lake histories using sediment cores

In 1992, a 323-m long core was drilled near the center of Owens Lake. Results from analysis of this core were published by Smith and Bischoff (1997). They included sedimentology, geochemistry, radiocarbon ages, data from a limited number of tephras, diatoms, ostracodes, and pollen. The presence of both the Bishop ash and the Matuyama-Brunhes paleomagnetic reversal near the bottom of the core indicated that the sediments spanned the last ~800,000 kyr. The results from the various studies performed on the core were consistent with the lacustrine-system history derived from core KM-3 at Searles Lake: that Owens Lake had overflowed for at least half of the past 800,000 kyr. No true evaporite minerals were found, indicating that the preponderance of solutes carried by the Owens River ended up in Searles Lake. Fluctuations in the $CaCO_3$ content, however, indicated large fluctuations in the inflow/outflow ratio over time. Bischoff et al. (1997), Menking et al. (1997), and Bischoff and Cummins (2001) attempted to reconstruct the extent of glaciers in the Sierra Nevada and corresponding variations in climatic wetness based on data from OL-92. Litwin et al. (1999) published pollen profiles measured both from OL-92 and core LDW-6 from Searles Lake. In considerable part, they used these to refine the chronology of Searles Lake, but also to analyze climate history.

The sampling interval on the OL-92 core was relatively large, leading to fairly coarse temporal resolution. Larry Benson and coworkers, in a series of papers (Benson et al., 1996; Phillips et al., 1996; Benson et al., 1997; Benson et al., 1998) analyzed at much shorter intervals other cores also drilled at Owens Lake in the early 1990's. These produced high-resolution time series of stable isotopes, geochemistry, and paleomagnetic properties. These time series were used as proxies for relative wetness and glacial extent and were compared with global ice-sheet/sea-level records to infer controls on continental climate. Li et al. (2004) went back to OL-92 and sampled at high resolution for the interval 160 to 60 ka and used the data to infer intervals of open and closed lake conditions. Similarly, Peaple et al. (2024) used samples from KM-3 to reconstruct temperature, stable isotope composition and other parameters for the period 3.6 to 2.4 Ma.

In 2017, two new cores, SLAPP-SRLS17-1A and -1B were drilled near the center of Searles Lake, recovering core to a depth of 76.7 m, corresponding to ~200 ka. Olson and Lowenstein (2021) used detailed mineralogical analyses of these cores to revisit one of G.I. Smith's original tools for lacustrine reconstruction: thermodynamics of evaporite precipitation and diagenesis. The results indicated that Searles Lake had been a perennial lake from 32 to 6 ka and explained anomalies in the evaporite sequences. Following up on this, Olson et al. (2023) used new techniques (Brillouin thermometry and branched glycerol dialkyl glycerol tetraether paleothermometry) to reconstruct Searles Lake temperatures from 42 to 6 ka. Stroup et al. (2023) performed 98 U/Th dating measurements on the SLAPP-SRLS17 core. These were used to construct an age/depth curve for the core. This demonstrated that the beginning of the deposition of the 'Bottom Mud', a thick interval without evaporites, indicating high lake levels, was at 178 ka, very close to the start of Marine Isotope Stage (MIS) 6. Deposition of less-soluble evaporites resumed at 39 ka. The 'Parting Mud', another evaporite-free interval, was dated to 22.5 to ~14 ka, indicative of the duration of the lake high stand associated with the last glacial maximum. Peaple et al. (2022) culminated this avalanche of new data and interpretations by measuring pollen, d^{2}H and d^{13}C in plant wax, and nine biomarker compounds influenced by temperature, salinity, stratification, productivity, and other properties. In general, these new paleoclimate records are in good agreement with independent time series of stable-isotope composition and relative wetness in the region.

Lake histories from outcrop data

As mentioned above, the opportunity to compare lake histories inferred from proxies in sediment cores with direct evidence for lake levels provided by ancient shorelines and associated deposits provides an invaluable ‘reality check’. Unfortunately, outcrop-based studies in the paleo-Owens River system have been sparse in comparison to the core-based ones.

The paleolake studies of Gale and Blackwelder, mentioned in the ‘Historical Background’ section above, were largely based on geomorphological observations and they captured the essentials of lacustrine history over the past several hundred thousand years. At the time that G.I. Smith was performing his notable research on KM-3 and other cores, another Smith, R.S.U. Smith, was completing his Ph.D. dissertation (Smith, 1976) on lacustrine outcrops in Panamint Valley. That dissertation has provided the foundation for all subsequent outcrop studies of the late Quaternary history of Panamint Valley. G.I. had been performing extensive mapping and outcrop studies and in Smith (1987) published a very small portion of that. This short field-trip guide provides an excellent overview of Searles Lake history and I highly recommend it to participants in the 2025 FOP trip. G.I. Smith’s *opus magnum* of Searles Valley Quaternary geology “Late Cenozoic geology and lacustrine history of Searles Valley, Inyo and San Bernadino Counties, California” was published posthumusly (Smith, 2009).

Steve Bacon has assiduously pursued the surficial late Quaternary record of the Owens Lake basin (Bacon et al., 2006; Jayko and Bacon, 2008; Bacon et al., 2018; Bacon et al., 2020). He will present those results, plus new ones integrating Owens Lake with China and Searles Lakes, during this field-trip stop. Rosenthal et al. (2017) utilized data from archeological investigations to provide a lake-level curve for the Indian Wells Valley (China Lake basin). Panamint Valley has seen little surficial geology with a paleoclimatic emphasis since R.S.U. Smith. The major contribution to both mapping and chronology is Jayko et al. (2008). Additional work on the tectonics, soils-geomorphology, and luminescence dating of alluvial fans and beach ridges in Panamint Valley was highlighted on the 2016 FOP lead by Eric Kirby and Eric McDonald.

Syntheses of the Paleo-Owens River history

Gale (1914a) and (Gale, 1914b) made a remarkably prescient, although sketchy, attempt at reconstructing the lacustrine history of the system, followed by Blackwelder (1954). G.I. Smith published several reconstructions of the system history, notably Smith (1979), Smith et al. (1983), Smith and Street-Perrott (1983), and Smith (2009). Jannik et al. (1991b) attempted a salt-balance history of the paleo-Owens River system. Phillips (2008) is an extensive exploration, starting in the Pliocene. The most recent contribution, covering the past 200 kyr, is Lowenstein et al. (2024), which has for the first time provided solid documentation of an Owens-Death Valley connection at the end of MIS 6. It draws upon all of the recent evidence derived from analysis of the new SLAPP-SRLS17 core.

The paleo-Owens River system, with Searles Lake as its centerpiece, has provided one of the most varied and detailed paleoenvironmental records anywhere in the world. The most recent studies have added a great deal to our understanding. What are the next steps?

One topic that has been relatively neglected is the lacustrine history prior to ~200 ka (i.e., the base of SLAPP-SRLS17). A new Searles Lake core to several hundred meters could enable the new analytical techniques that have been so productive on SLAPP-SRLS17 to be applied to the earlier portions of the sediment column.

Another neglected area is detailed surficial geology of Panamint Valley. Jannik et al. (1991) provided evidence that there may have been two or three overflows of Searles Lake into Panamint Valley between ~700 and 200 ka. If so, it is likely that a record of these can be found in the sediments of Panamint Valley.

Searles Valley and the rest of the paleo-Owens River system have made an enormous contribution to understanding the paleoclimate history of the western United States. There is little doubt that further investigations have the potential to extend that detailed record far back in time.

References

Bacon S. N., Burke R. M., Pezzopane S. K., and Jayko A. S. (2006) Last glacial maximum and Holocene lake levels of Owens Lake, eastern California, USA: *Quaternary Science Reviews* **25** 1264-1282.

Bacon S. N., Lancaster N., Stine S., Rhodes E. J., and McCarley Holder G. A. (2018) A continuous 4000-year lake-level record of Owens Lake, south-central Sierra Nevada, California, USA: *Quaternary Research* **90**(2) 276-302.

Bacon S. N., Jayko A. S., Owen L. A., Lindvall S. C., Rhodes E. J., Schumer R. A., and Decker D. L. (2020) A 50,000-year record of lake-level variations and overflow from Owens Lake, eastern California, USA: *Quaternary Science Reviews* **238** 106312.

Benson L., Burdett J., Lund S., Kashgarian M., and Mensing S. (1997) Nearly synchronous climate change in the Northern Hemisphere during the last glacial termination: *Nature* **388** 263-265.

Benson L. V., Burdett J. W., Kashgarian M., Lund S. P., Phillips F. M., and Rye R. O. (1996) Climatic and hydrologic oscillations in the Owens Lake Basin and adjacent Sierra Nevada, California: *Science* **274** 746-749.

Benson L. V., May H. M., Antweiler R. C., Brinton T. I., Kashgarian M., Smoot J. P., and Lund S. P. (1998) Continuous lake-sediment records of glaciation in the Sierra Nevada between 52,600 and 12,500 14C yr B.P: *Quaternary Research* **50** 113-127.

Bischoff J. L. and Cummins K. (2001) Wisconsin glaciation of the Sierra Nevada (79,000 - 15,000 yr BP) as recorded by rock flour in sediments of Owens Lake, California: *Quaternary Research* **55** 14-24.

Bischoff J. L., Menking K. M., Fitts J. P., and Fitzpatrick J. A. (1997) Climatic oscillations 10,000-155,000 yr B.P. at Owens Lake, California reflected in glacial rock flour abundance and lake salinity in Core OL-92: *Quaternary Research* **48** 313-325.

Bischoff J. L., Rosenbauer R. J., and Smith G. I. (1985) Uranium-series dating of sediments from Searles Lake : Differences between continental and marine climate records: *Science* **227** 1222-1224.

Blackwelder E. (1941) Lakes of two ages in Searles basin: *Geological Society of America Bulletin* **52** 1943-1944.

Blackwelder E. (1954) Pleistocene lakes and drainage in the Mojave region, southern California: In *Bulletin of the California Division of Mines 170*, In *Geology of Southern California* (R. H. Jahns; ed.), California Division of Mines and Geology, San Francisco, pp. 35-40.

Gale H. S. (1914a) Notes on the Quaternary lakes of the Great Basin, with special references to the deposition of potash and other salines: U.S. Geological Survey Bulletin 540, 399-475 pp.

Gale H. S. (1914b) Salines in the Owens, Searles, and Panamint Basins, Southeastern California: U.S. Geological Survey Bulletin 580-L, 251-323 pp.

Jannik N. O., Phillips F. M., Smith G. I., and Elmore D. (1991) A ^{36}C1 chronology of lacustrine sedimentation in the Pleistocene Owens River Systems, Eastern California: *Geological Society of America Bulletin* **103** 1146-1159.

Jayko A. S. and Bacon S. N. (2008) Late Quaternary, MIS 6-8 shoreline features of pluvial Owens Lake, Owens Valley, eastern California: Implications for paleohydrology of the Owens River System, In *Late Cenozoic Drainage History of the Southwestern Great Basin and Lower Colorado River Region: Geologic and Biotic Perspectives* (M. C. Reheis, R. Hershler, and D. M. Miller; eds.), Geological Society of America Speical Paper 439, Boulder, Colorado, pp. 185-206.

Jayko A. S., Forester R. M., Yount J. C., Kaufman D., McGeehin J., Phillips F. M., and Mahan S. A. (2008) Late Pleistocene lakes and wetlands, Panamint Valley, California, In *Late Cenozoic Drainage History of the Southwestern Great Basin and Lower Colorado River Region: Geologic and Biotic Perspectives* (M. C. Reheis, R. Hershler, and D. M. Miller; eds.), Geological Society of America Special Paper 439, Boulder, Colorado, pp. 151-184.

Li H.-C., Bischoff J. L., Ku T.-L., and Zhu Z.-Y. (2004) Climate and hydrology of the Last Interglaciation (MIS 5) in Owens Basin, California: isotopic and geochemical evidence from core OL-92: *Quaternary Science Reviews* **23**(1-2) 49-63.

Liddicoat J. C., Opdyke N. D., and Smith G. I. (1980) Paleomagnetic polarity in a 930-m core from Searles Valley, California: *Nature* **286** 22-25.

Litwin R. J., Smoot J. P., Durika N. J., and Smith G. I. (1999) Calibrating Late Quaternary terrestrial climate signals: radiometrically dated pollen evidence from the southern Sierra Nevada, USA: *Quaternary Science Reviews* **18** 1151-1171.

Lowenstein T. K., Olson K. J., Stewart B. W., McGee D., Stroup J. S., Hudson A. M., Wendt K. A., Peaple M. D., Feakins S. J., Bhattacharya T., and Lund S. (2024) Unified 200 kyr paleohydrologic history of the Southern Great Basin: Death Valley, Searles Valley, Owens Valley and the Devils Hole cave: *Quaternary Science Reviews* **336** 108751.

Menking K. M., Bischoff J. L., Fitzpatrick J. A., Burdette J. W., and Rye R. O. (1997) Climatic/hydrologic oscillations since 155,000 yr B.P. at Owens Lake, California, reflected in abundance and stable isotope composition of sediment carbonate: *Quaternary Research* **48** 58-68.

Olson K. J., Guillerm E., Peaple M. D., Lowenstein T. K., Gardien V., Caupin F., Feakins S. J., Tierney J. E., Stroup J., Lund S., and McGee D. (2023) Application of Brillouin thermometry to latest Pleistocene and Holocene halite from Searles Lake, California, USA: *Earth and Planetary Science Letters* **602** 117913.

Olson K. J. and Lowenstein T. K. (2021) Searles Lake evaporite sequences: Indicators of late Pleistocene/Holocene lake temperatures, brine evolution, and pCO2: *Geological Society of America Bulletin* **133**(11-12) 2319-2334.

Peaple M. D., Bhattacharya T., Lowenstein T. K., McGee D., Olson K. J., Stroup J. S., Tierney J. E., and Feakins S. J. (2022) Biomarker and Pollen Evidence for Late Pleistocene Pluvials in the Mojave Desert: *Paleoceanography and Paleoclimatology* **37**(10) e2022PA004471.

Peaple M. D., Bhattacharya T., Tierney J. E., Knott J. R., Lowenstein T. K., and Feakins S. J. (2024) Biomarker Evidence for an MIS M2 Glacial-Pluvial in the Mojave Desert Before Warming and Drying in the Late Pliocene: *Paleoceanography and Paleoclimatology* **39**(1) e2023PA004687.

Phillips F. M. (2008) Geological and hydrological history of the paleo-Owens River drainage since the late Miocene, Special Paper 439, In *Late Cenozoic Drainage History of the Southwestern Great Basin and Lower Colorado River Region: Geologic and Biotic Perspectives* (M. C. Reheis, R. Hershler, and D. M. Miller; eds.), Geological Society of America, Boulder, Colorado, pp. 115-150.

Phillips F. M., Campbell A. R., Kruger C., Johnson P., Roberts R., and Keyes E. (1992) A reconstruction of the response of the water balance in western United States lake basins to climatic change: New Mexico Water Resources Research Institute, 269, Las Cruces, New Mexico, 167 pp.

Phillips F. M., Smith G. I., Bentley H. W., Elmore D., and Gove H. E. (1983) Chlorine-36 dating of saline sediments : Preliminary results from Searles Lake, California: *Science* **222** 925-927.

Phillips F. M., Zreda M. G., Benson L. V., Plummer M. A., Elmore D., and Sharma P. (1996) Chronology for fluctuations in late Pleistocene Sierra Nevada glaciers and lakes: *Science* **274** 749-751.

Rosenthal J. S., Meyer J., Palacios-Fest M. R., Young D. C., Ugan A., Byrd B. F., Gobalet K., and Giacomo J. (2017) Paleohydrology of China Lake basin and the context of early human occupation in the northwestern Mojave Desert, USA: *Quaternary Science Reviews* **167** 112-139.

Smith G. I. (1979) Subsurface stratigraphy and geochemistry of late Quaternary evaporites, Searles Lake, California: U.S. Geological Survey Professional Paper 1043, 122 pp.

Smith G. I. (1987) Searles Valley, California: outcrop evidence of a Pleistocene lake and its fluctuations, limnology, and climatic significance, In *Centennial Field Guide, Cordilleran Section, Vol. 1* (M. L. Hill; ed.), Geological Society of America, Boulder, Colorado, pp. 137-142.

Smith G. I. (2009) Late Cenozoic geology and lacustrine history of Searles Valley, Inyo and San Bernadino Counties, California: U.S. Geological Survey Professional Paper 1727.

Smith G. I., Barczak V. J., Moulton G. F., and Liddicoat J. C. (1983) Core KM-3, a surface-to-bedrock record of late Cenozoic sedimentation in Searles Valley, California: U.S. Geological Survey Professional Paper 1256, 24 pp.

Smith G. I. and Bischoff J. L., eds. (1997) *An 800,000-year paleoclimatic record from Core OL-92, Owens Lake, southeast California*, Geological Society of America Special Paper 317, Boulder, Colorado, 165 pp.

Smith G. I. and Street-Perrott F. A. (1983) Pluvial lakes of the Western United States: In *Late Quaternary environments of the United States*, Vol. 1, In *The Late Pleistocene* (H. E. Wright, Jr.; ed.), University of Minnesota Press, Minneapolis, pp. 190-211.

Smith R. S. U. (1976) Late-Quaternary pluvial and tectonic history of Panamint Valley, Inyo and San Bernadino Counties, California: Ph.D. dissertation, California Institute of Technology, Pasadena, 295 pp.

Stroup J. S., Olson K. J., Lowenstein T. K., Jost A. B., Mosher H. M., Peaple M. D., Feakins S. J., Chen C. Y., Lund S. P., and McGee D. (2023) A >200 ka U-Th Based Chronology From Lacustrine Evaporites, Searles Lake, CA: *Geochemistry, Geophysics, Geosystems* **24**(3) e2022GC010685.

Discussion (B) Hydrogeomorphic setting and preliminary lake-level reconstructions of China and Searles Lakes

Field Stop Leader: Steven Bacon (Desert Research Institute, Division of Hydrologic Sciences, Reno, NV)

Introduction

During much of the middle to late Pleistocene, Owens Lake was a perennial freshwater lake that periodically overflowed its sill to form a chain of lakes occupying one or more successively lower-altitude basins in Indian Wells Valley, Searles Valley, and Panamint Valley (e.g., Smith and Street-Perrott, 1983; Smith and Bischoff, 1997). The Owens River watershed supplied most of the streamflow to the lower chain of lakes, although at times during extreme pluvials (e.g., MIS 6: ~140 ka), Lake Russell in Mono basin has intermittently overflowed to become the northernmost lake while Lake Manly in Death Valley formed the terminal lake in the Paleo-Owens River system (e.g., Reheis et al., 2002).

The primary goal of Stop 1b is to present preliminary analysis and existing data to evaluate temporal correspondence between the overflow history of Owens Lake and newly refined and preliminary lake-level histories of China and Searles Lakes over the past 50,000 years. The hydrogeomorphic settings of China and Searles basins along with the sources of information and approach used to reconstruct water levels from available and new geochronologic data will also be presented followed by a summary of the overflow history of Owens Lake.

Hydrogeomorphic setting of China and Searles basins

China Lake basin

The Indian Wells Valley watershed includes Rose Valley and China Lake basin, which collectively are tectonic grabens along the southeastern Sierra Nevada. The watershed has a drainage area of ~3390 km^2 and is bounded by the Sierra Nevada on the west, the Argus Range on the east, the Coso Range volcanic complex on the north, and the El Paso Mountains on the south (Figure 1-1b-1). The southern Sierra Nevada is the highest range in the watershed with elevations up to ~2990 m. Although the range has a strong orographic effect on the distribution of precipitation across the valley, the overall elevations are too low to accumulate perennial snow and geomorphic evidence along the crest indicates a lack of glaciation (e.g., Moore and Moring, 2013). The northern and southeastern parts of the watershed share drainage divides with the Owens River and Searles Valley watersheds, respectively. The depocenter of the lake basin is at an elevation of ~657 m and consists of an irregular shaped playa with an area of ~20 km^2 that is surrounded by distal alluvial fans and a variety of eolian features. The channel of the paleo-Owens River flows from Rose Valley, where a faulted and dissected late Pleistocene fan-delta complex with a surface modified by eolian processes is present near the inlet of the lake basin (Bullard et al., 2019; Bacon et al., 2019).

Evidence of former lake levels is present in the lake basin at and above the modern sill at an elevation of ~665 m. Preserved shorelines consist of isolated beaches, beach ridges, spits, and tombolos, as well as wave-formed scarps developed on both alluvial fans and on the flanks of bedrock hills (Rosenthal et al., 2017). These scattered shoreline remnants commonly are preserved in the northeastern and eastern sectors of the lake basin at ~665, 670, and 683 m, and up to the China-Searles Lake overflow level of ~690 m (Rosenthal et al., 2017; Figure 1-1b-2). Based on geomorphic mapping, erosional shoreline remnants developed on alluvial fans are also identified at elevations of 700–705 m in the eastern sector of the lake basin indicating possible evidence for higher and older lake levels (Bullard et al., 2019; Bacon et al., 2019).

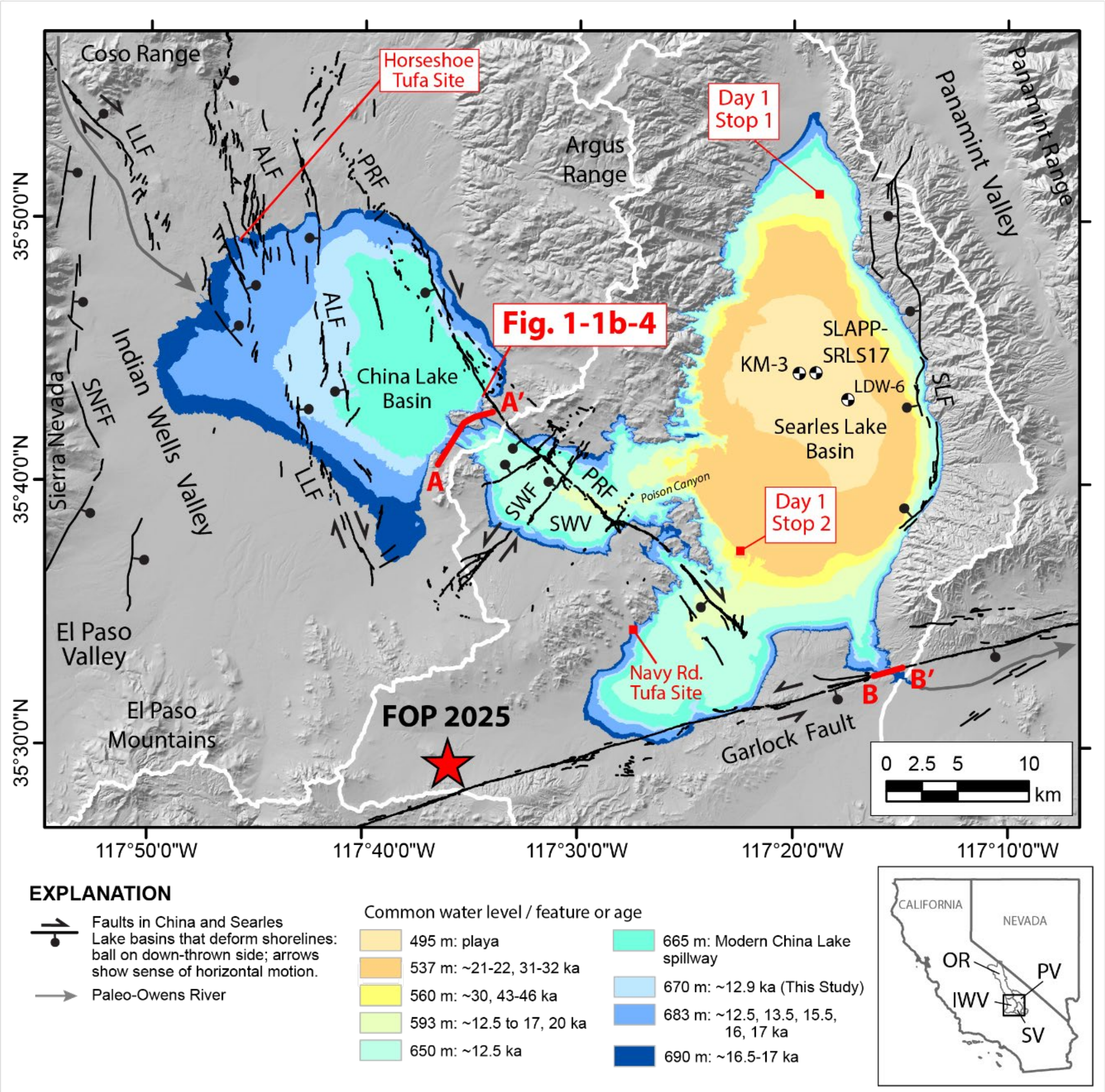

Figure 1-1b-1. Major physiographic features and unpublished water-level map of China and Searles Lake basins showing inferred ages from outcrop evidence and lake core data (KM-3; SLAPP-SRLS17; LDW-6). Location of primary active faults in the lake basins are also shown. SWV – Salt Wells Valley. Faults: ALF – Airport Lake fault; LLF – Little Lake fault; SLF – Searles Lake fault; SNFF – Sierra Nevada Frontal fault; and 2019 Ridgecrest earthquake surface ruptures: PRF – Paxton Ranch fault and SWF – Salt Wells fault. Location of transects A-A' and B-B' across the sills of China and Searles Lake basins, respectively, are shown. The location of the FOP campsite (red star), Day 1: Stops 1 and 2, and notable Tufa Sites are also shown.

Spillway of China Lake basin

China Lake occupies a topographically closed basin contained by a modern sill at ~665 m across its drainage divide (Smith and Street-Perrott, 1983). The overflow channel at the modern sill location is buried by alluvium and eolian deposits, thereby obscuring geomorphic evidence of shoreline and fluvial features related to the latest period of overflow across the drainage divide (Rosenthal et al., 2017). Two groundwater monitoring wells drilled in the sill area encountered an ~11 and 14 m thick section of fine to medium sand underlain by bedrock (Kunkel and Chase, 1969), indicating that bedrock in the overflow channel ranges in elevation from ~651 to 654 m, about 3–6 m below the lowest elevation of the modern playa. The subsurface data demonstrates that the current sill is “soft” and likely composed of alluvium, windblown sand, and/or shoreline deposits (Rosenthal et al., 2017). East of the drainage divide within Salt Wells Valley, however, geomorphic evidence for the overflow channel is in the form of a well-developed and deeply incised linear channel that has developed from headward erosion into mostly unconsolidated sandy sediment across the drainage divide.

A transverse topographic profile across the entire length of the sill area from a 10 m DEM was used to identify geomorphic features that coincide with the range of elevations of shorelines previously identified in China Lake basin. A profile positioned ~1 km west of the modern drainage divide in the sill area provided the best evidence for geomorphic features related to potential overflow water levels (A–A’; Figures 1-1b-1 and 1-1b-2). The transect crosses mostly bare granitic bedrock on steeper slopes and a thin veneer of unconsolidated sandy sediment over bedrock on gentle slopes. The geomorphic profile shows sharp breaks-in-slope, benches, knobs, and up to six channel features between the elevations of ~665 and 705 m (A–A’; Figure 1-1b-2). The largest channel feature consists of a v-shaped channel bottom at ~665 m and two benches at ~670 and 680 m that coincide with the elevations of shoreline features in the lake basin. Three shallow channel features are also present at and near the highstand overflow level of the China-Searles Lake system at ~690 m. In addition, there is geomorphic evidence of higher overflow channels developed on bedrock at an elevation of ~705 m in the form of benches, shallow channel features, and the top of knobs in the sill area, which also coincide with the elevation of erosional shoreline features identified in the eastern sector of the lake basin near the northern end of the transect (e.g., Bullard et al., 2019; Figure 1-1b-2).

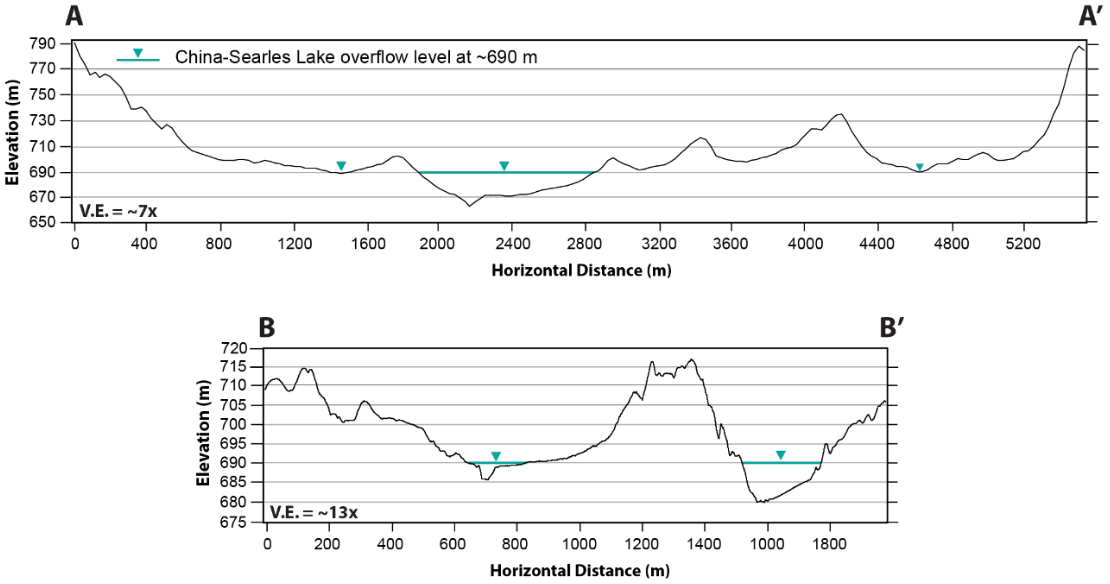

Figure 1-1b-2. Geomorphic profiles across the sill areas of China Lake (A–A') and Searles Lake (B–B') (Fig. 1-1b-1) showing sharp breaks-in-slope, benches, and channel features at the overflow level of ~690 m. The profiles show multiple points of hydrologic connection between China and Searles basins when it formed a coalesced lake (A–A'), whereas the sill area of Searles Lake shows a relatively narrow and confined spillway (B–B') adjacent to the Garlock fault. Both profiles show higher and older spillway features between ~700 and 705 m that coincide with erosional shorelines identified in each basin.

Searles basin

The Searles Valley watershed includes the Salt Wells Valley subbasin and Searles Lake basin. The watershed has a relatively small drainage area of ~1840 km^2 and is bounded by the Argus Range and El Paso Mountains on the west, the Slate Range on the east, and low-relief hills associated with the Garlock fault system on the south (Figure 1-1b-1). The Argus Range is the highest range in the watershed with elevations up to ~2000 m. The western and eastern parts of the watershed share drainage divides with the Indian Wells Valley and Panamint Valley watersheds, respectively. The best developed axial wash system in the watershed is sourced from the drainage divide near China Lake basin before it meanders through Salt Wells Valley and terminates in Searles Lake basin. The outlet of the wash system is in Poison Canyon on the western margin of Searles Lake basin, a deeply incised canyon formed on granitic rock and a well-developed delta complex that exposes a ~50–70 m thick section of the late Pleistocene Searles Lake Formation (Smith, 2009; Knott et al., 2019) (Figure 1-1b-1).

The depocenter of the lake basin is at an elevation of ~490 m and consists of a broad playa covering ~90 km^2 that is surrounded by remnants of gravelly beach plains and extensive alluvial fans, plus lesser eolian features. Evidence of former lake levels is present in the lake basin at and below the highstand overflow level that ranges from ~691 m in the northern sector of the lake basin up to ~695 m in the southern sector near the Garlock fault and sill area (Figure 1-1b-1). Preserved shoreline features consist of isolated beaches, beach ridges, spits, and lesser tombolos, as well as tufa mounds and towers, plus wave-formed scarps developed on both alluvial fans and the flanks of bedrock knolls and range fronts (Smith, 2009). There are at least six laterally continuous beach ridges with intervening recessional shoreline scarps that encompass the lake basin at high and intermediate levels. The best developed shoreline features are commonly preserved in the northern and southern sectors of the lake basin as beach ridges and spits at elevations of ~540, 570, 593, 644, 680, and 690 m. Below the elevation of 593 m, most shoreline features are erosional and preserved as recessional scarps on bedrock or buried by younger alluvium. The lowest prominent erosional shoreline features encompassing the lake basin occur at an elevation of ~505 m and a bit lower along the playa margin at ~495 m (Figure 1-1b-1). In addition, there is geomorphic evidence of older and higher shoreline features in the southern sector of the lake basin in areas near the Garlock fault in the form of planar beach plains with rounded gravel and tufa mounds, as well as beach ridges and shoreline scarps at elevations of ~700 and 715 m (e.g., Smith, 2009), informally referred to as “The Stairway to Heaven” surface (More discussion at Day 1, Stop 2b).

Spillway of Searles basin

The Searles Valley occupies a topographically closed basin contained by a modern sill at ~690 m across its southeastern drainage divide (Smith and Street-Perrott, 1983). The overflow channel of the lake basin is fault-controlled by the Garlock fault. The modern sill is located ~0.75 km south of the Garlock fault and has formed at the distal margins of coalescing alluvial fans in the paleo-Owens River channel (Figure 1-1b-1). The lacustrine and fluvial geomorphology of the overflow channel, however, indicates that during highstand water levels the sill was likely in the vicinity of the Garlock fault (More discussion at Day 1, Stop 2b). A transverse topographic profile across the entire length of the sill area from a 0.5 m LiDAR DEM (Earthscope, 2018) was used to identify geomorphic features that coincide with the range of elevations of highstand shorelines in the China-Searles Lake basin. A profile positioned along a prominent shutter ridge and across the overflow channel provided the best evidence for geomorphic features related to highstand water levels (B–B'; Figure 1-1b-2). The transect crosses dissected old Quaternary alluvial fans underlain by gently dipping Pliocene to Quaternary sedimentary and volcanic bedrock associated with the Dome Mountain anticline on steeper slopes, as well as a thin veneer of late Pleistocene to Holocene unconsolidated sands and gravels on gentle slopes (e.g., Smith and Church, 1980). The geomorphic profile shows sharp breaks-in-slope, benches, and two main channel features between the elevations of ~680 and 695 m (B–B'; Figure 1-1b-2). The largest channel feature is the main overflow channel with steep walls and a bottom at ~680 m that coincides with shoreline features in both China and Searles Lake basins. The other channel feature at an elevation of ~690 m is relatively shallow and broad with a lower and narrow v-shaped channel at ~686 m. There is a lack of subsurface data for the main overflow channel where it crosses the Garlock fault, however, the channel bottom is likely a strath terrace developed from uplift and subsequent incision from both overflow episodes directed to the south and post-lake fluvial processes that are now directed to the north into Searles Valley. There is also a lack of direct stratigraphic and geochronologic information from the Searles Lake overflow channel to confidently link the age of highstand shorelines in the lake basin to periods of overflow to Panamint Valley.

Preliminary lake-level reconstruction of China and Searles Lakes

Methodology and approach

A continuous lake-level curve of Owens Lake was previously constructed from integrating lake-core data and dated geomorphic and stratigraphic information. Since most geomorphic studies on lake-level reconstructions use landform and outcrop evidence from relative highstands, Bacon et al. (2018; 2020) developed an approach to estimate past lake levels in the absence of shoreline evidence by integrating both outcrop-based shoreline data and lake core datasets from Owens Lake with threshold lake-water depth estimates from wind-wave and sediment entrainment modeling of lake core sedimentology. Bacon et al. (2018) calibrated and verified this approach by first modeling the sedimentology described in the historical section of lake core OL-97 (Li et al., 2000; Smoot et al., 2000) with limnological conditions for the period 1872–1878 AD (Winkle and Eaton, 1910) when Owens Lake was at its historical maximum water level. The wind-wave and lake bottom sediment entrainment modeling of 22 sand and mud units of lake core OL-97 sedimentology yielded estimates for the duration of lake expansion and contraction, as well as relative water depth not reflected in the shoreline geomorphic record. The same approach was also used with lake core OL-92 (Smith and Bischoff, 1997) to extend the lake-level reconstruction over the past 50,000 years (Bacon et al., 2020). The integration of dated shorelines with the sediment entrainment modeling for relative depth of water-level changes produced continuous lake-level records that are useful for quantifying the magnitude and frequency of hydroclimate variability. The same approach was used to develop preliminary lake-level reconstructions for China and Searles Lakes to evaluate temporal correspondence between the Owens Lake overflow record and the magnitude of downstream lake levels.

Previous shoreline and outcrop stratigraphic sites in China Lake basin

China Lake was second in the sequence of pluvial lakes along the paleo-Owens River system. The lake basin has received relatively little attention compared to the other lake basins in the system that were the sites of numerous paleoclimate studies with long records of lake-level variations from stratigraphic and lake-core evidence (e.g., Smith and Pratt, 1957; Phillips, 2008). The majority of the early stratigraphic studies performed in China Lake basin were part of geoarcheological investigations of early human occupation and their association with extinct Pleistocene fauna and the environment (e.g., Davis, 1975). More recently, a detailed study by Rosenthal et al. (2017) developed the first comprehensive lake-level curve of China Lake during the terminal Pleistocene. Their investigation included data from mostly 36 shallow (<1.5 m deep) stratigraphic sites between the elevations of 658 and 684 m across China Lake basin and near the drainage divide with Salt Wells Valley (Figure 1-1b-1). The Rosenthal et al. (2017) lake-level curve was principally developed from radiocarbon-dated paleoenvironmental evidence, including lacustrine deposits and shoreline features, tufa outcrops, and mollusk, ostracode, and fish bone assemblages, as well as spring and other groundwater-related deposits from the author’s own research, as well as compilation of published data and unpublished cultural resources reports. The reported data in Rosenthal et al. (2017) was used to develop a refined lake-level curve of China Lake by accounting for relative water depth from a variety of geologic indicators that represent specific depositional environments (Figure 1-1b-3).

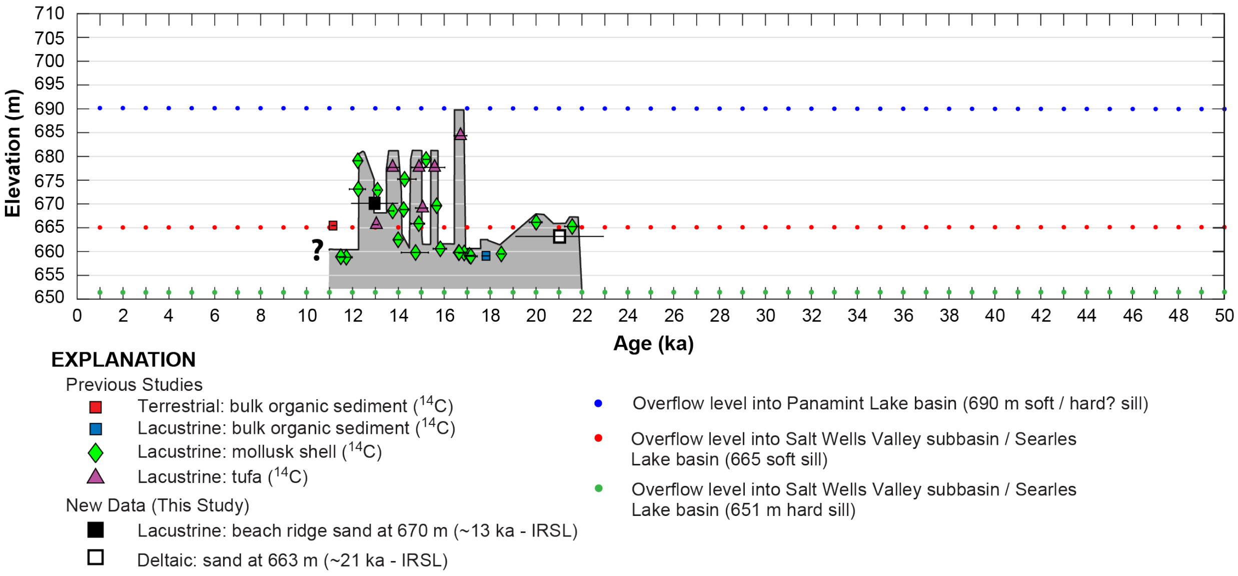

Figure 1-1b-3. Preliminary lake-level curve developed for China Lake over the past 50,000 years. Data mostly from Rosenthal et al. (2017) was used with the methods of Bacon et al. (2018; 2020) to determine relative water depth from a variety of geologic indicators. New preliminary infrared stimulated luminescence (IRSL) ages for the 670 m beach ridge and deltaic deposits are also shown. Also shown are the “current” positions of the overflow levels of China and Searles Lake basins. **NOTE:** Lake-level curve is not corrected for tectonic ground deformation.

New luminescence ages for 670 m beach ridge

Beach ridge sediment exposed in a road cut was investigated several months after the 2019 Ridgecrest earthquake sequence to provide a direct numerical age for the 670 m shoreline in China Lake basin to assist with on-going geomorphic research for the U.S. Navy. Here, the beach ridge along with discontinuous wave-formed strandlines developed on older near-shore deposits are preserved at the base of nearby colluvial slopes. The 670-m beach ridge has a broad crest with heights of 2–3 m. The road cut exposure crosses perpendicular to the crest of the beach ridge that formed within a saddle that connects bedrock (Figures 1-1b-1). The 670 m beach ridge has a surface covered by a moderately developed desert pavement with moderately to poorly developed desert varnish on a mix of meta-sedimentary and granitic clasts. The lacustrine section consisted of ~3 m of well-rounded, spherical to disk-shaped, medium to coarse sandy to gravelly beach ridge facies with parallel and basinward-dipping tabular beds, which based on their position, formed within the tombolo shoreline feature (i.e., topsets and foresets of Adams and Wesnousky, 1998). The near horizontal bounding erosional surface (i.e., abrasion platform) beneath the bedded beach ridge facies is formed on massive sandy silt to silty sand near-shore deposits (Figure 1-1b-4).

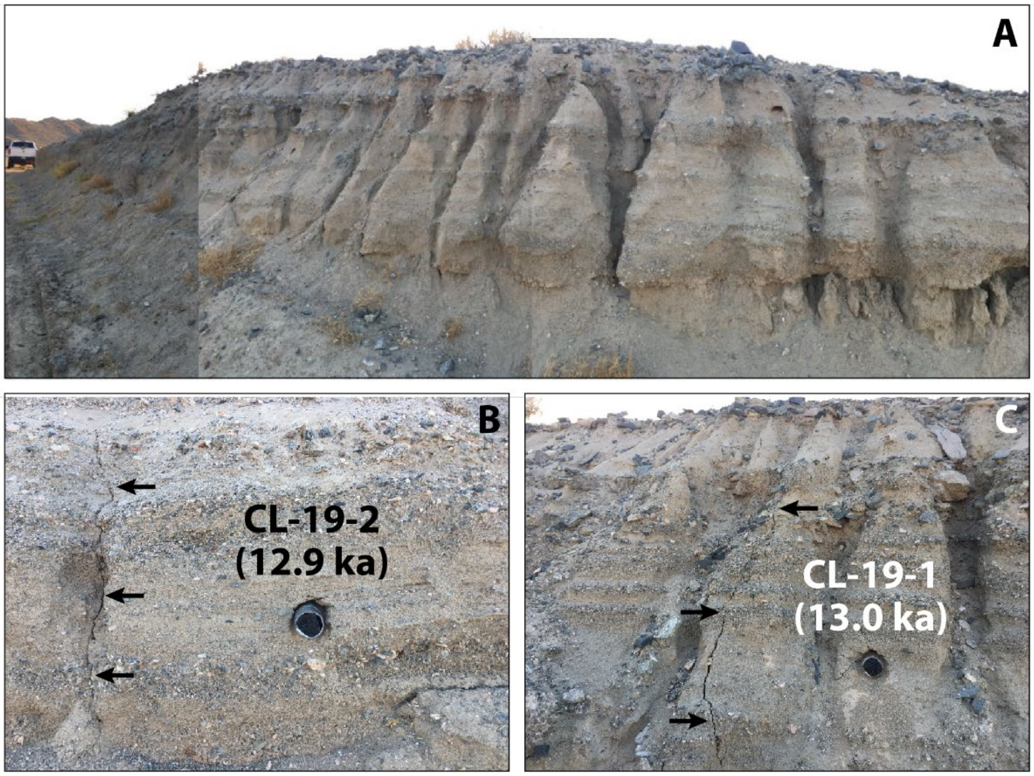

Figure 1-1b-4. Photographs of the 670 m Beach Ridge study site in China Lake basin showing: (A) road-cut exposure across the beach ridge in southeastern lake basin near the 2019 Ridgecrest surface rupture on the Paxton Ranch fault (Figure 1-1b-1); and (B and C) sample locations for age analysis by post infrared stimulated luminescence (post-IR-IRSL) dating (unpublished data, 2020). Both samples were collected within the same sandy forest bed located east (CL-19-1) and west (CL-19-2) of the crest of the beach ridge. Vertical fractures from strong seismic shaking are also evident near sample locations (black arrows).

Preliminary luminescence dating

Post-IR-IRSL methods were used to directly date sediment at the 670 m beach ridge study site. Two samples were collected in opaque tubes from depths between 0.9 and 1.1 m within stratified sandy layers that lacked bioturbation (CL-19-1 to CL-19-2). Several vertical fractures spaced evenly across the road-cut exposure were present at the time of sample collection (Figure 1-1b-4). The study site is located ~300 m west of the 2019 Ridgecrest earthquake surface rupture (Figure 1-1b-1), and the vertical fractures likely formed from strong ground shaking given that no fractures were observed at the site during earlier field visits prior to the earthquake. Preliminary ages are expressed as thousands of years before 2020 and rounded to the nearest 10 years. Analysis of duplicate samples in the same sandy foreset bed east (CL-19-1) and west (CL-19-2) of the crest of the beach ridge yielded IRSL ages of 13.00 ± 1.03 and 12.89 ± 1.03 ka, respectively. The ages from the same foreset bed are in stratigraphic order, within 1 sigma errors. The age and stratigraphy at the site indicate relatively stable water levels at ~670 m around ~13.0 ka in China Lake basin.

Previous shoreline and outcrop stratigraphic sites in Searles Lake basin

Searles Lake was third in the sequence of pluvial lakes along the paleo–Owens River system. Searles Lake basin has been extensively studied because the basin contains a nearly continuous and dateable sedimentary record of paleoclimate change from at least late Pliocene time (e.g., Phillips, 2008). The majority of the stratigraphic studies performed in the lake basin included many sediment core investigations with deep cores extracted from the playa basin (Smith and Pratt, 1957; Peng et al., 1978; Smith, 1979; Phillips et al., 1983; Bischoff et al., 1985; Jannik et al., 1991; Lin et al., 1998; Litwin et al., 1999; Olson and Lowenstein, 2021; Olson et al., 2023; Stroup et al., 2023; see Day 1, Stop 1a discussion by Fred Phillips for additional details of past research). There currently are no published geomorphic/stratigraphic studies that directly dated beach ridges in Searles Valley. As a result, the existing lake-level history of Searles Lake has been inferred from the integration of outcrop-based studies on the Searles Lake Formation and highstand tufa deposits with lake-core investigations (Smith, 2009). The most comprehensive study in the basin is by Smith (2009) who characterized the Searles Lake Formation and lacustrine history of the lake. Extensive stratigraphic studies on the Searles Lake Formation were previously performed at numerous sites along natural exposures within dissected reaches of the Salt Wells Valley and Poison Canyon axial wash system (Figure 1-1b-1).

The Searles Lake Formation includes an ~50–70 m section of deltaic and lacustrine sediments exposed around Searles Valley. Extensive ^{14}C dating of carbonate deposits and materials from the Searles Lake Formation and highstand tufa deposits was performed by Smith (2009). A total of 51 ^{14}C dates from Poison Canyon considered to be reliable by Smith (2009) are from samples of mollusk (bivalves and gastropods) and ostracode shells, lithoid and nodose tufa, oolites, marl, and organic-rich sediment between the elevations of ~500 and 625 m. In addition, paired ^{14}C and U/Th ages from highstand lithoid tufa deposits at an elevation of ~689 m from the Navy Road site in the southwestern subbasin of Searles Lake provide an age estimate for a highstand lake level (Garcia et al., 1993; Smith, 2009). Radiocarbon and U/Th dates of carbonate deposits of the Searles Lake Formation and the same highstand tufa deposits at the Navy Road site were also attained by Lin et al. (1998). In addition, a total of nine ^{14}C dates from Poison Canyon are from bulk marl samples between the elevations of ~509 and 590 m. Later studies of paired ^{14}C and U/Th ages from the same highstand lithoid tufa deposits at an elevation of ~689 m from the Navy Road site provide additional age estimates for highstand lake levels (Lin et al., 1998). Collectively, these investigations established the age of the upper Searles Lake Formation at ~33–11.7 cal kyr BP.

Recently, a stratigraphic investigation at sites in the eastern reaches of Poison Canyon yielded 13 ^{14}C dates from mussel shells of *Anodonta* sp. between the elevations of ~530 and 598 m, which together with paleomagnatic data, demonstrate that the base of the Searles Lake Formation is ~46–43 cal kyr BP, thereby extending the outcrop-based lake-level record ~10 ky (Knott et al., 2019). Additional ^{14}C dating of aquatic snails and bivalves in deltaic and shoreline deposits in the vicinity of Poison Canyon, along with a tufa cast from a juniper stump yielded ages from ~38.0 to 12.7 cal kyr BP at elevations of 540–640 m (Ken Adams, unpublished data, 2014; 2017). The majority of stratigraphic studies in Searles Valley have focused on the Searles Lake Formation in the western part of the lake basin in areas at the inlet of the paleo-Owens River.

Geologic observations and ^{14}C dates from a fault study on the Searles Valley fault (SVF) in the eastern sector of lake basin, however, provide additional ages for more recent and lower water levels. A total of three ^{14}C dates from lithoid tufa and marl between the elevations of ~548 and 622 m constrain the ages of latest Pleistocene water levels at these elevations (Numelin et al., 2007).

All available published and unpublished information was compiled and used to develop a refined lake-level curve of Searles Lake by accounting for relative water depth from a variety of geologic indicators that represent specific depositional environments (Figure 1-1b-5).

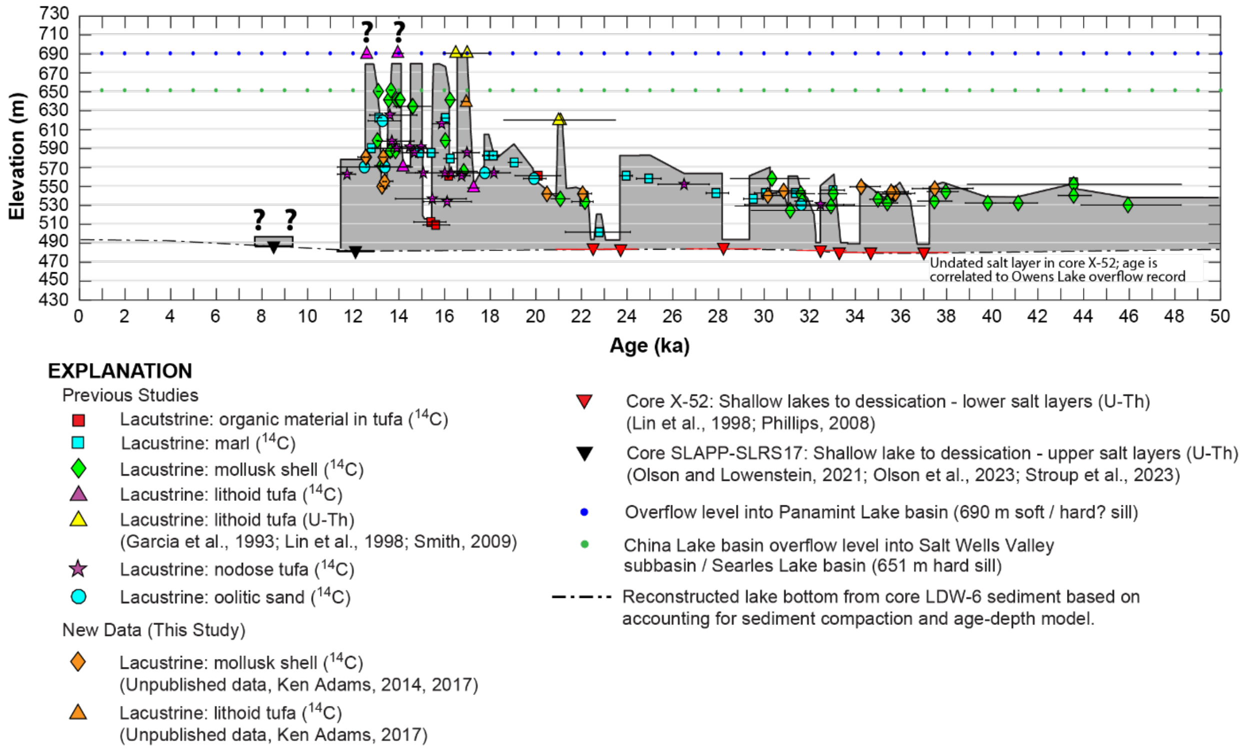

Figure 1-1b-5. Preliminary lake-level curve developed for Searles Lake over the past 50,000 years. All available published information and the unpublished data of Ken Adams were used with the methods of Bacon et al. (2018; 2020) to determine relative water depth from a variety of geologic indicators. Also shown are the “current” positions of the overflow levels of China and Searles Lake basins. Query marks denote uncertainty in potential water levels discussed in text. **NOTE:** Lake-level curve is not corrected for tectonic ground deformation.

Tufa ages from the ~690 m highstand and overflow level

The ~690 m shoreline in China and Searles basins lacks a direct age from stratified sedimentary deposits (i.e., beach ridges). Paired ^{14}C and U/Th isochron (U-series) ages from lithoid tufa formed at the elevation of the ~690 m shoreline, however, provide the only age estimates for highstand water levels in Searles Valley (Garcia et al., 1993; Lin et al., 1998). Both studies sampled the same tabular outcrop of tufa that overlies bedrock and pre-lake alluvium at an elevation near ~689 m in the southwest subbasin of Searles Valley (Navy Road site; Figure 1-1b-1). The sampled tufa is highly porous and composed of 1-10 mm diameter spheres and sphere fragments indicating growth of bubbles trapped in growing shoreline algae (Garcia et al., 1993). The study of Garcia et al. (1993) returned a ^{14}C date of 10,900 ± 40 yr BP, and after applying a 300 year reservoir correction as part of the revised lake-level reconstruction, yields a calibrated age of 12,720–12,490 cal yr BP. The same sample also yielded an older U-series age of 17,000 ± 1000 yr BP (uncorrected for initial high ^{230}Th). Similarly, the study of Lin et al. (1998) returned a ^{14}C date of 12,400 ± 100 yr BP, and after applying a 300 year reservoir correction, yields a calibrated age of 14,300–13,760 cal yr BP. The same tufa sample also yielded an older U-series age of 16,500 ± 560 yr BP (corrected for initial high ^{230}Th), which is similar to the U-series age of Garcia et al. (1993) (Figure 1-1b-5). Taken together, the two studies yielded different ^{14}C ages of ~12,640 and ~13,980 cal yr BP, but similar U-series ages of ~16,800 yr BP for the same outcrop of tufa. Both studies acknowledged potential problems and uncertainties with dating tufa carbonates and the possibility of post-depositional contamination of porous tufa with younger carbon. As a result, the U-series ages were favored as being more reliable at the Navy Road site (Garcia et al., 1993; Lin et al., 1998).

Additional age control for the 690 m shoreline and evidence of a brief transgression up to this level is from the ^{14}C dating of a remnant tufa tower formed on basalt flows in the northern sector of China Lake basin at the Horseshoe Tufa site (Rosenthal et al., 2017; Figure 1-1b-1). The tufa tower is at an elevation of 684.3 m and returned a ^{14}C date of 14,100 ± 70 yr BP, and after applying a 300 year reservoir correction, yields a calibrated age of 17,000–16,500 cal yr BP. The tufa site has a morphology consisting of low relief mounds and towers, thereby requiring a water level above ~684 m to have formed. The Horseshoe Tufa site is also the highest elevation site previously used to constrain the timing of a possible transgression that reached highstand water levels of ~690 m at ~17,000 cal yr BP (Rosenthal et al., 2017; Figure 1-1b-3). Although it has been demonstrated that ^{14}C dating of tufa carbonates at highstand water levels in Searles Valley are likely unreliable, the hydrologic conditions and post-depositional processes in China Lake basin maybe more favorable for influencing reliable tufa dates.

The available evidence in China and Searles Lake basins currently indicates that the last time the China-Searles Lake system reached its highstand and overflowed into Panamint Valley was likely at ~16,800 yr BP based on U-series dating and ~16,700 cal yr BP based on ^{14}C dating of tufa carbonates (Figures 1-1b-3, 1-1b-5). For the China-Searles Lake system to attain highstand and overflowing conditions requires large and sustained streamflow input from an overflowing Owens Lake.

Owens Lake overflow history and temporal correspondence with downstream lakes

A continuous lake-level curve was constructed for Owens Lake by integrating lake-core data and existing and new ages of shoreline deposits with wind-wave and sediment entrainment modeling of lake-core sedimentology (Bacon et al., 2018; 2020), which refined earlier water-level reconstructions of Owens Lake (Bacon et al., 2006; Reheis et al., 2014).

This effort enabled refinement of the overflow history and development of a better understanding of the effects of regional and global climate variability on lake levels of the paleo-Owens River-Lake system during the last 50,000 years. The elevations of stratigraphic sites, plus lake bottom and spillway positions were corrected for vertical tectonic deformation using a differential fault-block model to estimate the absolute hydrologic change of the watershed-lake system. All available geochronological data from the lake basin were used to constrain water levels, including ^{14}C dating of mollusk shells, tufa, and carbonized wood in fluvial-deltaic and shoreline deposits, plus luminescence dating of beach ridges, as well as alluvial and deltaic deposits in deep boreholes within the overflow channel. Geotechnical data show the overflow area is an entrenched channel that had erodible sills composed of unconsolidated fluvial-deltaic and alluvial sediment at elevations of ~1113–1165 m above mean sea level.

The lake-level reconstruction shows Owens Lake spilled most of the time at or near minimum sill levels, controlled by a bedrock sill at ~1113 m. Nine major transgressions at ~40.0, 38.7, 23.3, 19.3, 15.6, 13.8, 12.8, 11.6, and 10.5 ka reached levels ~10–45 m above the bedrock sill. Several notable regressions at or below the bedrock sill from 36.9–28.5 ka, and at ~17.8, 12.9, and 10.4–8.8 ka indicate either little or no overflow during these times based on sedimentology in outcrops and lake cores. Additionally, lake-core proxy geochemical evidence also indicates the occurrence of numerous dry periods that are used to control the direction of water-level change. Relatively new dating of beach ridges and sediment in the overflow channel indicates the latest period of overflow of Owens Lake occurred ~10–20 m above the bedrock sill from ~8.4–6.4 ka that was followed by closed basin conditions after ~6.4 ka (Figure 1-1b-6).

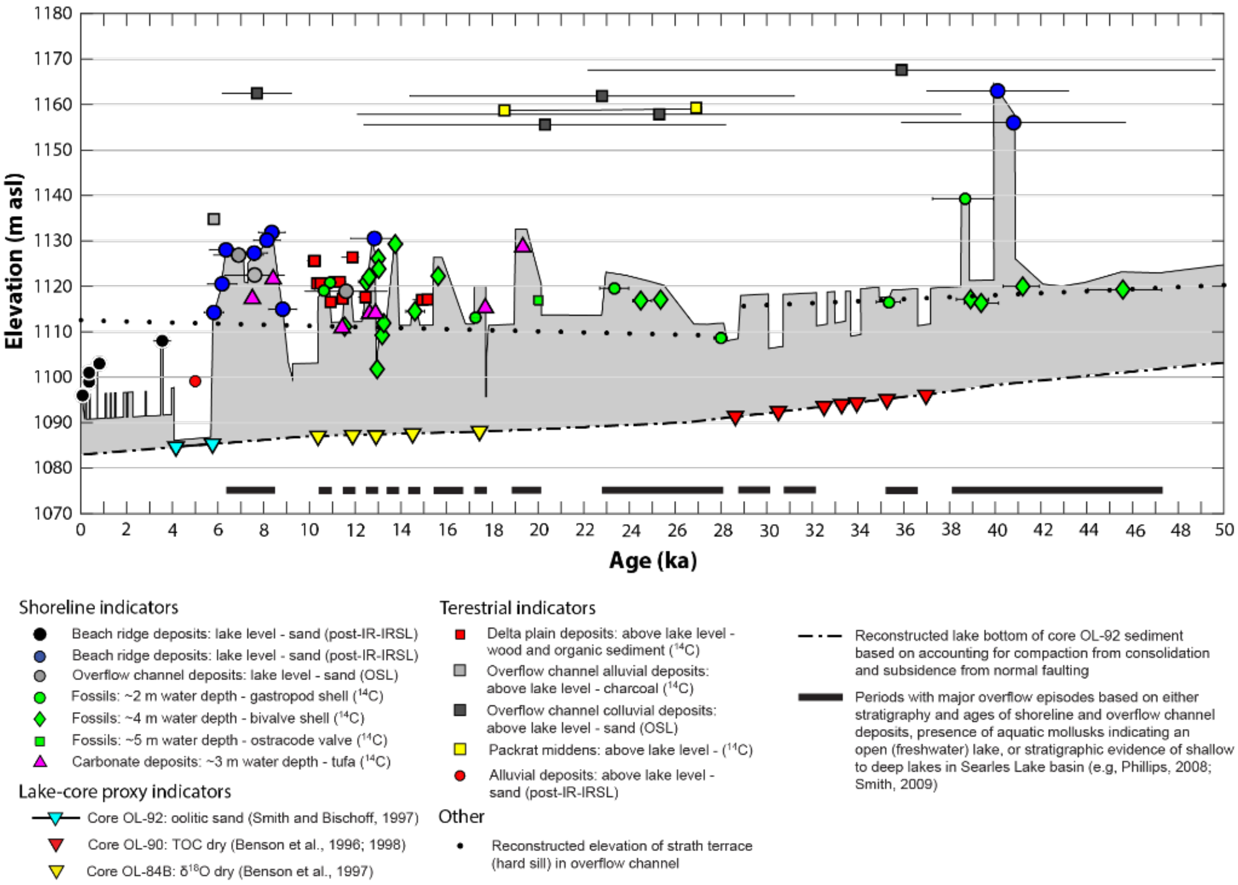

Figure 1-1b-6. Continuous lake-level curve developed for Owens Lake over the past 50,000 years with reconstructed lake bottom and spillway positions. Shown are a variety of geologic indicators used to determine relative water depth (Bacon et al., 2018; 2020). Also shown are estimates of potential periods with major overflow episodes. Lake-level curve is corrected for tectonic ground deformation.

The lake-level record of Owens Lake is the only complete archive in the paleo-Owens River system that shows the magnitude of lake-level variations of high and low water levels, as well as the duration of potential overflowing lake conditions controlled by soft sills in the overflow channel (Bacon et al., 2018; 2020). At least fourteen periods of potential overflow were identified from the Owens Lake water-level record over the past 50,000 years (Figure 1-1b-6). These overflow episodes range in duration from ~500 to as long as ~9000 years. A general comparison between the Owens Lake overflow record and the China and Searles Lakes water-level records shows relatively good temporal correspondence. In particular, the five large water-level oscillations of China-Searles Lake centered at ~12.5, 13.8, 14.8, 15.8, and 16.8 ka that reached elevations at or above ~680 m all coincide with periods of major overflow episodes of Owens Lake (Figures 1-1b-6). In addition, Owens Lake overflowed during the early Holocene from ~8.7 to 6.5 ka that coincides with a period of shallow lakes and salt deposition in Searles basin from 9.4 to 7.6 ka based on new ^{14}C and

U-series dating of carbonate and salt layers in core SLAPP-SLRS17 (Olson and Lowenstein, 2021; Olson et al., 2023; Stroup et al., 2023; Figures 1-1b-5, 1-1b-6). The maximum depth and extent of Searles Lake during the early Holocene is unknown. Current work is focused on compiling and refining all water-level records of Owens, China, and Searles Lakes with new luminescence dating of key beach ridges and shoreline deposits of China and Searles Lakes to improve the existing record of hydrologic connectivity throughout the paleo-Owens River system.

References

Adams, K.D., and Wesnousky, S.G., 1998. Shoreline processes and the age of the Lake Lahontan highstand in the Jessup embayment, Nevada. Geological Society of America Bulletin 110, 1318–1332.

Bacon, S.N., Burke, R.M., Pezzopane, S.K., and Jayko, A.S., 2006. Last glacial maximum and Holocene lake levels of Owens Lake, eastern California, USA. Quaternary Science Reviews 25, 1264–1282.

Bacon, S.N., Lancaster, N., Stine, S., Rhodes, E.J., and McCarley Holder, G.A., 2018. A continuous 4000-year lake-level record of Owens Lake, south-central Sierra Nevada, California, USA. Quaternary Research 90, 276–302.

Bacon, S.N., Bullard, T.F., Adams, K.D., and Decker, D.L., 2019. Geomorphic map of China Lake basin below 700 m elevation, Inyo, Kern, and San Bernardino Counties, California. Prepared by Naval Earth Sciences and Engineering Program, Desert Research Institute for Naval Air Warfare Center, Weapons Division, China Lake, NAWCWD TP 8839, 1:50,000-scale.

Bacon, S.N., Jayko, A.S., Owen, L.A., Lindvall, S.C., Rhodes, E.J., Schumer, R.A., and Decker, D.L., 2020. A 50,000-year record of lake-level variations and overflow from Owens Lake, eastern California, USA. Quaternary Science Reviews 238, 106312.

Bischoff, J.L., Rosenbauer, R.J., and Smith, G.I., 1985. Uranium-series dating of sediments from Searles Lake: differences between continental and marine climate records. Science 227, 1222–1224.

Bullard, T.F., Bacon, S.N., Adams, K.D., and Decker, D.L., 2019. Geomorphic Map of the China Lake Basin below 700 m in Support of Cultural Resource Management at Naval Air Weapons Station China Lake. Prepared by Naval Earth Sciences and Engineering Program, Desert Research Institute for Naval Air Warfare Center, Weapons Division, China Lake, NAWCWD TP 8839, 24 pp. including appendices.

Davis, E.L., 1975. The “exposed archaeology” of China Lake, California. Am. Antiq. 40, 39–53.

Earthscope, 2018. LiDAR data were accessed from the NSF SAGE data archive operated by EarthScope Consortium (NSF award 1724509).

Garcia, J.F., Bischoff, J.L., Smith, G.I., and Trimble, D., 1993. Uranium-series and radiocarbon dates on tufas from Searles Lake, California. U.S. Geological Survey Open-File Report 93-311, 8 p.

Knott, J.R., Liddicoat, J.C., Coe, R.S., and Negrini, R.M., 2019, Radiocarbon and paleomagnetic chronology of the Searles Lake Formation, San Bernardino County, California, USA. In: Starratt, S.W., Rosen, M.R. (Eds.), From Saline to Freshwater: The Diversity of Western Lakes in Space and Time: Geological Society of America Special Paper 536, doi.org/10.1130/2018.2536(06).

Jannik, N.O., Phillips, F.M., Smith, G.I., Elmore, D., 1991. A 36Cl chronology of lacustrine sedimentation in the Pleistocene Owens River system. Geological Society of America Bulletin 103, 1146–1159.

Knott, J.R., Liddicoat, J.C., Coe, R.S., and Negrini, R.M., 2019. Radiocarbon and paleomagnetic chronology of the Searles Lake Formation, San Bernardino County, California, USA. In From Saline to Freshwater: The Diversity of Western Lakes in Space and Time. Geological Society of America Special Paper.

Kunkel, F., and Chase, G.H., 1969. Geology and Ground Water in Indian Wells Valley, California. U.S. Geological Survey Open-File Report 69-329, 84 p.

Li, H., Bischoff, J.L., Ku, T., Lund, S.P., Stott, L.D., 2000. Climate variability in east-central California during the past 1000 years reflected by high-resolution geochemical and isotopic records from Owens Lake sediments. Quaternary Research 54, 187–197.

Lin, J.C., Broecker, W.S., Hemming, S.R., Hajdas, I., Anderson, R.F., Smith, G.I., Kelley, M., Bonani, G., 1998. A reassessment of U-Th and 14C ages for late-glacial high-frequency hydrological events at Searles Lake, California. Quaternary Research 49, 11–23.

Litwin, R.J., Smoot, J.P., Durika, N.J., and Smith, G.I., 1999. Calibrating Late Quaternary terrestrial climate signals: radiometrically dated pollen evidence from the southern Sierra Nevada, USA. Quaternary Science Reviews 18, 1151–1171.

McGill, S., and Sieh, K., 1993. Holocene slip rate of the central Garlock fault in southern Searles Valley, California. Journal of Geophysical Research 98, 14,217–14,231.

Moore, J.G., and Moring B.C., 2013. Range wide glaciation in the Sierra Nevada, California. Geosphere 9, 1804–1818.

Numelin, T., Kirby, E., Walker, J.D., and Didericksen, B., 2007. Late Pleistocene slip on a low-angle normal fault, Searles Valley, California. Geosphere 3, 163 -176.

Olson, K.J., and Lowenstein, T.K., 2021. Searles Lake evaporite sequences: Indicators of late Pleistocene/Holocene lake temperatures, brine evolution, and pCO2. Geological Society of America Bulletin 133, 2319–2334.

Olson, K.J., Guillerm, E., Peaple, M.D., Lowenstein, T.K., Gardien, V., Caupin, F., Feakins, S.J., Tierney, J.E., Stroup, J., Lund, S., and McGee, D., 2023. Application of Brillouin thermometry to latest Pleistocene and Holocene halite from Searles Lake, California, USA. Earth and Planetary Science Letters 602. 117913.

Peng, T.H., Goddard, J.G., & Broecker, W.S. (1978). A direct comparison of 14C and 230Th ages at Searles Lake, California, Quaternary Research 9, 319–329.

Phillips, F.M., 2008. Geological and hydrological history of the paleo-Owens River drainage since the late Miocene, in Reheis, M.C., Hershler, R., and Miller, D.M., eds., Late Cenozoic Drainage History of the Southwestern Great Basin and Lower Colorado River Region: Geologic and Biotic Perspectives: Geological Society of America Special Paper 439, p. 115–150.

Phillips, F.M., Smith, G.I., Bentley, H.W., Elmore, D., and Gove, H.E., 1983. Chlorine-36 dating of saline sedments: preliminary results from Searles Lake, California. Science 222, 925–927.

Reheis, M.C., Stine, S., and Sarna-Wojcicki, A.M., 2002. Drainage reversals in Mono Basin during the late Pliocene and Pleistocene. Geological Society of America Bulletin 114, 991–1006.

Reheis, M.C., Adams, K.D., Oviatt, C.G., & Bacon, S.N. (2014). Pluvial lakes in the Great Basin of the western United States – A view from the outcrop. Quaternary Science Reviews, 97, 33–57.

Rosenthal, J.S., Meyer, J., Palacios-Fest, M.R., Young, D.C., Ugan, A., Byrd, B.F., Goblet, K., and Giacomo, J., 2017. Paleohydrology of China Lake basin and the context of early human occupation in the northwestern Mojave Desert, USA. Quaternary Science Reviews 176, 112–139.

Smith, G.I. (1979). Subsurface stratigraphy and geochemistry of Late Quaternary evaporates, Searles Lake, California. U.S. Geological Survey Professional Paper 1043, 130 p.

Smith, G.I., 2009, Late Cenozoic geology and lacustrine history of Searles Valley, Inyo and San Bernardino Counties, California. U.S. Geological Survey Professional Paper 1727, 115 p.

Smith, G.I. and Pratt, W.P., 1957. Core logs from Owens, China, Searles, and Panamint Basins, California. US Geological Survey Bulletin 1045-A, 1–62.

Smith, G.I., and Street-Perrott, F.A., 1983. Pluvial lakes of the western United States. In: Porter, S.C. (Ed.), The Late Pleistocene. Univ. Minn. Press, Minneapolis, pp. 190–212.

Smith, G.I., and Bischoff, J.L., eds., 1997. An 800,000-year paleoclimatic record from core OL-92, Owens Lake, southeast California. Geological Society of America Special Paper 317, 165 p.

Smoot, J.P., Litwin, R.J., Bischoff, J.L., and Lund, S.P., 2000, Sedimentary record of the 1872 earthquake and “Tsunami’’ at Owens Lake, southeast California: Journal of Sedimentary Geology, 135, 241–254.

Stroup, J. S., Olson, K. J., Lowenstein, T.K., Jost, A.B., Mosher, H.M., Peaple, M.D., et al., 2023. A >200 ka U-Th based chronology from lacustrine evaporites, Searles Lake, CA. Geochemistry, Geophysics, Geosystems 24, e2022GC010685.

Winkle, W.V., Eaton, F.M., 1910. Quality of the surface waters of California. U.S. Geological Survey, Water-Supply Paper 237. United States Government Printing Office, Washington.

Discussion (C) New stratigraphic investigations and preliminary luminescence ages of the Valley Wells beach ridge complex, northern subbasin of Searles Valley

Field Stop Leaders: Maggie Duncan, Steve Bacon, and Kathleen Rodrigues (Desert Research Institute, Reno, Nevada)

Introduction

The history and hydrology of the paleo-Owens River system have been well documented by numerous past studies (e.g., Smith and Street-Perrott, 1983; Benson et al., 1990; Phillips, 2008; Smith, 2009). However, a data gap remains regarding the timing of lake-level oscillations in China and Searles Lakes during the late Pleistocene to early Holocene from directly dated landforms. Stratigraphic and geochronologic data from the Valley Wells beach ridge complex will be used to refine the late Pleistocene lake-level history of Searles Lake, and improve our understanding of the hydrologic connections of lakes within the paleo-Owens River system

Geomorphic setting

The Valley Wells beach ridge complex is in the northern sector of Searles Valley and within the subbasin of Valley Wells (Figure 1-1c-1). The beach ridge complex consists of a suite of nine well-developed beach ridges preserved near the axis of the subbasin between the elevations of ~570 and 690 m (Figure 1-1c-2). The surface morphology consists of curvilinear and parallel ridge crests with intervening shoreline scarps and beach plains, and broad ridges that follow the elevation contours of the subbasin. The lateral margins of the beach ridge complex are buried by distal alluvial fans derived from the Argus Range on the west and the Slate Range on the east (Figure 1-1c-1). Wave-formed scarps at the highstand elevation of ~690 m are present and poorly preserved in a few areas along the Slate Range. The north–south oriented Valley Wells axial wash dissects the beach ridge complex nearly perpendicular to ridge crests, thereby providing excellent exposures of beach ridge, back barrier lagoonal, and alluvial stratigraphy (Figure 1-1c-2).

Preliminary luminescence dating

Over two field campaigns in January and April 2025, twenty-two luminescence samples were collected from sand-rich shoreline, alluvial, and aeolian deposits between the elevations of 570 and 670 m at the Valley Wells beach ridge complex. Five beach ridges at elevations of 570, 585, 594, 607, and 645 m were targeted for stratigraphic analysis and luminescence sampling. Of the twenty-two samples taken, ten samples were prioritized for single-grain infrared stimulated luminescence (IRSL) analysis at the Desert Research

Institute Luminescence Lab (DRILL), and preliminary results of these samples are presented for the 2025 FOP fieldtrip (Table 1-1c-1). The preliminary results provide direct ages of beach ridge, beach plain, and aeolian sand interbedded with back barrier lagoonal deposits.

Deposits below beach ridge crests were preferentially targeted for sampling because this is the best paleolake indicator of relative lake-level stability. Luminescence samples were collected at a minimum of 0.5 m below the surface to avoid zones of bioturbation and 0.3 m away from stratigraphic boundaries to minimize the chance of incomplete bleaching of mineral grains from differing particles sizes (Roberts and Plater, 2007; Tamura, 2012). When beach ridge deposits could not be sampled due to either lack of exposure, poor grain size distribution or presence of depositional $CaCo_3$ cementation (i.e., beach rock), samples were taken from nearby exposures determined to be stratigraphically informative of the depositional setting and that could also place elevation constraints on water levels.

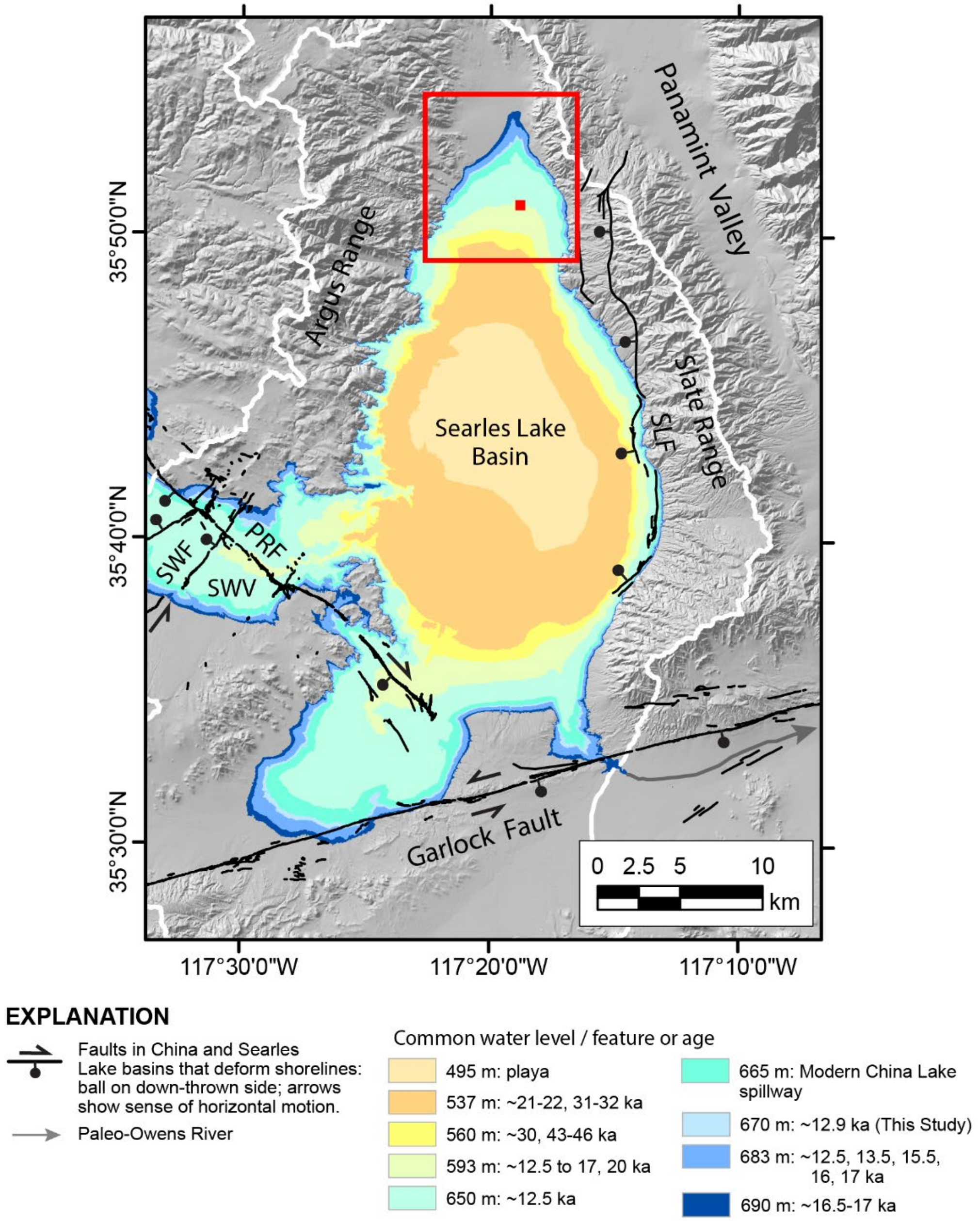

Figure 1-1c-1. Major physiographic features and unpublished water-level map of Searles Lake basin showing inferred ages from outcrop evidence and lake core data. Red rectangle is map extent of Valley Wells beach ridge complex shown on Figure 1-1c-2. Red box is location of Day 1, Stop 1. SWV – Salt Wells Valley. Location of primary active faults in the lake basins are also shown. Faults: SLF – Searles Lake fault; and southeastern extent of the 2019 Ridgecrest earthquake surface ruptures: PRF – Paxton Ranch fault and SWF – Salt Wells fault.

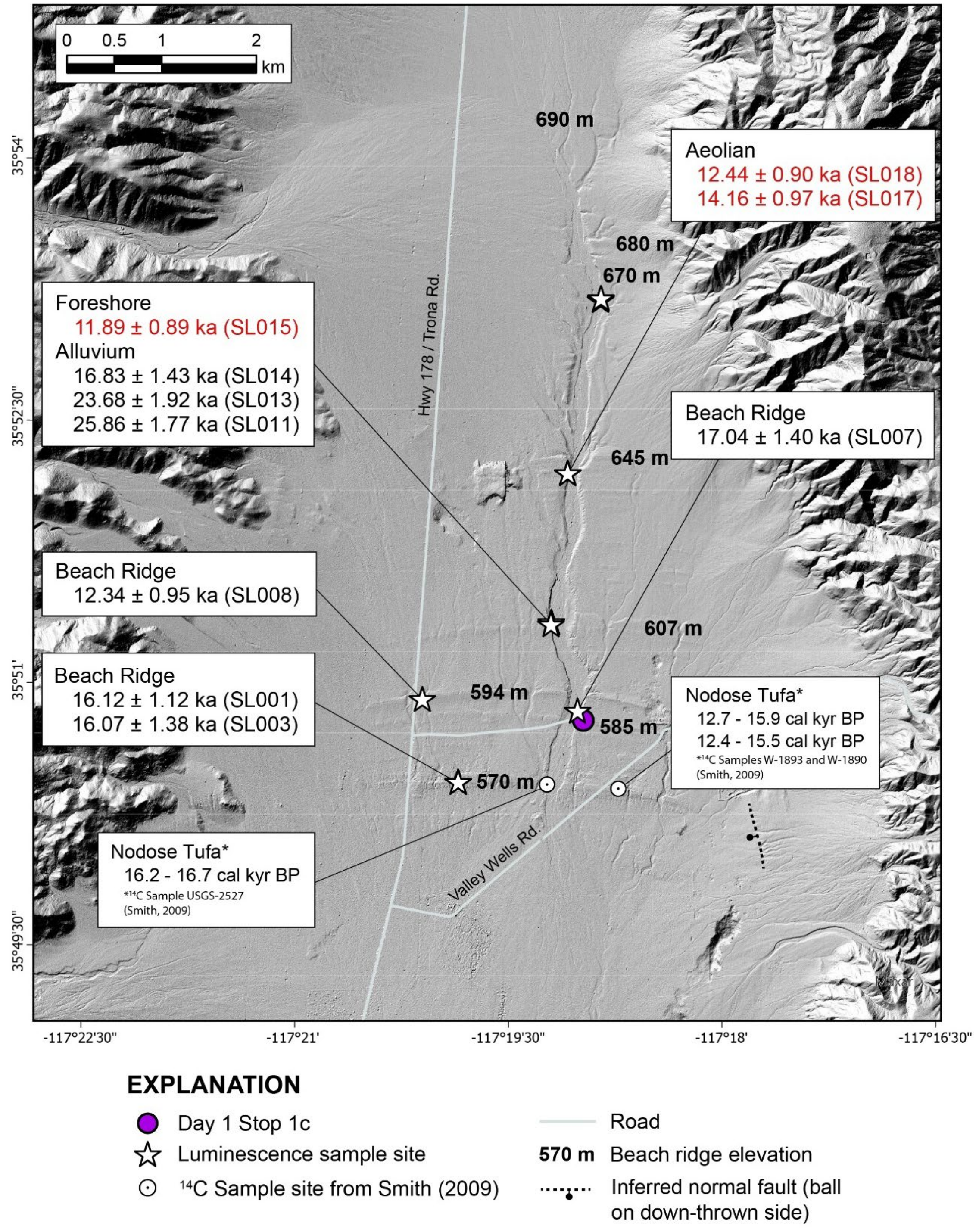

Figure 1-1c-2. Hillshade map from a 2-meter DEM of the Valley Wells beach ridge complex showing new stratigraphic study sites and luminescence sample locations. Preliminary luminescence ages are categorized by the type of deposit (i.e., depositional environment) sampled at stratigraphic sites. Red ages represent results that returned U/Th ratios >0.5, that are considered minimum ages and require additional analysis. Elevations for eight prominent beach ridges in the complex are shown. Mapped faults are also shown. The locations of reservoir-corrected (300 years) calibrated radiocarbon ages of nodose tufa from the 570 m beach ridge of Smith (2009) are shown.

Table 1-1c-1. Summary of equivalent dose and luminescence age data. Preferred ages are shown in bold-face type. Ages with elevated U/Th ratios are shown in bold-face red type and are considered minimum preliminary ages

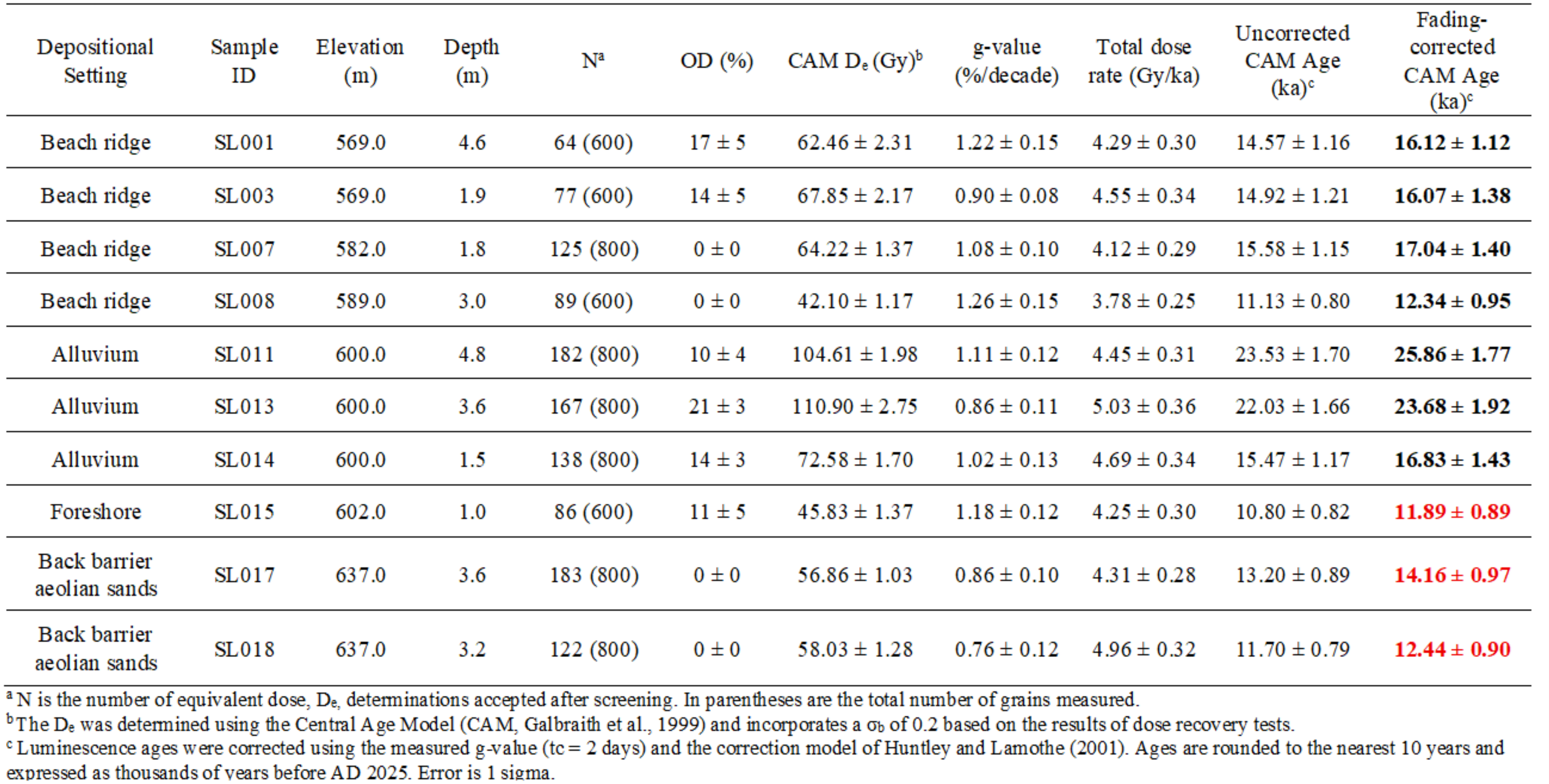

Depositional Setting	Sample ID	Elevation (m)	Depth (m)	N[a]	OD (%)	CAM D_e (Gy)[b]	g-value (%/decade)	Total dose rate (Gy/ka)	Uncorrected CAM Age (ka)[c]	Fading-corrected CAM Age (ka)[c]
Beach ridge	SL001	569.0	4.6	64 (600)	17 ± 5	62.46 ± 2.31	1.22 ± 0.15	4.29 ± 0.30	14.57 ± 1.16	**16.12 ± 1.12**
Beach ridge	SL003	569.0	1.9	77 (600)	14 ± 5	67.85 ± 2.17	0.90 ± 0.08	4.55 ± 0.34	14.92 ± 1.21	**16.07 ± 1.38**
Beach ridge	SL007	582.0	1.8	125 (800)	0 ± 0	64.22 ± 1.37	1.08 ± 0.10	4.12 ± 0.29	15.58 ± 1.15	**17.04 ± 1.40**
Beach ridge	SL008	589.0	3.0	89 (600)	0 ± 0	42.10 ± 1.17	1.26 ± 0.15	3.78 ± 0.25	11.13 ± 0.80	**12.34 ± 0.95**
Alluvium	SL011	600.0	4.8	182 (800)	10 ± 4	104.61 ± 1.98	1.11 ± 0.12	4.45 ± 0.31	23.53 ± 1.70	**25.86 ± 1.77**
Alluvium	SL013	600.0	3.6	167 (800)	21 ± 3	110.90 ± 2.75	0.86 ± 0.11	5.03 ± 0.36	22.03 ± 1.66	**23.68 ± 1.92**
Alluvium	SL014	600.0	1.5	138 (800)	14 ± 3	72.58 ± 1.70	1.02 ± 0.13	4.69 ± 0.34	15.47 ± 1.17	**16.83 ± 1.43**
Foreshore	SL015	602.0	1.0	86 (600)	11 ± 5	45.83 ± 1.37	1.18 ± 0.12	4.25 ± 0.30	10.80 ± 0.82	**11.89 ± 0.89**
Back barrier aeolian sands	SL017	637.0	3.6	183 (800)	0 ± 0	56.86 ± 1.03	0.86 ± 0.10	4.31 ± 0.28	13.20 ± 0.89	**14.16 ± 0.97**
Back barrier aeolian sands	SL018	637.0	3.2	122 (800)	0 ± 0	58.03 ± 1.28	0.76 ± 0.12	4.96 ± 0.32	11.70 ± 0.79	**12.44 ± 0.90**

[a] N is the number of equivalent dose, D_e, determinations accepted after screening. In parentheses are the total number of grains measured.

[b] The D_e was determined using the Central Age Model (CAM, Galbraith et al., 1999) and incorporates a σ_b of 0.2 based on the results of dose recovery tests.

[c] Luminescence ages were corrected using the measured g-value (tc = 2 days) and the correction model of Huntley and Lamothe (2001). Ages are rounded to the nearest 10 years and expressed as thousands of years before AD 2025. Error is 1 sigma.

Stratigraphic site descriptions

In general, the stratigraphy of the Valley Wells beach ridge complex consists of beach ridge sediments composed of varying mixtures of subrounded to well-rounded, fine to coarse sand and gravel, with varying consistencies (i.e., strength) ranging from loose to very hard due to depositional carbonate-cementation (i.e., beach rock). Beach ridge deposits also commonly display foreset, backset, and topset bedding. In addition, the stratigraphy exposed in the axial wash consists of sandy foreshore facies and back barrier lagoonal silts/sands interbedded with aeolian sands in areas between well-developed beach ridges. Older alluvial deposits also commonly occur at the base of described sections at lower elevations within the beach ridge complex. Collectively, the stratigraphy represents at least two transgressive-regressive sequences in the northern sector of Searles basin.

Stratigraphic columns documenting the lithofacies and luminescence sample locations were developed for each beach ridge investigated, beginning with the lowest-elevation 570 m beach ridge and ascending to the highest site at the 670 m beach plain (Figure 1-1c-2).

570 m beach ridge

The surface of the 570 m beach ridge consists of a coating of nodose tufa that forms moderately weathered, rubbly to very hard sheets and mounds. Stratigraphy was described from a 6 m high natural stream cut below the crest of 570 m beach ridge. The exposure consists entirely of shoreline deposits capped by nodose tufa (Figure 1-1c-3). The base of the section is composed of loose, subrounded gravel with backset bedding that is overlain by 4-m of interbedded sand and gravel with foreset, topset, and backset bedding. The interbedded sand is moderately sorted and fine to medium grained, whereas the gravel is fine to coarse, poorly sorted, and subrounded to subangular. The upper 1.5 m of the exposure is composed of massive nodose tufa.

Two samples for luminescence dating were collected in the sandy lithofacies of the beach ridge sediment in a near vertical profile (Table 1-1c-1; Figure 1-1c-3). Sample SL001 was collected at a depth of 4.6 m and returned a luminescence age of 16.12 ± 1.12 ka. Sample SL003 was collected at a shallower depth of 1.9 m and yielded a luminescence age of 16.07 ± 1.38 ka. The ages are in stratigraphic order and within their uncertainties indicating shoreline depositional process and construction of the 570 m beach ridge at ~16.1 ka.

In addition, nodose tufa on the 570 m beach ridge east of our stratigraphic site was previously dated by Smith (2009) (Figure 1-1c-2). The three tufa ages are 13,830 ± 500, 13,650 ± 500, and 15,250 ± 60 ^{14}C yr BP. After correcting for reservoir effects (300 years) yield calibrated ages of [15,920–12,690; 15,470–12,350; and 16,650–16,210 cal yr BP], having median probability ages of 14,360; 14,100; and 16,300 cal yr BP, respectively. The

^{14}C age of the nodose tufa closest to our stratigraphic site of ~16,300 cal yr BP is within the uncertainties of the luminescence ages of the 570 m beach ridge.

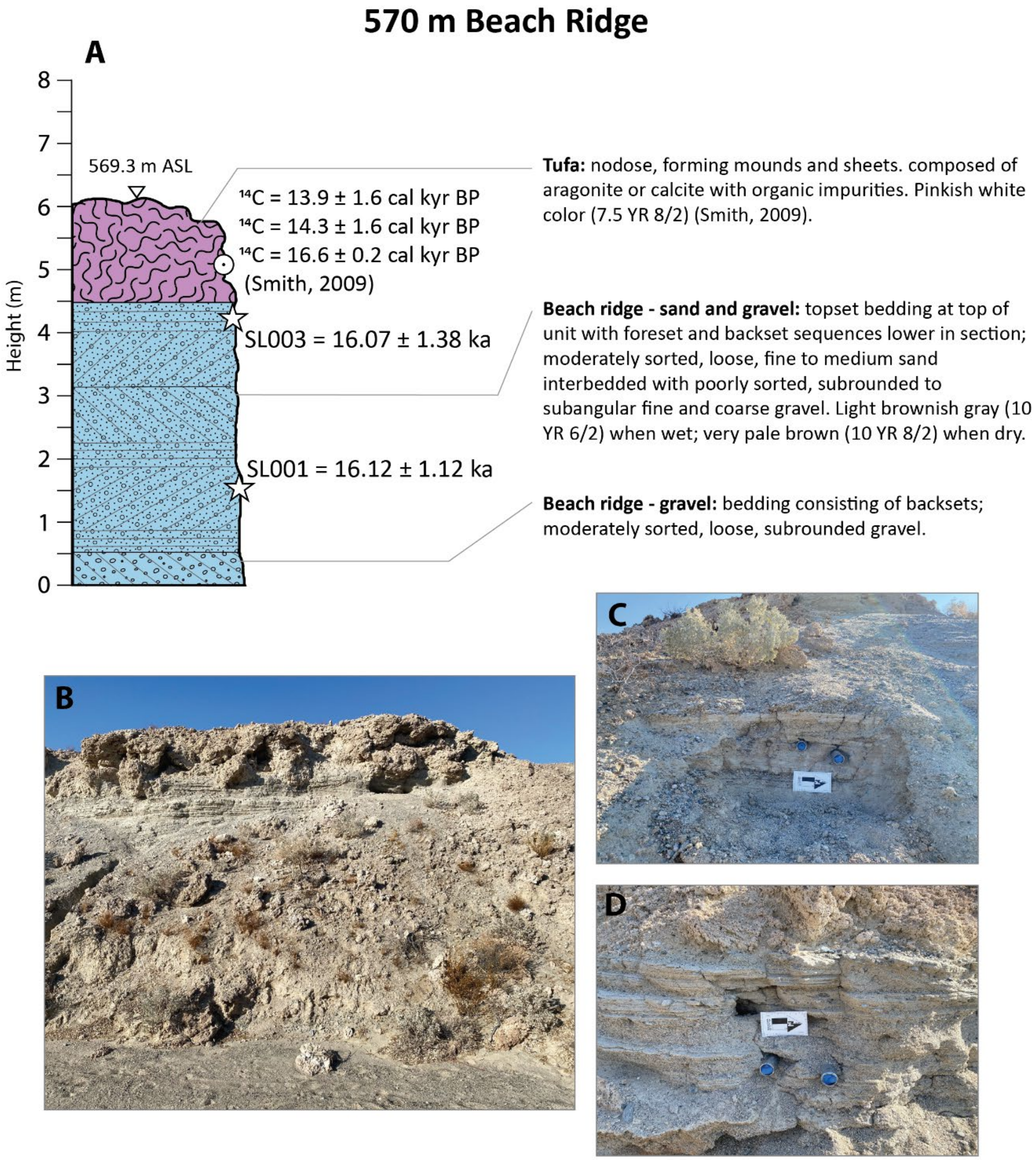

Figure 1-1c-3. (A) Simplified stratigraphic column and unit descriptions of the 570 m beach ridge site. White stars indicate location of luminescence samples (see Table 1-1c-1). Reservoir-corrected and calibrated radiocarbon ages of nodose tufa sampled from the 570 m beach ridge by Smith (2009) are indicated by white circles. Photographs of: (B) stream-cut exposure of shoreline deposits capped by a thick accumulation of nodose tufa; (C) luminescence sample location of SL003; and (D) sample location of SL001, both in fine to medium sand. Duplicates samples were collected at both locations.

585 m beach ridge

The surface of the 585 m beach ridge consists of a well-developed desert pavement surface with moderately-developed varnish on gravel clasts. Stratigraphy was described from a 7.1 m high bluff on the eastern margin of the Valley Wells axial wash near the crest of the beach ridge. The exposure consists entirely of shoreline deposits composed of varying mixtures of sand and gravel (Figure 1-1c-4). The base of the section is composed of massive, coarse gravel with fine to medium, oxidized sand. Patchy carbonate coatings are present on the undersides of gravel clasts throughout the unit and a platy, carbonate-cemented gravel lag is present in the top 5 cm of the basal unit. The gravel is overlain by beach ridge gravel and foreshore sandy facies consisting of interbedded sand and gravel with foreset, backset, and parallel bedding. The interbedded sand is moderately sorted and fine to medium grained, whereas the gravel is loose, coarse, and subrounded. The upper 1.25 m of the exposure is composed of beach ridge sediment composed of subrounded to rounded gravel with foreset bedding. Carbonate coatings are present on the undersides of clasts within the upper gravel deposit.

One sample for luminescence dating (SL007) was collected in a predominately sandy layer within foreshore facies of the beach ridge (Table 1-1c-1; Figure 1-1c-4). Sample SL007 was collected at a depth of approximately 1.8 m and returned a luminescence age of 17.04 ± 1.40 ka.

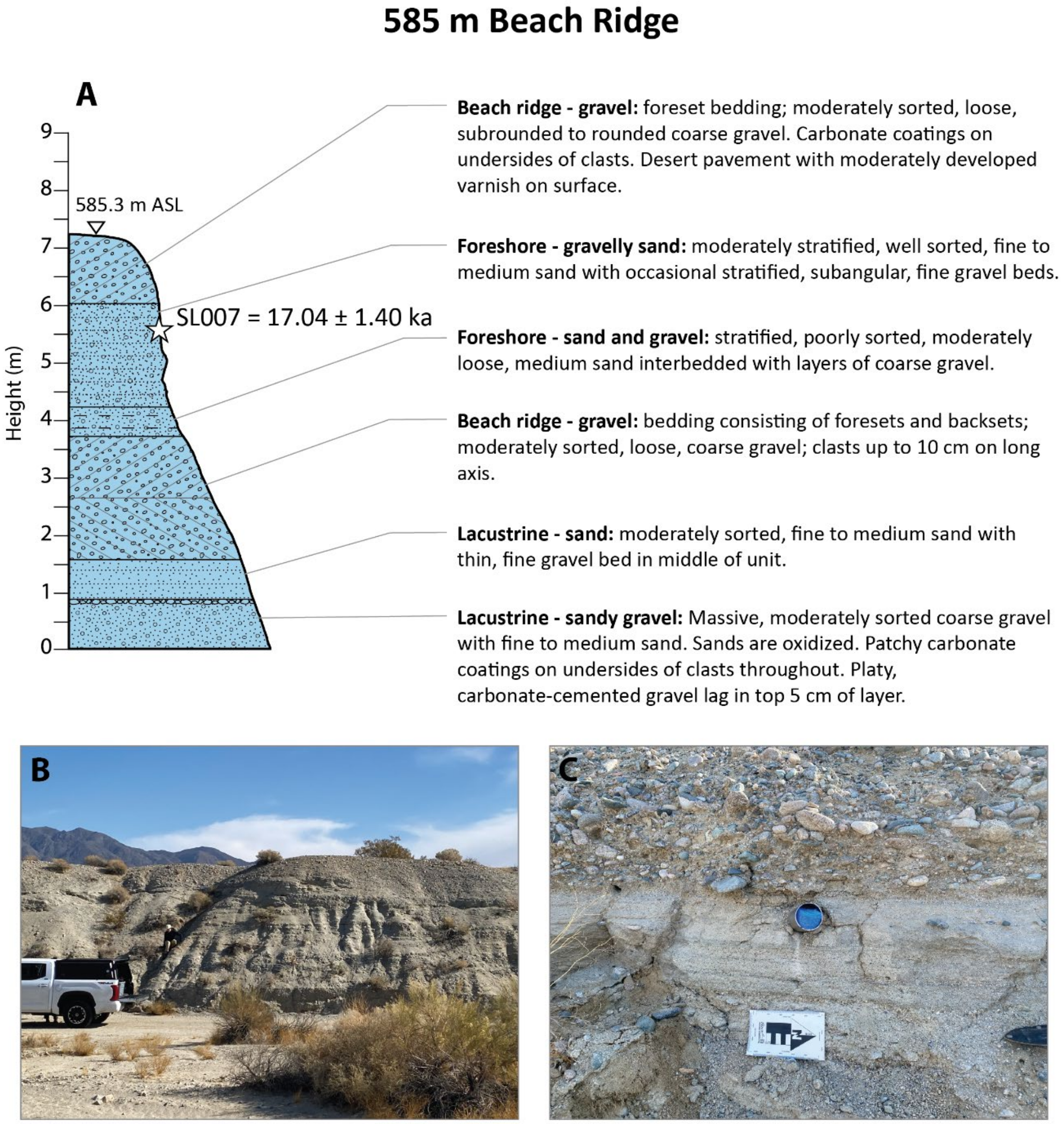

Beach ridge - gravel: foreset bedding; moderately sorted, loose, subrounded to rounded coarse gravel. Carbonate coatings on undersides of clasts. Desert pavement with moderately developed varnish on surface.

Foreshore - gravelly sand: moderately stratified, well sorted, fine to medium sand with occasional stratified, subangular, fine gravel beds.

Foreshore - sand and gravel: stratified, poorly sorted, moderately loose, medium sand interbedded with layers of coarse gravel.

Beach ridge - gravel: bedding consisting of foresets and backsets; moderately sorted, loose, coarse gravel; clasts up to 10 cm on long axis.

Lacustrine - sand: moderately sorted, fine to medium sand with thin, fine gravel bed in middle of unit.

Lacustrine - sandy gravel: Massive, moderately sorted coarse gravel with fine to medium sand. Sands are oxidized. Patchy carbonate coatings on undersides of clasts throughout. Platy, carbonate-cemented gravel lag in top 5 cm of layer.

Figure 1-1c-4. (A) Simplified stratigraphic column and unit descriptions of the 585 m beach ridge site. White star indicates location of luminescence sample (see Table 1-1c-1). Photographs of: (B) bluff exposure of shoreline sediment consisting of mostly stratified sandy and gravelly foreshore lithofacies that are capped by gravelly beach ridge lithofacies; and (C) luminescence sample location of SL007 in layer of fine to medium, stratified sand.

594 m beach ridge

The surface of the 594 m beach ridge consists of a lag of mostly sandy gravel on a moderately preserved and broad crest on the western margin of the Valley Wells beach ridge complex (Figure 1-1c-2). Stratigraphy was described from a 5.1 m high natural stream cut below the crest of the beach ridge. The exposure consists entirely of gravelly sand to sandy gravel beach ridge facies. The base of the exposure is composed of parallel bedded, moderately well sorted, medium grained sand interbedded with layers of fine, subrounded gravel. The upper ~3.5 m of the exposure is composed of interbedded gravel and sand with foreset bedding. The gravel is moderately sorted, subrounded to rounded, and fine to coarse, while the interbedded sand is fine to coarse grained and moderately sorted.

One sample for luminescence dating (SL008) was collected in the sandy facies of the beach ridge sediment (Table 1-1c-1; Fig. 1-1c-5). Sample SL008 was collected at a depth of ~3 m and yielded a luminescence age of 12.34 ± 0.95 ka.

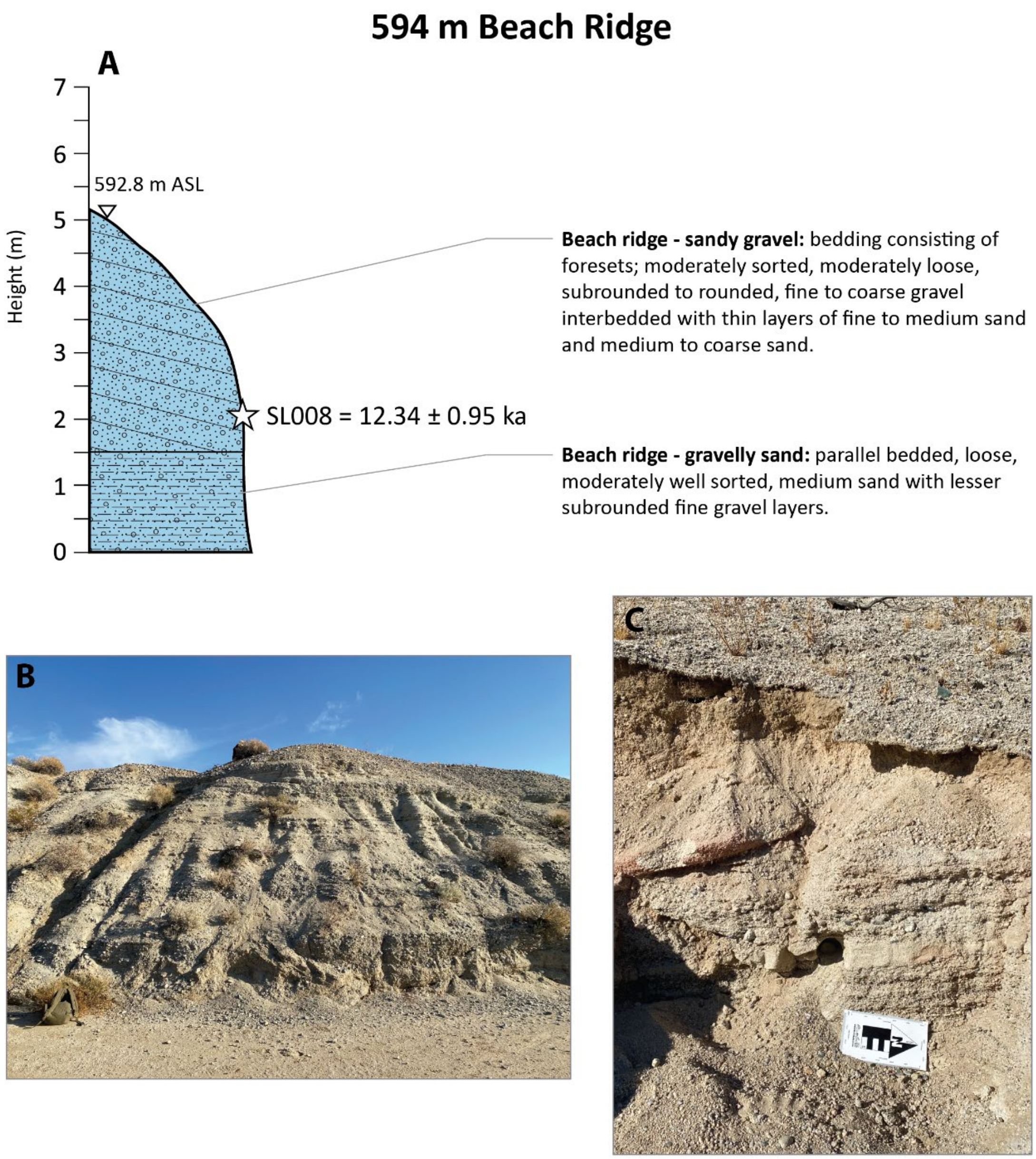
594 m Beach Ridge

Beach ridge - sandy gravel: bedding consisting of foresets; moderately sorted, moderately loose, subrounded to rounded, fine to coarse gravel interbedded with thin layers of fine to medium sand and medium to coarse sand.

Beach ridge - gravelly sand: parallel bedded, loose, moderately well sorted, medium sand with lesser subrounded fine gravel layers.

Figure 1-1c-5. (A) Simplified stratigraphic column and unit descriptions of the 594 m beach ridge site. White star indicates location of luminescence sample (see Table 1-1c-1). Photographs of: (B) stream-cut exposure of stratified sandy and gravelly foreshore facies that are capped by gravelly beach ridge facies; (C) luminescence sample location of SL008 in medium to coarse sand layer interbedded with stratified sandy gravel.

607 m beach ridge

The surface of the 607 m beach ridge exhibits moderately developed and varnished desert pavement surfaces. The beach ridge is not as well developed compared to lower beach ridges and shows a higher degree of dissection west of the axial wash than on the east. Two exposures separated by ~30 m were described along the western margin of the Valley Wells axial wash near the crest of the beach ridge (Figure 1-1c-2). The southern exposure provided conditions that were favorable for luminescence sampling higher in the section, whereas the northern exposure was more favorable for sampling lower in the section.

South exposure

The southern exposure (South) is located 30 m basin ward of the crest of the beach ridge. Stratigraphy was described from an 8.75 m high bluff composed of alluvium overlain by a thin layer of cemented beach rock that is in turn overlain by mostly cemented gravelly beach ridge deposits (Figure 1-1c-6). The alluvium at the base of the section is ~2.5 m thick, and composed of massive, poorly sorted, medium to coarse sand with trace angular to subrounded fine gravel. The alluvium is overlain by an ~10 cm thick layer of cemented, subangular to rounded gravel lag. The gravel lag layer is in turn overlain by interbedded sandy gravel and sand with foreset, topset, and backset bedding. The sand is moderately sorted and fine to medium grained, whereas the gravel is fine to coarse and subrounded to rounded. Moderate cementation is present in the lower sandy gravel shoreline facies, and discontinuous and patchy carbonate coatings are present on the undersides of clasts in the upper sandy gravel units. The cementation at the site is attributed to depositional $CaCO_3$ precipitation that has formed beach rock.

One sample for luminescence dating (SL015) was collected from the less cemented sandy facies of the beach ridge sediment (Table 1-1c-1; Figure 1-1c-6). Sample SL015 was collected at a depth of 1.0 m and returned a preliminary luminescence age of 11.89 ± 0.89 ka. The U/Th ratio measured for this sample is >0.5, indicating authigenic uranium enrichment may have occurred. This suggests that dose rates are likely overestimated, and therefore the calculated age of this sample is considered a minimum. Additional analysis of the sample to correct for authigenic uranium enrichment is currently pending.

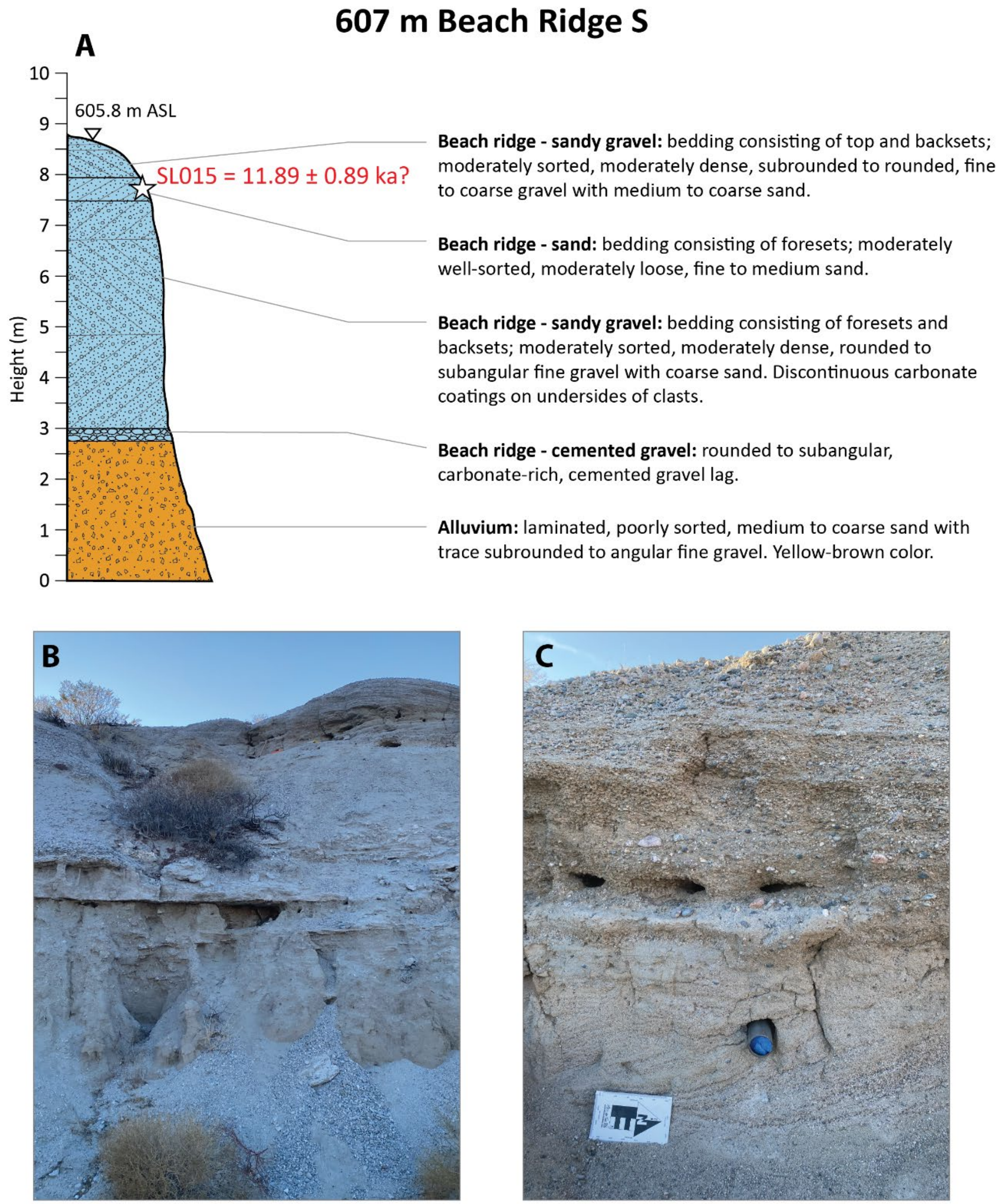

Beach ridge - sandy gravel: bedding consisting of top and backsets; moderately sorted, moderately dense, subrounded to rounded, fine to coarse gravel with medium to coarse sand.

Beach ridge - sand: bedding consisting of foresets; moderately well-sorted, moderately loose, fine to medium sand.

Beach ridge - sandy gravel: bedding consisting of foresets and backsets; moderately sorted, moderately dense, rounded to subangular fine gravel with coarse sand. Discontinuous carbonate coatings on undersides of clasts.

Beach ridge - cemented gravel: rounded to subangular, carbonate-rich, cemented gravel lag.

Alluvium: laminated, poorly sorted, medium to coarse sand with trace subrounded to angular fine gravel. Yellow-brown color.

Figure 1-1c-6. (A) Simplified stratigraphic column and unit descriptions of the 607 m beach ridge site (South exposure). White star indicates location of luminescence sample (see Table 1-1c-1). Photographs of: (B) bluff exposure of alluvial and shoreline deposits; and (C) luminescence sample location of SL015 in sandy foreset overlain by stratified sandy gravel backsets and topsets.

North exposure

The northern exposure is located near the crest of the 607 m beach ridge. Stratigraphy was described from a 6.75 m high bluff exposure that consists of a thick section of interbedded alluvial and shoreline deposits (Figure 1-1c-7). The lower half of the section is comprised of two alluvial units. The lower alluvial unit at the base of the section is composed of fine to medium sand with fine gravel and thinly stratified gravel stringers and exhibits soil development, having rubification and subangular blocky structure near the top of the unit indicating a buried soil. The buried soil has a clear and wavy upper boundary and is more strongly rubified than an overlying second alluvial unit, which consists of ~1.5 m of weakly stratified, poorly sorted, medium sand with trace angular to subrounded fine gravel. The second alluvial unit has no obvious attributes indicating soil development.

The second alluvial unit is unconformably overlain by a ~3 m-thick section of interbedded shoreline and alluvial deposits. A ~0.5 m-thick beach ridge deposit composed of moderately sorted, coarse sand with subangular to subrounded fine gravel with foreset bedding is present with patchy carbonate coatings on the undersides of gravel clasts and moderate beach rock cementation. The gravelly beach deposit is overlain by a thin layer of alluvium consisting of poorly sorted, fine to medium sand with fine gravel, followed by another beach ridge deposit composed of stratified gravelly sand to sandy gravel with backset, foreset, and topset bedding and well-developed beach rock carbonate cementation. Two ~5-cm thick layers of cemented gravel lag are laterally continuous and separate the gravelly beach ridge units with backsets and foresets (see Figure 1-1c-7). The exposure is capped by a thin alluvial unit consisting of poorly sorted, moderately dense, medium sand with fine gravel.

Four samples for luminescence dating were collected within the sand-rich zones of three alluvial units in a near vertical profile (Table 1-1c-1; Figure 1-1c-7). Sample SL011 was collected from the lowest alluvial unit with a buried soil at a depth of ~5.75 m and returned a luminescence age of 25.86 ± 1.77 ka. Sample SL013 was collected at a shallower depth of 4.57 m near the top of the second alluvial unit and returned a luminescence age of 23.68 ± 1.92 ka. Sample SL014 was collected from the interbedded alluvial unit with beach ridge gravels at a depth of 3.37 m, and yielded a luminescence age of 16.83 ± 1.43 ka (Figure 1-1c-7). The ages for the two lower alluvial units are in stratigraphic order and within their uncertainties. Combined with the soils-geomorphology, the ages indicate a period of alluvial aggradation and land surface stability at ~25.9 ka. A second period of alluvial aggradation at ~23.7 ka was likely closely followed by the first of a transgressive-regressive sequence between ~23.7 and ~16.8 ka, followed by a second and maybe third transgressive-regressive sequence after ~16.8 ka.

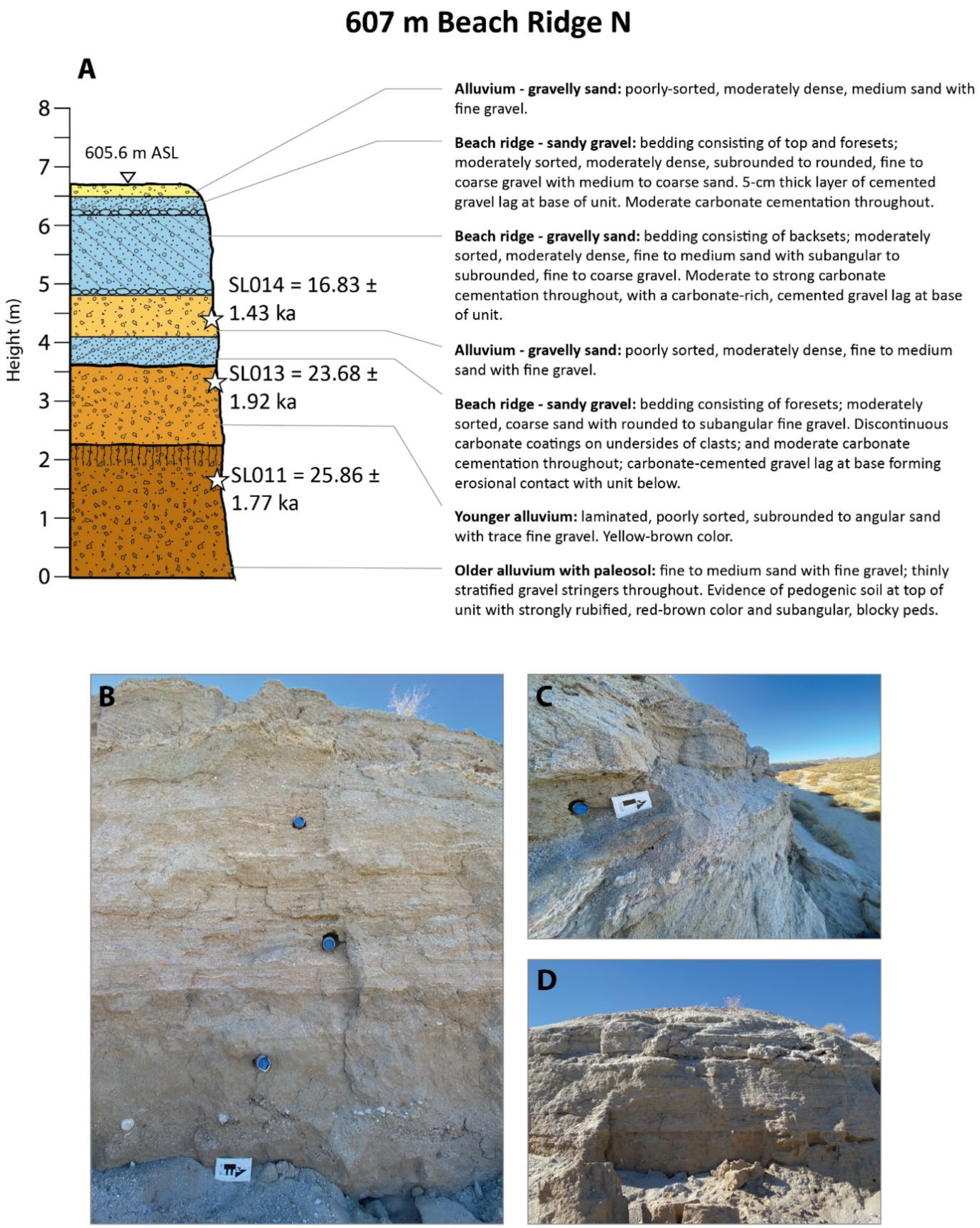

Alluvium - gravelly sand: poorly-sorted, moderately dense, medium sand with fine gravel.

Beach ridge - sandy gravel: bedding consisting of top and foresets; moderately sorted, moderately dense, subrounded to rounded, fine to coarse gravel with medium to coarse sand. 5-cm thick layer of cemented gravel lag at base of unit. Moderate carbonate cementation throughout.

Beach ridge - gravelly sand: bedding consisting of backsets; moderately sorted, moderately dense, fine to medium sand with subangular to subrounded, fine to coarse gravel. Moderate to strong carbonate cementation throughout, with a carbonate-rich, cemented gravel lag at base of unit.

Alluvium - gravelly sand: poorly sorted, moderately dense, fine to medium sand with fine gravel.

Beach ridge - sandy gravel: bedding consisting of foresets; moderately sorted, coarse sand with rounded to subangular fine gravel. Discontinuous carbonate coatings on undersides of clasts; and moderate carbonate cementation throughout; carbonate-cemented gravel lag at base forming erosional contact with unit below.

Younger alluvium: laminated, poorly sorted, subrounded to angular sand with trace fine gravel. Yellow-brown color.

Older alluvium with paleosol: fine to medium sand with fine gravel; thinly stratified gravel stringers throughout. Evidence of pedogenic soil at top of unit with strongly rubified, red-brown color and subangular, blocky peds.

Figure 1-1c-7. (A) Simplified stratigraphic column and unit descriptions of the 607 m beach ridge site (North exposure). White stars indicate location of luminescence samples (see Table 1-1c-1). Photographs of: (B) bluff exposure of alluvial and shoreline deposits; (C) luminescence sample location of SL014 in thinly interbedded alluvium; and (D) sample locations of SL013 and SL011 in lower alluvial units.

645 m beach ridge

The 645 m beach ridge and associated beach plain are preserved near the Valley Wells axial wash where its margins are buried by distal alluvial fans (Figure 1-1c-2). The surface of the 645 m beach ridge consists of moderately developed and varnished desert pavement surfaces. Stratigraphy was described from a 9.6 m high bluff ~180 m basinward of the crest of the beach ridge (Figure 1-1c-8). The exposure consists of a ~3.5 m-thick cemented beach rock composed of very coarse sand and gravel at the base of the section. The massive beach rock is overlain by a sequence of gravelly shoreline deposits and back barrier deposits consisting of interbedded aeolian sand and lagoonal silty sand facies.

The massive beach rock deposit consists of cemented, coarse sand and subrounded to rounded, fine gravel with foreset bedding. Differential erosion of the cemented sand and gravel has produced irregular, pillar-like structures. The thick beach rock unit is unconformably overlain by massive to weakly stratified, subangular to subrounded, loose, sandy gravel facies of beach ridge sediment. Overlying the beach gravel is a <1 m thick unit of well sorted, massive, loose, fine to medium sand having the characteristics of aeolian sand sheet deposits. The aeolian sand also exhibited a 10 cm thick layer of dense, organic-rich silty sand (see figure 1-1c-8D). Carbonate nodules and oxidized root casts in the upper 10 cm of the aeolian sand unit are present and indicate incipient soil development. Overlying the aeolian sand is a 0.5 m thick layer of laminated, dense, silty sand to sandy silt that is light brown to white in color having the characteristics of lagoonal to playette deposits.

The silty sand is in turn overlain by beach ridge deposits consisting of moderately sorted, subrounded to rounded, fine to coarse gravel with medium to coarse sand and foreset bedding. The exposure is capped by a thin layer of alluvium composed of angular to subangular, coarse gravel.

Two samples for luminescence dating were collected in a vertical profile within the fine to medium aeolian sand facies of the back barrier deposit (Table 1-1c-1; Figure 1-1c-8). Sample SL017 was collected at a depth of 3.6 m and yielded a luminescence age of 14.16 ± 0.97 ka. Sample SL018 was collected at a shallower depth of 3.2 m and yielded a luminescence age of 12.44 ± 0.90 ka. The U/Th ratio measured for both samples are >0.5, indicating authigenic uranium enrichment may have occurred. This suggests that dose rates are likely overestimated, and therefore the calculated age of the samples are considered a minimum. Additional analysis of the samples to correct for authigenic uranium enrichment is currently pending.

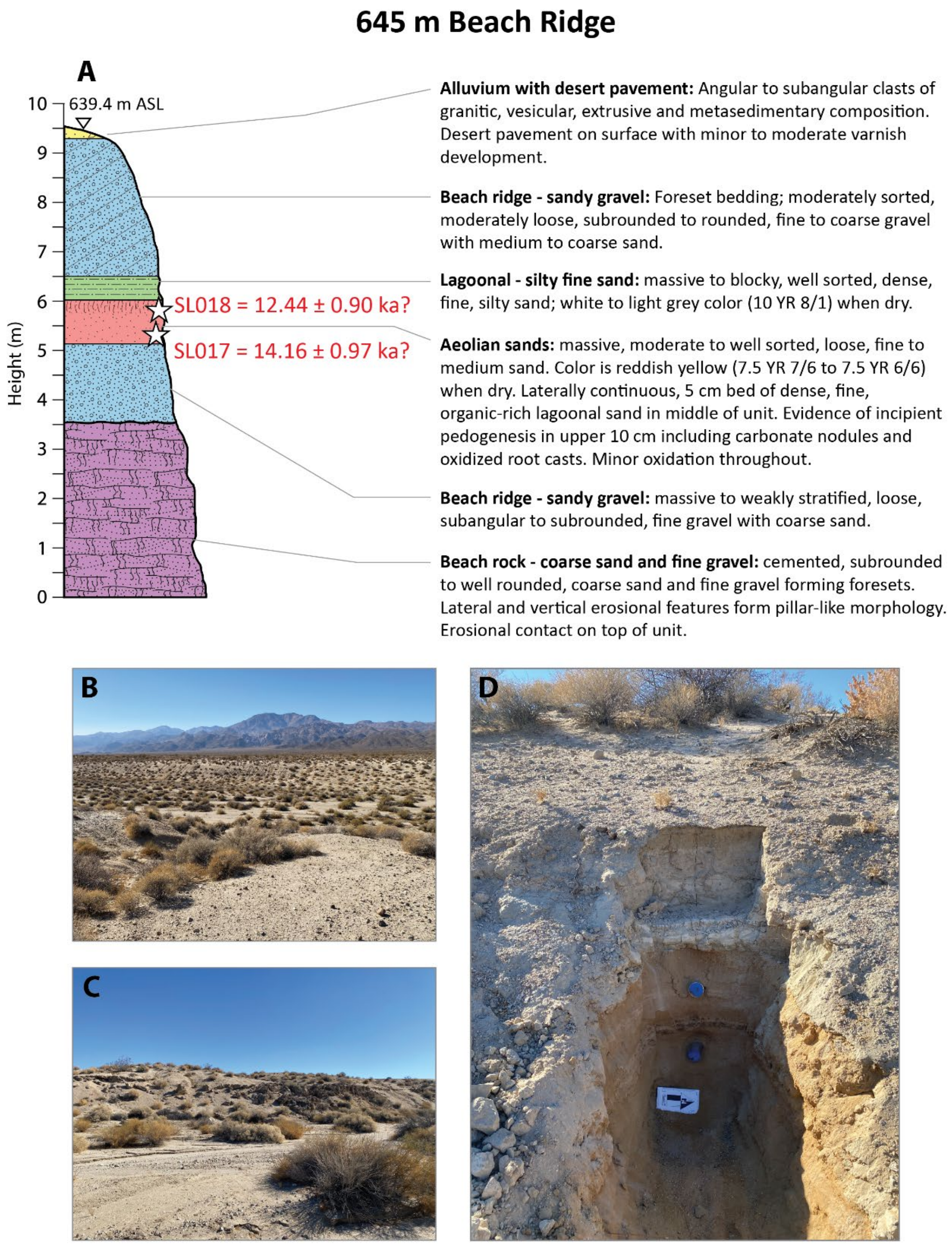

Alluvium with desert pavement: Angular to subangular clasts of granitic, vesicular, extrusive and metasedimentary composition. Desert pavement on surface with minor to moderate varnish development.

Beach ridge - sandy gravel: Foreset bedding; moderately sorted, moderately loose, subrounded to rounded, fine to coarse gravel with medium to coarse sand.

Lagoonal - silty fine sand: massive to blocky, well sorted, dense, fine, silty sand; white to light grey color (10 YR 8/1) when dry.

Aeolian sands: massive, moderate to well sorted, loose, fine to medium sand. Color is reddish yellow (7.5 YR 7/6 to 7.5 YR 6/6) when dry. Laterally continuous, 5 cm bed of dense, fine, organic-rich lagoonal sand in middle of unit. Evidence of incipient pedogenesis in upper 10 cm including carbonate nodules and oxidized root casts. Minor oxidation throughout.

Beach ridge - sandy gravel: massive to weakly stratified, loose, subangular to subrounded, fine gravel with coarse sand.

Beach rock - coarse sand and fine gravel: cemented, subrounded to well rounded, coarse sand and fine gravel forming foresets. Lateral and vertical erosional features form pillar-like morphology. Erosional contact on top of unit.

Figure 1-1c-8. (A) Simplified stratigraphic column and unit descriptions of the 645 m beach ridge site. White stars indicate location of luminescence samples (see Table 1-1c-1). Photographs of: (B) bluff exposure of shoreline and back barrier lagoonal deposits prior to excavating stratigraphic pits (photographed from east side of axial wash); (C) view of basal beach rock deposit directly east of the axial wash from sample location; and (D) stratigraphic pit and sample locations of SL017 and SL018 in aeolian sands that are overlain by laminated lagoonal silty fine sand to sandy silt.

668 m beach plain

The surface of the 668 m beach plain locally consists of alluvium with a moderately developed soil and abundant vegetation. Stratigraphy was described from a 7.3 m high bluff between the 645 and 680 m beach ridges (Figure 1-1c-2). The exposure consists of back barrier lagoonal and aeolian deposits interbedded with shoreline deposits that are in turn overlain by alluvium (Figure 1-1c-9). The lower half of the section is composed of a sequence of back barrier deposits consisting of laminated, very fine to fine sand with silt lagoonal facies and weakly stratified, loose, fine to medium aeolian sand facies. The sequence of back barrier deposits is overlain by a 2-m thick unit of thinly stratified sand and gravel with backset and topset bedding characteristic of beach ridge facies. The sands are moderately sorted and medium to coarse grained, while the stratified gravels are moderately sorted, subrounded to rounded, and coarse. Patchy carbonate coatings are present on the bottom of gravel clasts throughout the unit.

The beach ridge deposit is overlain by another sequence of interbedded back barrier lagoonal sandy silts and aeolian sand that is overlain by thinly interbedded aeolian sand and beach ridge gravelly sands. The base of this sequence consists of a ~10 cm thick layer of lagoonal sandy silt overlain by aeolian sand that exhibits attributes of a buried soil with rubification and subangular blocky structure (Figure 1-1c-9D). The buried soil is overlain by 0.4 m of unweathered aeolian sand and ~0.5 m of thinly interbedded sandy gravel beach ridge and aeolian sand layers. The beach ridge facies consist of coarse sand and subrounded to rounded, fine to coarse gravel. The layers of sand are massive, well sorted, and fine to medium.

The upper 1.5 m of the exposure is composed of massive, poorly sorted, silty sand with subangular to subrounded fine gravel. A moderately developed soil has formed on within the upper 40 cm of the alluvial deposit and is reflected by rubification and soil structure.

Four samples for luminescence dating were collected in the aeolian sand and beach ridge sediment (Figure 1-1c-9). Two samples were collected in a vertical profile in the lower section of the exposure within aeolian sand deposits at depths of 6.4 and 5.9 m. Two additional samples were collected from the same exposure, but ~20 m to the north, and higher in section at depths of 2.3 and 1.5 m. Analyses of the samples from the 668 m beach plain are in progress and results are pending.

668 m Lake Plain

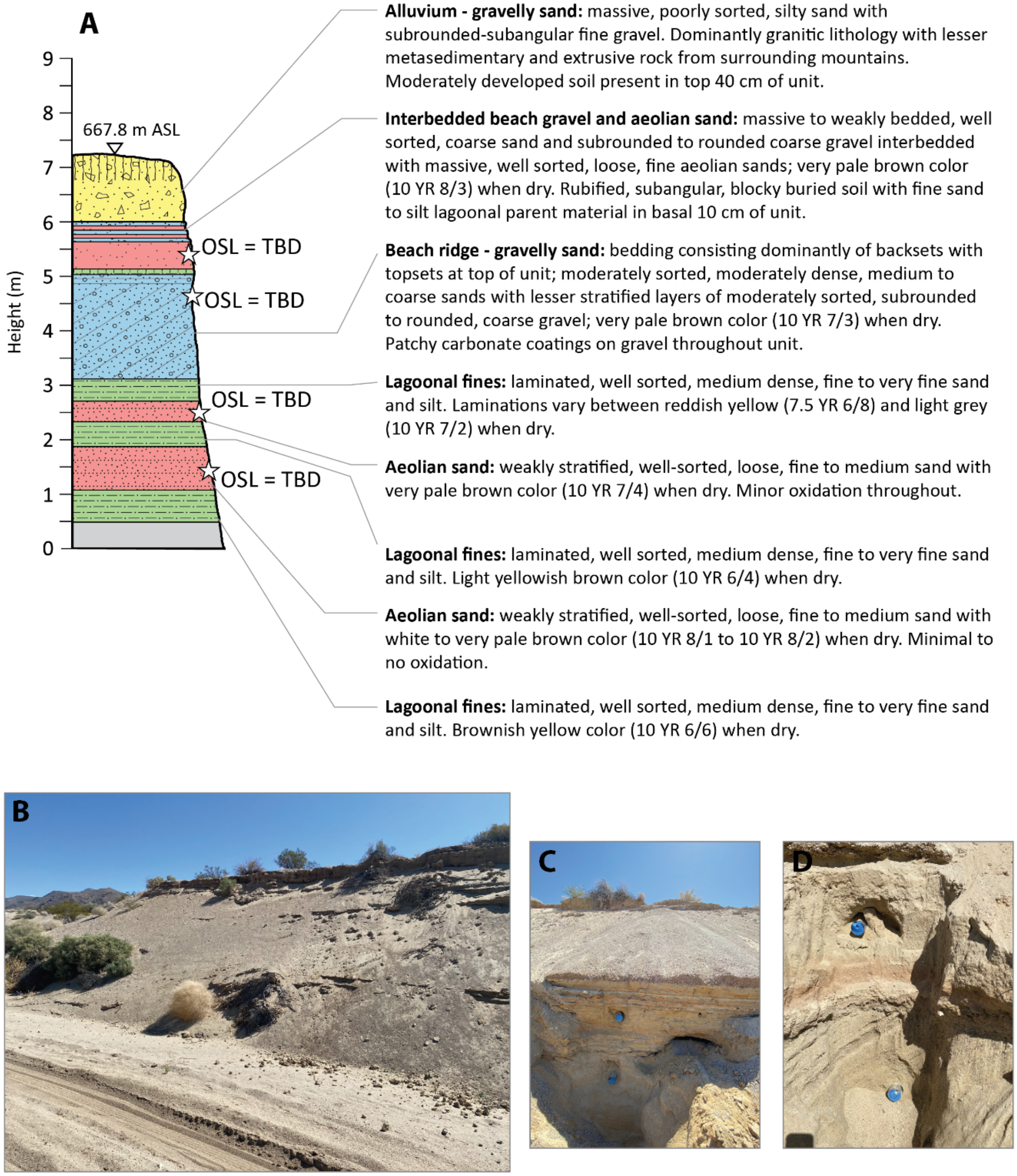

Alluvium - gravelly sand: massive, poorly sorted, silty sand with subrounded-subangular fine gravel. Dominantly granitic lithology with lesser metasedimentary and extrusive rock from surrounding mountains. Moderately developed soil present in top 40 cm of unit.

Interbedded beach gravel and aeolian sand: massive to weakly bedded, well sorted, coarse sand and subrounded to rounded coarse gravel interbedded with massive, well sorted, loose, fine aeolian sands; very pale brown color (10 YR 8/3) when dry. Rubified, subangular, blocky buried soil with fine sand to silt lagoonal parent material in basal 10 cm of unit.

Beach ridge - gravelly sand: bedding consisting dominantly of backsets with topsets at top of unit; moderately sorted, moderately dense, medium to coarse sands with lesser stratified layers of moderately sorted, subrounded to rounded, coarse gravel; very pale brown color (10 YR 7/3) when dry. Patchy carbonate coatings on gravel throughout unit.

Lagoonal fines: laminated, well sorted, medium dense, fine to very fine sand and silt. Laminations vary between reddish yellow (7.5 YR 6/8) and light grey (10 YR 7/2) when dry.

Aeolian sand: weakly stratified, well-sorted, loose, fine to medium sand with very pale brown color (10 YR 7/4) when dry. Minor oxidation throughout.

Lagoonal fines: laminated, well sorted, medium dense, fine to very fine sand and silt. Light yellowish brown color (10 YR 6/4) when dry.

Aeolian sand: weakly stratified, well-sorted, loose, fine to medium sand with white to very pale brown color (10 YR 8/1 to 10 YR 8/2) when dry. Minimal to no oxidation.

Lagoonal fines: laminated, well sorted, medium dense, fine to very fine sand and silt. Brownish yellow color (10 YR 6/6) when dry.

Figure 1-1c-9. (A) Simplified stratigraphic column and unit descriptions of the 668 m beach plain site. White stars indicate location of luminescence sample sites (results pending). Photographs of: (B) bluff exposure of back barrier interbedded lagoonal and aeolian facies with beach ridge facies capped by alluvium; (C) luminescence sample locations in two aeolian sand layers lower in section; and (D) sample locations in gravelly sand beach ridge and aeolian sand deposits. The sample locations are separated by a buried soil developed on back barrier lagoonal sandy silts and aeolian sand.

Summary

The exposures in the axial drainage through the Valley Wells beach ridge complex provided an excellent opportunity to directly date deposits that will constrain the timing of water levels of Searles Lake. Stratigraphic analysis and targeted geochronologic sampling of sand-rich shoreline, back barrier aeolian, and alluvial deposits yielded the first luminescence ages to either directly date or constrain the age of shorelines in Searles Valley.

Ten IRSL ages have been processed to date, yielding preliminary ages for beach ridge, back barrier aeolian, and alluvial deposits between the elevations of 570 and 645 m. The youngest age of 12.34 ± 0.95 ka was collected in a sandy gravel deposit at the 594 m beach ridge site, while the oldest age of 25.86 ± 1.77 ka was collected from an alluvial deposit displaying a buried soil at the 607 m beach ridge site. Furthermore, the luminescence samples collected at the lowest beach ridge site at 570 m of 16.12 ± 1.12 and 16.07 ± 1.38 ka are in agreement with ^{14}C ages of nodose tufa collected by Smith (2009) at a nearby site.

Stratigraphic analyses and preliminary luminescence ages indicate at least three transgressive-regressive cycles occurred in the Valley Wells subbasin between ~26 and ~12.3 ka. The lowest alluvial unit at the northern 607 m beach ridge exposure shows a period of alluvial aggradation and land surface stability at ~25.9 ka, followed by a second period of alluvial aggradation at ~23.7 ka. The lack of soil development on the ~23.7 ka alluvium and the overlying gravelly sandy beach ridge deposit suggests the period of alluvial aggradation and the first transgressive-regressive sequence reaching an elevation of at least 607 m occurred close in time, sometime between ~23.7 and ~16.8 ka. Stratigraphy at this site also suggests that a second and possibly a third transgression reached an elevation of at least 607 m after ~16.8 ka.

Lake levels appeared to have regressed and stabilized at the 585 m beach ridge by ~17 ka and then dropped again stabilizing at the 570 m beach ridge by ~16.1 ka. Dated shoreline deposits in the subbasin at elevations below the 607 m beach ridge site also show evidence of a third transgression that occurred between ~17 and ~12.3 ka. This third transgression stabilized at ~12.3 ka and formed the 594 m beach ridge.

Results of four luminescence samples collected from interbedded aeolian and beach ridge deposits at the highest 668 m beach plain site investigated are pending, with preliminary results expected in late fall 2025 that will provide insight to the timing of water levels reaching elevations up to ~670 m. Of note, a well-developed beach ridge at 670 m in China Lake basin yielded preliminary luminescence ages of ~13 ka (see Day 1, Stop 1b; Figure 1-

1b-4). The luminescence ages of ~13 ka for the 670 m beach ridge in China Lake basin and ~12.3 ka for the 594 m beach ridge in Searles basin indicate the third transgressive-regressive lake cycle may have reached an elevation of at least ~670 m by ~13 ka and dropped to an elevation of ~594 m by ~12.3 ka. The lower range of ^{14}C tufa dates of ~12.7 and 12.4 cal kyr BP coating the lower 570 m beach ridge are similar to the luminescence ages of the third transgressive-regressive lake cycle.

Additional luminescence analysis to correct for authigenic uranium enrichment in samples at the 607 m (South) beach ridge site and back barrier aeolian deposits of the 645 beach ridge site is planned. Additional duplicate luminescence samples from the 570, 594, and 607 m beach ridges are also awaiting analysis, with results expected in spring 2025. These data will help strengthen the chronological record by testing and potentially revising the preliminary stratigraphic framework established from the current dataset.

Future fieldwork will focus on additional stratigraphic studies and luminescence sampling of the 680 and 690 m highstand shorelines in the Valley Wells subbasin, as well as at southern end of Searles Valley in an area informally referred to as the “Stairway to Heaven” geomorphic surface (see Day 1, Stop 2b for details).

References

Benson, L. V., Currey, D. R., Dorn, R. I., Lajoie, K. R., Oviatt, C. G., Robinson, S. W., Smith, G. I., & Stine, S. (1990). Chronology of expansion and contraction of four great Basin lake systems during the past 35,000 years. *Palaeogeography, Palaeoclimatology, Palaeoecology*, *78*(3), 241–286. https://doi.org/10.1016/0031-0182(90)90217-U

Phillips, F. M. (2008). Geological and hydrological history of the paleo-Owens River drainage since the late Miocene. *Late cenozoic drainage history of the southwestern Great Basin and lower Colorado River region: geologic and biotic perspectives*, 439, 115–150. https://doi.org/10.1130/2008.2439(06)

Roberts, H.M. & Plater, A.J. (2005). Optically stimulated luminescence (OSL) dating of sands underlying the gravel beach ridges of Dungeness and Camber, southeast England, UK. *The Holocene*, 17(4), 495-505. https://doi.org/10.1177/0959683607077034

Smith, G.I., and Street-Perrott, F.A., 1983. Pluvial lakes of the western United States. In: Porter, S.C. (Ed.), The Late Pleistocene. Univ. Minn. Press, Minneapolis, pp. 190–212.

Smith, G. I. (2009). Late Cenozoic geology and lacustrine history of Searles Valley, Inyo and San Bernardino counties, California. U.S. Geological Survey Professional Paper 1727, 115 p., 4 plates.

Tamura, T. (2012). Beach ridges and prograded beach deposits as palaeoenvironment records. *Earth-Science Reviews*, 114(3–4), 279–297. https://doi.org/10.1016/j.earscirev.2012.06.004

Day 1 Stop 2

Day 1, Stops 2a & 2b: (N35.62562°, W 117.378942°)

Field Stop Leaders: Steven Bacon[1] and Silvio Pezzopane[2] ([1]Desert Research Institute, Reno, Nevada; [2]Paisley, Oregon)

LOGISTICS

From the TIS General Store and Gas Station in Trona, we will drive south along Trona Road for 6.3 miles before turning left onto a well-graded road that is marked as the Pinnacles Entrance. Continue south 4.4 miles following a well-established dirt road to our destination. Our destination is a large gravelly beach barrier with a well-developed desert pavement and varnished surface within the Trona Pinnacles National Natural Landmark. Bring a chair to enhance your level of comfort at Stop 2 because we plan to give two presentations for you to enjoy. There is also nice stratigraphy of the beach barrier exposed in a railroad cut.

The goals of Stop 2 are to: (2a) discuss the history of water levels of Searles Lake inferred from the elevation of previously dated mollusk shells in Searles basin (Bacon); and (2b) present preliminary analysis of high and old shoreline features in the vicinity of the overflow channel of Searles Lake and the Garlock fault (Bacon and Pezzopane).

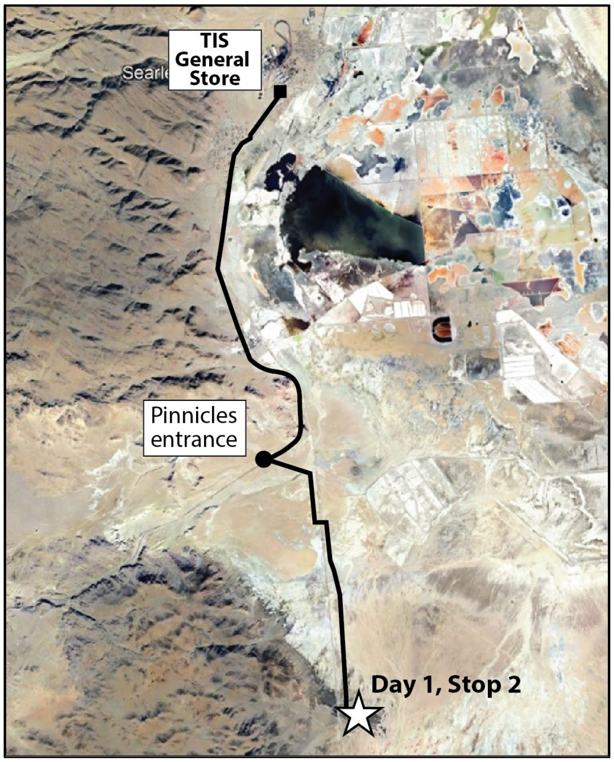

Route to Day 1, Stop 2 from the TIS General Store and Gas Station in Trona.

Discussion (A) Topographic analysis of freshwater mollusk sites to infer the position of water levels of Searles Lake

Field Stop Leader: Steven Bacon (Desert Research Institute, Reno, NV)

Introduction

Previous studies of sediment lake cores in Searles basin demonstrate that Searles Lake has been the predominant terminal lake in the paleo-Owens River system for the past ~1 Myr (Phillips et al., 1983; Jannik et al., 1991; Bischoff et al., 1985; Smith, 2009). The record of overflow from Owens Lake also shows that it spilled most of the time at or near minimum sill levels during the past 50,000 years (Bacon et al., 2020), supporting lake core studies in both Owens and Searles basins. If Searles Lake was indeed the predominant terminal lake in the paleo-Owens River system, one would expect there to be geomorphic evidence for terminal lakes. Given the large size of Searles basin, one would also expect that these terminal lakes would not be very deep because of the amount of water required to support a large body of water at relatively low elevations where evaporative demand is high, even during pluvials.

Of all the shoreline features surveyed in Searles basin, there is one feature that exhibits the geomorphic attributes of reflecting long-term stable water levels. This shoreline feature is referred to as the Pinnacles bar by Smith (2009) and is preserved on the northwestern margin of the Trona Pinnacles National Natural Landmark in the western sector of Searles basin and is the focus of Day 1, Stop 2a (Figure 1-2a-1).

Pinnacles bar

The Pinnacles bar is a prominent beach barrier that has formed between the eastern range front of the Spangler Hills and The Pinnacles (Figure 1-2a-1). The barrier is actively being eroded on its southern margins by drainages from the Spangler Hills, as well as on its southeastern margin by Teagle Wash. The barrier also exhibits a well-developed and varnished desert pavement surface. The degree of desert pavement and varnish development makes The Pinnacle bar unique compared to other geomorphic surfaces (alluvial and lacustrine) that are older based on higher topographic positions, but have relatively less desert pavement developed. The desert pavement surface is underlain by a thick dust cap (Av/Bw horizons) that is observed in railroad and stream exposures, and on the roadbed where bladed.

Previous ^{14}C and U/Th dating of tufa

The stratigraphy of The Pinnacles bar is well exposed in a railroad through cut and in Teagle Wash and consists of extremely hard, interbedded, carbonate-cemented sand and gravel beach facies, ~0.3 to 1.0-thick lithoid tufa layers, and alluvium. The Pinnacles bar was previously investigated and the site of paired ^{14}C and U/Th dating of tufa in exposures near Teagle Wash (Garcia et al., 1993; Smith, 2009; Figure 1-2a-1). Tufa layers in three different stratigraphic units returned the following mean U/Th dates of replicate samples in descending stratigraphic order: **Unit 1**: 25.3 ± 1.0 ka (n = 3); **Unit 2**: 85.4 ± 4.0 (n = 3) and 65.6 ± 3.0 ka (n = 4); and **Unit 3**: 164.0 ± 9.0 ka (n = 3). Inconsistency in the U/Th dating of Unit 2 was acknowledged by Garcia et al. (1993) because there is ~20 kyr difference in age of tufa sampled from the same stratigraphic horizon.

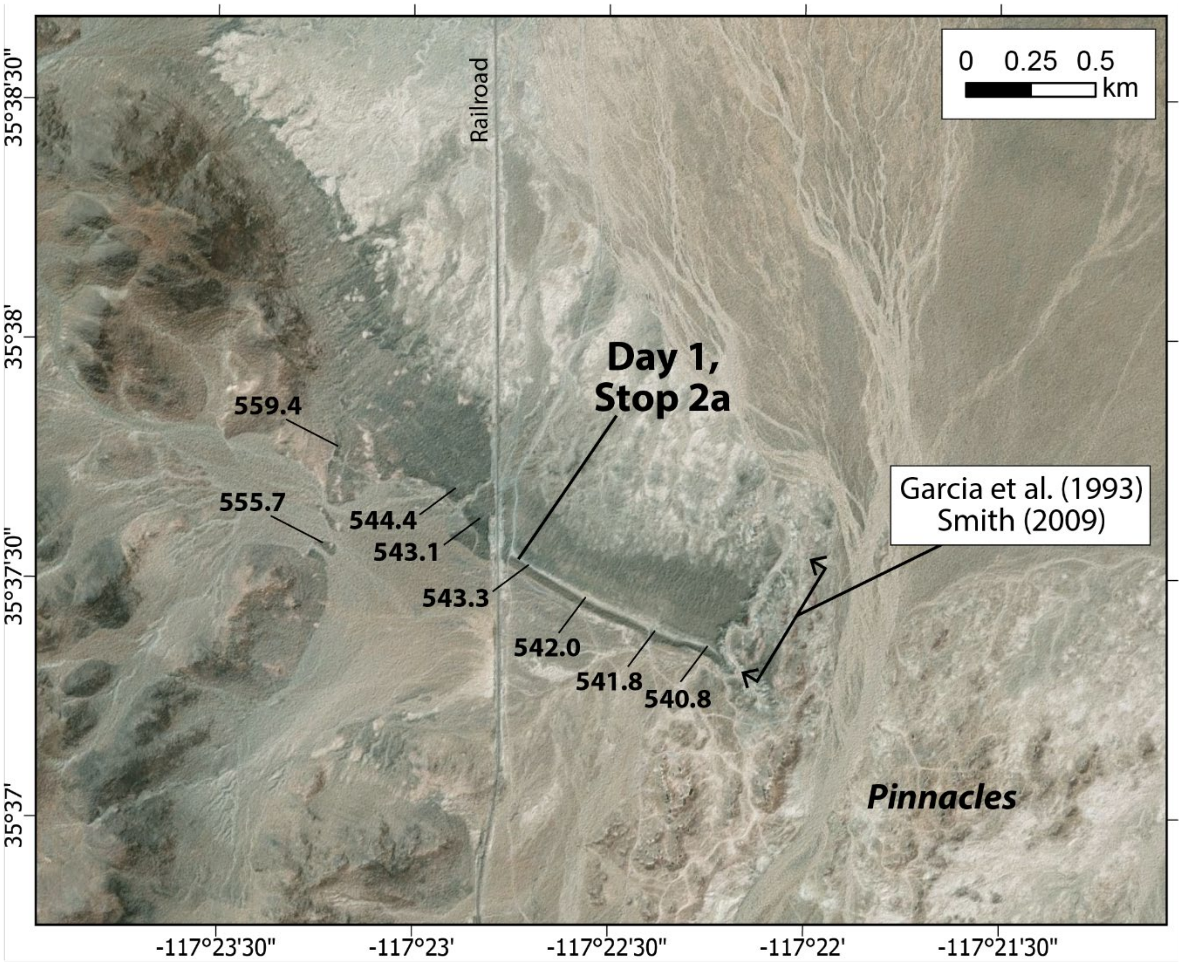

Figure 1-2a-1. NAIP imagery showing location of Day 1, Stop 2 on the Pinnacles bar of Garcia et al. (1993) and Smith (2009). The elevations of the crest of the bar from a 2-m DEM and location of the Pinnacles tufa tower complex are also shown.

The ^{14}C dates yielded systematic younger ages compared to corresponding U/Th dates of the same tufa sample. The conventional ^{14}C dates for the same units are in stratigraphic order, which are: **Unit 1**: 18.1 ± 0.17 kyr BP; **Unit 2**: 25.4 ± 0.14 and 29.1 ± 0.24 kyr BP; and **Unit 3**: 32.3 ± 0.29 kyr BP. Although the dates are in stratigraphic order, Garcia et al. (1993) cautioned their reliability because of the paired U/Th dates that were much older.

An explanation for the much younger ^{14}C dates of the tufa was attributed to contamination by exchange with young carbon from the atmosphere if the tufa was exposed to air during low water levels or from groundwater when the tufa was submerged by subsequent water levels at or above the sample sites. In general, the U/Th dates were considered more reliable than ^{14}C dates, but given The Pinnacles bar's low topographic setting, there is also the possibility that groundwater with differing water chemistries could have added or dissolved the tufa's initial uranium (Garcia et al., 1993). This may explain the 20 kyr difference in age of Unit 2. Smith (2009) also considered both the ^{14}C and U/Th dates unreliable, however, it is not clear why he did not favor the U/Th dates.

Topographic analysis of dated mollusk shell sample sites

The preliminary lake-level curve of Searles Lake presented in the Day 1, Stop 1b discussion (see Figure 1-1b-5) shows that water levels prior to ~11.5 ka mostly occur between the elevations of 530 and 570 m during the past 50 kyr. Interestingly, the elevation of the The Pinnacles bar falls within this range. This range in water level is strongly controlled by the elevation of dated mollusk shells in deltaic and shoreline deposits sampled in the vicinity of Poison Canyon. The dated mollusk shells include a variety of aquatic snails and clams, and along with their reported sample site elevation, can be used as a proxy indicator for the position of paleolake levels.

A non-parametric statistical analysis was performed to better estimate the long-term water level history of both China and Searles Lake based on simply using the elevation of dated shells with ^{14}C ages ranging from ~46.0 to 11.5 cal kyr BP, that are the same data shown on the preliminary lake-level curves. A kernel density estimate was used to produce a probability distribution of elevations for 25 shells from China Lake basin and 47 shells from Searles basin (Figure 1-2a-2). A kernel density estimate with a corresponding histogram was used because it provides a statistical tool to visualize and quantify the probabilistic elevation of dated shells in both basins.

The kernel density estimate identified elevations defined by either unimodal or bimodal peaks in the probability distributions (Figure 1-2a-2). A unimodal peak at an elevation of 662.0 m was determined for shell elevations in China Lake with ^{14}C ages from ~22.0 to 11.5 cal kyr BP. Interestingly, the elevation of 662.0 m is ~3 m below the modern soft sill of China

Lake basin. The kernel density estimate also shows a bimodal peak for Searles Lake, having a lower probability peak at 642.1 m controlled by shells with ^{14}C ages from ~16 to 13 cal kyr BP. and a higher probability peak at 539.5 m controlled by shells with ^{14}C ages from ~46 to 12.5 cal kyr BP. (Figure 1-2a-2). These elevations also coincide with geomorphic features in the basin, where the elevation of 642.1 m is ~3 m below the elevation of the well-developed 645 m beach ridge at the Valley Wells beach ridge complex (see Day 1, Stop 1c; Figure 1-1c-2). The higher probability peak at a much lower elevation of 539.5 m also corresponds to 1.3 m below the lowest elevation of The Pinnacles bar at 540.8 m (Figure 1-2a-1).

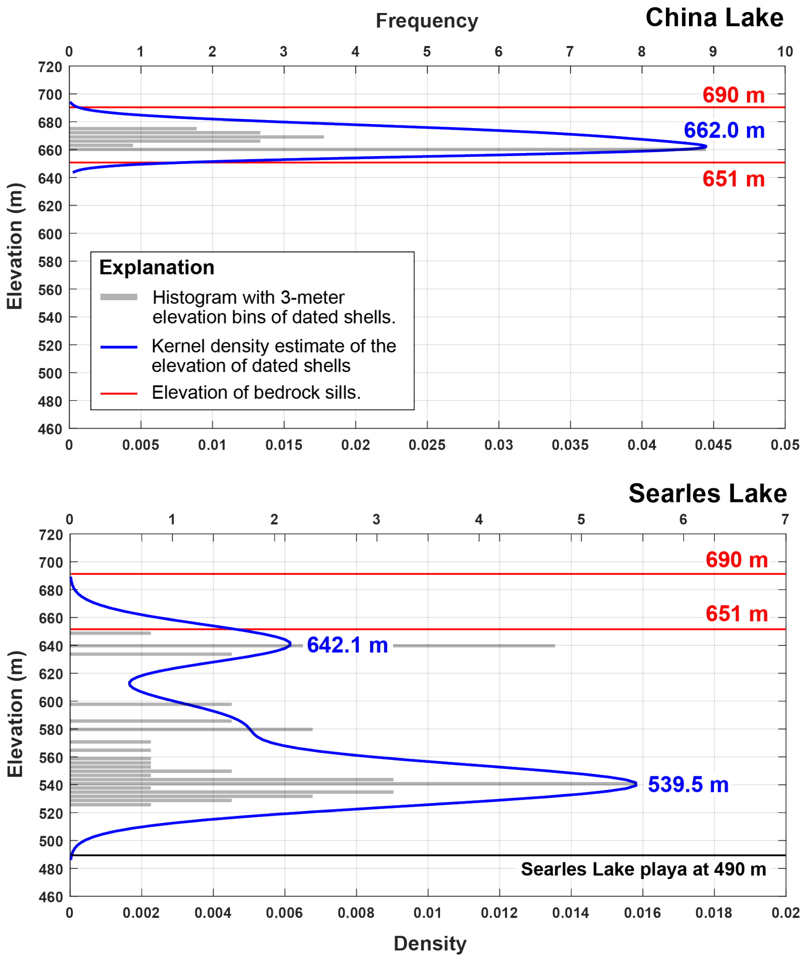

Figure 1-2a-2. Plots showing kernel density estimates and corresponding histograms of the elevation of dated mollusk shell sites in China basin (above) and Searles basin (below). The elevation of bedrock sills at the overflow level of Searles Lake at 690 m and China Lake at 651 m, and playa are also shown. Histogram bars represent 3-m elevation bins of shell sample sites in China basin (n = 25) and Searles basin (n = 47).

Furthermore, the minor shoulder on the higher probability peak at 580 m also corresponds to the well-developed 585 m beach ridge at the Valley Wells beach ridge complex. Lastly, the probabilistic elevations of shell sites at 662.0, 642.1, and 539.5 m are all lower than corresponding beach ridges and barriers in the lake basins by a few meters. This is consistent with expectations because the shell elevations provide a maximum constraint on water level and the crest of beach ridges and barriers form above the mean water level.

Thoughts

The use of a kernel density estimate combined with the elevation of dated shell sample sites provided a first-order method to identify potential stable water levels independent of ^{14}C age. The analysis performed for Searles Lake identified probabilistic water levels that correspond reasonably well with two beach ridges of the Valley Wells beach ridge complex, as well as with the elevation of The Pinnacles bar. Previous ^{14}C and U/Th dating of The Pinnacles bar yielded a range of ages and geomorphic uncertainties, having U/Th dates from ~164 to 25 ka. Given the dating uncertainties, the stratigraphy and well-developed form of The Pinnacles bar also suggest that it is likely the product of long-term stable water levels at ~542 m(Figure 1-2a-1). The higher probability peak at an elevation of 539.5 m is used as a proxy for long-term Searles Lake water levels. This elevation likely reflects a hydrologic regime that has a long-term equilibrium between water inputs and outputs, wherein precipitation, open-water evaporation, and discharge from the paleo-Owens River are balanced such that lake levels at ~542 m have remained quasi-stable over millennial timescales.

References

Bischoff, J.L., Rosenbauer, R.J., and Smith, G.I., 1985. Uranium-series dating of sediments from Searles Lake: differences between continental and marine climate records. Science 227, 1222–1224.

Garcia, J.F., Bischoff, J.L., Smith, G.I., and Trimble, D., 1993. Uranium-series and radiocarbon dates on tufas from Searles Lake, California. U.S. Geological Survey Open-File Report 93-311, 8 p.

Jannik, N.O., Phillips, F.M., Smith, G.I., Elmore, D., 1991. A 36Cl chronology of lacustrine sedimentation in the Pleistocene Owens River system. Geological Society of America Bulletin 103, 1146–1159.

Phillips, F.M., 2008. Geological and hydrological history of the paleo-Owens River drainage since the late Miocene, in Reheis, M.C., Hershler, R., and Miller, D.M., eds., Late Cenozoic Drainage History of the Southwestern Great Basin and Lower Colorado River Region: Geologic and Biotic Perspectives: Geological Society of America Special Paper 439, p. 115–150.

Smith, G.I., 2009, Late Cenozoic geology and lacustrine history of Searles Valley, Inyo and San Bernardino Counties, California. U.S. Geological Survey Professional Paper 1727, 115 p.

Discussion (B) Preliminary analysis of high and old shoreline features of Searles Lake in the vicinity of the overflow channel and the Garlock fault

Field Stop Leader: Steven Bacon and Silvio Pezzopane

Introduction

In the south-southeastern sector of Searles basin, on the north side of the Garlock fault, is a small tectonic block we call "Heaven" that, during high and overflowing water levels, forms a trapezoidal-shaped peninsula between the lake basin and sill area. The "Stairway" is what we call the suite of almost uncountable shoreline scarps and beach ridges developed best on the north- and west-facing slopes of "Heaven" below the overflow level of ~690 m (Figure 1-2b-1). The goal of Day 1, Stop 2b is to present initial observations and preliminary analysis of: 1) a geomorphic surface with shorelines features above ~690 m that we refer to as the "Stairway to Heaven" and 2) the local tectonic setting of the overflow channel of Searles basin that is controlled by transpression on the Garlock fault.

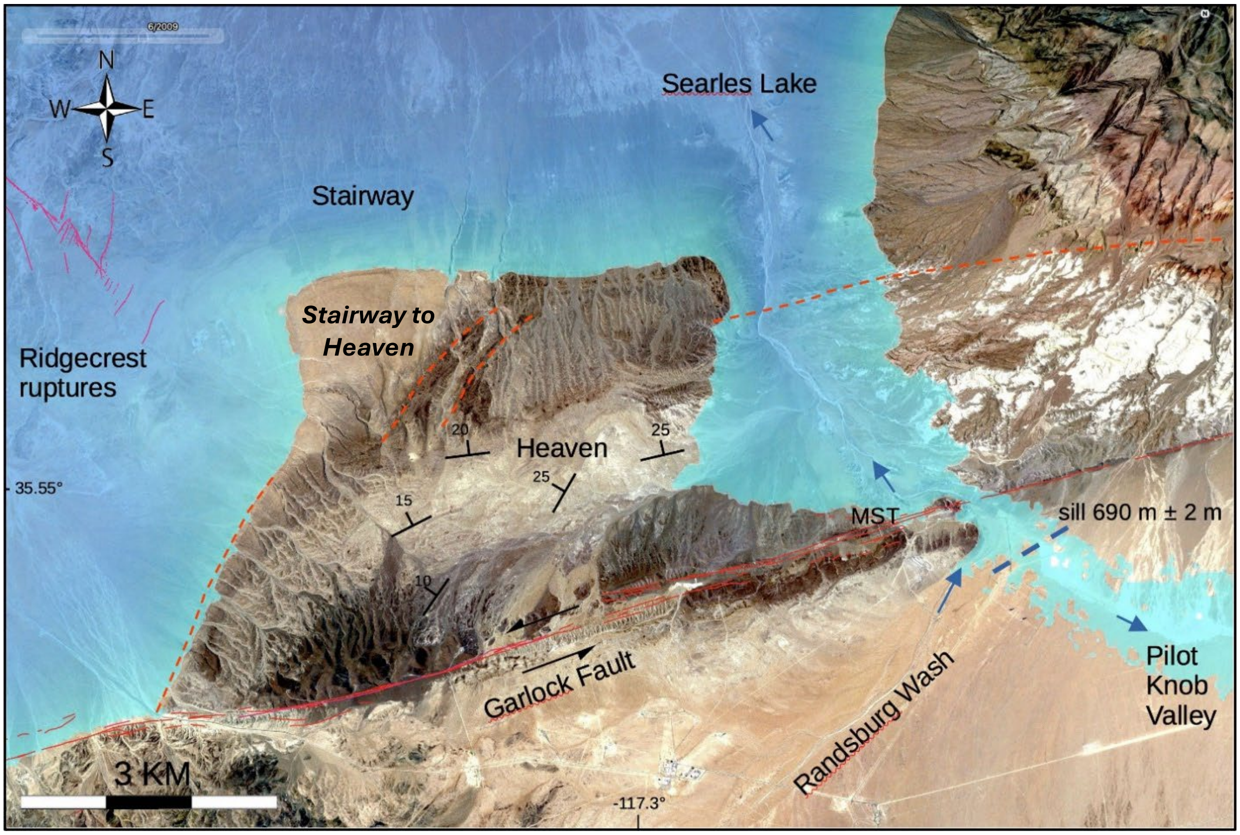

Figure 1-2b-1. Satellite image showing a reconstructed water level of Searles Lake (blue colors) while overflowing into Pilot Knob Valley. The "Stairway to Heaven" surface and sill at an elevation of 690 m are also shown. Red lines are faults associated with the Garlock fault system and the southeastern extent of the 2019 Ridgecrest fault ruptures (Paxton Ranch fault). Dashed red lines are probable faults mapped in this study. Location shown by MST near the overflow channel is the fault trench site of McGill and Sieh (1993). Blue arrows show direction of surface flow from Randsburg Wash to the north into Searles basin and to the south into Pilot Know Valley controlled by a modern drainage divide (sill) at 690 ± 2 m.

Geologic setting of the “Heaven” tectonic block and overflow channel

Early work by Jennings et al. (1962) mapped the central portion of the fault block “Heaven” as Plio-Pleistocene, non-marine sediments, named the Funeral fanglomerate (their QP), later called the Funeral Formation, having a type section farther east in the Death Valley region with a whole-rock K-Ar age 4.0 +/-0.1 Ma [Pliocene] (Marvin et al., 1989). Smith (2009) mapped the bedrock of “Heaven” as Plio-Pleistocene sandstones and siltstones (his unit QTs). The QTs rocks are lacustrine and alluvial in origin and appear to underlie older gravel (unit og) of Pliocene or early to middle Pleistocene age. In the Spangler Hills located west of the overflow channel, the QTs unit is found at elevations as much as 43 m higher than “Heaven” and any deposits of the late Pleistocene Searles Lake Formation, which Smith (2009) divided into seven, dominantly lacustrine units, which can be correlated with subsurface units known from sediment lake cores from Searles Lake playa.

Smith (2009 states “Geologic relations consistently show that these rocks [QTs] unconformably underlie sediments of the Christmas Canyon Formation and unconformably overlie the siltstone and sandstone of Tertiary age. The Christmas Canyon Formation has a radiometrically and paleomagnetically estimated age of 0.57 Ma for the top of a subsurface unit and a 0.64 Ma age from the Lava Creek B ash near the top of the lacustrine facies of the Christmas Canyon Formation at its type section (Smith, 2009).

Smith shows the bedrock of “Heaven” strikes NE-SW to almost E-W having dips to the NW–N at relatively low angles of 10° to 25° (Figure 1-2b-1).

The topography and mapped geology on the western edge of “Heaven” appears to form en echelon right-steps that may be associated with left-oblique slip from the E-W splay of the Garlock fault, located north of the fault and marked by red dashed lines where coinciding with a prominent drainage below a denuded hillslope exposing different units aligned with mapped Garlock fault scarps to the east (Figure 1-2b-1). Collectively, the structural attitudes and structures observed in the area of “Heaven” may indicate the northern severed limb of a gently plunging fold, possibly an anticline, that has been split and displaced by the Garlock fault. In addition, we speculate that the apparent vertical slip on the three en echelon dashed faults on the western-northwestern margin of “Heaven” helps to form the Spangler Valley graben in the middle of the tectonic block. We also speculate that the suite of old and high shoreline features above an elevation ~690 m associated with the “Stairway to Heaven” are uplifted due to growth on a northward dipping limb of an anticline formed by long-term transpressional tectonics on the Garlock fault (Figure 1-2b-1).

Evidence of active faulting in the overflow channel area is from a paleoseismic study site (MST) on the Garlock fault (McGill and Sieh, 1993; Figure 1-2b-1). Numerous fault trenches excavated across several parallel fault splays and the highstand shoreline at ~690 m revealed a ~2 m section of nearshore lacustrine sands over an abrasion platform developed on older alluvium and lacustrine sediment. The fault trenches show the abrasion platform and associated shoreline angle is vertically offset (north-side up) between the elevations of ~689 and 694 m across the fault zone. Nearby channel features formed after the most recent highstand of Searles Lake are also laterally offset 82 to 106 m, with a preferred value of 90 m (McGill and Sieh, 1993).

The “Stairway to Heaven” geomorphic surface

The “Stairway to Heaven” geomorphic surface is preserved on the northwestern corner of the “Heaven” tectonic block above an elevation of ~690 m. This surface has a noticeably smoother surface expression and preserves wave-formed scarps and beach terraces, whereas other areas that bound the surface are heavily dissected, contain remnant shoreline features, and exhibit differential erosion of gently dipping fanglomerate units of the Plio-Pleistocene Funeral Formation. Below an elevation of ~690 m is the “Stairway”, a beach plain that consists of a remarkable high-fidelity record of lake levels beginning ~20 m above the playa of Searles basin and continuing upslope for 3 to 4 km (Figure 1-2b-2). The beach plain below ~690 m consists of many low-relief, erosional shoreline scarps and fewer poorly developed beach ridges on the north facing slope. The shoreline features on the northern slope transition to mostly constructional features in the form of well-developed beach ridges and spits to the west as they cross the northwest corner of the “Heaven” tectonic block. The southeastern extent of the 2019 surface ruptures on the Paxton Ranch fault also terminates in a series of north-striking fault splays halfway up the “Stairway” beach plain and within the area of the northwestern corner of the “Heaven” tectonic block (Figure 1-2b-2).

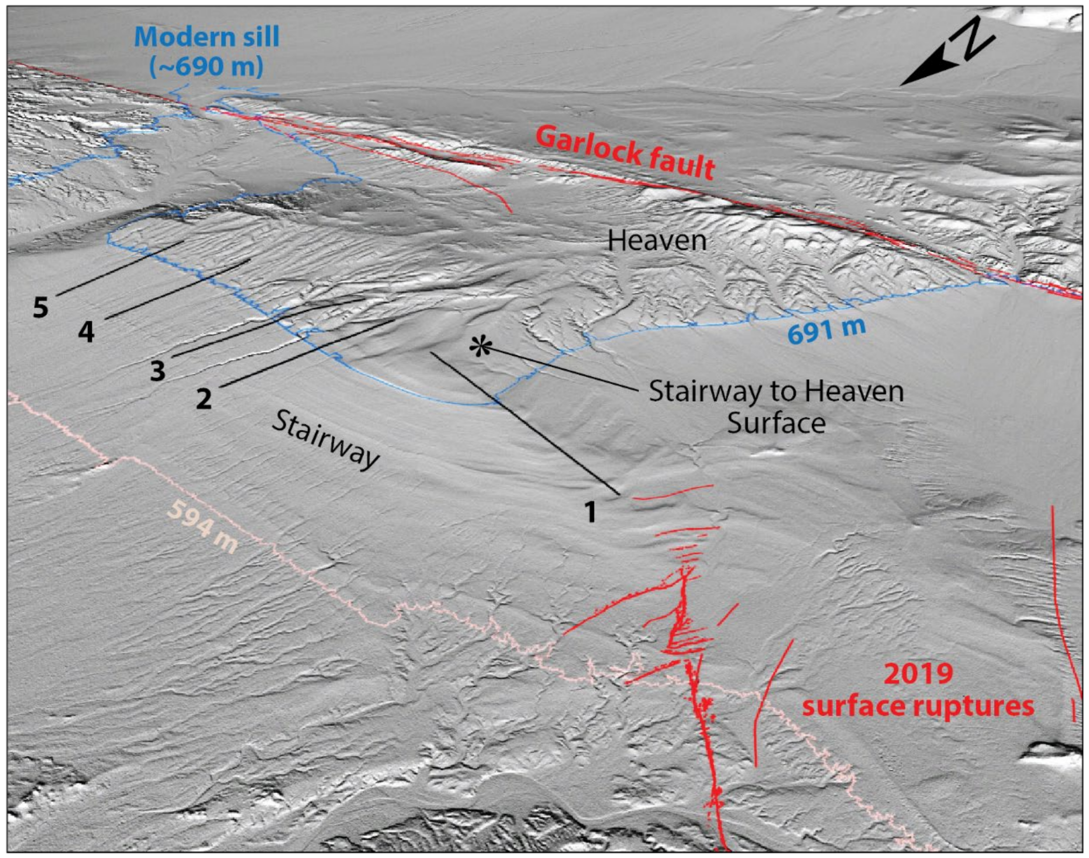

Figure 1-2b-2. Oblique hillshade showing the Stairway beach plain, Heaven tectonic block, the modern sill of Searles Lake, and the Garlock fault and 2019 surface ruptures (Duross et al., 2020; Ponti et al., 2020). The location of transects for topographic profiles (1–5) are also shown. Elevation contours at 594 and 691 m are shown for reference. View to the southeast and shading from the northwest.

Topographic profiles

Five topographic profiles were used to survey the elevation of prominent shoreline features on the “Stairway” beach plain between 645 and 690 m, as well as to identify the elevations of potentially higher shoreline features above 690 m developed on the “Stairway to Heaven” geomorphic surface (Figures 1-2b-2 and 1-2b-3). Profile 1 exhibits the best shoreline geomorphology in the area since it is situated along a transect that crosses well-developed beach ridges and spits on the northwest corner of the “Heaven” tectonic block. Profiles 2–5 show similar topography, but the features are reflected mostly as poorly developed erosional shorelines and fewer low relief beach ridges.

Eight distinct elevations coinciding with major topographic breaks were identified from all five profiles based on a histogram analysis. These breaks coincide with the more prominent shoreline features in the area with elevations ranging from 643 to 715 m (Figure 1-2b-3). The elevations identified at 643, 673, 680, and 691 m on the “Stairway” shoreline profiles are nearly the same elevations of beach ridges in the northern subbasin of Searles basin (e.g., Valley Wells beach ridge complex; Day 1, Stop 1c). The histogram analysis also indicates three additional shoreline features at 700, 706, and 715 m, where the 706 m elevation is strongly controlled by a bench that contains a remnant tufa mound at ~708 m first identified by Smith (2009; Figure 1-2b-4).

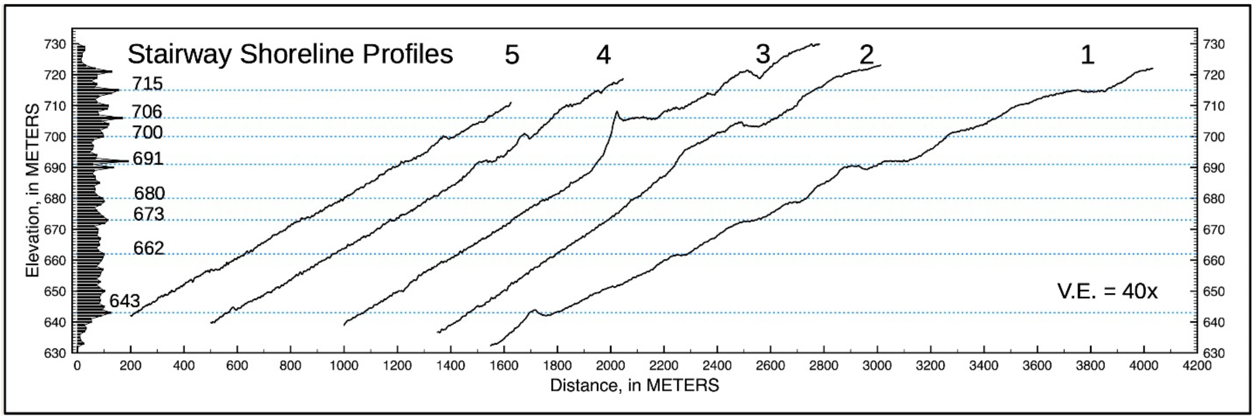

Figure 1-2b-3. Five topographic profiles of the uppermost Stairway beach plain below an elevation of 690 m and the Stairway to Heaven geomorphic surface above 690 m. Profiles are from a 2-m DEM with ~0.5 m vertical accuracy and 2-m horizontal sample spacing. A relative histogram of the shoreline profile elevations is along the left column. Blue dotted lines are selected elevations that have been verified in the field as having an associated shoreline feature.

The elevations of prominent shoreline features at and above 690 m are nicely exhibited on a hillshade map of the “Stairway to Heaven” geomorphic surface. A reconnaissance field visit also verified the presence of both erosional and constructional shoreline features, as well as a remnant tufa mound at ~708 m perched high above surrounding beach plains (Figure 1-2b-4).

Future work

We have planned more stratigraphic mapping and luminescence dating of the ~690 m and higher beach ridges at the “Stairway to Heaven” site. The new ages and shoreline elevations will be used to refine the timing of the latest overflow episode(s). Geologic history of overflow contributes to understanding better the Pilot Knob Valley drainage, which crosses the Garlock fault downstream. Secondly, it bears upon the Garlock fault slip rates inferred from 14C ages of tufa from the Navy tufa site to indirectly date the ~690 m shoreline and faulted stratigraphy exposed in the trenches of McGill and Sieh (1993). We intend to use lidar maps and luminescence dating to develop longer-term tectonic models of vertical and lateral offsets of the Garlock fault at the Searles basin inflow/overflow channel in Randsburg Wash and Pilot Knob Valley, and define better the structural history of the “Stairway to Heaven” geomorphic surface.

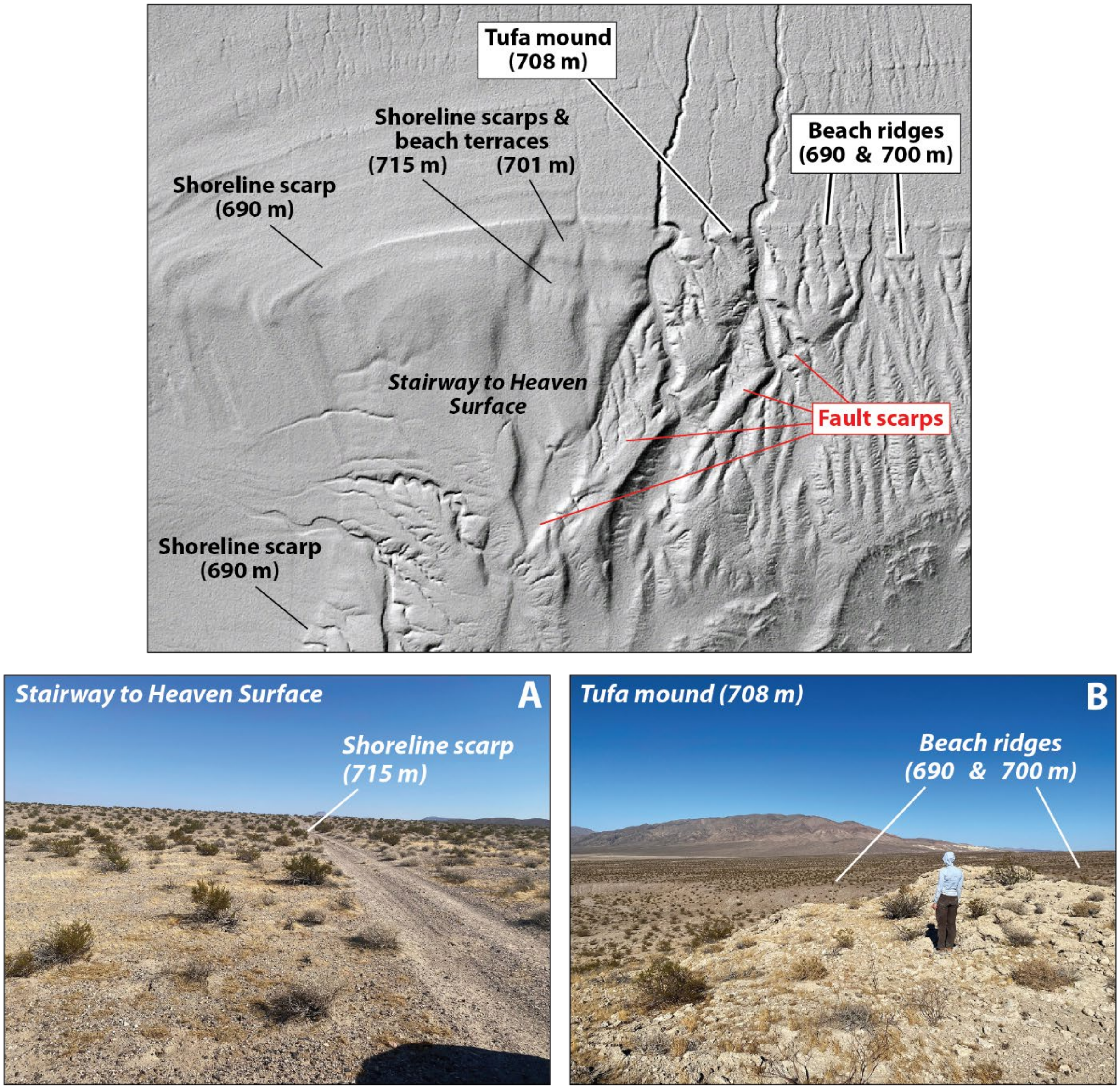

Figure 1-2b-4. Hillshade map from a 2-m DEM showing notable shoreline features at ~690, 701, and 715 m, as well as the location of a tufa mound at 708 m, developed on the Stairway to Heaven geomorphic surface. Also shown are two well-defined fault scarps. Photographs of: (A) the Stairway to Heaven surface and shoreline scarp at 715 m, view south. Surface is moderately covered by small creosote bushes and a lag of subrounded to well-rounded gravel; and (B) a tufa mound at 708 m, view to the east. Beach ridges at 690 and 700 m are also shown in middle distance.

References

DuRoss, C.B., R.D. Gold, T.E. Dawson, K.M. Scharer, K.J. Kendrick, S.O. Akciz, S.J. Angster, J. Bachhuber, S. Bacon, E.K. Bennett, et al., 2020. Surface Displacement Distributions for the July 2019 Ridgecrest, California, Earthquake Ruptures. Bulletin Seismological Society of America, 110(4), 1400–1418. doi: 10.1785/0120200058.

Jennings, C.W., Burnett, J.L., and Troxel, B.W., 1962. Geologic Map of California, Trona Sheet, Scale 1:250,000, California Geological Survey, Sacramento.

McGill, S., and Sieh, K., 1993. Holocene slip rate of the central Garlock fault in southern Searles Valley, California. Journal of Geophysical Research 98, 14,217–14,231.

Marvin, R.F., Mehnert, H.H., and Naeser, C.W., 1989. U.S. Geological Survey radiometric ages: Compilation "C"; Part three, California and Nevada. Isochron/West, no. 52, p. 3-11.

Ponti, D.J., Blair, J.L., Rosa, C.M., Thomas, K., Pickering, A.J., Akciz, S., Angster, S., Avouac, J-P., Bachhuber, J., Bacon, S., et al., 2020. Documentation of surface fault rupture and ground deformation features produced by the RidgecrestM6.4 and M7.1 earthquake sequence of July 4 and 5, 2019. Seismological Research Letters, 91(5), 2942–2959. doi: 10.1785/0220190322.

Smith, G.I., 2009. Late Cenozoic geology and lacustrine history of Searles Valley, Inyo and San Bernardino Counties, California. U.S. Geological Survey Professional Paper 1727, 115 p.

Day 1 Stop 3: M6.4

Topics

A) Earthquake Overview (Pierce)
B) Response (Hudnut, Pierce)
C) Flipped rocks (Zuckerman), fault mapping (Curran)
D) M6.4 PG&E Fault Displacement and Timing of Last Event (Kozaci, Madugo)
E) M6.4 Trench Site (Pierce et al.)
F) On/off fault deformation, slip variability and max offset of 6.4 (Pierce)

Discussion (A) Earthquake Overview / Tectonic Background

See introduction section of this guidebook for Pierce contribution.

Discussion (B) Earthquake Response

“Early Days” of the Ridgecrest 2019 Earthquake Sequence; Response and Coordination Efforts on July 4 & 5, 2019 by USGS, CGS and the US Navy

Field Team:

Hudnut, Ken (former USGS, now at Southern California Edison)

Hernandez, Janis (former CGS, now retired)

Blake, Kelly (former US Navy, now with Ormat)

Acknowledgements:

CAPT Paul Dale (former Commanding Officer, NAWS China Lake; US Navy)

Jed McLaughlin (City EOC Incident Commander; former Ridgecrest PD Chief, now retired)

Chris Maloney (Base EOC Incident Commander; US Navy)

Bill Willard (Base Security, US Navy)

Margo Allen (PIO, US Navy)

Jay Montenero (Senior Chief; US Navy)

Matt Boggs (Engineer of Ranges; US Navy)

Preface: During July 4 and 5, Janis, Kelly and I worked together mostly "inside the base," and on this 2025 FoP field trip, I will provide a brief glimpse of that experience, and hope to answer questions about this earliest part of the response efforts within the Navy's perimeter.

Abstract: After the M 6.4 on July 4th, Janis & Ken met up with Kelly for the first time, and together we made measurements of the left-lateral offsets where they cross Highway 178. We made a plan and met up early on July 5th inside the base, and Kelly introduced us to the many key people inside the base. From this point on, none of what the USGS and CGS were able to accomplish inside the base could have possibly happened without the acceptance of our mission by the US Navy, and most notably by the base commanding officer, CAPT Dale. Margo connected us with Bill, who took us out to a restricted portion of the base to allow us to perform initial ground-based reconnaissance mapping in the Skytop area. Our idea was to locate ruptures that were along the same M 6.4 aftershock trend where we had already measured the surface ruptures at the Hwy. 178 intersection. Our hunch was that the zone of left-lateral surface breaks would continue inside the base, and we found some minor cracks in a few places consistent with that hunch. However, we were not very impressed with these little cracks and figured we must not yet have found all the best ruptures. Kelly and Bill helped make all of the ground recon possible the morning of July 5 inside the base. Meanwhile, we had filed our flight plan with Margo and she got it approved by CAPT Dale, and we got help from the CGS at the State Operations Center in Sacramento to arrange for us a CHP overflight in an AS-350BA with both a pilot and co-pilot. Janis and I were able to go aloft on the afternoon of July 5th with CHP out of Inyokern airport with our cameras ready. The flight pattern was to first go to the M 6.4 rupture at Hwy. 178 crossing, then to follow the rupture towards the northeast. Upon doing so, we encountered the larger slip section of the fault, and we were very excited to have "found it," and we followed it to the southwest end and then back along the M 6.4 rupture towards the northeast end, photographing in stereo overlap along the way. From the M 6.4 aftershock pattern, we knew it formed a 'Capital L' pattern that included the northwest-southeast oriented trend, and we did our best to locate that and fly across it as well near the northeast end of the Skytop valley. At the time, of course, we did not know that NW-SE section would later rupture in the M 7.1 that same evening.

With fuel running low, the CHP said, ‘better head back to base,’ so we made one higher altitude pass back from east to west across the south side of China Lake playa and did not observe any faulting in that vicinity. In retrospect, one area of special interest that was located inside the base we later called "the intersection," where the M 6.4 fault rupture intersected with the subsequent M 7.1 fault rupture pattern. We did get some low altitude helicopter hand-held air photos in this area after the M 6.4 but before the M 7.1. All of this is documented in better detail in the slides from my Fall 2019 AGU presentation and a talk I gave at Scripps in February 2020, which are available upon request. After the CHP overflight on July 5th in the afternoon, Janis and I reported out to three different groups on our findings about the M 6.4 surface rupture; 1) the Navy Emergency Operations Center (EOC) meeting led by Chris, 2) the Ridgecrest Mayor's EOC meeting led by Jed, and then finally 3) the California Earthquake Clearinghouse meeting, which was interrupted by the M 5.8 immediate foreshock and then the M 7.1 mainshock. How this series of three briefings got started was that, when we reported back to Margo to have our photos checked, she invited us to come into the Navy EOC command meeting, led by Chris, that was in progress and report out to that group. Janis and I showed the aftershock pattern and talked about our observations of the M 6.4 surface faulting, all of which was along the SW-NE oriented left-lateral zone of surface rupture. We opened up for questions and Jed McLaughlin asked, "Have you ever seen anything like this before?" That got me talking about prior examples of cross-fault triggering, such as the 1987 Superstition Hills earthquake sequence (the subject of most of my Ph.D. dissertation), as well as the 1927 Tango, Japan and other doublets involving orthogonal fault ruptures. I showed, with my hand and fingers, the 'Capital L' formed by the 1987 ruptures, then flipped my hand up to the computer display to overlay it onto the Ridgecrest sequence seismicity up to that point in time. Of course, the 'L' by analogy showed that you could have a larger event on the other leg of the 'L' that had not yet ruptured, as a result of the reduced normal stress caused by the M 6.4 cross-fault rupture. Janis and I were asked to follow Jed to the Mayor's EOC and gave them a similar presentation, and Jed asked the same question and we had a similar discussion of what might be next, based on those examples. So it was quite a surprise when the M 7.1 happened and we saw its location was precisely where I had pointed out on the map seismicity display, and said that you could get a later triggered event, if things were to play out symmetrically as they had in 1987. After the M 7.1, many people remarked they thought it seemed like a successful earthquake *prediction*, but we made it clear to the Mayor and others that this had *not* been an earthquake prediction. Instead, it was an example of using knowledge of past earthquakes' behavior to inform scenarios for what *might* happen next. I showed possible location and specified the cross-fault triggering mechanism, but I did not speculate by specifying much about the magnitude, or timing. I simply said - in response to Jed's question - that in past examples, a cross-fault had sometimes triggered a larger rupture later on an orthogonal fault. I then showed how that cross-fault triggering mechanism *could* play out, but also made it clear we had no way of knowing what would happen next for sure. At best, it was like a "called shot," not a successful prediction.

After the M 7.1 occurred, many of our friends and colleagues joined into the response efforts and on July 6th, together we conducted aerial and ground-based initial reconnaissance and began scaled-up mapping and other efforts to study and document the entire sequence and its effects. A much larger team effort ensued both inside and outside the base after the M 7.1, so I will end my recollections here for now. I'd like to also mention Matt, who later on helped greatly with arrangements for the joint airborne lidar project, flown by NCALM. In retrospect, had it not been for *any* of the above things happening in this particular sequence, many other things might not have fallen into place. So, for all they did, I am forever incredibly grateful to everyone named in the Field Team and Acknowledgements above. Many others, too many to name, also were importantly involved and I look back on this time with great appreciation for all that so many of you contributed to the overall response effort. Most of the above is from July 4 & 5, but a couple of the photos below are from July 6th, the day after the M 7.1

Figure 1 - Janis Hernandez "sharing the stoke" of post-earthquake surface fault rupture mapping

Figure 2 - Janis & I met and worked along side of some really cool people, like Chris, head of the Navy EOC

Figure 3 - After the M 7.1, tons more support arrived, like a couple of blackhawks and lots of great people. Here, Janis (pink hat) shares her knowledge and experience with the next generation of surface rupture mappers. Lots going on here!

Figure 4 – Pretty hefty offset from the M 7.1 on the east-west road across the south side of China Lake playa (most famous 'anonymous' USGS photo that I ever took). Note the asphalt fractured ~perpendicular, not quite in line with the rupture zone; it acts like a rigid surficial plate breaks differently than the soil here. Note, too, the wheel and shadow are distinctive.

Figure 5 - Here I am using my hands to explain strike-slip surface fault rupture to Mark Ghilarducci, head of CalOES and Bob Fenton, head of FEMA Region 9. Later, they took me on board Air Force 2 to give a briefing to the U.S. Vice President. Can't find a picture of that just now, but longer versions of this episode in earthquake history are available upon request.

Figure 6 - Mini-Reunion of Jed, Chris and me for ShakeOut 2024, held at SCE's EOC in Irwindale. We listened to these Ridgecrest Community leaders about the response effort from both Navy and City perspectives. In preparation for a future Big One, we will all benefit by having learned from their experiences. Chris has moved to San Diego and Jed has moved to Florida, but we were able to have them visit for an all-day Seismic Resiliency Workshop to generously share their knowledge.

Pierce, Koehler, Williams et al. drone recon

High-Resolution Structure-From-Motion Models and Orthophotos of the Southern Sections of the 2019 Mw 7.1 and 6.4 Ridgecrest Earthquakes Surface Ruptures

Ian Pierce, Alana Williams, Richard D. Koehler, and Colin Chupik

Published in 2020 in Seismological Research Letters

Ian Pierce & Rich Koehler left Reno a few hours after the July 4 earthquake. Ian had a friend living in Ridgecrest at the time who he asked to look at possible fault crossing locations along Highway 178 and see if there was any evidence of surface rupture. She took some of the only photos of the highway crossing of the 6.4 before the road was repaired just hours later. Pierce & Koehler arrived to Ridgecrest around 3 am and spent the remainder of the night getting rocked by aftershocks close to the surface trace of the M6.4. The next morning (July 5) they started flying drones to collect high resolution imagery along the rupture. With limited knowledge of the extent and location of the surface ruptures (insar and other satellite products would not become available for a few days), this was all done by manually piloting the drone along the ruptures and following them on the iPad screen at a height of around 30 m above the ground. Ruptures were found by crisscrossing dirt roads throughout the region. All day long on the 5th, other scientists began showing up, and that night over dinner at the infamous Casey's Barbeque in Ridgecrest, the M7.1 hit. Restaurant staff mentioned that this was larger than the preceding day's event. Dodging emergency vehicles, fires, and general chaos, with spotty-at-best cell service allowing a few key phone calls to Jayne Bormann and Steve Wesnousky, Pierce and Koehler raced out in the dark of night and found that the M7.1 had ruptured a different fault farther to the east along Highway 178. On July 6, the team was joined by Alana Williams, who aided in collecting additional drone imagery along the southern 12 or so kilometers of the M7.1 rupture. Other members who joined this team include Sinan Akciz, Colin Chupik, Heath Sawyer, and others. Rich Koehler walked most of the ruptures taking field measurements, while Ian & Alana flew the drones and shuttled cars around. After a few days in the field the team returned home and began processing orthomosaics that resulted in sub-centimeter pixel size aerial imagery along most of the publicly accessible portions of the M6.4 and M7.1 ruptures. The data volume was huge, with tens of thousands of photographs. The resulting images created a highly detailed basemap to map rupture traces. Much of this mapping was conducted at a scale between 1:50 and 1:100.

From Pierce et al. (2020): UAS image with detailed fault mapping overlay along southern portion of M7.1 rupture.

Many of the fine-scale rupture features documented by drone imagery were ephemeral and degraded rapidly after the earthquakes. Wind erosion, flash floods, and rain smoothed scarps and erased small cracks within months of the events. This highlights the critical role of rapid post-earthquake imaging for preserving details that are essential for understanding rupture complexity and off-fault deformation.

Sunrise on July 5, 2019

Oblique UAS photo of M6.4 rupture taken July 5 2019.

Taken near parking area of Stop 1-3 on July 5, 2019

Rich Koehler walking some of the M6.4 surface rupture on the morning of July 5th, 2019.

Surface rupture of M7.1 taken hours after the rupture along Highway 178 (July 5, 2019).

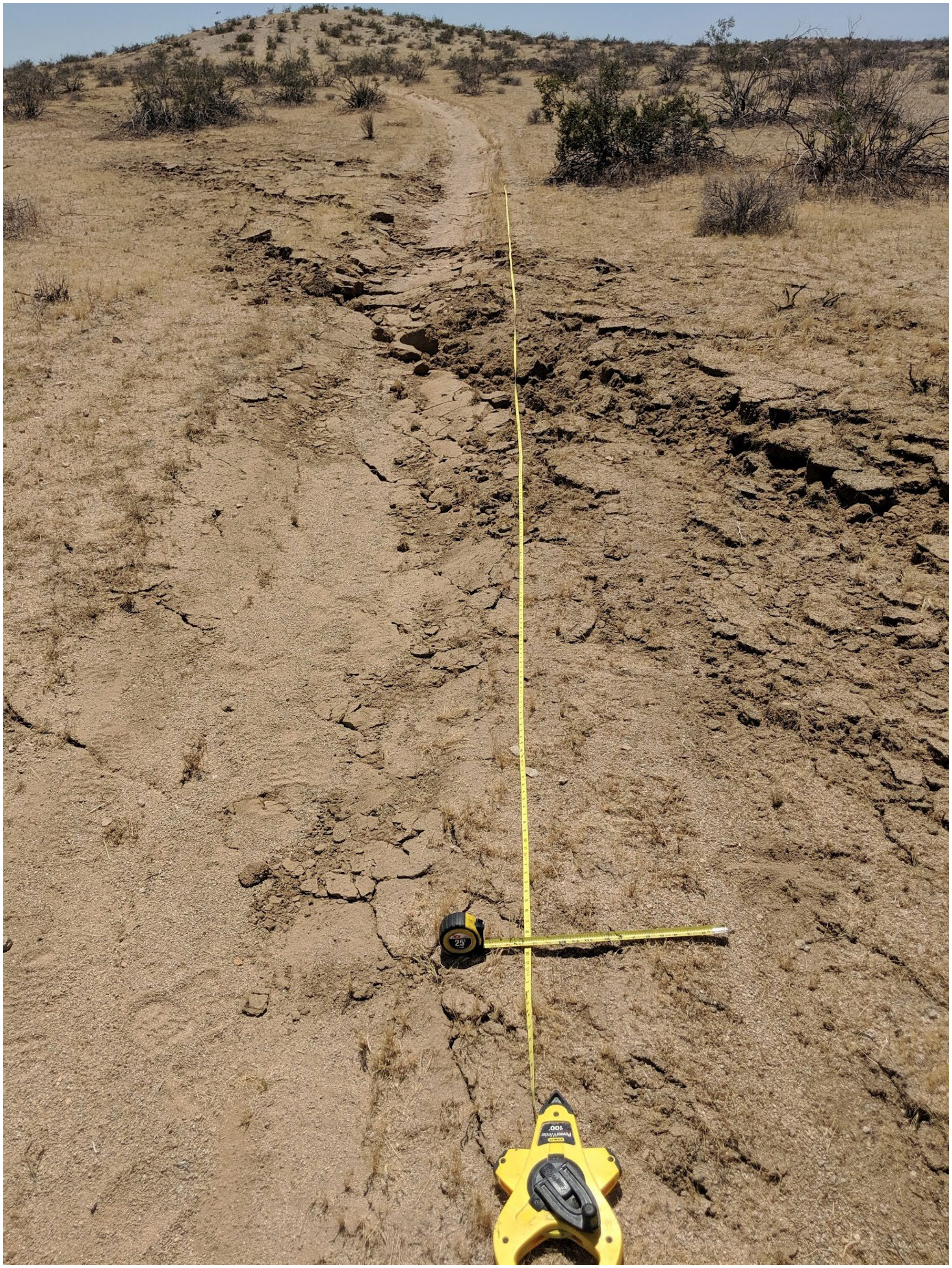

Measuring displacements in the field.

Charging drone batteries and processing models at night.

2 flat tires occurred during the Koehler-Pierce-Williams recon push. Finding an open tire shop in the aftermath of an earthquake was challenging.

Running a generator to charge drone batteries in the field.

Discussion (C) Rocks displaced by shaking during the M6.4 Ridgecrest earthquake

Stop leaders: Mindy Zuckerman, Arizona State University and Chris Madugo, Pacific Gas & Electric, Co.

Introduction

Fragile geologic features, including rocks or rock formations displaced or toppled during earthquakes, can provide insight into the spatial extent and intensity of strong ground shaking (e.g., Oldham, 1897; Bolt & Hansen, 1977; Ohmachi & Midorikawa, 1992; Baker et al., 2013). Seismic instruments are often spaced kilometers apart and only rarely capture ground motion in the near-field (<1 km) of an earthquake fault rupture. When present, fragile geologic structures can physically preserve evidence of extreme ground motion and can allow for more densely spaced coverage than seismic instruments. With a better idea of how the ground moves during earthquakes, smarter infrastructure can be implemented to avoid human injury and costly damage.

Displaced rocks, or rocks near the surface rupture that exhibit evidence of shifting during the earthquake, can be used to characterize near-field ground motion during the 4 July 2019 M 6.4 Ridgecrest, California earthquake. Displaced rocks may record spatial patterns of ground motions during large earthquakes, but because of complex variables dictating shaking amount and direction, they may not give a quantifiable record of ground motion. In addition, displaced rocks, and rocks in general, are not evenly distributed on the ground surface along the Ridgecrest rupture trace, so we cannot use them to characterize spatial patterns of ground motions.

Because of Ridgecrest's location in the arid Mojave Desert, displaced rocks can be traced back to their initial pre-seismic resting place by identifying their vacant sockets in the desert floor. The distance and direction the rock traveled can be measured between the rock and the socket with a simple tape measure and compass. We use these measurements along with qualitative descriptions of the geologic environment to understand more about how the ground accelerates during earthquakes.

Background: Fragile Geologic Features

When evaluating the usefulness of displaced rocks, it is important to take into account that the sockets are a fragile geologic feature that can quickly be eroded away by elements such as wind, rain, and animal disturbance. Many ground motion studies have been conducted using fragile geologic features, but they are mainly concerned with precariously balanced boulders. These boulders can be used to determine the limits of ground motion if they have not been knocked over by an earthquake (e.g., Ohmachi & Midorikawa, 1992; Stirling & Anooshehpoor, 2006; Balco et al., 2011; Haddad et al., 2012; Anooshehpoor et al., 2013; Baker et al., 2013). Toppling balanced boulders requires a different physical mechanism than that of a smaller rock shifting or popping up from the ground, so our studies do not directly compare (Bolt & Hansen, 1977). However, there have been three modern studies that also used displaced rocks. After the Borrego Mountain earthquake in 1968, Clark (1972) noticed what he called "displaced stones" near the surface rupture. This earthquake occurred in a region with similar geology and climate to Ridgecrest. Clark (1972) measured the distance between the stones and their former seats, the friction of the stones against the ground surface, and the dip of the hillside the rocks were sitting on to estimate the force applied to the rocks by the earthquake shaking. His results suggest that rocks on ridges with higher elevation reacted most strongly, and higher topography increases ground motion. Clark (1972) further notes that these results could be impacted by adhesion of the rocks to the ground surface, and notes that different substrates could control shaking, but in the end, those topics were beyond the scope of that study.

Thirty years after the Borrego Mountain event, the 1999 Hector Mine earthquake, also in southeastern California, presented an additional opportunity to study displaced rocks. In order to describe ground motion, Michael and Stenner (2002) followed transects along and perpendicular to the surface rupture to locate displaced rocks and find the coefficient of friction between the rocks and the ground surface. They used Clark's (1972) equation to determine how much ground acceleration would be needed to displace a rock with a certain amount of friction on a certain slope angle. Additionally, by noting the percent of rocks that had been displaced at evenly spaced sites along their transects, they concluded that the magnitude of shaking was not actually greater closer to the fault as anticipated.

A 2019 study in Northern Territory, Australia, of the Mw 6.1 Petermann earthquake measured over 1000 rocks displaced from bedrock outcrops in the near field (King et al., 2020; 2021). These rocks recorded directionality of shaking, including changes in directionality along the length of the rupture trace. Results were non-random and support the idea that displaced rocks can act as strong ground motion records.

Two studies use rocks as fragile geologic features to describe ground motion during the Ridgecrest sequence. Hough et al. (2020) compare displaced rocks along the mainshock rupture and structural damage in the area to data from seismic instrumentation. The researchers consider the topography and cementation to the ground surface and determine that, because of the distance rocks were thrown, PGA values close to the rupture could have been over 1 g. The second study noticed large boulders a few kilometers from the ruptures that had shifted during the earthquakes (Sleep and Hough, 2020). They documented the boulders' movement by photographing centimeters-wide moat-like gaps surrounding the boulders. Because of the size of the boulders and the estimated amount they had moved during the main shock, the authors determined the PGA there to be between 0.5 and 1 g.

Methods

Planning

Considering the fragility of the sockets, data needed to be gathered as soon as possible. We collected our field data in October 2019. Because most of the rupture crossed the Naval Air Weapons Station China Lake, and there was not enough time to acquire permission to access the station, only the western half of the Mw 6.4 rupture could be surveyed.

For the field campaign, we used the ArcCollector iPad app (now called Field Maps) because it allowed for collecting consistent information from dozens of GPS located sites. The app included a portable map created in ArcGIS Pro that included the satellite image, topography, the surface rupture trace, and a superimposed 100 by 100-meter grid parallel to the fault trace. After Michael et al. (2002), the plan was to follow parallel transects perpendicular to the main rupture. The field crew planned to zigzag along the fault along fault-perpendicular transects spaced 500 m apart. At each field site, 100 m apart along the transects, a drop-down menu with a list of measurements to take would appear in ArcCollector along with a prompt to take a photo. The trip included six full days, 24-30 October 2019 in the field at the end of October 2019 to collect not only information on displaced rocks, but on areas near the rupture where surface cobbles are present but did not move.

Data Collection

Each day, the protocol was to follow the grid, stop at the intended intersections and collect all data called for by the rubric. Each site area was defined as a circle with a diameter of two meters, and within this circle, the rock I measured should be representative of the displaced rocks in the site. A representative rock was defined as a rock typical of all other displaced rocks in the site in regards to size and magnitude, direction, and type of displacement (Figure 1-3C-1). If there were no rocks present or if no rocks had moved, the site should still be described, but no representative clast was needed. The set-up for each site included a scale and a whiteboard with the sample number and a North arrow (Figure 1-3C-2). A picture was taken with the iPad, and a camera for redundancy, which retained the GPS location. Following the rubric in ArcCollector, measurements included the size of the clast assuming rectangular dimensions, the distance moved (from a point of the clast easily matched to the corresponding shape in the socket), the

direction of movement, and the strike and dip of the ground surface. Additionally, the average size of clasts, the general type of substrate, and the style of displacement--flipped, translated, jumped, or rotated--were noted. The fraction of clasts that moved in the site was estimated, and, similar to research conducted after the Hector Mine earthquake, the proportion of the surface covered by rocks (as opposed to fine matrix) was tallied to remove any statistical bias from a greater number of rocks in one site over another (Michael et al., 2002).

Figure 1-3C-1. *Example of flipped displaced rock and socket in alluvium.*

Considering the geology of the site area, which consists of alluvium from the surrounding mountains and some exposed bedrock, we specified the options as old alluvium, young alluvium, and bedrock. However, in all instances but one, we collected our data from alluvial substrate. This is because, save one rock obviously knocked off its bedrock base, we could only tell if a rock moved by the existence of a socket (Figures 1-3C-1 & -2). A socket, in this case, is a depression in the ground surface in the vicinity of its corresponding rock. The sockets we are interested in only exist because of the departure of their rock inhabitant during the earthquake.

To account for the clasts' varying degrees of cementation and adhesion to the ground surface, the field crew created a scale from zero to three of what we called "unlocked to locked". Further, a second rock (other than the representative rock) was tested in each site to see if it was a zero, simply sitting on the surface with or without a socket; one, in a socket with silt covering the bottom of the rock; two, needed to be popped out from its socket; or a three, partially buried and cemented into its socket. The degree of adhesion is valuable to record because the more adhered a rock is to a surface, the more force is required to cause it to detach and move (Clark, 1972).

Figure 1-3C-2. *Site set up, including clear view of clast and socket, whiteboard with site number and North arrow, and tape measure scale.*

While traversing our route, it quickly became obvious that in some areas of the field area there were wide swaths of desert without displaced rocks or often any rocks at all. With saving time in mind, in these regions a grid point was skipped if there was no change since the collection point before it. The rubric was still completed at collection points without displaced rocks, but criteria dependent on movement, such as magnitude and direction, were omitted.

Preliminary Results

The field data amount to a roughly 23 square kilometer online map of 170 sites. Each point on the map represented a clickable site that revealed the completed rubric and paired photographs. The map can be loaded into GIS software and manipulated and interpolated.

At each site that contained a rock that moved, we recorded azimuth and magnitude to display the motions as vectors (Figure 1-3C-3).

The rocks studied were either stationary or displaced in four different motion regimes: (1) translated, or motion only in one lateral direction, (2) rotated, or motion from an angular velocity, (3) flipped, or (4) jumped, where there was evidence that the rock left the ground surface completely (Figure 1-3C-4).

Proposed Work and Discussion

The next steps in this research include simple testing of rock displacement regimes with a virtual shake robot. Field data were collected in October 2019.running the virtual shake robot with simple yet progressively more complex additions and plotting the primary motion of the displaced object. We expect to see similar motion regimes as in the field (Figure 1-3C-4). We aim to create a schematic diagram similar to flow regime diagrams of different types of explosive volcanic eruptions. To make the regime diagram, we will run the virtual shake robot repeatedly at increasing velocities and record the motion classification of each displacement. First, we will record and plot toppling results using the method from Chen (2022). Next, we will repeat the tests with different size and shape blocks and record the motion regime of each displacement. We will then introduce the pedestal with a socket and repeat the tests and plot the regimes. Finally, we will repeat the experiment with a tilted pedestal at dips measured in the field and plot the motion regimes. In all experiments, we will plot when the blocks are stationary in addition to the velocities that caused them to move.

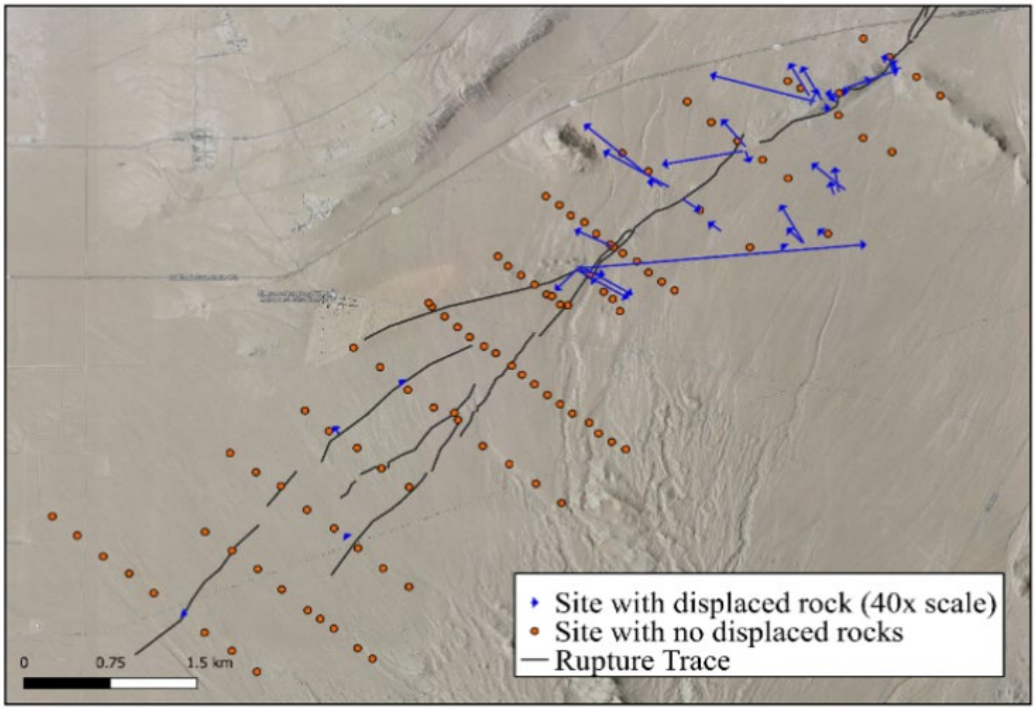

Figure 1-3C-3. *Field area with displaced rock vectors measured from azimuth and magnitude of rock motion.*

Displaced rocks as indicators of rock motion should be an important part of earthquake reconnaissance, especially in arid climates where sockets are preserved with some longevity. Due to economic and other restrictions, seismometers and accelerometers cannot be placed with the potential density of displaced rocks and other thrown objects. Although it takes time and manpower to collect displaced rock data, the dataset achieved is unique and can offer an interesting perspective on near-field ground motions.

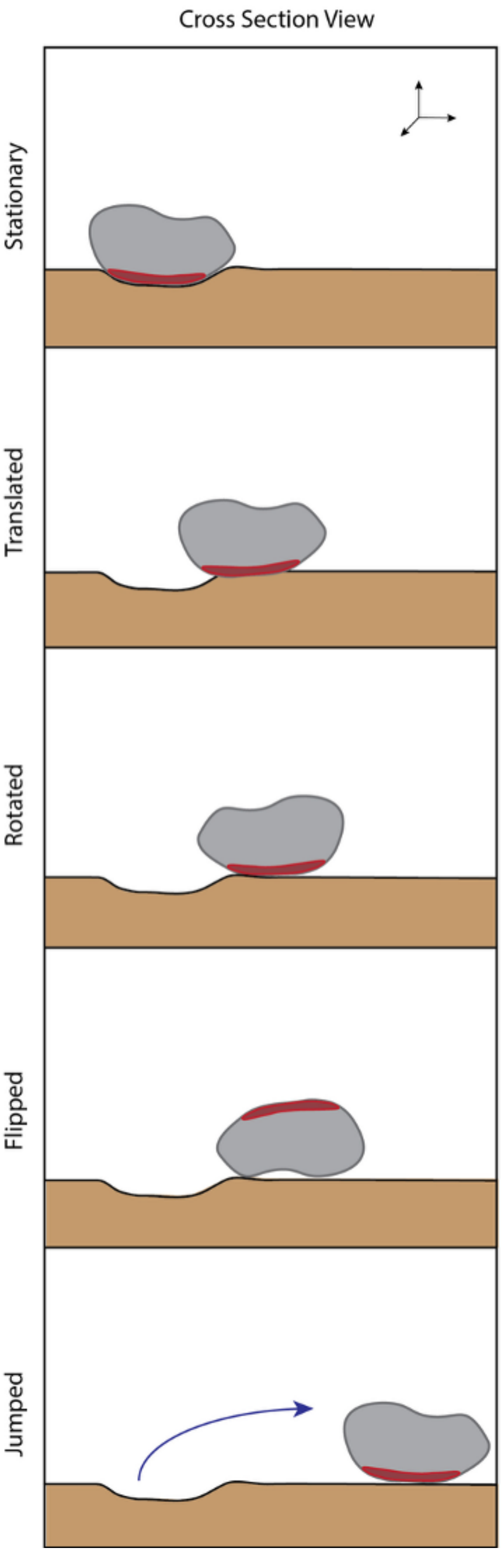

Figure 1-3C-4. *Left: Classification of primary rock motion regime based on field observations. Right: Photos of displaced rocks (solid purple outline) and sockets (dashed yellow line). White arrows from a to a' show direction of motion. Rocks 153 and 124 translated, rocks 142 and 81 rotated, and rocks 86 and 155 flipped. Translucent purple area on flipped rocks highlight the pre-earthquake base.*

References

Anooshehpoor, A., Brune, J.N., Daemen, J., and Purvance, M.D., 2013, Constraints on ground accelerations inferred from unfractured hoodoos near the Garlock Fault, California: Bulletin of the Seismological Society of America, v. 103, p. 99–106, doi:10.1785/0120110246.

Baker, J.W., Abrahamson, N.A., Whitney, J.W., Board, M.P., and Hanks, T.C., 2013, Use of fragile geologic structures as indicators of unexceeded ground motions and direct constraints on probabilistic seismic hazard analysis: Bulletin of the Seismological Society of America, v. 103, p. 1898–1911, doi:10.1785/0120120202.

Balco, G., Purvance, M.D., and Rood, D.H., 2011, Exposure dating of precariously balanced rocks: Quaternary Geochronology, v. 6, p. 295–303, doi:10.1016/j.quageo.2011.03.007.

Bolt, B.A. and Hansen, R.A., 1977, The upthrow of objects in earthquakes: Bulletin of the Seismological Society of America, v. 67, no. 5, p. 1415-1427.

Chen, Z., 2022, Automated geoscience with robotics and machine learning: a new hammer of rock detection, mapping, and dynamics analysis [Ph.D. dissertation]: Arizona State University, 282 p.

Clark, M.M., 1972, Intensity of shaking estimated from displaced stones: U.S. Geological Survey Professional Paper 787, 175–182 p., doi:10.3133/pp787.

Haddad, D.E., Zielke, O., Arrowsmith, J.R., Purvance, M.D., Haddad, A.G. and Landgraf, A., 2012, Estimating two-dimensional static stabilities and geomorphic settings of precariously balanced rocks from unconstrained digital photographs: Geosphere, v. 8, no. 5, p. 1042-1053.

Hough, S.E., Altidor, J.R., Anglade, D., Given, D., Janvier, M.G., Maharrey, J.Z., Meremonte, M., Mildor, B.S.-L., Prepetit, C., and Yong, A., 2010, Localized damage caused by topographic amplification during the 2010 M 7.0 Haiti earthquake: Nature Geoscience, v. 3, p. 778–782, doi:10.1038/ngeo988.

Hough, S.E. et al., 2020, Near-field ground motions from the July 2019 Ridgecrest, California, earthquake sequence: Seismological Research Letters, v. 91, p. 1542–1555, doi:10.1785/0220190279.

King, T.R., Quigley, M., and Clark, D., 2020, Near-field directionality of earthquake strong ground motions measured by displaced geological objects, EGU General Assembly 2020, Online, 4–8 May 2020, EGU2020-12092, doi: 10.5194/egusphere-egu2020-12092.

King, T.R., Quigley, M., Clark, D., Zondervan, A., May, J., and Alimanovic, A., 2021, Paleoseismology of the 2016 MW 6.1 Petermann earthquake source: Implications for intraplate earthquake behaviour and the geomorphic longevity of bedrock fault scarps in a low strain-rate cratonic region: Earth Surface Processes, Landforms, v. 46, p. 1238-1256, doi: 10.1002/esp.5090.

Michael, A.J., Ross, S.L., and Stenner, H.D., 2002, Displaced rocks, strong motion, and the mechanics of shallow faulting associated with the 1999 Hector Mine, California, earthquake: Bulletin of the Seismological Society of America, v. 92, p. 1561–1569, doi:10.1785/0120000927.

Ohmachi, T. and Midorikawa, S., 1992, Ground-motion intensity inferred from upthrow of boulders during the 1984 Western Nagano Prefecture, Japan, earthquake: Bulletin of the Seismological Society of America, v. 82, no. 1, p. 44-60.

Oldham, R.D., 1897, Report of the great earthquake of 12th June, 1897: Memoirs of the Geological Survey of India, v. 29, 379 p.

Sleep, N.H., and Hough, S.E., 2020, Mild displacements of boulders during the 2019 Ridgecrest earthquakes: Bulletin of the Seismological Society of America, v. XX, p. 1–10, doi:10.1785/0120200029.

Stirling, M.W. and Anooshehpoor, R., 2006, Constraints on probabilistic seismic-hazard models from unstable landform features in New Zealand: Bulletin of the Seismological Society of America, v. 96, p. 404–414, doi:10.1785/0120050034.

Discussion (D) Rapid post-earthquake reconnaissance and paleoseismic trenching results for the M6.4 Ridgecrest earthquake

Stop leaders: Özgür "Oz" Kozacı, Pacific Gas & Electric Company (PG&E), Christopher Madugo (PG&E)

Introduction

PG&E operates a network of over 6700 miles of gas transmission lines across most of California, including two lines that serve the towns of Ridgecrest and Trona. The PG&E Geosciences Department works with the Gas Transmission Integrity Program to identify, evaluate and mitigate pipeline fault crossings before large earthquakes and support response efforts after large earthquakes that impact PG&E assets, such as the 2014 M6.0 Napa earthquake and M6.4/M7.1 Ridgecrest earthquake sequence.

After the M6.4 earthquake, PG&E Gas control center quickly assessed that there were no measurable major leaks on transmission pipelines in the area and initiated a Gas OEC to conduct a comprehensive gas leak survey and repair effort, as necessary. Geosciences supported this effort, focused on evaluation/documentation of surface fault rupture and ground failure throughout the local gas system. This is a good example of how science studies and data are implemented for safety and risk reduction

At this stop, we will discuss the Geosciences Department's efforts, in collaboration with InfraTerra, to rapidly evaluate impacts from the M6.4 earthquake to buried gas infrastructure, including a gas transmission line and follow-up studies to characterize displacement, rupture complexity and the timing of past events to inform repair efforts. The following text and figures are adapted from Kozaci et al., 2021 and a presentation to the 2020-2021 ASCE Lifelines Conference.

Figure 1-3D-1. *PG&E gas transmission system overlain on Holocene active faults in California*

Study sites

(*Kozacı et al., 2021*)

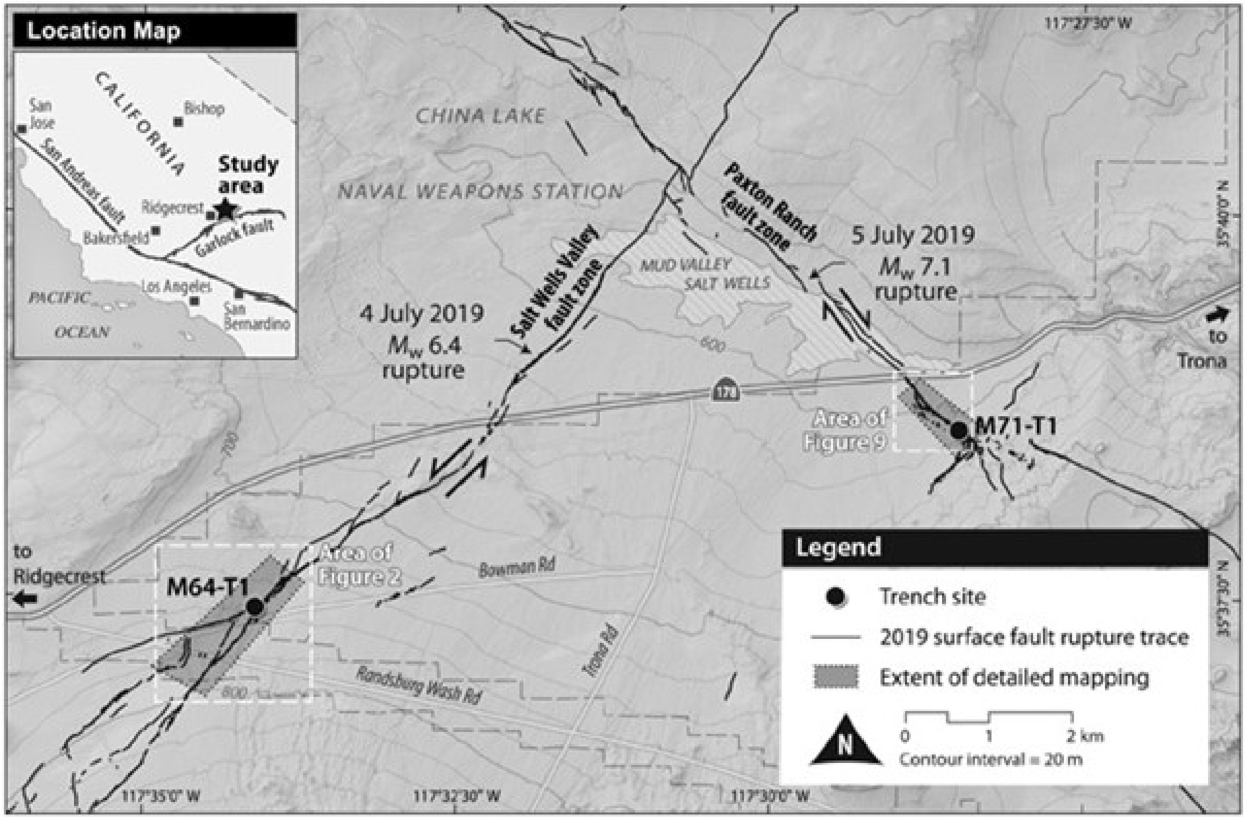

- The Geosciences response team arrived at Ridgecrest within 18 hours of the M6.4 earthquake and began field reconnaissance
- The initial regional reconnaissance focused on rupture traces and various soft sediment deformation localities between Ridgecrest and Trona
- Detailed mapping focused primarily on two pipeline – fault rupture crossing sites south of highway 178
- Both sites are located where the rupture trace transitions into a complex zone of faulting

Impacts to buried infrastructure

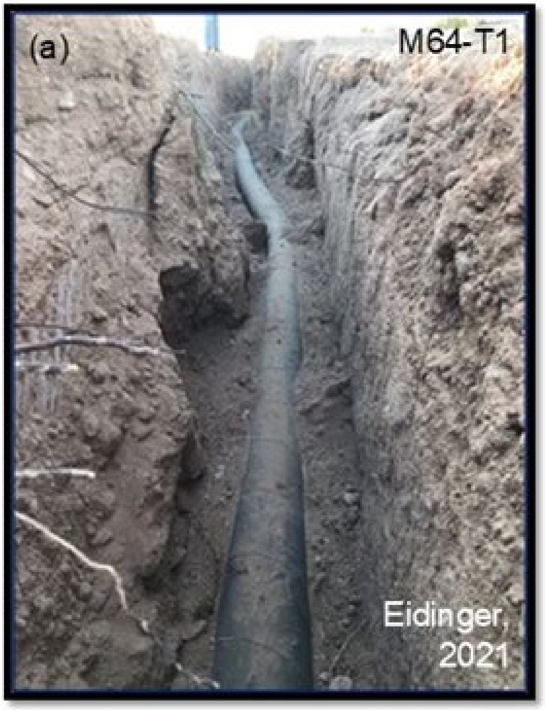

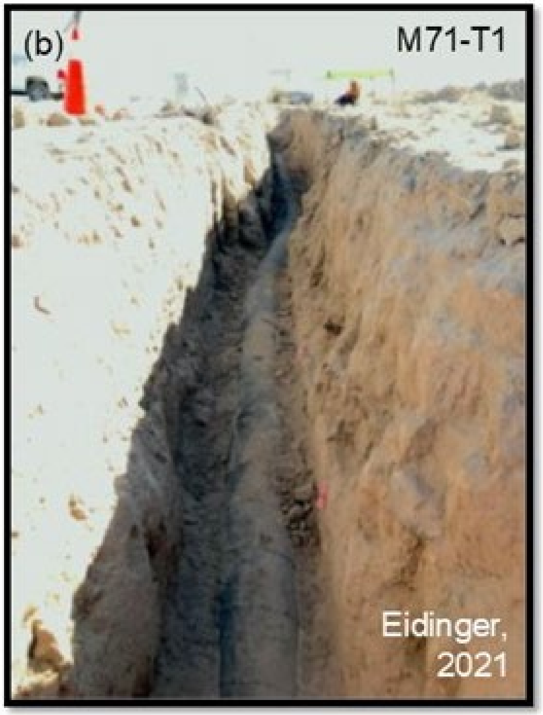

- Photographs (a) and (b) show excavations of ductile steel gas transmission pipelines following the M6.4 and M7.1 earthquakes. Fault ruptures cross the trenches at high angles to the pipes. The pipes are still embedded in the soil, preserving the elastic deformation.
- While there were no leaks on either gas transmission line, both deformed pipe sections were replaced shortly after the ruptures
- Photograph (c) shows offset of a brittle concrete water line near Highway 178 following the M7.1 earthquake

M6.4 rupture - mapping

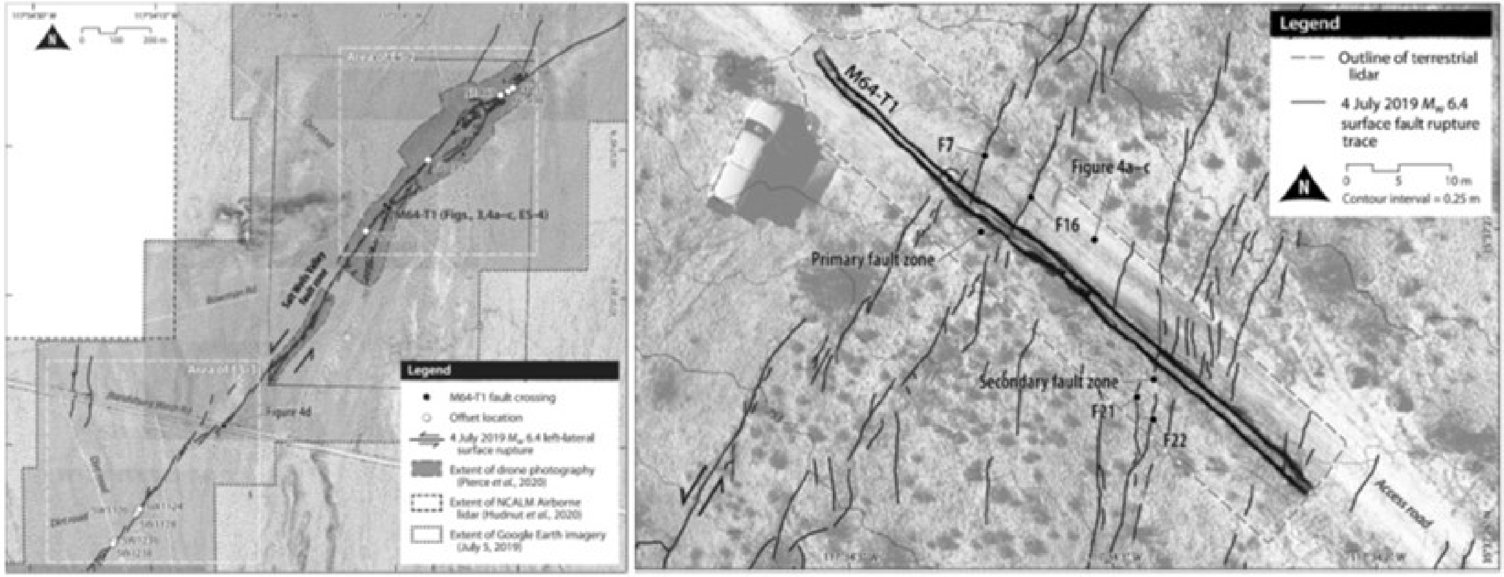

(*Kozacı et al., 2021*)

- We mapped a section of the fault in detail centered around the M6.4 rupture gas transmission pipeline crossing
- Our mapping was based on field observations, satellite imagery, 1 m resolution digital elevation models, PG&E lidar data and drone imagery by Pierce et al., 2020
- Availability of such a complementary set of base maps proved extremely useful for covering large swaths of the fault zone and also mapping deformation in detail
- On the upper right, an example of our detailed rupture mapping based on drone imagery is fused with the terrestrial lidar scan of the pipeline trench re-excavation across the fault rupture zone
- Pipeline re-excavations were performed with dry-vacuum systems primarily for safety reasons but proved extremely helpful because it helped preserve the displacements on the original pipeline construction trench walls
- Examples of this are shown on the following pages

M6.4 rupture – displacement measurements

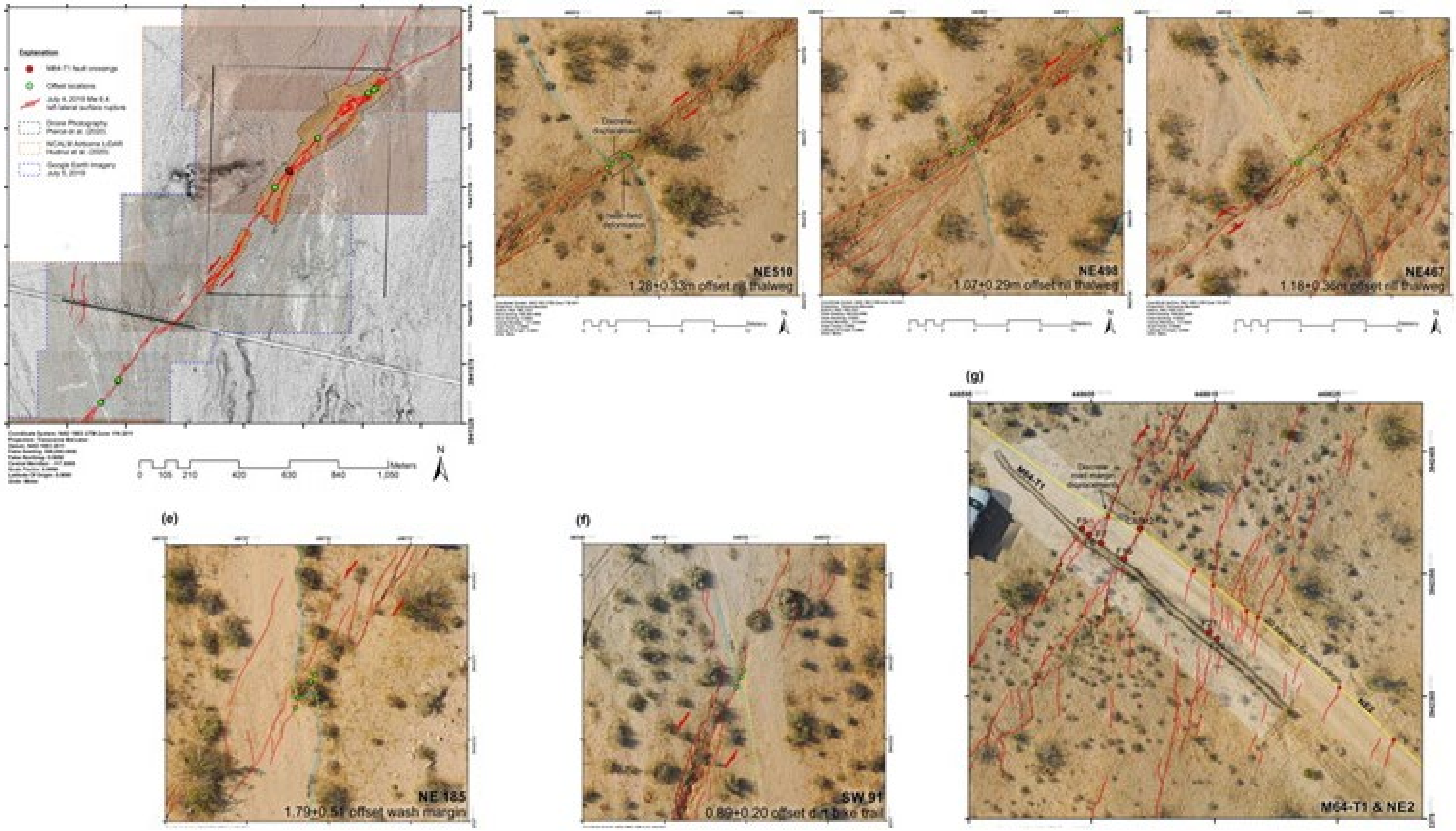

- Examples of locations and types of mapped offsets along the M6.4 rupture
- Green dots on the upper left map show individual offset sites shown in detail on the color base maps
- Offset features along the rupture include rill thalwegs, wash margins, dirt bike trails, and original pipeline construction trenches
- The desert environment provided a major advantage and opportunity for ultra high-resolution deformation mapping thanks to the drone-based surveys

M6.4 rupture – cumulative displacement and along-strike variation

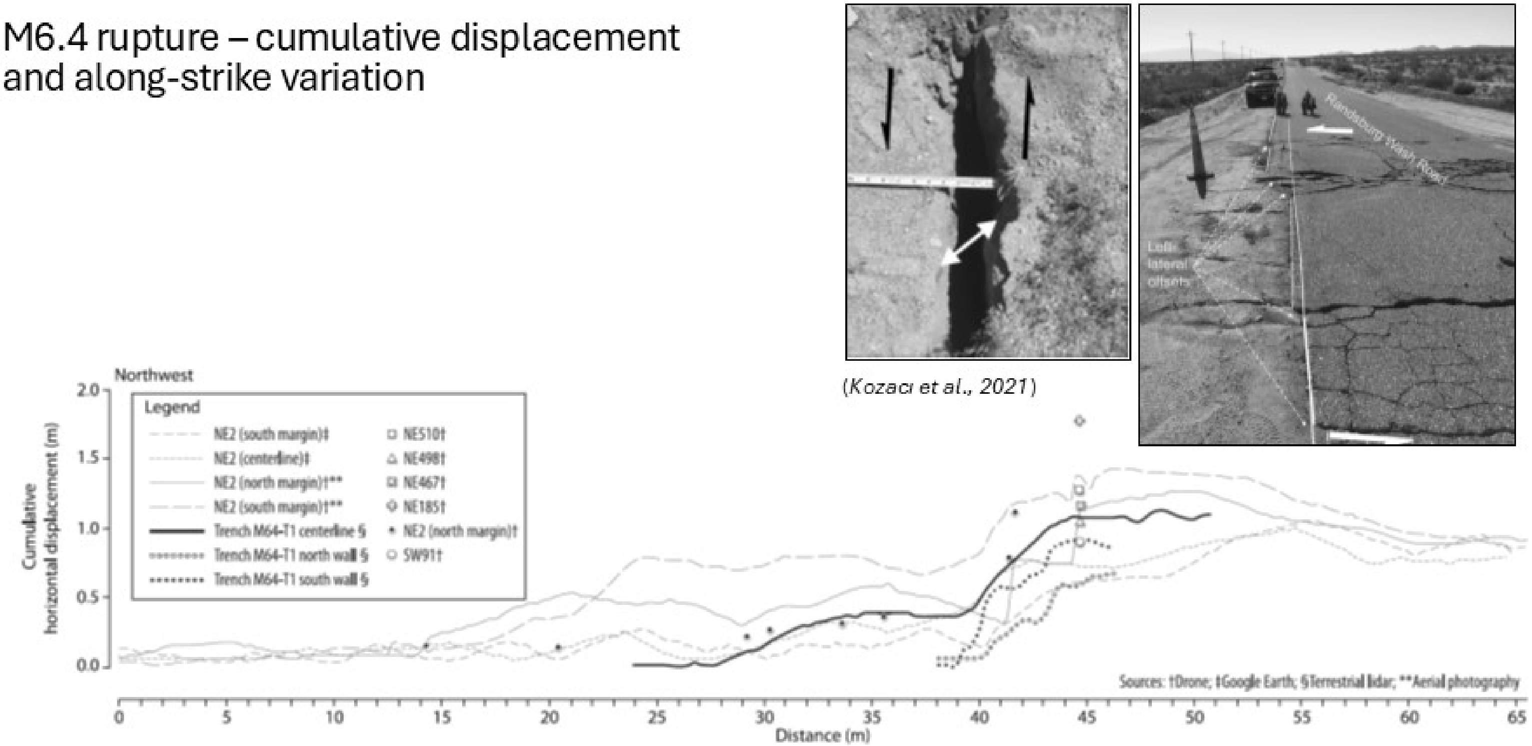

(Kozacı et al., 2021)

Sources: †Drone; ‡Google Earth; §Terrestrial lidar; **Aerial photography

- Offset measurements were plotted on the cumulative horizontal displacement plot shown above
- Points indicate offset measurements at discrete locations such as the thalweg of a rill at a fault crossing, while the lines represent surveyed linear features for example margin of a paved road across the entire fault zone
- The offsets measured from these two approaches were generally in agreement, but the line features captured off-fault deformation between discrete fault strands
- Within the study area, maximum left-lateral displacement reached approximately 1.4 m (4.6 ft)
- Even though the deformation zone, including primary and secondary ruptures as well as minor fractures with no discernable offset, was up to approximately 460 m (1509 ft) wide, most displacement was concentrated within approximately 10 m (32 ft)

M6.4 rupture – fault trenching

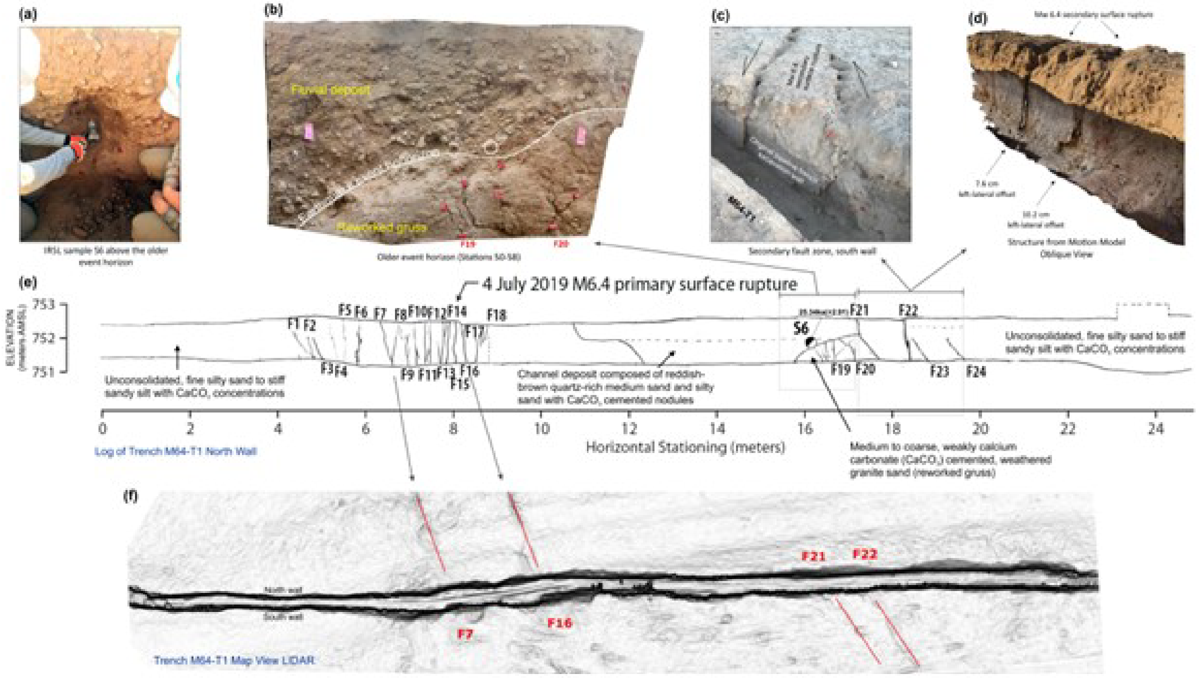

- The bottom figure is the terrestrial lidar scan of the trench across the pipeline fault rupture intersection. Main surface fault rupture traces are marked by red lines. The figure in the middle is the log of the trench wall.
- The primary fault zone is between stations 4 and 9. A secondary fault zone can be seen between stations 16 and 20. These stationing values are in meters.
- In this trench an older rupture terminates at the basal contact of a buried channel
- OSL dating revealed that this event was older than approximately 25 thousand years
- Because the stratigraphic record is incomplete due to the erosional nature of this contact, we do not know if there are missing events in the stratigraphic record
- We do know that the same location experienced at least one more past ruptures
- Photo (a) shows the OSL sampling in action. Photo (b) shows the stratigraphic event horizon for the older earthquake. Photos (c) and (d) show the offset original pipeline construction trench wall

Conclusions

- Displacement varied significantly both along and across fault strike
    - Displacement variability strongly correlated with structural (fault rupture) complexity
    - Detailed mapping proved critical in capturing pre-rupture fault complexity

- Deformation zones were considerably wide, however, main displacement was concentrated
    - ~70-80% of displacement was discrete vs 20-30% off-fault deformation (OFD)
    - <30% OFD along structurally complex rupture sections may be rapidly eroded or obscured by surface processes, which can result in underestimation of fault rupture hazard assessments for critical infrastructure

- Discrete versus distributed deformation have implications for fault rupture mitigation of critical infrastructure
    - "Knife-edge" models in which deformation is concentrated within a relatively narrow zone are generally considered more conservative in terms for assessing the capacity of structures
    - This study shows that, even in relatively complex fault ruptures with broad deformation zones, surface fault deformation can be concentrated within narrow zones and across discrete fault strands.

References

Eidinger, John. (2021). Seismic Fragility of Natural Gas Transmission Pipelines and Wells. Prepared by G&E Engineering Systems Inc., G&E Report, Revision 4, dated November 14 2021.

Kozaci O. Madugo C. M. Bachuber J. L. Hitchcock C. S. Kottke A. R. Higgins K. Wade A , and Rittenour T. (2021). Rapid postearthquake field reconnaissance, paleoseismic trenching, and GIS-based fault slip variability measurements along the Mw 6.4 and Mw 7.1 Ridgecrest earthquake sequence, southern California, *Bull. Seismol. Soc. Am.* **111,** no. 5, 2334–2357

GEER Team: Stewart, J. P. (Editor), Stewart, J. P., S. J. Brandenberg, P. Wang, C. C. Nweke, K. Hudson, S. Mazzoni, Y. Bozorgnia, K. W. Hudnut, C. A. Davis, S. K. Ahdi, et al. (2019). Preliminary report on engineering and geological effects of the July 2019 Ridgecrest Earthquake sequence, Geotechnical Extreme Events Reconnaissance Association Rept. GEER-064, doi: 10.18118/G6H66K.

Discussion (E) M6.4 Pierce et al. Trench Site

Ian Pierce University of Nevada, Reno, now at PG&E
Alana Williams Arizona State University
Rich Koehler Nevada Bureau of Mines and Geology, University of Nevada Reno
Ramon Arrowsmith Arizona State University
Kathleen Rodrigues Division of Earth and Ecosystem Sciences, Desert Research Institute

Salt Wells Valley Fault Trenches

Two trenches (SWV-T1 and SWV-T2) were excavated at one location across the surface ruptures of the Salt Wells Valley fault between Highway 178 and Randsburg Wash Road (Figure 1-3E-1). The site was chosen as there appeared to be older alluvial units exposed at the surface that may preserve evidence of older earthquakes. The SWV-T1 trench (117.5627°W 35.6276°N, Figure 1-4-E2) was excavated across a pediment surface and the SWV-T2 trench (117.5625°W 35.6277°N; Figure 1-4-E3) was excavated in the center of a sandy wash with a left-lateral offset of the northeast bank of ~124 cm.

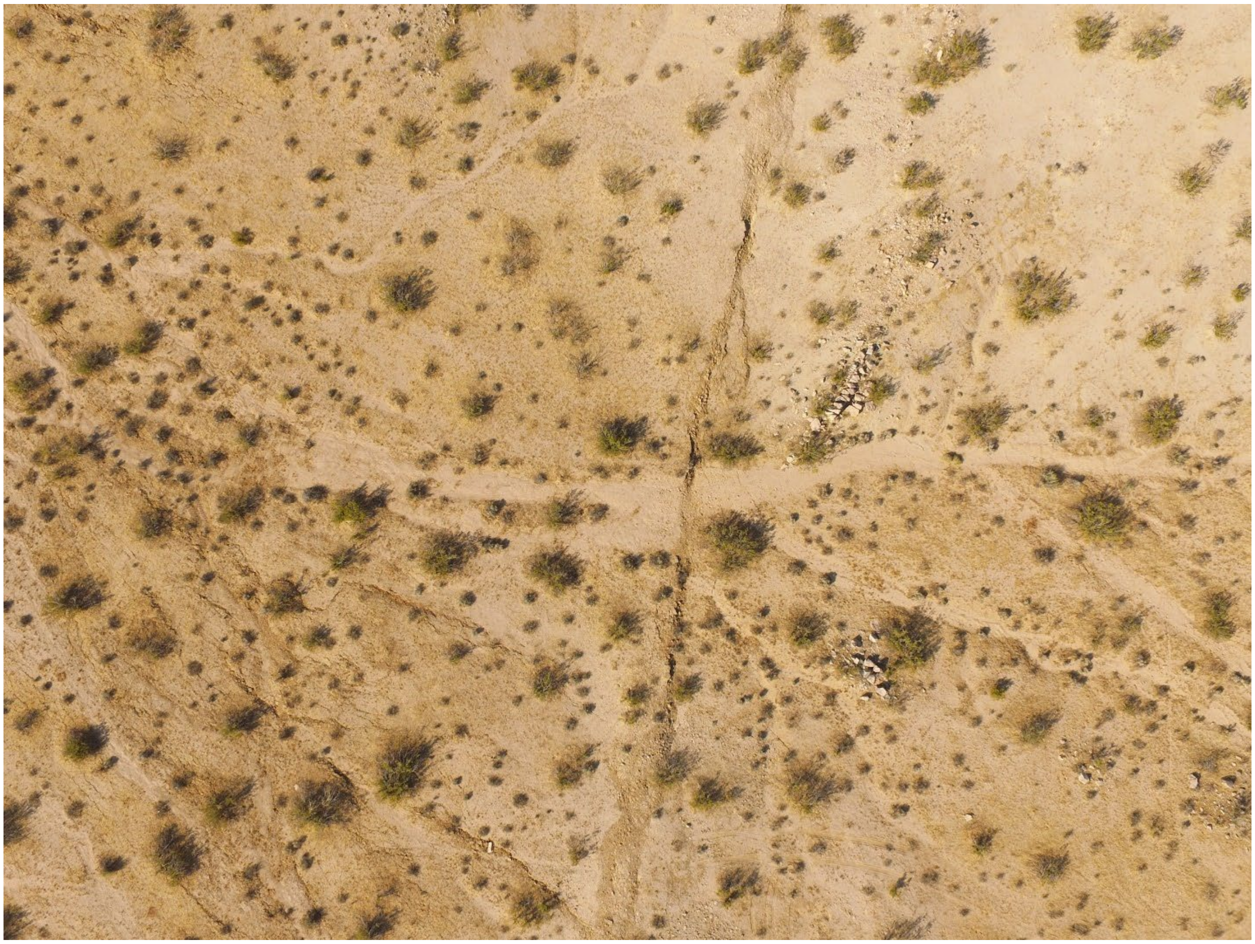

UAS photo of trench site taken July 5, 2019

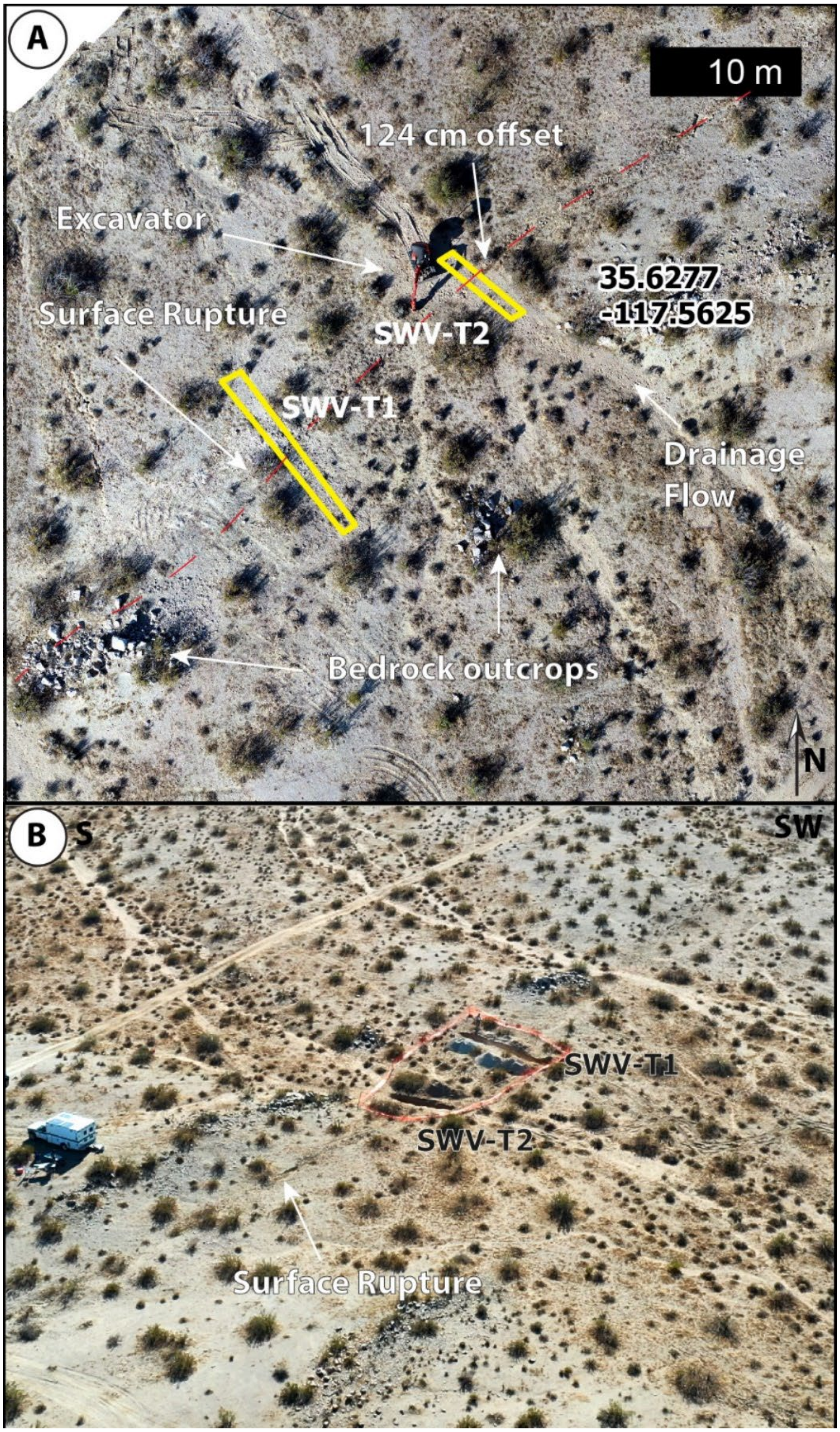

Figure 1-3E-1. *Salt Wells Valley (SWV-T1/2) trench sites. A: UAV orthophotomosaic from November 2020 showing the two trench outlines (yellow) prior to excavation. Note the* *shallow bedrock outcrops at the surface and sharp surface rupture (red dashed line). Drainages flow to the northwest. B: Oblique aerial photo looking southward showing opened trenches.*

Figure 1-3E-2 (following). *Salt Wells Valley fault trench SWV-T1. This trench revealed heavily faulted granitic bedrock in fault contact with Pleistocene alluvium and all capped with thin Late-Pleistocene to Holocene alluvium. Two luminescence samples limit the event horizon above faults that terminate at the Unit 3-5 contact on the northwest end of the trench.*

Figure 1-3E-3 (following +2). *Salt Wells Valley fault trench SWV-T2. A simple fault zone in Holocene sands only displays evidence of the 2019 M6.4 earthquake.*

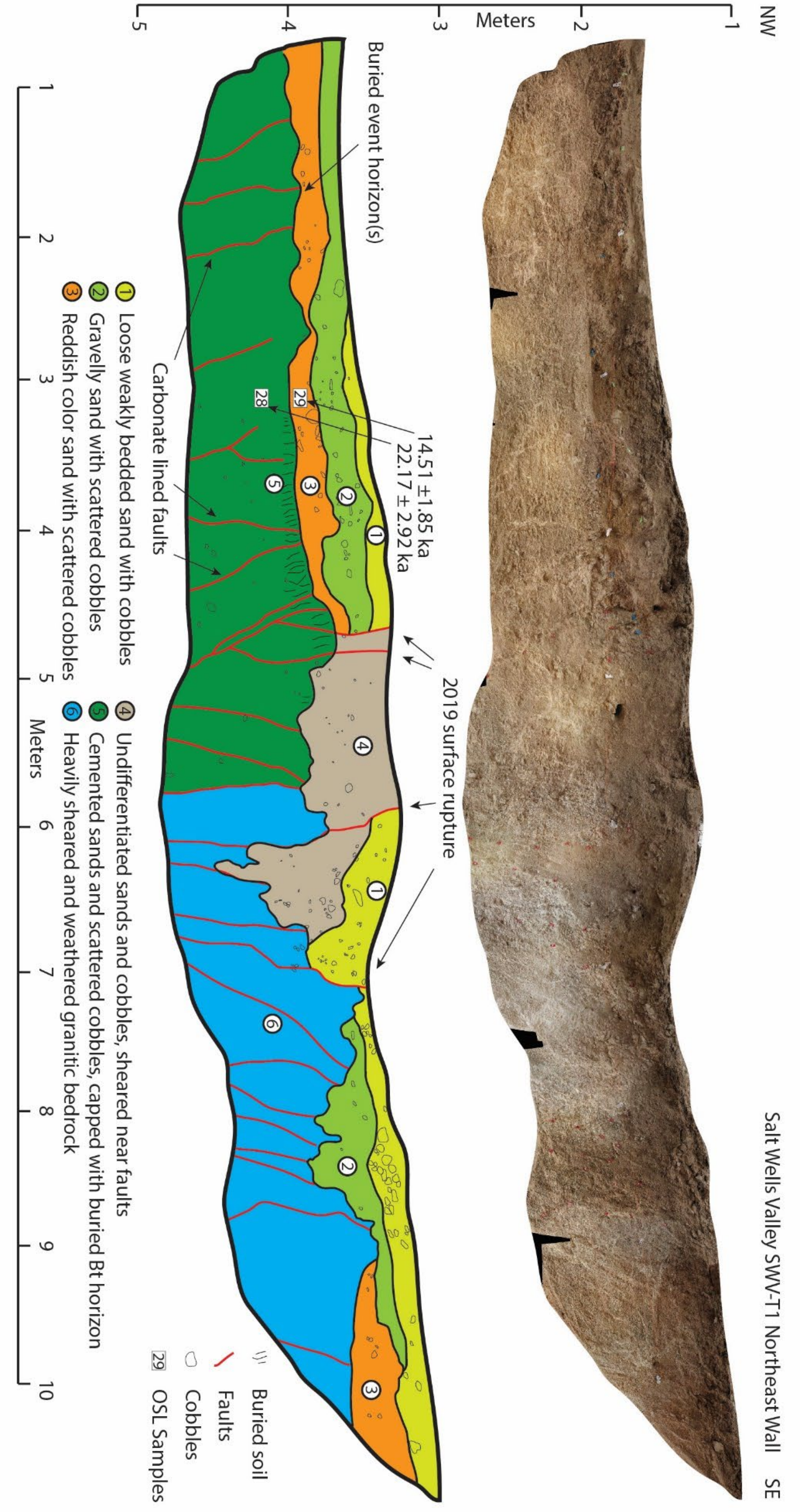

Day 1 Stop 3: M6.4

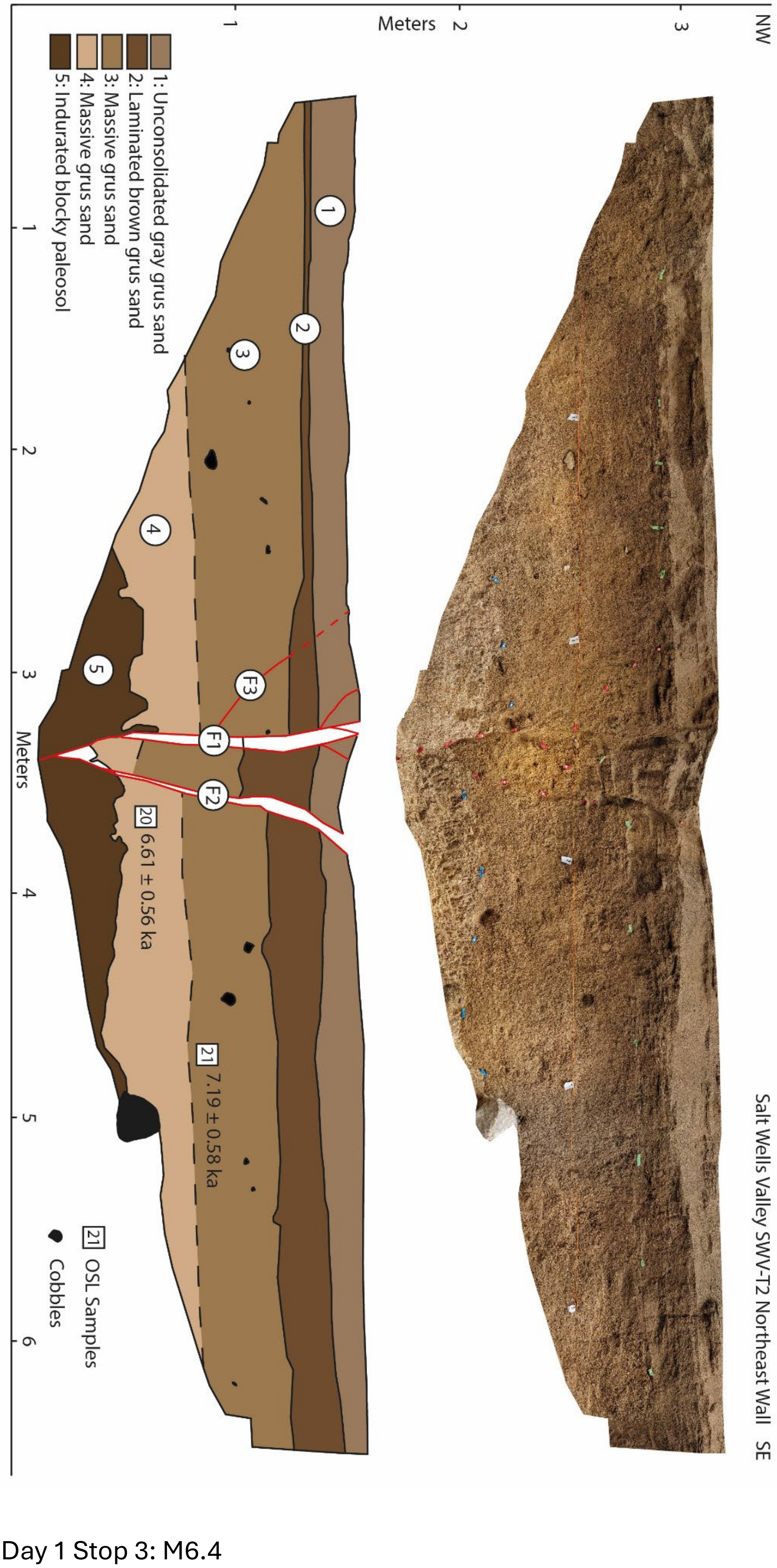

Day 1 Stop 3: M6.4

SWV-T1 (**Figure 1-3E-3**): was a 10-m-long, 1.9-m-deep trench oriented N45°W across the M6.4 surface rupture in a pediment surface. The trench primarily exposed intensely fractured granitic bedrock overlain by thin colluvial and alluvial sediments. **Figure 1-3E-2** shows the orthophotomosaic and log of the northeast wall of the trench.

The lowest unit on the southeast end of the trench is an intensely fractured and weathered light-blue to gray and brown granitic bedrock unit. In places, the faulting in this unit forms pulverized fault gouge. The top of Unit 6 has characteristics consistent with a weathered C horizon, with blocks of material surrounded by finer grained sands filtering in from above forming a wavy to irregular gradational contact.

Abutting Unit 6 across the fault zone to the northwest is Unit 5, a sedimentary unit comprised primarily of light tan sandy grus with scattered cobbles. Unit 5 is moderately cemented (Stage 2 carbonate) and contains numerous carbonate-lined fractures and faults. The top of part of Unit 5 has a blocky texture, interpreted to be a buried Bt soil horizon. Above Unit 5 is a sharp contact with Units 3 and 4.

Unit 4 is an undifferentiated group of primarily massive loose gray sandy deposits with scattered pebbles and cobbles. In places, Unit 4 is highly sheared and has an erosional relationship with Unit 6.

Unit 3, Unit 2, and Unit 1 are sandy deposits with scattered gravels and cobbles of varying color and gradational contacts. Unit 3 is reddish, unstratified, and ~10-30 cm thick. Unit 2 is brown, also unstratified, and ~20-30 cm thick. Unit 1 caps the deposit and is lighter gray, weakly bedded, and ~10-30 cm thick.

We interpret Units 1-3 to be Holocene/latest Pleistocene alluvial/slope wash deposits. Unit 4 is interpreted to be a mixture of sheared and bioturbated materials derived from the surrounding units. Unit 5 is interpreted to be a late Pleistocene alluvial deposit that was stable long enough to develop a soil prior to the younger depositional episodes. Unit 6 is bedrock.

Steeply dipping faults were identified throughout the exposure. Overall, the faults form a broad positive flower structure with most faults dipping slightly towards the center of the exposure. No discrete vertical displacements were observed across units due to the irregularity of contacts and difficulty correlating units across fault zones. Unit 5 contains numerous carbonate-lined fractures, and Unit 6 contains gouge-lined fractures.

The 2019 surface ruptures are confined to the central part of the trench along 4 primary fault strands. Carbonate- and gouge-lined fractures in Units 5 and 6 that terminate at the base of Units 2, 3, and 4 provide evidence of at least one penultimate earthquake, while the pulverized bedrock in Unit 6 provides evidence for additional older events.

Two luminescence samples (OV029 and OV028) were collected from the northwest side of the exposure in Units 3 and 5, respectively. Both yielded late Pleistocene ages—14.51 ± 1.85 and 22.17 ± 2.92, respectively using the central age model. These ages place upper and lower limits on the timing of at least one penultimate earthquake on the Salt Wells Valley fault.

SWV-T2 (**Figure 1-3E-3**) was a 6-m-long, 1.5-m-deep trench oriented N50°W across the M6.4 rupture in the active channel. The trench primarily revealed sandy grus units overlying an indurated Pleistocene paleosol cut by a simple fault zone. **Figure 1-3E-3** shows the orthophotomosaic and log of the northeast wall of the trench.

The lowest unit, Unit 5, is a fine-grained, light-gray, indurated sedimentary unit with scattered pebbles. The excavator created clay smears in this unit. It exhibits a blocky/prismatic structure, most pronounced on the southeast side of the fault zone, and we interpret it as a mid-Pleistocene paleosol based on its degree of induration and pedogenic structure. The top of Unit 5 is a sharp, wavy to irregular contact with the unconformably overlying Unit 4.

Units 4 through 1 are composed of sandy, decomposed granitic grus with infrequent scattered pebbles and cobbles. They show increasing rubification with depth:

- Unit 4 is reddish-brown and massive, ~25-30 cm thick, with a gradational contact with overlying Unit 3;
- Unit 3 is a darker red-brown massive unit, ~35-50 cm thick, in sharp contact with Unit 2;
- Unit 2 is dark brown with cross-bedded laminations, ~25 cm thick, thinning across the fault zone to the northwest to ~4 cm thick, in sharp contact with Unit 1;
- Unit 1 is a light gray, loose, cross-bedded laminated sand at the top of the section, ~15 cm thick.

We interpret Units 1–4 as Holocene channel deposits, each conformably overlying the previous, and based on the lack of stratigraphy we interpret moderate bioturbation of Units 3 and 4.

Two steeply dipping primary fault strands, F1 and F2, merge in Unit 5 at the trench base, forming a ~45-cm-wide negative flower structure (graben) in the overlying sediments. Units 1–4 are downdropped between F1 and F2, with Unit 2 being thickest in the graben block. The Unit 2–3 and 3–4 contacts are down-dropped by ~20 cm between faults F1 and F2. Each fault strand is 2–4 cm wide and creates local fissures in the upper units. F1 is vertical in Units 1–4 and dips 72°SE in Unit 5, while antithetic F2 dips 75°NW. A small splay fault, F3, branches from F1 with a 48°SE dip through Units 1–3. No vertical fault terminations, colluvial wedges, or other distinct event horizons were observed.

Based on the relatively simple fault zone structure and lack of discrete paleoearthquake markers, we infer that Units 1–4 experienced only the 2019 earthquake rupture. Although the vertical displacement of the Unit 1–2 contact is clearly less than that of the Unit 2–3 and 3–4 contacts, we attribute this to lateral unit thickness variations and predominantly strike-slip motion.

Two luminescence samples (SWV-T2, OV021 and OV020) were collected from the southeast side of the fault zone in Units 3 and 4, respectively (**Figure 1-3E-3**). Both yielded mid-Holocene ages—7.19 ± 0.58 ka and 6.61 ± 0.56 ka, respectively, using the central age model. Since these units were only faulted in 2019, these mid-Holocene ages place a minimum bound on any earlier rupture. Hence, the penultimate event on this segment of the Salt Wells Valley fault predates ~7.2 ka.

Trench Interpretations on the Salt Wells Valley Fault (M6.4 2019 earthquake)

At SWV-T2 (**Figure 1-3E-3**), uniform deformation in the youngest deposits (Units 1–4) indicates only the 2019 M6.4 event was preserved. Luminescence ages suggest any earlier rupture must predate ~7 ka. The stratigraphy and faulting relationships in SWV-T1 (**Figure 1-3E-2**) are consistent with this result and provide evidence of at least one pre-2019 event between 14.51 ± 1.85 and 22.17 ± 2.92 ka. In a nearby trench ~600 m to the southwest (**Figure I-1**), Kozaci et al. (2021) documented at least one event older than 25.34 ± 2.91 ka but could not exclude the possibility of a younger Holocene rupture. These results confirm at least one pre-2019 surface rupture along the Salt Wells Valley fault, with no clear evidence for a penultimate event younger than ∼14.5 ka. Combining the ages from the Kozaci et al. (2021) and SWV-T1 trenches limits the timing of a penultimate event to ~22-25 ka, however this result is based on only two luminescence samples.

Slip Rate Estimation for Salt Wells Valley Fault

The Salt Wells Valley fault is constrained by a single closed interval of ~22-25 ka since the penultimate event. In 2019, the Salt Wells Valley fault produced a mean left-lateral slip of

0.3-0.5 m and a maximum of 0.7-1.6 m (DuRoss et al., 2020). Assuming these measurements represent the total slip accumulated over the duration of the single closed interval results in a mean rate of 0.01-0.02 mm/yr, and a max rate of 0.03-0.07 mm/yr. While this rate is low relative to some other Walker Lane faults, it is consistent with the observations presented in this paper, and the absence of a more detailed paleoseismic record limits our ability to refine the fault's longer-term rate. A more detailed event chronology or additional offsets on datable landforms would be required to resolve whether the Salt Wells Valley fault regularly accommodates slip in sub-millimeter-per-year increments or experiences more sporadic displacement episodes.

Discussion (F) Max slip location along M6.4, surface rupture slip variability, off-fault deformation

For this discussion, we will hike a bit farther northeast from the Pierce et al. M6.4 trench site to examine a segment of the rupture characterized by a series of offset channels. This area is particularly interesting because it exhibits high variability in slip over a relatively short distance, despite following a relatively simple rupture trace. Such variability provides an opportunity to explore the processes that control along-strike slip distribution and how these are expressed in both field and remote-sensing datasets.

We will first review the field measurement distribution of both ruptures (Figure 1-3F-3; DuRoss et al., 2020), which captures the fine-scale heterogeneity in slip along the fault. Next, we will compare these observations with pixel-tracking results from Gold et al. (2021) (Figures 1-4F-3 through -7), which provide a smoothed representation of displacement derived from optical image correlation. These comparisons are valuable because pixel tracking serves as a proxy for near-field off-fault deformation, integrating distributed strain that is not captured by discrete on-fault field measurements.

A few key points to consider during this discussion:

- Field measurements show highly variable slip along strike, reflecting local structural complexities, surface material properties, and measurement limitations.
- Pixel-tracking estimates, in contrast, tend to be smoother because they average displacement over a broader window, effectively filtering out small-scale variability.
- Interestingly, the difference between these two datasets is variable itself, raising questions about the spatial scale of deformation and the role of off-fault processes.

This leads us to broader questions:

1. What causes the observed variability in slip? Is it primarily a function of fault geometry, material heterogeneity, rupture dynamics, or post-seismic processes?
2. What does a “slip rate” mean in this context? When surface slip is so heterogeneous, how do we reconcile these observations with long-term slip rates derived from geologic or geodetic data? Does the concept of a single representative slip rate oversimplify the complexity of earthquake rupture? Or should we think in terms of a spectrum of slip behaviors, from localized offsets to distributed deformation, when linking paleoseismic observations to long-term fault slip rates? Understanding these nuances is critical because assumptions about slip uniformity directly influence rupture models, seismic hazard estimates, and the design of infrastructure in fault-adjacent regions.

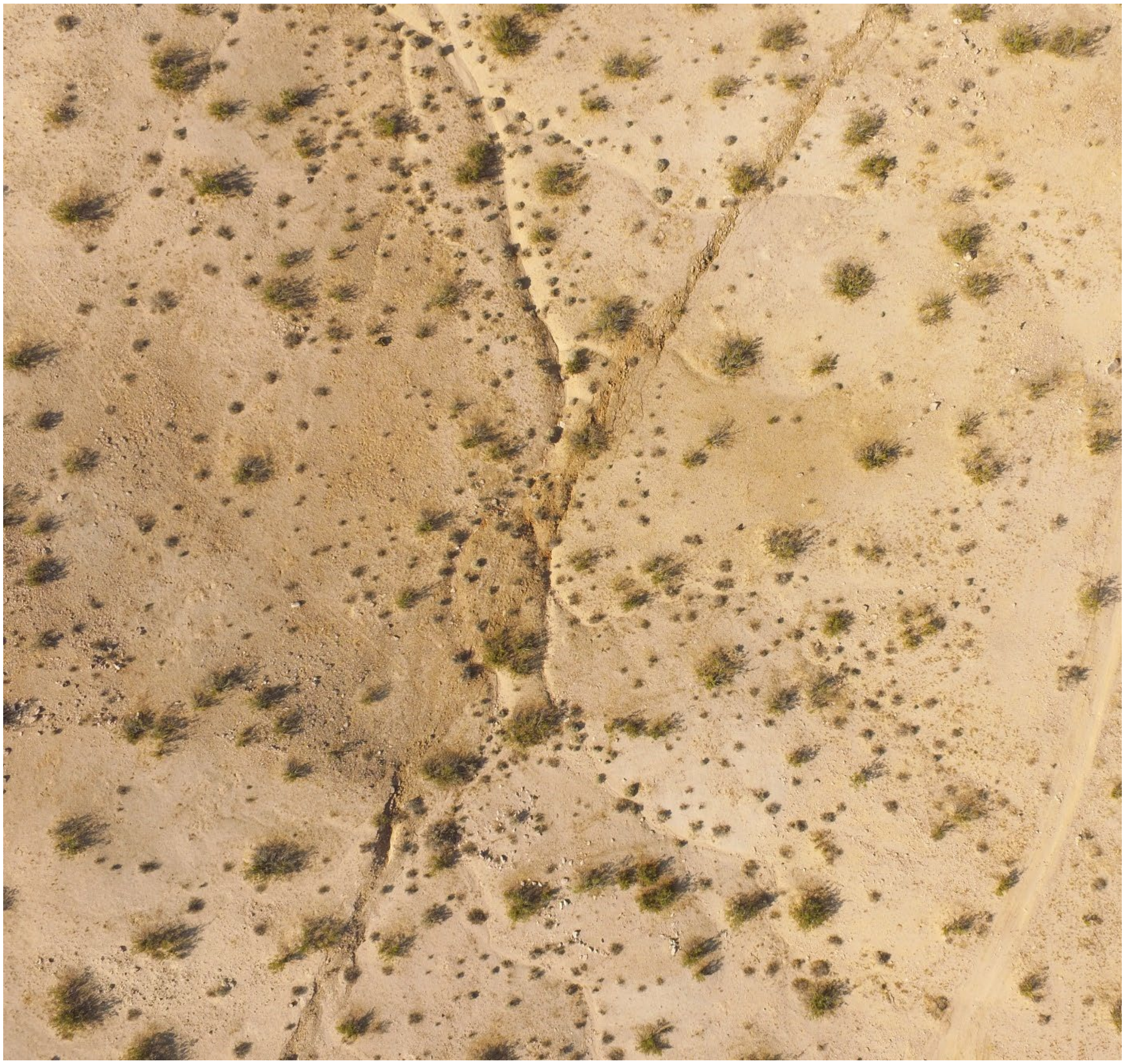

Figure 1-3F-1 UAS image of offset channels along the M6.4 rupture taken July 5, 2019.

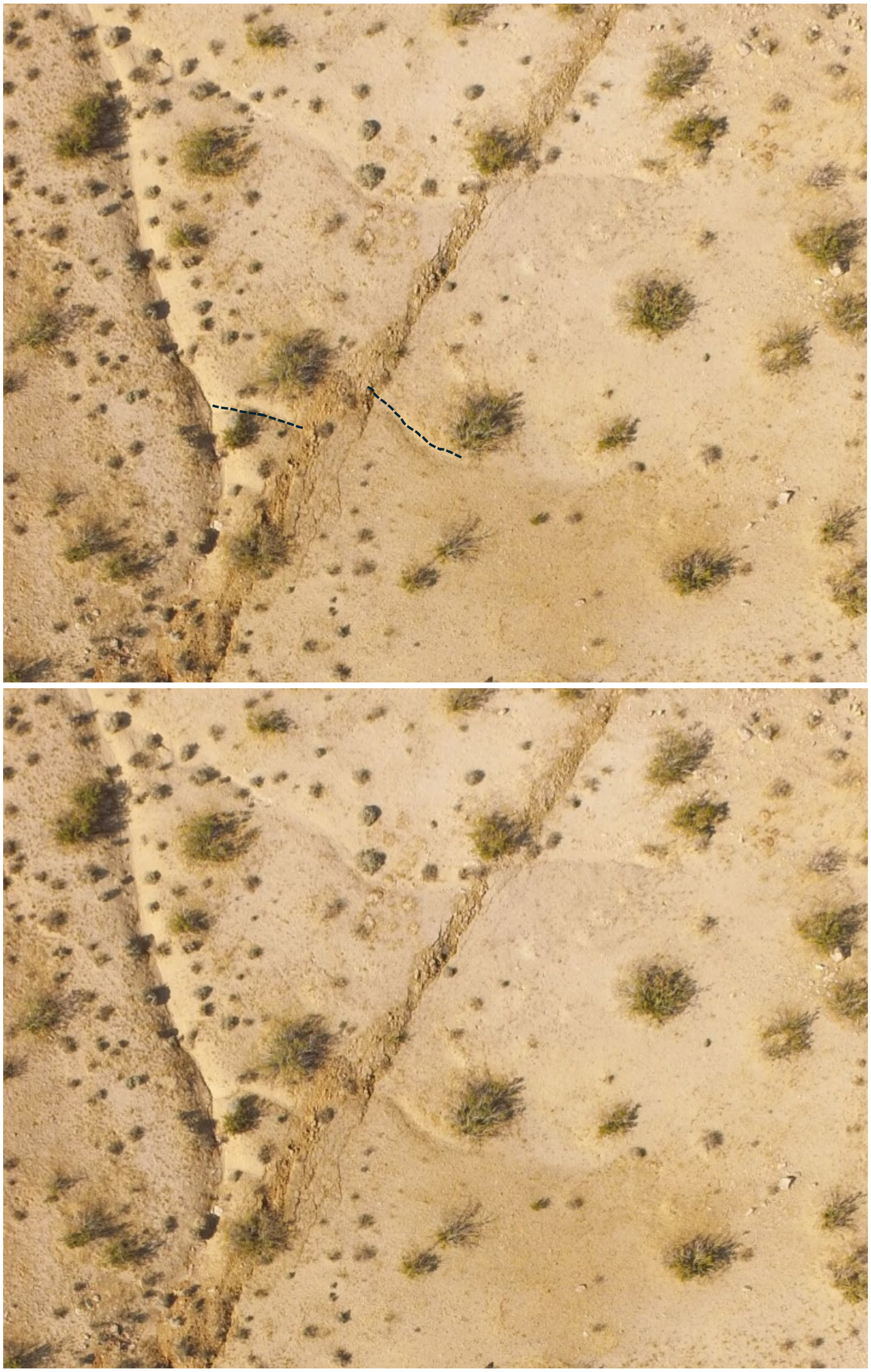

Figure 1-3F-2 UAS photo showing ~2.9 m left-lateral offset of channel along M6.4 rupture.

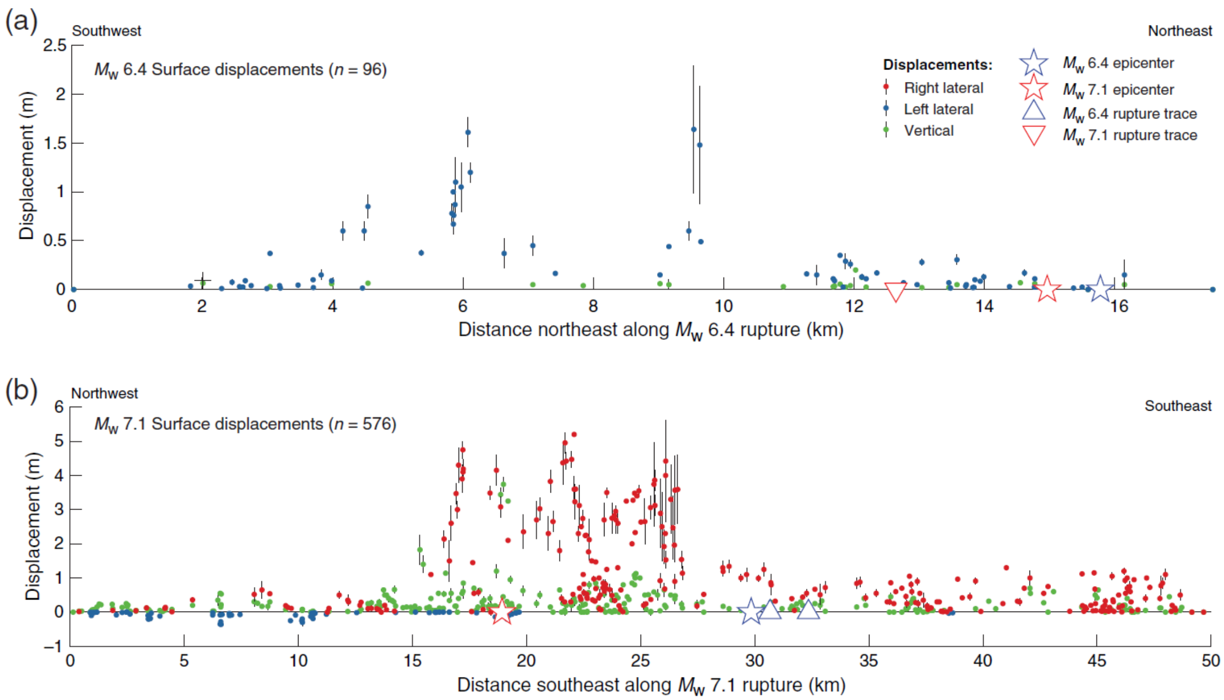

Figure 1-3F-3 Copied from DuRoss et al. (2020) Surface displacement measured along the (a) Mw 6.4 and (b) 7.1 ruptures and projected to 18 km long (Mw 6.4) and 50 km long (Mw 7.1) linear rupture traces (Fig. 2). Vertical bars show displacement uncertainty. Stars indicate Mw 6.4 and 7.1 epicenters projected to the linear traces. Triangle in (a) shows intersection of the Mw 7.1 rupture (strand 1) along the Mw 6.4 linear trace; triangles in (b) show intersection of two subparallel Mw 6.4 rupture traces (strands 21 and 23) along the Mw 7.1 linear trace (Fig. 2).

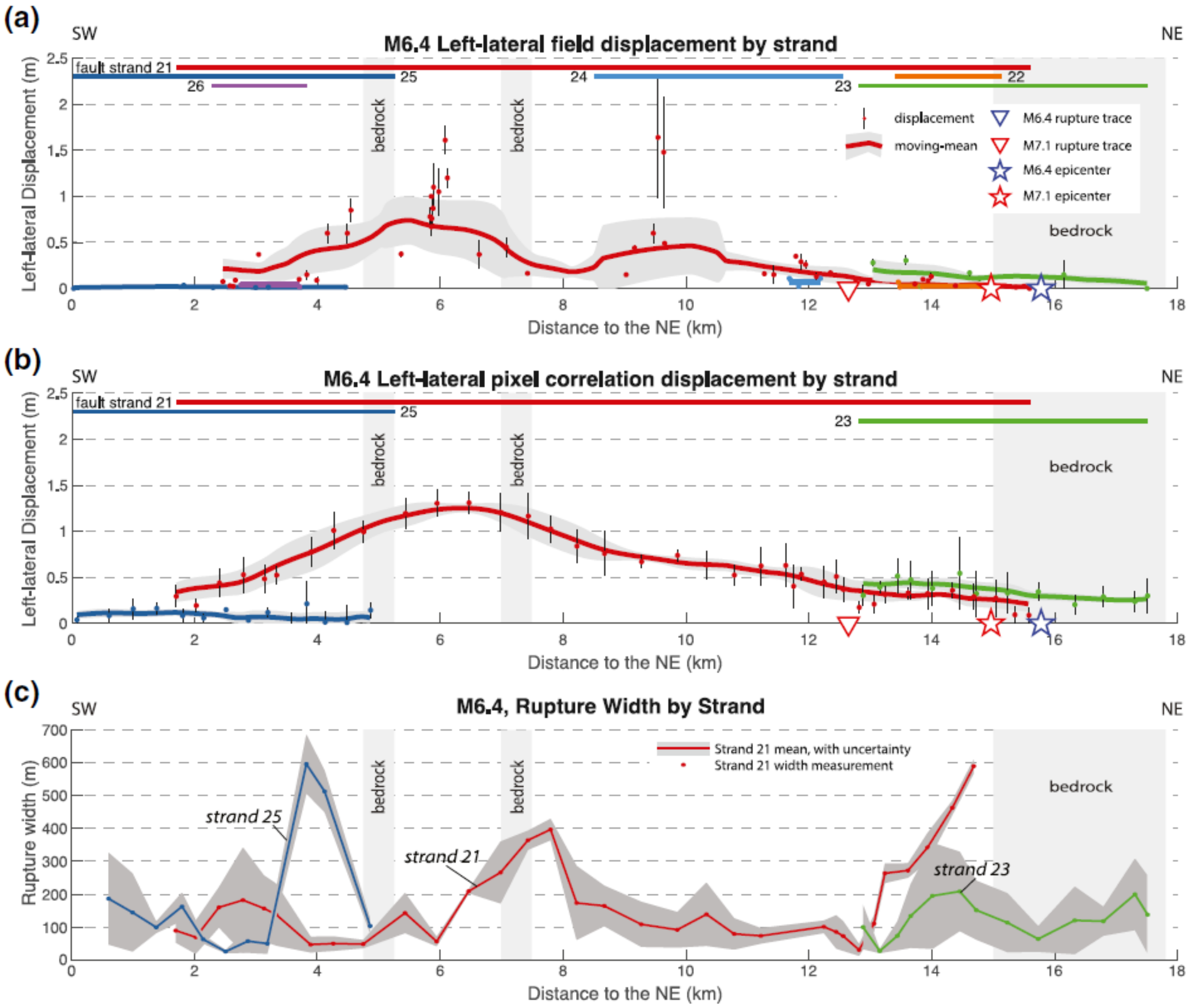

Figured 1-3F-4 Copied from Gold et al. (2021). Comparison of lateral surface displacement measurements made for the Mw6.4 rupture, separated by fault strand. (a) Field observations from DuRoss et al. (2020a). (b) Displacements measured from 0.5 m optical pixel correlation results from comparison of pre- and post-earthquake WorldView imagery. Displacement measurements depicted using color-coded circles and vertical bars (~95% uncertainty range). Moving-mean and 1-sigma uncertainty presented for each rupture strand. (c) Local rupture width across individual principal rupture strands, measured from the displacement profiles across optical pixel correlation results.

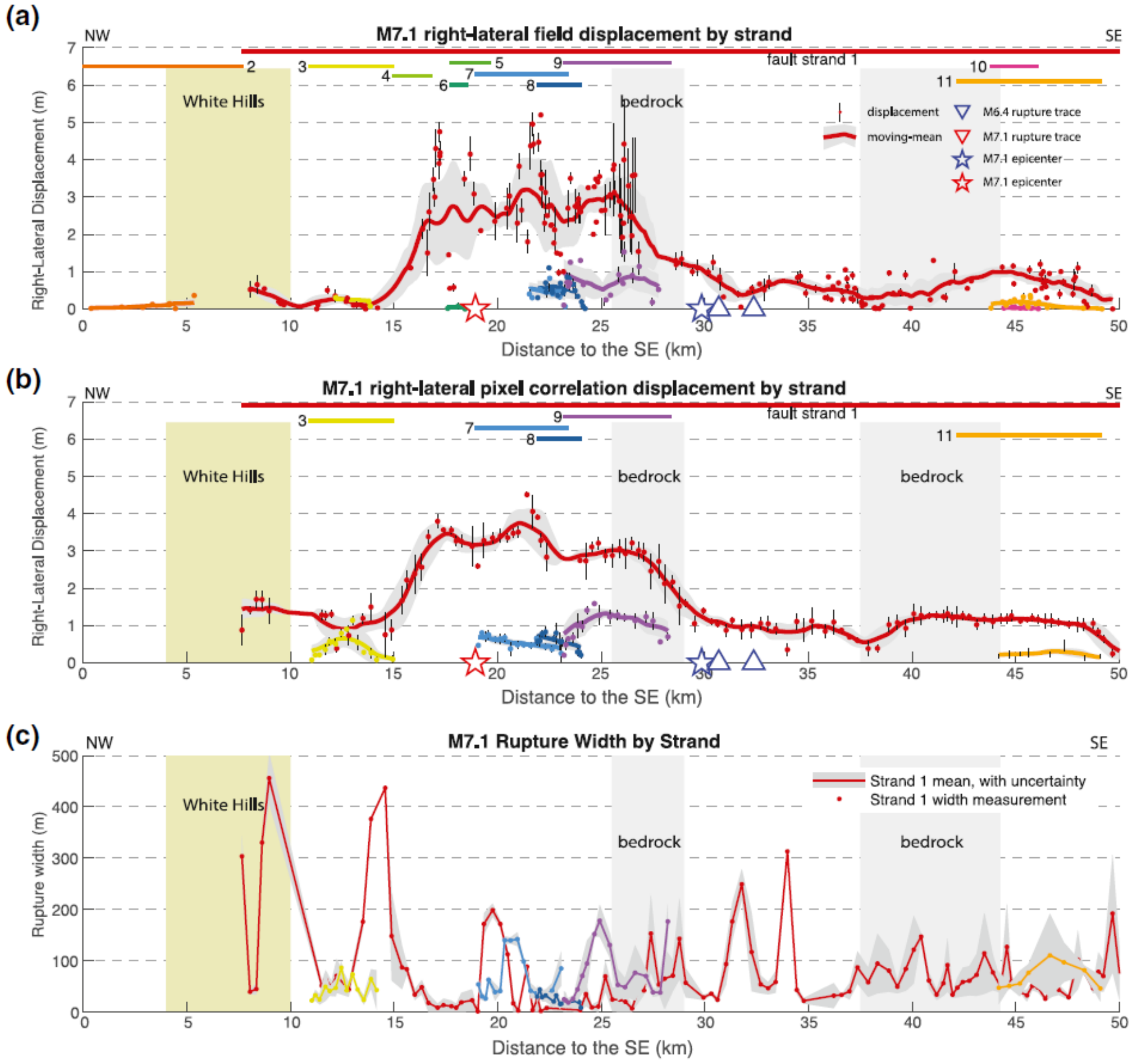

Figure 1-3F-5 Copied from Gold et al. (2021). Comparison of lateral surface displacement measurements made for the Mw7.1 rupture, separated by fault strand. (a) Field observations from DuRoss et al. (2020a). (b) Displacements measured from 0.5 m optical pixel correlation results from comparison of pre- and post-earthquake WorldView imagery. Displacement measurements depicted using color-coded circles and vertical bars (~95% uncertainty range). Moving-mean and 1-sigma uncertainty presented for each rupture strand. (c) Local rupture width across individual principal rupture strands, measured from the displacement profiles across optical pixel correlation results.

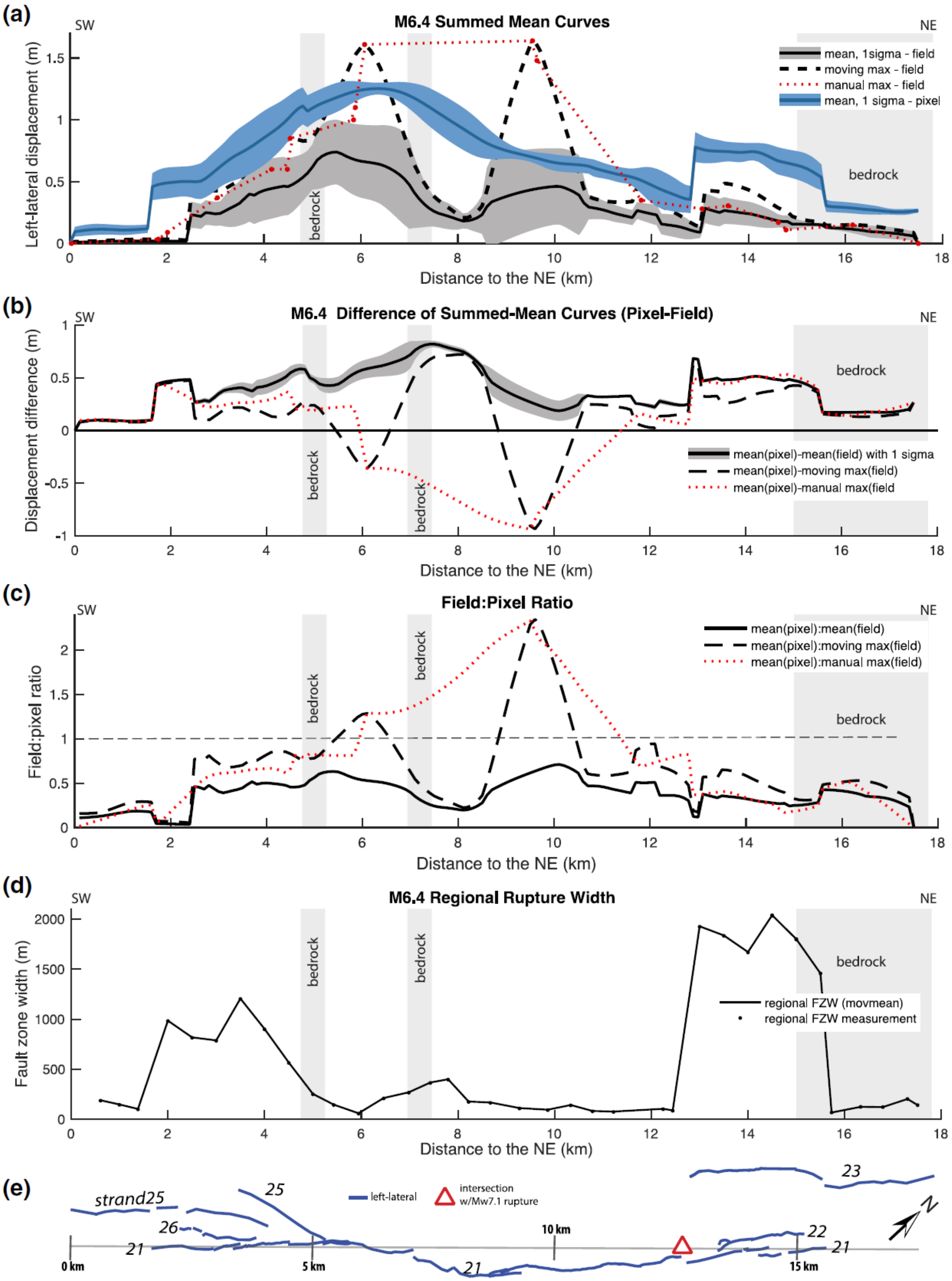
(a)
M6.4 Summed Mean Curves
SW
NE
Left-lateral displacement (m)
1.5
1
0.5
0
mean, 1sigma - field
moving max - field
manual max - field
mean, 1 sigma - pixel
bedrock
bedrock
0
2
4
6
8
10
12
14
16
18
Distance to the NE (km)
(b)
M6.4 Difference of Summed-Mean Curves (Pixel-Field)
SW
NE
Displacement difference (m)
1
0.5
0
-0.5
-1
bedrock
bedrock
bedrock
mean(pixel)-mean(field) with 1 sigma
mean(pixel)-moving max(field)
mean(pixel)-manual max(field
0
2
4
6
8
10
12
14
16
18
Distance to the NE (km)
(c)
Field:Pixel Ratio
SW
NE
Field:pixel ratio
2
1.5
1
0.5
0
bedrock
bedrock
bedrock
mean(pixel):mean(field)
mean(pixel):moving max(field)
mean(pixel):manual max(field)
0
2
4
6
8
10
12
14
16
18
Distance to the NE (km)
(d)
M6.4 Regional Rupture Width
SW
NE
Fault zone width (m)
2000
1500
1000
500
0
bedrock
bedrock
bedrock
regional FZW (movmean)
regional FZW measurement
0
2
4
6
8
10
12
14
16
18
Distance to the NE (km)
(e)
strand25
25
26
21
21
21
22
23
left-lateral
intersection w/Mw7.1 rupture
0 km
5 km
10 km
15 km
N

Figure 1-3F-6 Copied from Gold et al. (2021) (Prior page) Cumulative surface displacement field and pixel correlation measurements for the Mw6.4 rupture. (a) Cumulative displacement curves for the field (black) and optical pixel correlation (blue) displacements. Moving maximum curve for the field observations (dashed) plotted, for comparison. We use a 2-km window for the moving mean and 1-km window for the moving maximum. (b) Residual displacement calculated by subtracting field displacement measurements from the pixel correlation results. (c) Ratio of field:pixel displacement measurements. A ratio value of 1 (dashed horizontal line) indicates agreement between the measurements. In general, the field measurements are less than the optical pixel correlation results. (d) Regional rupture width measurements that span the entire zone of mapped rupture traces. Location of bedrock (gray) is indicated, while white areas of plot correspond to Quaternary playa and alluvial fan deposits. (e) Rupture strand map, simplified from Figure 1.

Figure 1-3F-7 Copied from Gold et al. (2021) (Following page) Comparison of cumulative surface displacement documented for the pixel correlation and field-based measurements for the Mw7.1 rupture. (a)Cumulative displacement curves for the field (black) and optical pixel correlation (blue) displacements. Moving maximum curve for the field observations (dashed) also plotted, for comparison. We use a 2-km window for the moving mean and 1-km window for the moving maximum. Rupture strands from pixel correlation measurements. (b) Residual displacement calculated by subtracting field displacement measurements from the pixel correlation results. (c) Ratio of field:pixel displacement measurements. A ratio value of 1 (dashed horizontal line) indicates agreement between the measurements. In general, the field measurements are less than the optical pixel correlation results. (d) Regional rupture width measurements that span the entire zone of mapped rupture traces. The location of the White Hill lacustrine deposits (yellow) and bedrock (gray) are indicated, while white areas of plot correspond to Quaternary playa and alluvial fan deposits. (e) Rupture strand map, simplified from Figure 1. Gray fault strands not used for regional-scale rupture width presented in panel (d)

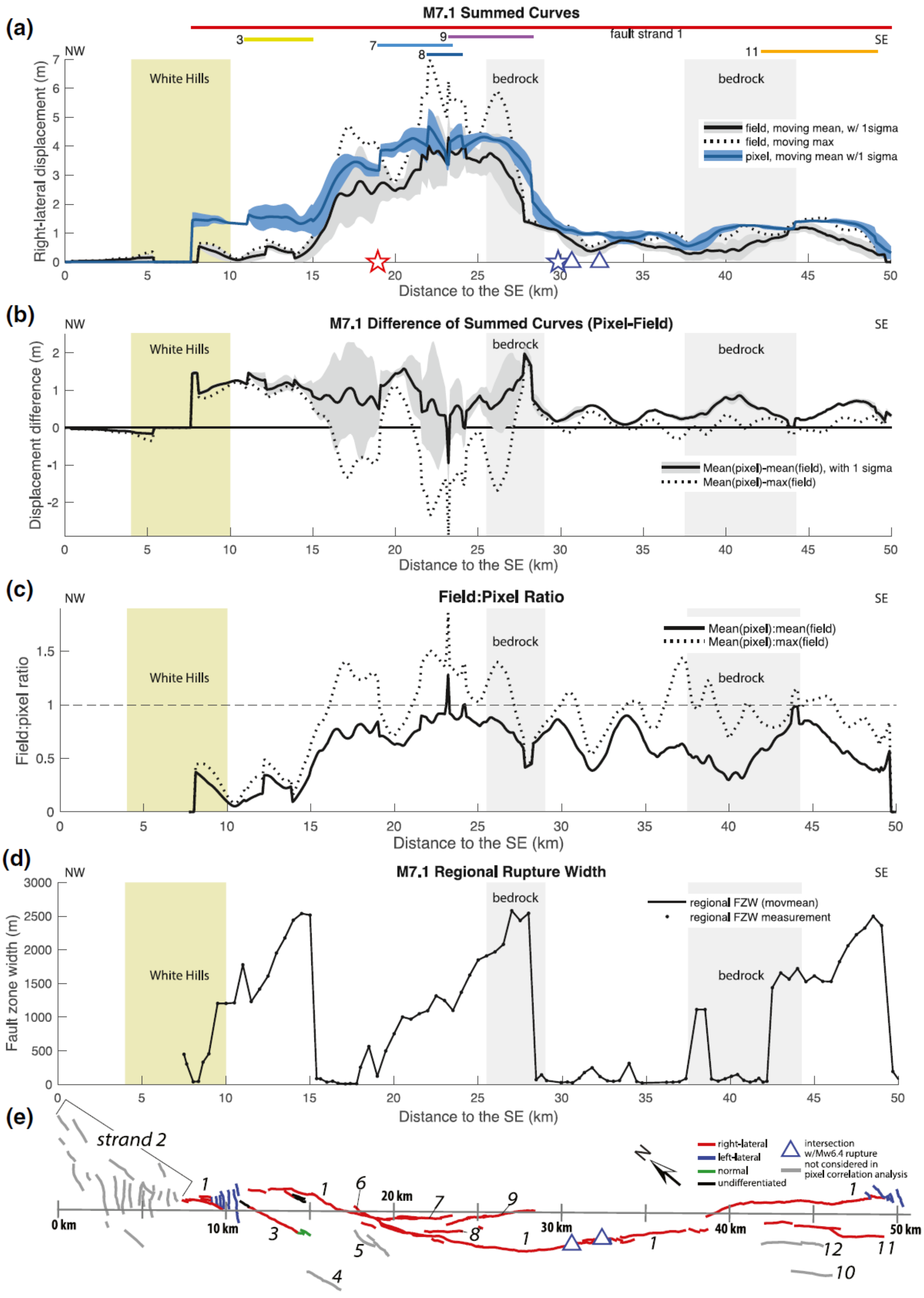

(a)
M7.1 Summed Curves
fault strand 1
3
9
7
8
11
NW
SE
White Hills
bedrock
bedrock
Right-lateral displacement (m)
field, moving mean, w/ 1sigma
field, moving max
pixel, moving mean w/1 sigma
Distance to the SE (km)
(b)
M7.1 Difference of Summed Curves (Pixel-Field)
Displacement difference (m)
Mean(pixel)-mean(field), with 1 sigma
Mean(pixel)-max(field)
Distance to the SE (km)
(c)
Field:Pixel Ratio
Field:pixel ratio
Mean(pixel):mean(field)
Mean(pixel):max(field)
Distance to the SE (km)
(d)
M7.1 Regional Rupture Width
Fault zone width (m)
regional FZW (movmean)
regional FZW measurement
Distance to the SE (km)
(e)
strand 2
0 km
10 km
20 km
30 km
40 km
50 km
right-lateral
left-lateral
normal
undifferentiated
intersection w/Mw6.4 rupture
not considered in pixel correlation analysis
N
1
3
4
5
6
7
8
9
10
11
12

Day 1 Stop 4: M7.1 & CA 178

Discussion (A) Timing and Kinematics of Orthogonal Faulting During the 2019 Mw 6.4 and Mw 7.1 Ridgecrest Earthquake Sequence

Stop 4: Intersection between secondary surface rupture of Mw 6.4 and primary rupture of Mw 7.1

Stop Location: 35.641592°N, -117.472533°W

Field Stop Leader: Chris Milliner, RMS Moody's, Caltech.

Logistics

- **Access:** Park along the dirt road near the fault intersection.
- **Goals of Stop:**
    - Examine an intersection between two fault systems that ruptured during the 2019 Ridgecrest earthquake sequence.
    - Discuss the timing and kinematics of orthogonal fault ruptures, with a focus on how a **NE-trending secondary fault** (ruptured during the Mw 6.4 foreshock) intersects a **NW-trending primary fault strand** (ruptured during the Mw 7.1 mainshock). This stop is the closest analogy to the main intersection (located ~5 km to the NE on the Navy base) that involved both primary strands that ruptured during the foreshock and mainshock events.
    - Discuss highly unusual distributed retrograde slipping faults – the first ever observed structures.

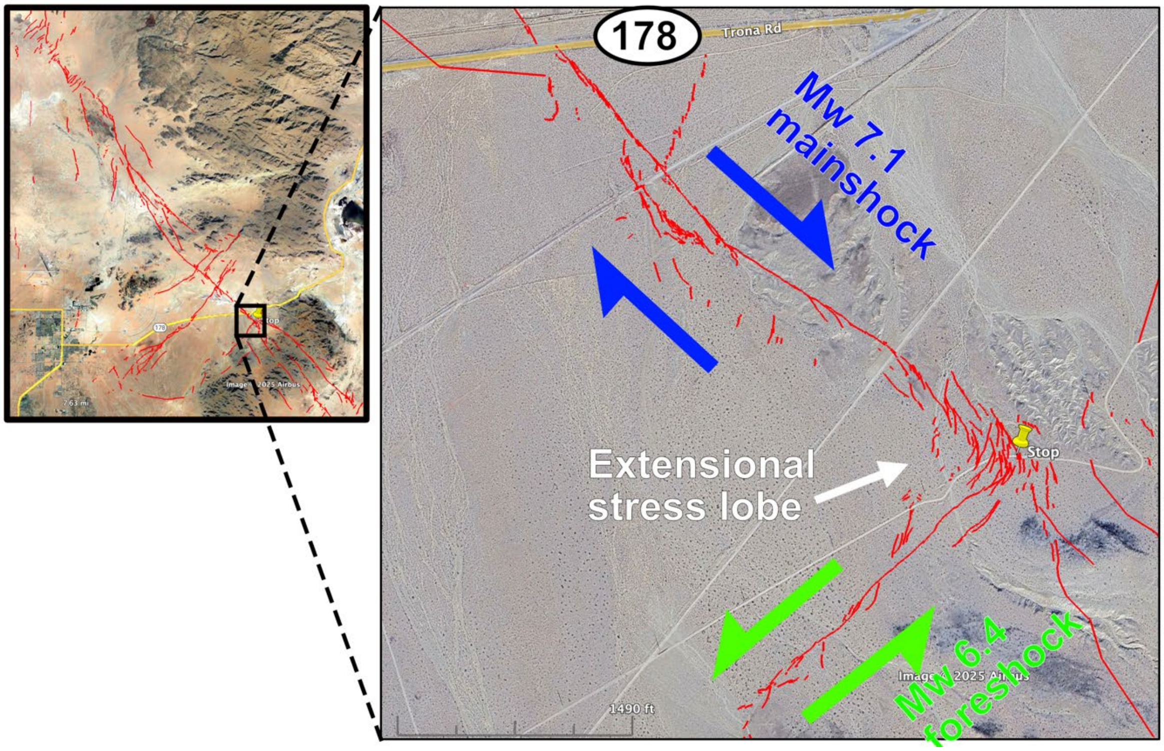

Fig. 1-4A-1. Google Earth map showing location of stop (yellow pin) at site of intersection between a **secondary** NE-trending strand of the Mw 6.4 foreshock (sense of shear illustrated by green arrows) and the **primary** NW-trending Mw 7.1 mainshock rupture (sense of shear shown by blue arrows). Note ~300m wide region of distributed faulting on NW quadrant of intersection where large extensional stresses are expected. This stop is ~5 km SE from the main intersection between both **primary** strands that ruptured during the Mw 6.4 and Mw 7.1 events.

Discussion Point 1: Which Faults Ruptured When?

In the hours following the foreshock, multiple teams surveyed the surface rupture in the field and from the air. However, with the mainshock occurring only ~34 hours later, this made it difficult to understand which faults ruptured when and specifically whether faults that initially ruptured during the Mw 6.4 foreshock later re-ruptured during the mainshock, or vice-versa if faults involved in the Mw 7.1 mainshock also partook in the foreshock. Optical images from the Planet satellite constellation that had daily acquisition were able to help separate which faults ruptured when, either during the foreshock and/or mainshock (Milliner & Donnellan 2020). Differencing of satellite images that bracketed each earthquake could highlight regions of surface rupture (Fig. 1-4A-2). However, this analysis found no clear evidence at the surface of faults (those with slip exceeding 10 cm) that initially ruptured during the foreshock later re-ruptured during the mainshock. In addition, there was also no clear evidence at the surface that faults that ruptured during the mainshock had already experienced prior rupture during the M_w 6.4 foreshock. Nevertheless, photography from a helicopter survey immediately after the Mw 6.4 foreshock may have seen some evidence of minor surface fracturing along NW-trending faults that later ruptured in the Mw 7.1 mainshock.

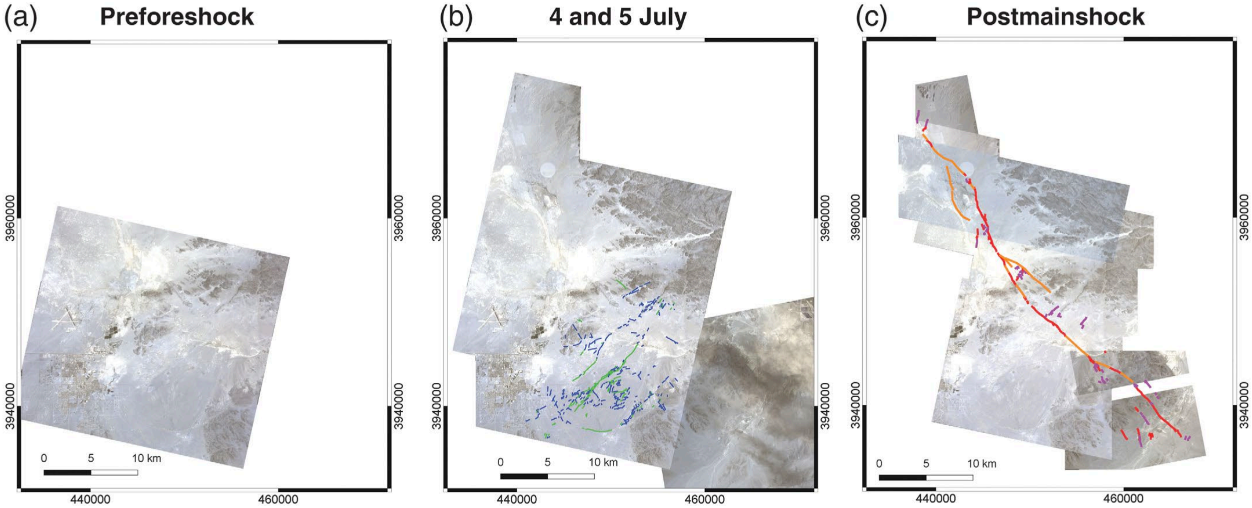

Fig. 1-4A-2. Overview optical satellite imagery from Planet Labs that bracket the July 4th Mw 6.4 foreshock and July 5th Mw 7.1 mainshock (Milliner et al., 2020). Images were acquired (a) before the foreshock, (b) after the Mw 6.4 foreshock and before the Mw 7.1 mainshock, and (c) after the 7.1 mainshock. (b) Fault mapping interpretations shown as green and blue lines that are traces mapped with high and low confidence, respectively. (c) Red, purple, and orange traces indicate fractures mapped with high and low confidence, and those mapped from the optical correlation dataset

Analysis of these satellite images revealed clear differences in the surface rupture geometrical complexity between the two earthquakes (see Fig. 1-4A-2 and -3). The Mw 6.4 foreshock produced a far greater degree of fault rupture complexity than the Mw 7.1 mainshock. This is thought to reflect differences in fault maturity, with the foreshock faults being less mature and thus more geometrically segmented. However, these differences in fault geometrical complexity could also be a function of the rupture dynamics, stress heterogeneity, and variations in ground shaking.

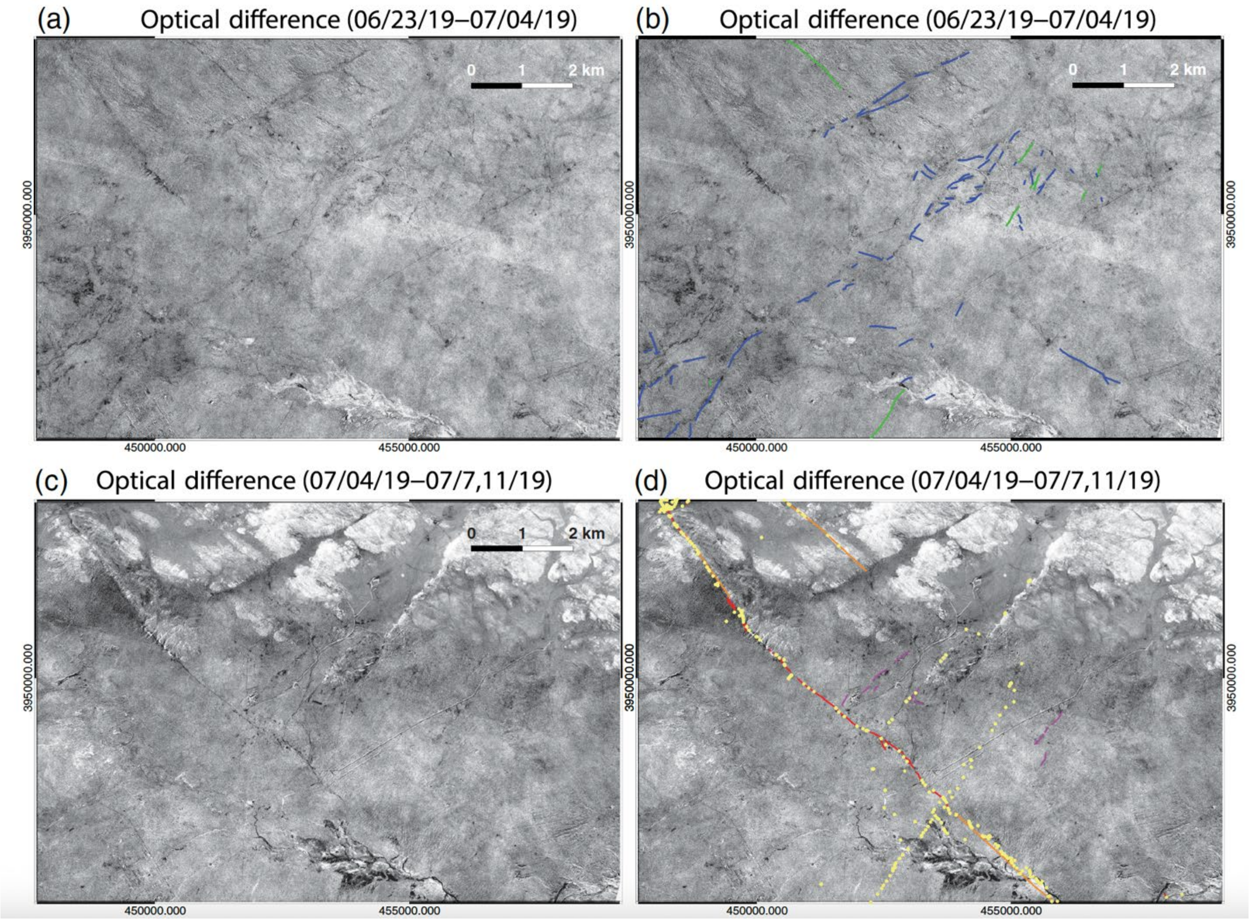

Fig. 1-4A-3. Sequence of surface fracturing captured during the (a,b) foreshock, and (c,d) mainshock, around the area of the fault intersection (see scale in top right of each plot). (a,b) Difference maps from Planet satellite images spanning just the foreshock (Milliner et al., 2020). (b) Mapping interpretation of fractures, green and blue lines indicate traces that are of high and low confidence, respectively, value ranges are normalized differences and range from 0 to 1. (c,d) Difference maps from images spanning just the mainshock with (d) showing mapping interpretations with red, purple, and orange colors indicating fractures mapped with high and low confidence, and those mapped from the optical correlation dataset (Fig. -3b), respectively. Yellow dots are observation points from field surveys of Kendrick et al. (2019).

Discussion Point 2: Kinematic Explanation for Pervasive Orthogonal Faulting

A striking feature of the Ridgecrest earthquakes is the nature of orthogonal cross-faulting. Rock experiments in the lab, show conjugate shear faults typically form at ~30° to one another as predicted by Mohr-Coulomb failure criteria, but here, orthogonal faulting is pervasive. The explanation likely lies in bookshelf kinematics, where regional dextral shear is partly accommodated by left-lateral faults striking at nearly perpendicular orientations (Fig. 1-4A-4). This behavior has been well-documented elsewhere in the Eastern California Shear Zone and in other tectonic regions (Ron et al. 1984; McKenzie & Jackson, 183; Wesnousky, 2005). Strain maps from the northern region of the Mw 7.1 rupture vividly illustrate these coseismic bookshelf kinematics in action (Fig. 1-4A-4 shows the vorticity, or regions of rotation associated with simple shear near the northern termination of the Mw 7.1 rupture ~30 km NE of here). These strain maps also provide an analogue for larger-scale bookshelf faulting, where the Little Lake fault zone (~15 km to the west of here, see Fig. 1-4A-4c) may serve as the western bounding structure. At this stop, we can interpret our position as being on the southernmost edge of one of the "books" in this deforming system, with a length and width of ~ 5×15, respectively.

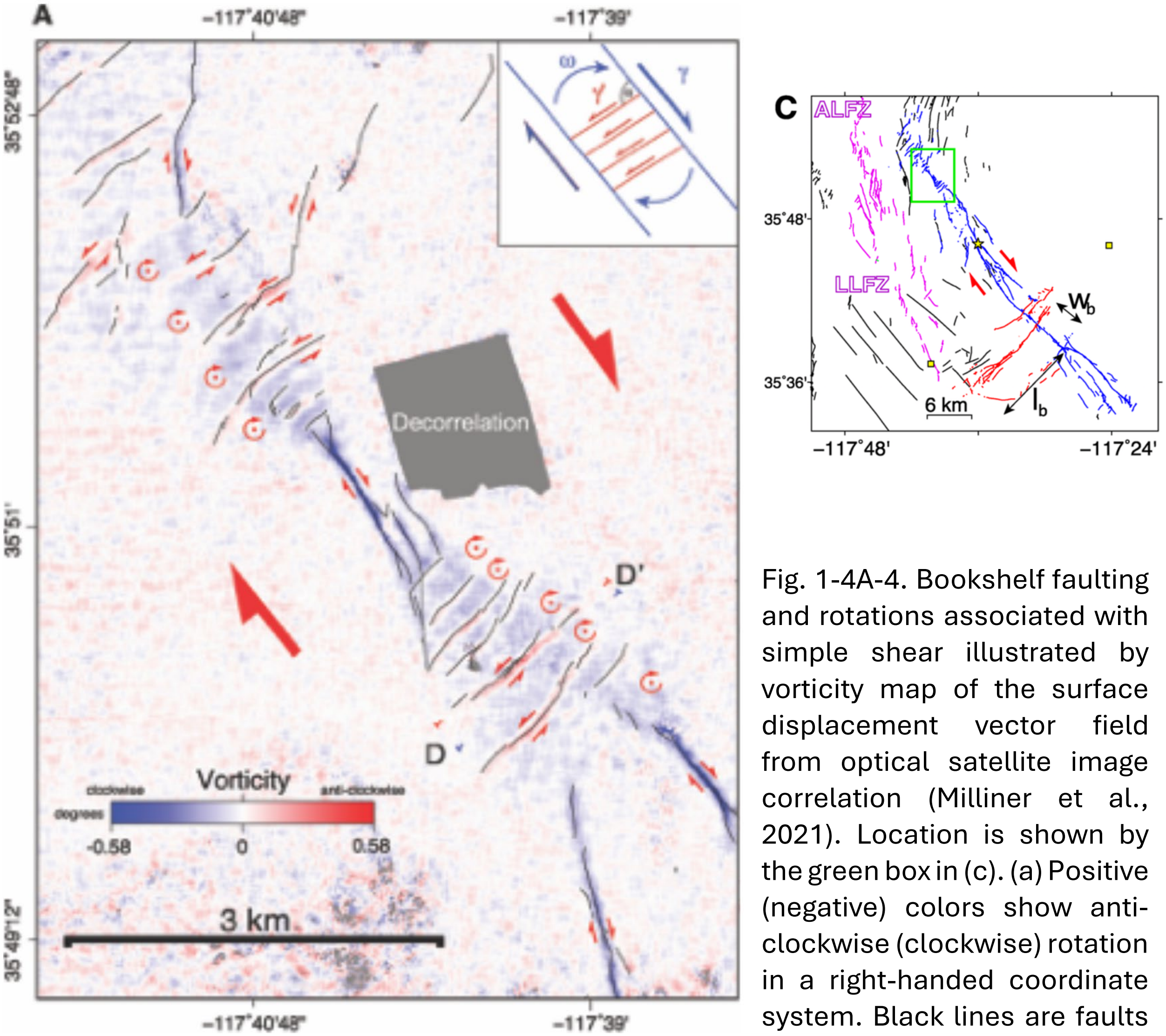

Fig. 1-4A-4. Bookshelf faulting and rotations associated with simple shear illustrated by vorticity map of the surface displacement vector field from optical satellite image correlation (Milliner et al., 2021). Location is shown by the green box in (c). (a) Positive (negative) colors show anti-clockwise (clockwise) rotation in a right-handed coordinate system. Black lines are faults mapped in the field (Ponti et al., 2019). The vorticity illustrates that strain beyond the fault tips of dextral faults transition to regions of broad rotation (red circular arrows). Inset shows schematic illustrating the kinematics of bookshelf slip model consisting of regional dextral displacement (blue lines, γ), rotation of blocks (ω), rotation of sinistral oblique fault (α), and slip on oblique faults (red, γ'), modified from Platt and Becker (2013). (c) Fault traces of the foreshock rupture (red), mainshock (blue), and Little Lake and Airport Lake fault zones (LLFZ, ALFZ, magenta), illustrating the larger scale "bookshelf" with block width (wb).

Discussion Point 3: Highly Distributed Cracking & Retrograde Slip

Radar observations provide additional insight into the distributed deformation associated with the Ridgecrest earthquakes (Xu et al., 2020). Sentinel-1 radar phase gradient maps captured fascinating prograde and retrograde (sense of slip that is reverse from that expected by the prevailing tectonic stress regime) faulting across the region, representing some of the first such observations during a major surface rupture (Fig. 1-4A-5). For instance, several NE-trending secondary faults that were ~5 km from the primary strand and parallel to the Mw 6.4 left-lateral rupture slipped dextrally. These highly distributed cracks were located between 0.5-18 km away from the primary rupture strand with lengths up to 8 km, yet with displacements typically only on the order of millimeters to centimeters. Many (but not all) of these hairline cracks were ground-truthed in the field.

The presence of these highly distributed retrograde slipping cracks raises new questions about what features should be prioritized during field mapping. The key issue is whether such cracks are integral parts of the main rupture zone, or whether they are remotely triggered, far-field responses to stress imposed by the main rupture. Determining the sense of slip along these narrow cracks is particularly difficult, as offset piercing points are rarely preserved. Instead, slip sense was typically inferred from micro-stepovers and the presence of small transpressional pop-ups or transtensional releasing structures (see Fig. 6d).

One explanation proposed by Xu et al. (2020, Science) for the occurrence of these far-field, small retrograde slipping distributed faults are static stress changes imposed by rupture from the fault primary strands. Note that the satellite radar phase gradient mapping is sensitive to motion only in the look direction and therefore may have missed fractures with an orientation and/or sense of slip that is close to orthogonal. Ultra-high resolution drone imagery collected over wider regions and extensive field mapping would be one way to more fully understand the spatial distribution, fracture density and sense of slip of these highly distributed retrograde cracks.

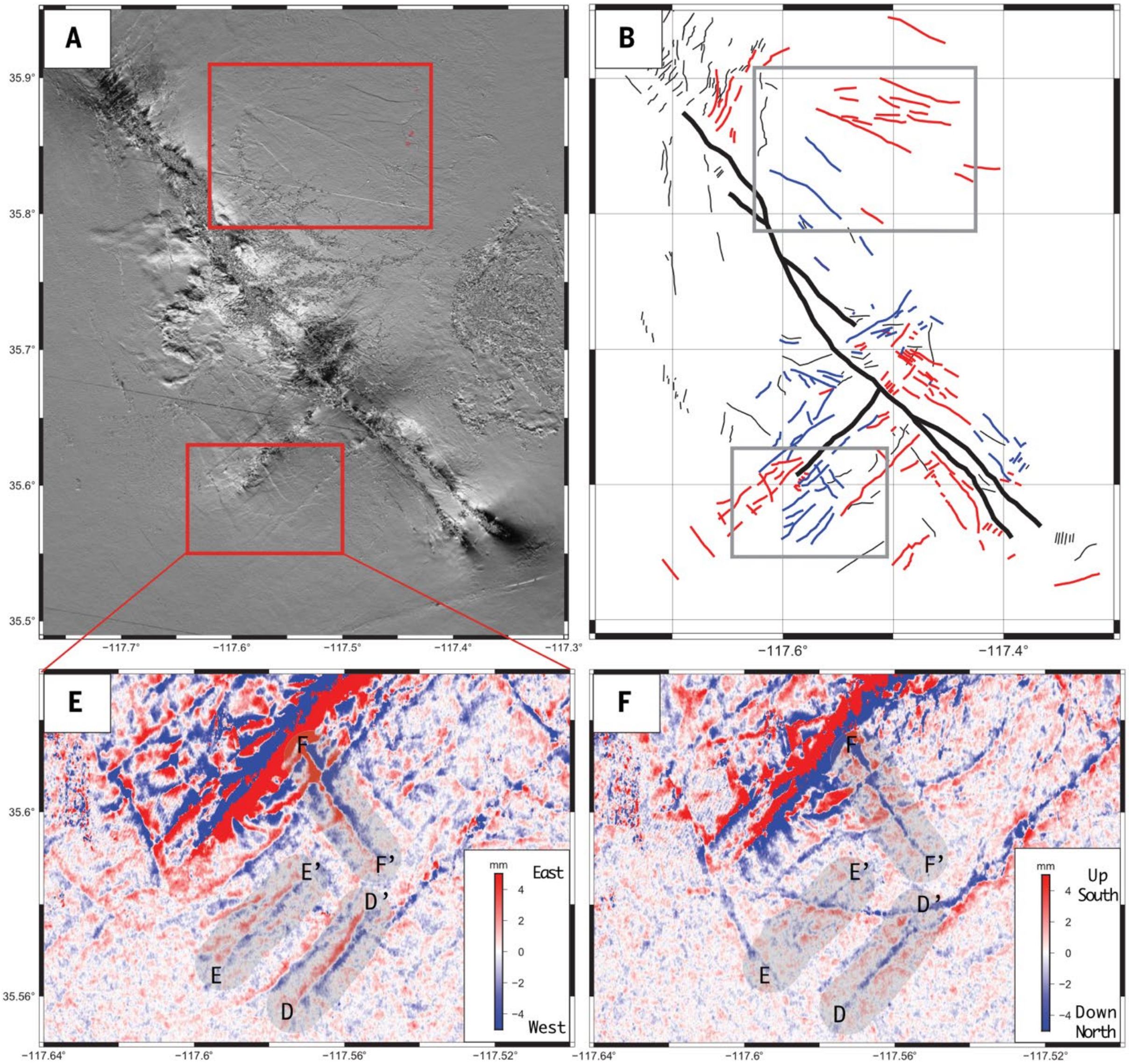

Fig. 1-4A-5. Observations of fractures nearby the Ridgecrest earthquake sequence revealed by Sentinel-1 radar interferometry (Xu et al., 2020). A) Phase gradient map from stacked Sentinel-1 interferograms revealing ~300 surface fractures around the Ridgecrest earthquake sequence region (13). (B) These fractures have been classified as prograde (red, 109 fractures), retrograde (blue, 60 fractures), and undetermined (black, 122 fractures) based on high-pass filtered (800 m) and decomposed (13) LOS deformation maps (upper and lower rows). (E and F) The south quadrant near the Mw 6.4 rupture has several right-lateral (retrograde) fractures (D-D' and E-E') as well as left-lateral (retrograde) fractures (F-F'). Both sets are in an area of negative Coulomb stress based on the respective fault orientations. Many of the fractures (D-D' and F-F') have prominent downward vertical signatures resulting from extensional stress.

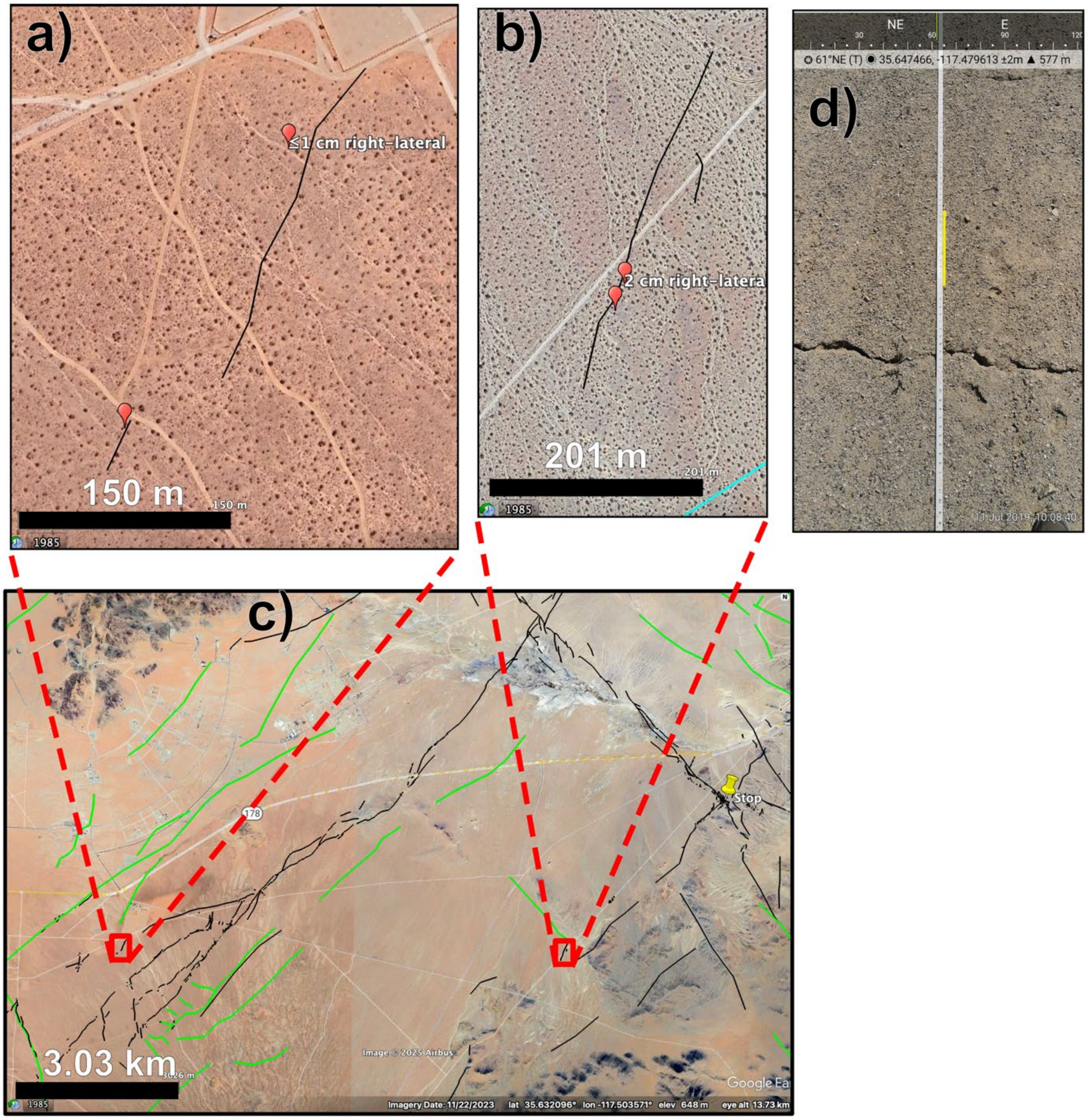

Fig. 1-4A-6. Examples of distributed cracking measured in the field. A) and b) show the locations of where possible retrograde slip was measured in the field. However, some of these structures could be 'prograde' slip occurring along conjugate faults. C) shows location of a) and b) which are right-lateral ruptures sub-parallel to trend of Mw 6.4 left-lateral rupture. Green lines in c) show faults with right-lateral slip from mapping using phase gradients of Xu et al. (2020), which are mostly retrograde with respect to left-lateral Mw 6.4 rupture. d) shows hairline surface fracture along the Mw 7.1 mainshock with right-lateral prograde motion from Goulet et al. (2021).

References

Goulet CA, Wang Y, Nweke CC, Tang BX, Wang P, Hudson KS, Ahdi SK, Meng X, Hudson MB, Donnellan A, Lyzenga GA (2021). Comparison of near-fault displacement interpretations from field and aerial data for the M 6.5 and 7.1 ridgecrest earthquake sequence ruptures. Bulletin of the Seismological Society of America. 2021 Oct 1;111(5):2317-33.

Kendrick, K. J., S. O. Akciz, S. J. Angster, J. Avouac, J. L. Bachhuber, S. E. Bennett, K. Blake, S. Bork, B. A. Brooks, P. Burgess, et al. (2019). Geologic observations of surface fault rupture associated with the Ridgecrest M6.4 and M7.1 earthquake sequence by the Ridgecrest rupture mapping group, Poster Presentation at 2019 SCEC Annual Meeting, Palm Springs, California, 8–11 September 2019.

Milliner, C., Donnellan, A., Aati, S., Avouac, J., Zinke, R., Dolan, J. F., et al. (2021). Bookshelf kinematics and the effect of dilatation on fault zone inelastic deformation: Examples from optical image correlation measurements of the 2019 Ridgecrest earthquake sequence. Journal of Geophysical Research: Solid Earth, 126(3), e2020JB020551. https://doi.org/10.1029/2020JB020551

Milliner, C., & Donnellan, A. (2020). Using Daily Observations from Planet Labs Satellite Imagery to Separate the Surface Deformation between the 4 July Mw 6.4 Foreshock and 5 July Mw 7.1 Mainshock during the 2019 Ridgecrest Earthquake Sequence. Seismological Research Letters, 91(4), 1986–1997. https://doi.org/10.1785/0220190271

McKenzie, D., & Jackson, J. (1983). The relationship between strain rates, crustal thickening, palaeomagnetism, finite strain and fault movements within a deforming zone. Earth and Planetary Science Letters, 65, 182–202. https://doi.org/10.1016/0012-821X(83)90198-X

Platt, J. P., & Becker, T. W. (2013). Kinematics of rotating panels of E–W faults in the San Andreas system: What can we tell from geodesy? Geophysical Journal International, 194, 1295–1301. https://doi.org/10.1093/gji/ggt189

Ponti, D. J., Blair, J. L., Rosa, C. M., Thomas, K., Pickering, A. J., Morelan, A., et al. (2019). Digital datasets documenting surface fault rupture and ground deformation features produced by the Ridgecrest M6.4 and M7.1 earthquake sequence of July 4 and 5, 2019: US Geological Survey Data Release. https://doi.org/10.5066/P9BZ5IJ9

Ron, H., Freund, R., Garfunkel, Z., & Nur, A. (1984). Block rotation by strike-slip faulting: Structural and paleomagnetic evidence. Journal of Geophysical Research, 89, 6256–6270. https://doi.org/10.1029/JB089iB07p06256

Wesnousky, S. G. (2005). The San Andreas and Walker Lane fault systems, western North America: Transpression, transtension, cumulative slip and the structural evolution of a major transform plate boundary. Journal of Structural Geology, 27, 1505–1512. https://doi. org/10.1016/j.jsg.2005.01.015

Xu, X., Sandwell, D. T., & Smith-Konter, B. (2020). Coseismic displacements and surface fractures from Sentinel-1 InSAR: 2019 Ridgecrest earthquakes. Seismological Research Letters. 91(4), 1979–1985. https://doi.org/10.1785/0220190275

Xu X, Sandwell DT, Ward LA, Milliner CW, Smith-Konter BR, Fang P, Bock Y. (2020) Surface deformation associated with fractures near the 2019 Ridgecrest earthquake sequence. Science. 370(6516):605-8. DOI: 10.1126/science.adu9116

Discussion (B) Mw 7.1 Rupture – Tracking Postseismic Surface Rupture Evolution with High Resolution Smartphone LiDAR

Zachary Smith, UC Berkeley

The 2019 Ridgecrest earthquake sequence began with a magnitude 6.4 earthquake on July 4, 2019, followed 34 hours later by a significantly larger magnitude 7.1 earthquake on July 5 (Ross et al., 2019). The Ridgecrest ruptured a distributed fault network resulting in numerous surface ruptures (Pierce et al., 2020; Ponti et al., 2020; Xu et al., 2020; Rodriguez Padilla et al., 2022 a-b). At this stop we will be viewing the surface rupture of the Mw 7.1 earthquake. The scarp exhibits up to 0.3 m of vertical offset. Further to the south the rupture begins to bifurcate. At the intersection of the bifurcation, ruptures are distributed over a 1-2 km wide zone (Ponti et al., 2020). Large fissures that opened during the earthquake have yet to fill and still continue to capture small drainages.

Since the 2019 Ridgecrest rupture, there have been major precipitation events (Figure 1-4B-1) that have rapidly altered the morphology of the surface ruptures. To quantify this evolution, we track fissures using high resolution repeat iPhone LiDAR and imaging (Figure 1-4B-2) with real-time kinematic corrections allowing for ~1-2 cm horizontal and vertical accuracy positioning. We tracked the post-seismic evolution of a fissure just to the south between 2023-2025 (Figure 1-4B-2). The years of 2023-2024 experienced unusually large amounts of precipitation during the winter months causing the fissures to evolve rapidly. Our analysis unfortunately does not cover this time period, but we were able to track changes during the following year. Preliminary results suggest an exponential relationship between absolute surface change and cumulative precipitation for the fissure we tracked.

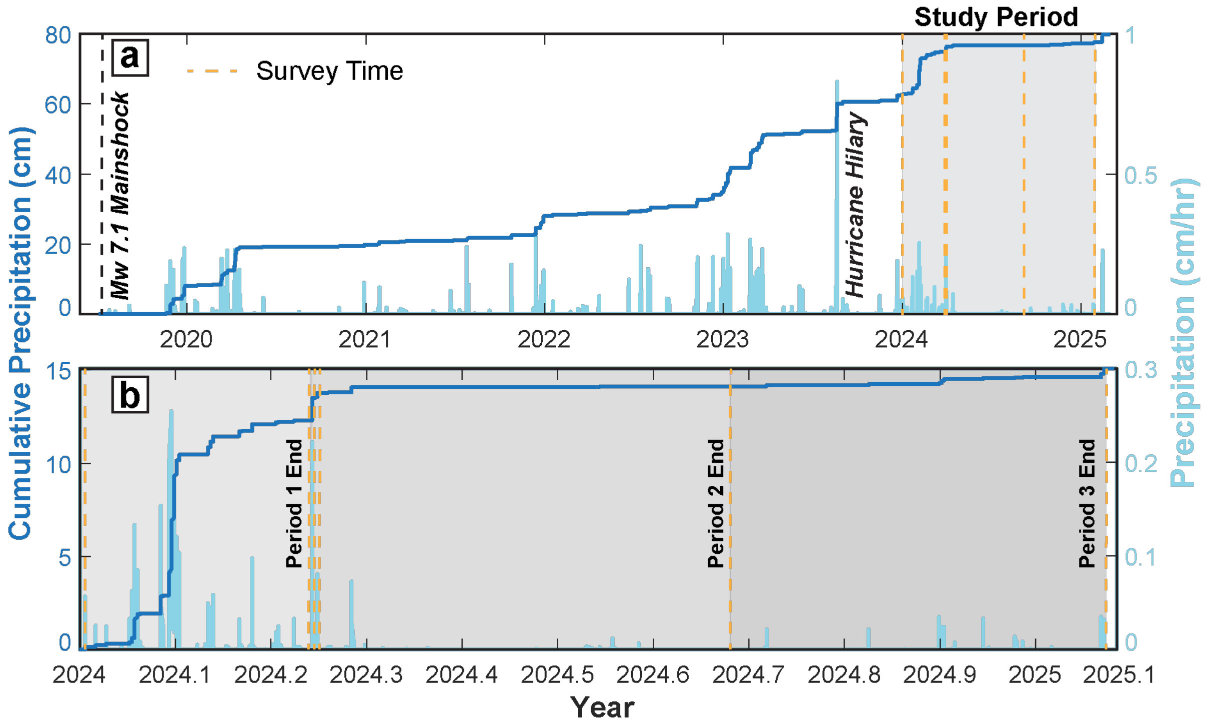

Figure 1-4B-1. Precipitation since the 2019 Ridgecrest earthquake as predicted by ERA-5 weather model. Yellow lines represent survey times and we focus on three time periods. (Smith et al., in prep).

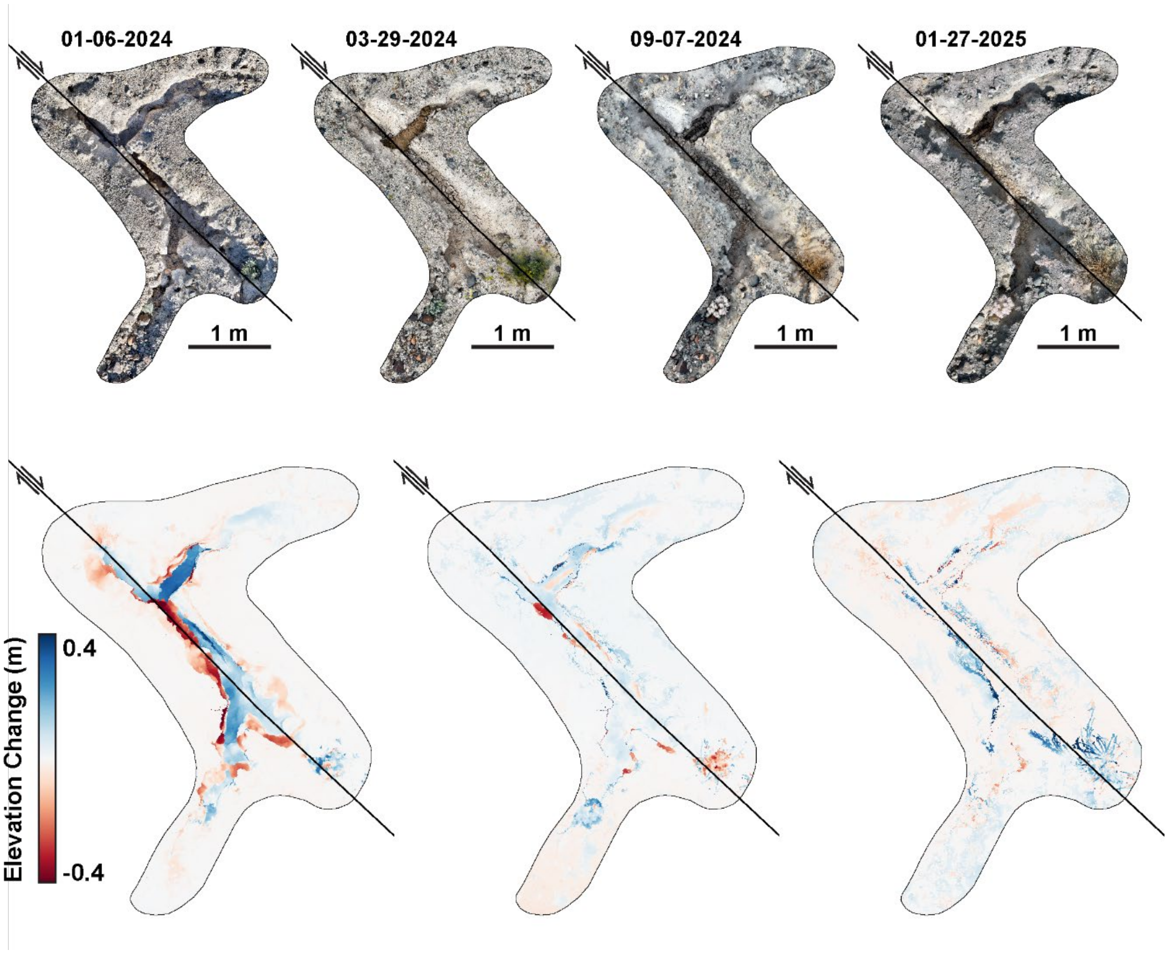

Figure 1-4B-2. Orthophotos and elevation change maps from iPhone imagery and LiDAR using RTK corrections for a fissure along the Mw 7.1 earthquake rupture.(Smith et al., in prep).

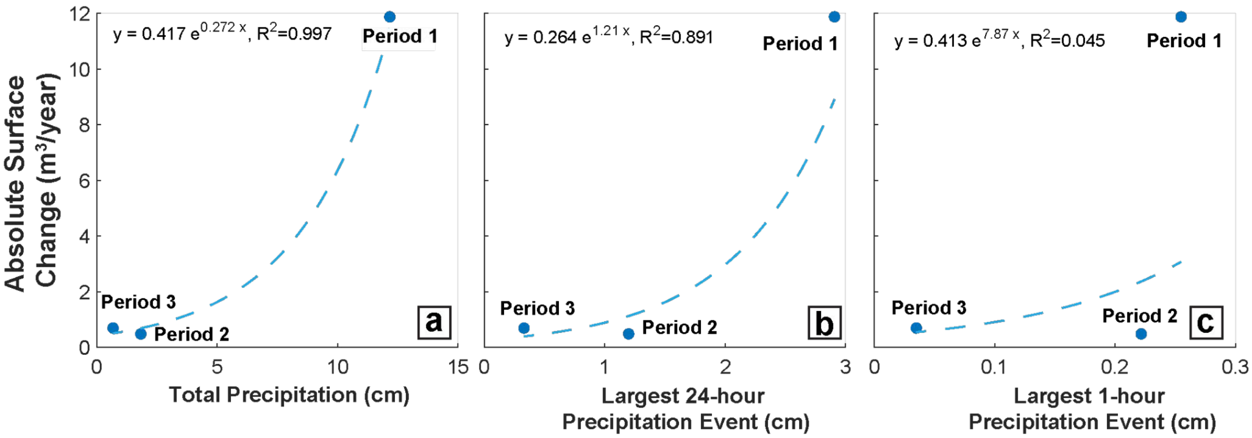

Figure 1-4B-3. Absolute surface change compared to (A) total precipitation during preceding interval, (B) largest 24-hour precipitation event, and (C) largest 1-hour precipitation event per time interval. (Smith et al., in prep).

References Cited

Pierce, I., Williams, A., Koehler, R. D., & Chupik, C. (2020). High-resolution structure-from-motion models and orthophotos of the southern sections of the 2019 M w 7.1 and 6.4 Ridgecrest earthquakes surface ruptures. Seismological Research Letters, 91(4), 2124-2126.

Ponti, D. J., Blair, J. L., Rosa, C. M., Thomas, K., Pickering, A. J., Akciz, S., ... & Zinke, R. (2020). Documentation of surface fault rupture and ground-deformation features produced by the 4 and 5 July 2019 Mw 6.4 and Mw 7.1 Ridgecrest earthquake sequence. Seismological Research Letters, 91(5), 2942-2959.

Rodriguez Padilla, A. M., Quintana, M. A., Prado, R. M., Aguilar, B. J., Shea, T. A., Oskin, M. E., & Garcia, L. (2022). Near-field high-resolution maps of the Ridgecrest earthquakes from aerial imagery. Seismological Society of America, 93(1), 494-499.

Rodriguez Padilla, A. M., Oskin, M. E., Milliner, C. W., & Plesch, A. (2022). Accrual of widespread rock damage from the 2019 Ridgecrest earthquakes. Nature Geoscience, 15(3), 222-226

Ross, Z. E., Idini, B., Jia, Z., Stephenson, O. L., Zhong, M., Wang, X., ... & Jung, J. (2019). Hierarchical interlocked orthogonal faulting in the 2019 Ridgecrest earthquake sequence. Science, 366(6463), 346-351.

Xu, X., Sandwell, D. T., Ward, L. A., Milliner, C. W., Smith-Konter, B. R., Fang, P., & Bock, Y. (2020). Surface deformation associated with fractures near the 2019 Ridgecrest earthquake sequence. Science, 370(6516), 605-608.

Discussion (C) Rapid post-earthquake reconnaissance and paleoseismic trenching results for the M7.1 Ridgecrest earthquake

Stop leaders: Özgür “Oz” Kozacı, Pacific Gas & Electric Company (PG&E), Christopher Madugo (PG&E)

Note: For background and references, see writeup for stop 1-3D

M7.1 rupture - mapping

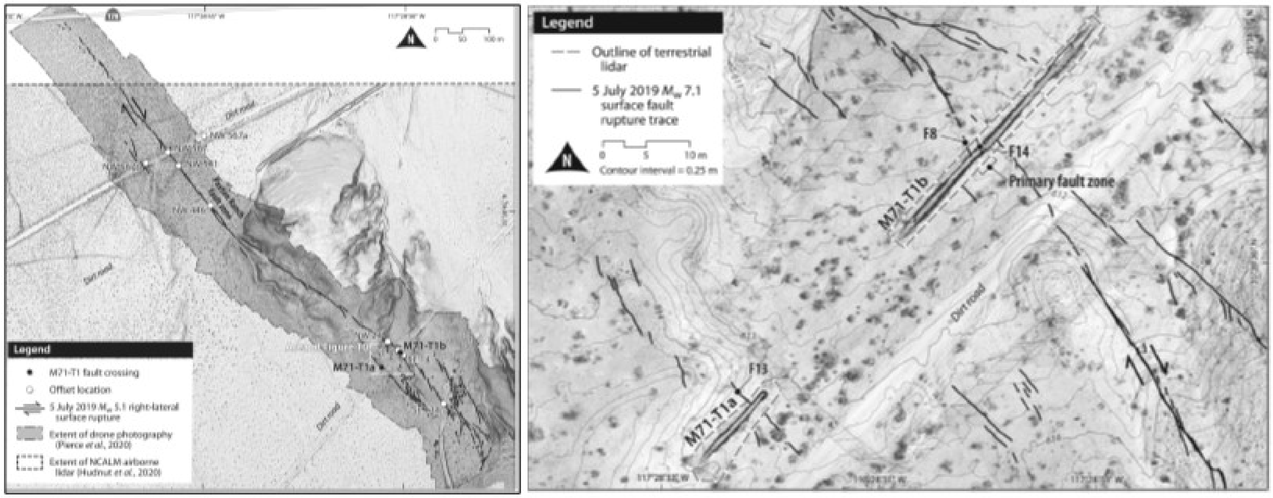

- At this stop we highlight findings from the rapid post-earthquake assessment to characterize rupture location, complexity, displacement and timing of past earthquakes by PG&E Geosciences and InfraTerra where the M7.1 fault rupture crossed a second PG&E gas transmission line. We took the same approach documenting the M7.1 rupture at local to sit-specific scale as for the M6.4 rupture (see stop 1-3D)
- The map on the left shows our mapping from highway 178, southeast through the pipeline crossing site and further southeast, where the rupture gets very complex
- The map on the right shows detailed fault rupture mapping based on the fused drone-based imagery and terrestrial lidar survey of the pipeline trench site
- As at the M6.4 pipeline fault crossing, the M7.1 pipeline fault crossing did not have any leaks

Public

M7.1 rupture – displacement measurements

1m DEM

Drone Imagery
(*Pierce et al., 2020*)

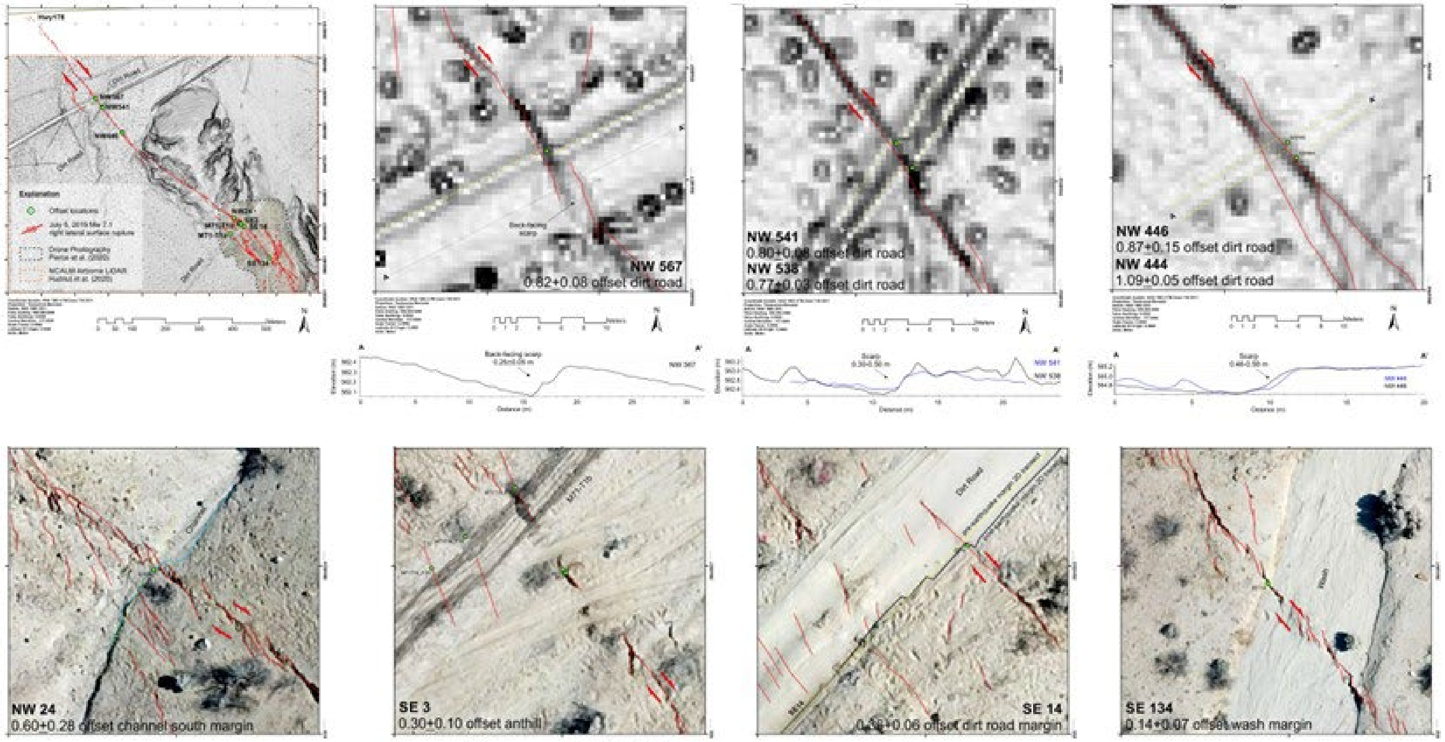

(*Kozacı et al., 2021*)

- We mapped both linear and point offset features such as dirt road margins, channels, wash margins and even an offset ant hill
- The grayscale maps in the upper row above have 1 m resolution DEM basemaps and still provided useful offset measurements based on dirt road margins
- The color imagery in the lower row was acquired by Pierce et al., 2020 drone survey
- The resolution difference provided a great opportunity for comparing mappability of various features at different resolutions

M7.1 rupture – cumulative displacement and along-strike variation

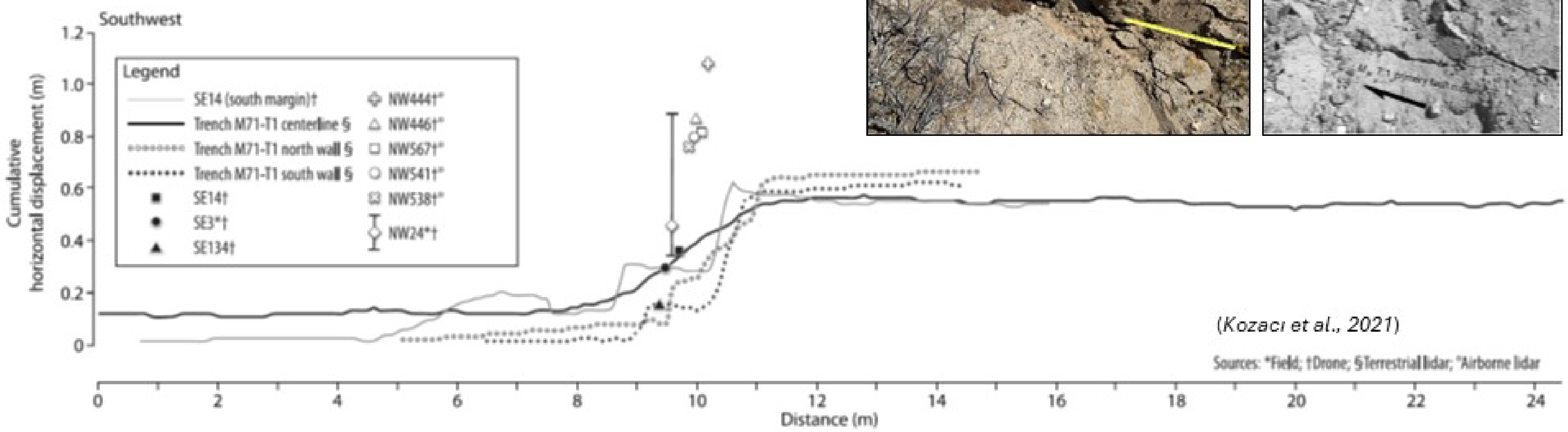

(*Kozacı et al., 2021*)

Sources: *Field; †Drone; §Terrestrial lidar; "Airborne lidar

- The lower plot shows cumulative horizontal displacement values across the fault zone on the horizontal axis. Features are coded for distance northwest and southeast of the pipeline trench
- For example, the color photo above shows the right laterally offset ant hill flank 3 m southeast of the trench (SE3) and the black and white photo shows a small offset channel 24 m northwest of the pipeline (NW24)
- Offset measurements of point features northwest of the pipeline are higher than linear features in the vicinity of the pipeline, such as pipeline trench walls and road southeast line, which have displacements less than half the maximum displacement documented near the M6.4 site. We believe this may represent a steep structurally controlled southeast slip gradient from the northwest to the southeast, toward a structural complexity south of the pipeline
- A striking observation is that even though the rupture zone is relatively wide, the majority of deformation is concentrated to within only a few meters, similar to finiings at the M6.4 pipeline fault crossing location

Public

M7.1 rupture - trenching

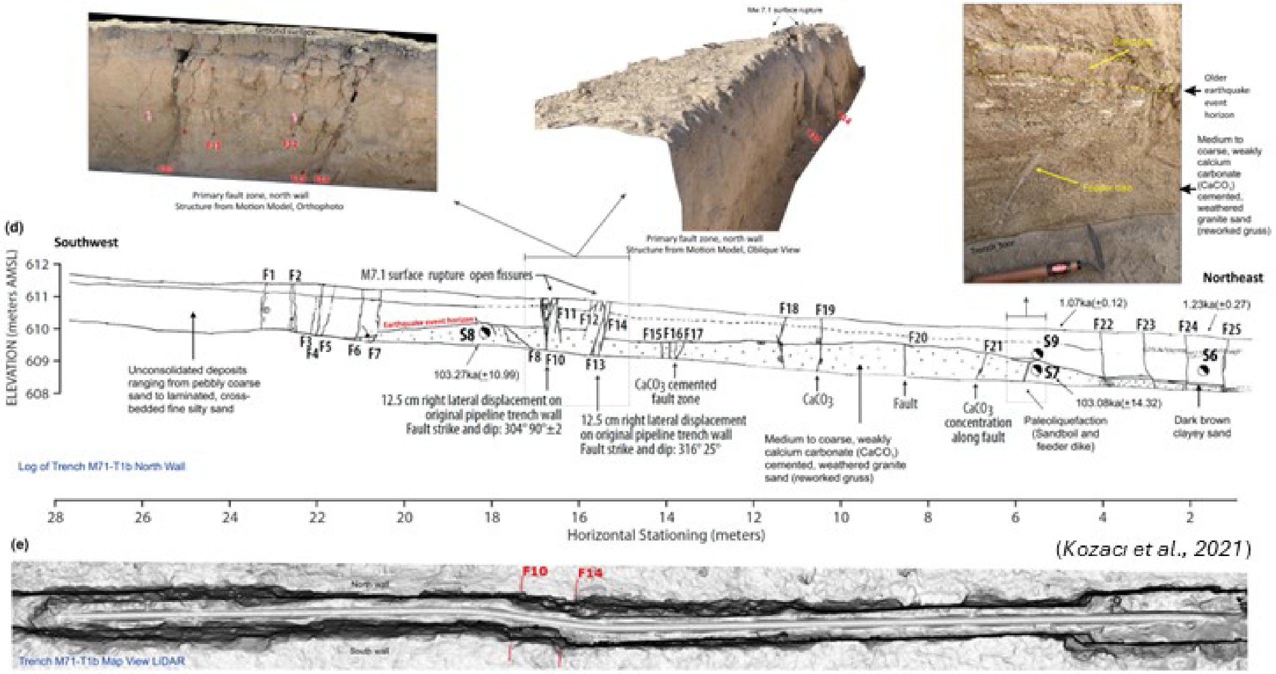

(*Kozacı et al., 2021*)

- As at the M6.4 site, PG&E used the dry-vacuum method to expose the pipeline across the fault zone at the magnitude 7.1 rupture pipeline crossing
- The lower figure is the terrestrial lidar scan of the trench exposure showing the right lateral deformation
- The middle figure is the log of this trench showing the details of splays across the fault zone
- The log and lidar scan highlight the finding of the cumulative displacement plot on the previous page - though the fault zone at this location is approximately 25 meters wide, the primary fault zone with the majority of deformation is only 2-3 meters wide
- The upper left photo shows the primary fault zone in the trench and the upper middle photo is a structure from motion 3D construction of the trench wall with an oblique view showing the discrete offsets of the original pipeline construction trench wall
- We documented an older earthquake horizon in this trench as evidenced by upward fault truncations and a buried paleliquefaction feature
- Unfortunately, OSL dating results did not allow us to narrowly constrain the timing this older event. The results indicate that this event is older than a thousand years and younger than approximately 103 thousand years due to the erosional nature and missing stratigraphic record at this horizon
- Nevertheless, this trench showed that this fault zone also previously ruptured at the same location at least once prior to 2019

Day 2 Stop 1: Railroad Cut Splay Fault Outcrop

Discussion (A) Long term reactivation of preexisting structures

Zachary Smith, UC Berkeley

The Mw 7.1 and 6.4 ruptures occurred across a broad zone of nearly orthogonal faults. Multiple mechanisms have been suggested to explain the orthogonal orientation of faults that ruptured during the 2019 Ridgecrest earthquake sequence. A simple shear mechanism proposed by Fialko and Jin (2021) suggests that the Ridgecrest faults originally formed at optimal orientations and then rotated to their current position. In contrast, Scholz and Choi (2022) argue that simultaneous rupture of high angle conjugate faults, such as those at Ridgecrest, occur because lower-crustal ductile shear is more important in controlling the orientation of large faults than the brittle upper crust. Finally, it is possible that the faults that slipped during the Ridgecrest earthquakes are extremely frictionally weak.

Nevitt et al. (2023) demonstrated that the orientation of the mainshock rupture, and its slip distribution, are likely controlled by the existence of the Independence dike swarm which extends along the southern Walker Lane and northern Eastern California Shear Zone. This analysis focused primarily on the mainshock rupture and not on the relationship between the thousands of other fault ruptures during the foreshock, mainshock, and aftershock earthquake sequences and dike orientations. Our subsequent analysis (Smith et al., in prep) has revealed the presence of both orthogonal mylonitic shear zones and dikes at the location of the foreshock and mainshock intersection. Detailed field and InSAR displacement analysis reveals that the right-lateral mainshock-parallel faults have reactivated left-lateral mylonitic shear zones and the left-lateral foreshock-parallel faults have reactivated right-lateral mylonitic shear zones (Figure 2-1A-1). Current estimates of cumulative fault displacement for the major faults are from offset dikes and geodetic analysis of bookshelf kinematics of faults activated during the 2019 Ridgecrest earthquakes (Andrew and Walker, 2020; Milliner et al., 2021). These estimates suggest that the foreshock- and mainshock-hosting faults have offsets of 256–600 m and 1600 m, respectively. However, the fact that there has been a slip reversal indicates that we may be missing a complete estimate of the cumulative displacement on the mainshock or foreshock faults as it is unclear how much slip accumulated in the opposite shear sense before the onset of the current tectonic regime.

Pseudotachylyte (Figure 2-1A-2) exhibiting right lateral shear fabrics along foreshock-parallel subsidiary faults and high-temperature mineral fracture filling (titanite and hornblende) of pulverized rock suggests that late Mesozoic to early Cenozoic earthquakes along these low cumulative displacement faults occurred close to the brittle ductile transition at temperatures between 300-700 °C and then have been exhumed. Sometime during the exhumation process, and continuing today, the faults switched to left-lateral slip. These findings show that the distributed fault system at Ridgecrest is not only the result of recent shallow fault processes.

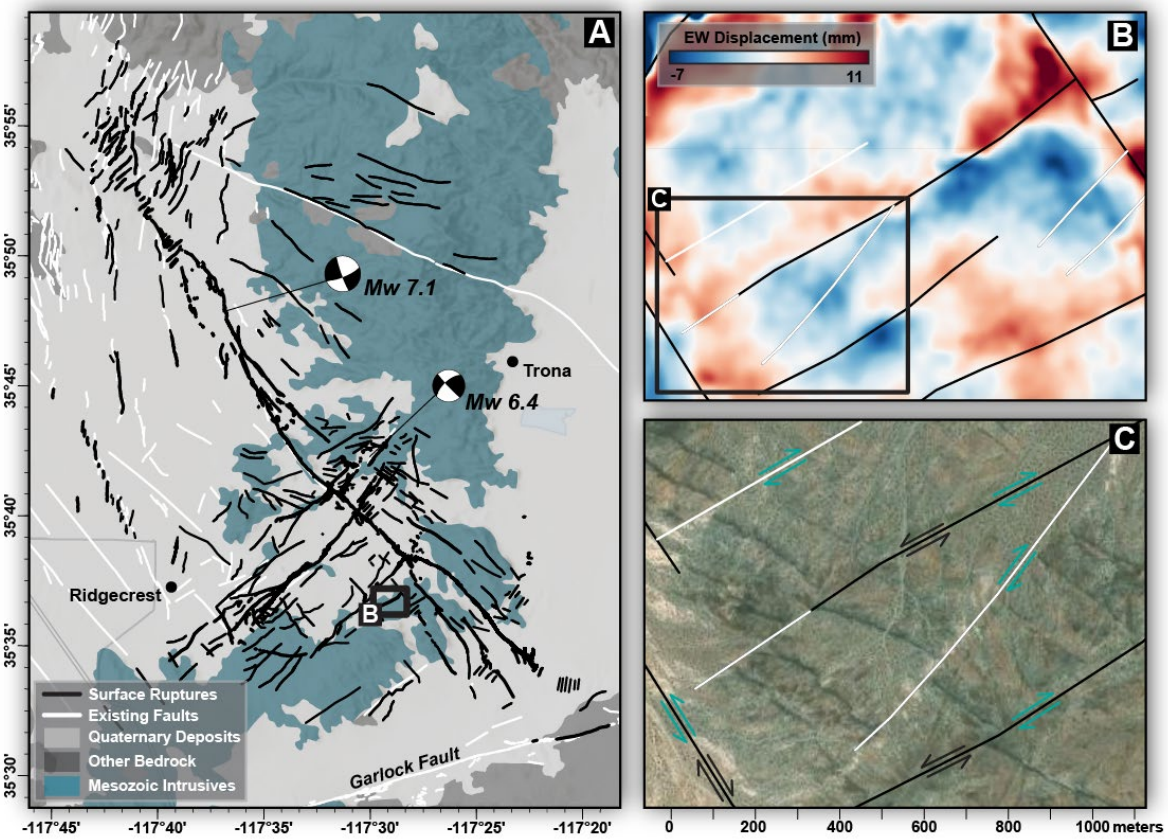

Figure 2-1A-1. (A) New fault maps generated from COSMO-Skymed InSAR. (B) Left lateral displacement along faults with right lateral cumulative offset (InSAR displacements from Xu et al., 2020). (C) Map showing sections of fault that slipped (black) during 2019 Ridgecrest earthquakes (Smith et al., in prep).

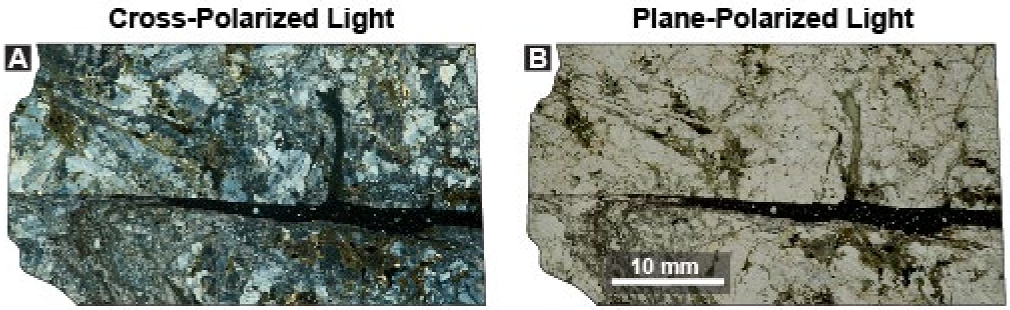

Figure 2-1A-2. Pseudotachylite along an exhumed right lateral mylonitic shear zone that has been reactivated as a left-lateral strike slip fault during the 2019 Ridgecrest earthquake ruptures (Smith et al., in prep).

References Cited

Andrew, J. E., & Walker, J. D. (2020). Total Slip Estimates of the M7.1 (July 2019) Seismogenic Airport Lake Fault System, Ridgecrest, Califor-nia, GSA meeting. Abstract: 31-4.

Fialko, Y., & Jin, Z. (2021). Simple shear origin of the cross-faults ruptured in the 2019 Ridgecrest earthquake sequence. Nature Geoscience, 14(7), 513-518.

Milliner, C., Donnellan, A., Aati, S., Avouac, J. P., Zinke, R., Dolan, J. F., ... & Bürgmann, R. (2021). Bookshelf kinematics and the effect of dilatation on fault zone inelastic deformation: Examples from optical image correlation measurements of the 2019 Ridgecrest earthquake sequence. Journal of Geophysical Research: Solid Earth, 126(3), e2020JB020551.

Nevitt, J. M., Brooks, B. A., Hardebeck, J. L., & Aagaard, B. T. (2023). 2019 M7. 1 Ridgecrest earthquake slip distribution controlled by fault geometry inherited from Independence dike swarm. Nature Communications, 14(1), 1546.

Scholz, C. H., & Choi, E. (2022). What comes first: The fault or the ductile shear zone?. Earth and Planetary Science Letters, 577, 117273.

Xu, X., Sandwell, D. T., Ward, L. A., Milliner, C. W., Smith-Konter, B. R., Fang, P., & Bock, Y. (2020). Surface deformation associated with fractures near the 2019 Ridgecrest earthquake sequence. Science, 370(6516), 605-608.

Discussion (B) Relationship of basin structure and bedrock lithology to faulting in the 2019 Ridgecrest earthquake region, California, from gravity and aeromagnetic data

V.E. Langenheim and E.K. Haddon

U.S. Geological Survey, Moffett Field, CA

We investigate patterns of cumulative offsets on the faults that ruptured in 2019 and along the Garlock Fault in the Ridgecrest region, California using recently published gravity and aeromagnetic data. We also examine the relationship of basin structure and bedrock structure to the 2019 M7.1 Ridgecrest earthquake ruptures (Fig. 2-1B-1A), which were primarily along a dextral northwest-striking fault system, and along a sinistral northeast-striking fault, which ruptured hours earlier with a M6.4 event.

New gravity and aeromagnetic data collected since 2020 shed light on patterns of fault offset north of the Garlock Fault. Although several rupture zones were mapped after the 2019 earthquakes, we limit much of our study to the main rupture zone along the northwest-striking Paxton Ranch fault (Fig. 2-1B-1A). Previous work based on gravity data (Saltus and Jachens, 1995) indicated the main rupture zone is characterized by thin basin fill except at the northwest and southeast ends of the rupture. New gravity measurements integrated with older measurements (Langenheim et al., 2025) reveal small gravity lows (amplitudes of 0.5-2 mGal) above the main northwest-trending rupture (Fig. 2-1B-1B), indicating in some cases shallow basins or undulations of the Mesozoic bedrock surface. Gravity lows above exposed Mesozoic bedrock, however, indicate lower densities caused by either fracturing or more felsic bedrock. The rupture appears to coincide with small-amplitude aeromagnetic lows (U.S. Geological Survey, 2002), which are more consistent with felsic compositions. This pattern may also apply to the 2019 M6.4 northeast-striking ruptures that are approximately parallel to the edges of a more felsic pluton defined by gravity and magnetic anomalies.

About 15 km southeast from the northwest end of the M7.1 rupture (X in Figure 2-1B-1B), a deeper pocket of basin fill is located in an apparent right step in the rupture, a possible pull-apart basin. Using the length of the basin as a proxy for long-term offset, this local gravity low indicates ~5 km of offset.   Continuing along the rupture about 15 km to the southeast, apparently offset magnetic anomalies suggest 1-2 km of cumulative offset. Continuing even farther southeast along the M7.1 rupture, the new gravity data suggest <1 km offset of the northern margin of a gravity low (Y in Figure 2-1B-1B) reflecting a basin filled with 2-3 km of Cenozoic sediments. If these estimates are valid, a long-term pattern is indicated of either northwest increasing offset away from the Garlock Fault or distributed, nascent faulting at the southeast terminus of the rupture (Paxton Ranch fault) north of the Garlock Fault.

The new gravity data also sharpen delineation of basins bounded by the sinstral Garlock Fault zone. The basin at the southeast end of the 2019 M7.1 rupture is bounded on the south by the Garlock Fault and coincides with a 10-mGal gravity gradient. This basin margin is imaged by a seismic-reflection profile (Monastero et al., 2002) but not by seismic tomography (White et al., 2021; Yang et al., 2021) although both the tomography and gravity anomalies indicate denser, high-velocity crust north of this basin. The Ridgecrest ruptures lie within this gravity high, unlike the 1992 Landers and 1999 Hector Mine earthquake ruptures located about 150 km to the southeast of the Ridgecrest events. There, the ruptures closely follow the margins of a dense, magnetic body (Langenheim and Jachens, 2002).

The position of the northern margin of the basin likely reflects an older strand of the Garlock Fault, which may adjoin mapped Quaternary fault segments to the east. The basin is ~ 30 km long. Along strike to the west, the Garlock Fault forms a transtensional left step marked by a narrow 40-km long gravity low (Z in Figure 2-1B-1B) and geomorphic trough containing Koehn Lake. This decrease in basin length to the east may result from a pattern of non-uniform cumulative sinistral offset along the Garlock Fault or offset distributed along multiple strands through time.

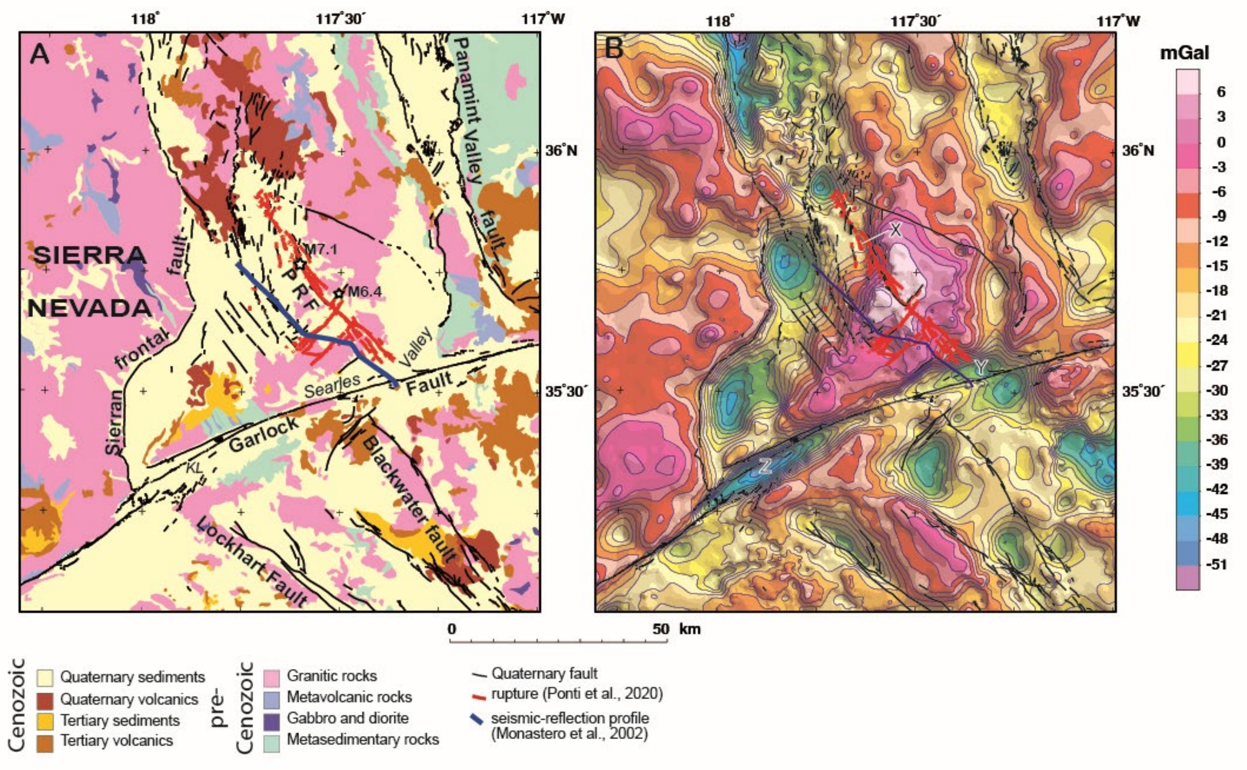

Figure 2-1B-1. A) Geologic map of study area showing location of 2019 Ridgecrest earthquake epicenters (stars) and rupture. Geology from Jennings et al. (2010). KL, Koehn Lake; PRF, Paxton Ranch fault. B) Isostatic gravity map of study area (Langenheim et al., 2025). Prominent gravity lows are associated with thick (> 1 km) Cenozoic basin fill and low-density volcanic rocks. Quaternary faults from U.S. Geological Survey (2020).

REFERENCES

Jennings. C.W., with modifications by Gutierrez, C., Bryant, W., Saucedo, G., and Wills, C., 2010, Geologic map of California: California Geological Survey Geologic Data Map No., 2, scale 1:750,000.

Langenheim, V.E., and Jachens, R.C., 2002, The Emerson Lake body: A link between the Landers and Hector Mine earthquakes, southern California, inferred from gravity and magnetic anomalies, Bulletin of the Seismological Society of America, vol.92, pp.1606-1620.

Langenheim, V.E., Anderson, J.E., Katzenstein, A.M., Morbeck, B.L., Zielinski, L.A., Haddon, E.K., Phelps, G.A., Felger, T.J., and Schermerhorn, W.D., 2025, Gravity and physical property data of the 2019 Ridgecrest earthquakes region, Mojave Desert, California: U.S. Geological Survey data release, https://doi.org/10.5066/P1VG6MPK.

Monastero, F.C., Walker, J.D., Katzenstein, A.M., and Sabin, A.E., 2002, Neogene evolution of the Indian Wells Valley, east-central California: Geological Society of America Special Paper 195, p. 199-228.

Ponti, D.J., Blair, J.L., Rosa, C.M., Thomas, K., Pickering, A.J., Dawson, T. E., compilers, 2020, Digital datasets documenting surface fault rupture and ground deformation features produced by the Ridgecrest M6.4 and M7.1 earthquake sequence of July 4 and 5, 2019: U.S. Geological Survey data release, https://doi.org/10.5066/P9BZ5IJ9.

Saltus, R.W., and Jachens, R.C., 1995, Gravity and basin-depth maps of the Basin and Range province, western United States: U.S. Geological Survey Geophysical Investigations Map GP-1012, scale 1:2,500,000, https://doi.org/10.3133/gp1012.

U.S. Geological Survey, 2002, Digital aeromagnetic datasets for the conterminous United States and Hawaii; a companion to the North American magnetic anomaly map: U.S. Geological Survey Open-File Report 2002-361, https://pubs.usgs.gov/of/2002/ofr-02-361, accessed July 20, 2019.

U.S. Geological Survey, 2020, Quaternary Fault and Fold database for the Nation, U.S. Geological Survey data release, https://doi.usgs.ogv/10.5066/P9BCVRCK, accessed February 21, 2021.

White, M., Fang. H., Catchings, R., Goldman, M., Steidl, J., Ben-Zion, Y., 2021, Detailed traveltime tomography and seismic catalog around the 2019 Mw 7.1 Ridgecrest earthquake, using dense rapid-response seismic data: Geophysical Journal International, v. 227, p. 204-227.

Yang, Z., Zhao, D., Cheng, B., and Dong, Y., 2022, Structural control on the 2019 Ridgecrest earthquake from local seismic tomography: Physics of the Earth and Planetary Interiors, v. 324, 106853.

Discussion (C) Evidence of Previous Faulting

Evidence of Previous Faulting along the 2019 Ridgecrest, California, Earthquake Ruptures (Presented by Pierce)

Jessica Ann Thompson Jobe, Belle Philibosian, Colin Chupik, Timothy Dawson, Scott E. K. Bennett, Ryan Gold, Christopher DuRoss, Tyler Ladinsky, Katherine Kendrick, Elizabeth Haddon, Ian Pierce, Brian Swanson, and Gordon Seitz

Published in 2020 in the Bulletin of the Seismological Society of America

Abstract

The July 2019 Ridgecrest earthquakes in southeastern California were characterized as surprising by some, because only ~35% of the rupture occurred on previously mapped faults. Employing more detailed inspection of pre-event high-resolution topography and imagery in combination with field observations, we document evidence of active faulting in the landscape along the entire fault system. Scarps, deflected drainages, and lineaments and contrasts in topography, vegetation, and ground color demonstrate previous slip on a dense network of orthogonal faults, consistent with patterns of ground surface rupture observed in 2019. Not all of these newly mapped fault strands ruptured in 2019. Outcrop-scale field observations additionally reveal tufa lineaments and sheared Quaternary deposits. Neotectonic features are commonly short (< 2 km), discontinuous, and display en echelon patterns along both the M6.4 and M7.1 ruptures. These features are generally more prominent and better preserved outside the late Pleistocene lake basins. Fault expression may also be related to deformation style: scarps and topographic lineaments are more prevalent in areas where substantial vertical motion occurred in 2019. Where strike-slip displacement dominated in 2019, the faults are mainly expressed by less prominent tonal and vegetation features. Both the northeast- and northwest-trending active-fault systems are subparallel to regional bedrock fabrics that were established as early as ~150 Ma, and may be reactivating these older structures. Overall, we estimate that 50%–70% (i.e., an additional 15%–35%) of the 2019 surface ruptures could have been recognized as active faults with detailed inspection of pre-earthquake data. Similar detailed mapping of potential neotectonic features could help improve seismic hazard analyses in other regions of eastern California and elsewhere that likely have distributed faulting or incompletely mapped faults. In areas where faults cannot be resolved as single throughgoing structures, we recommend a zone of potential faulting should be used as a hazard model input.

Railroad Cut Site Overview

Where the fault scarp intersects the Trona Railroad tracks, a natural cut exposes a >10 m-wide fault zone with a subvertical core and distributed secondary fractures (Fig. 19). Six stratigraphic units are present, interpreted as alluvial fan and lacustrine deposits, but they do not correlate across the main fault zone, likely due to lateral slip and juxtaposition of different units. Fractures from the 2019 rupture extend to the surface, but vertical offset was minimal (<10 cm). The amount of lateral slip in 2019 could not be determined because there were no clear piercing points to measure offset, however the lack of offset of the railroad cut is minimal. Mineralized fractures and sheared zones indicate older deformation, and upward fault terminations in lower units suggest multiple past ruptures. Carbonate-rich deposits in one unit may reflect reworked tufa from a late Pleistocene lake highstand (~17 ka).

Interpretation

The Railroad Cut site preserves evidence for at least two paleoearthquakes predating the 2019 sequence, recorded in sheared zones and fracture terminations below younger units. Juxtaposition of contrasting deposits and pervasive secondary shears highlight the complexity of fault architecture and distributed deformation within this strand. The interpreted juxtaposition of units suggests that displacement during older events at this site may have been significantly larger than in 2019. These observations indicate that rupture behavior has varied over time, with lateral slip dominating and older events exploiting the same structural zone but not necessarily producing identical surface expressions. capture event variability.

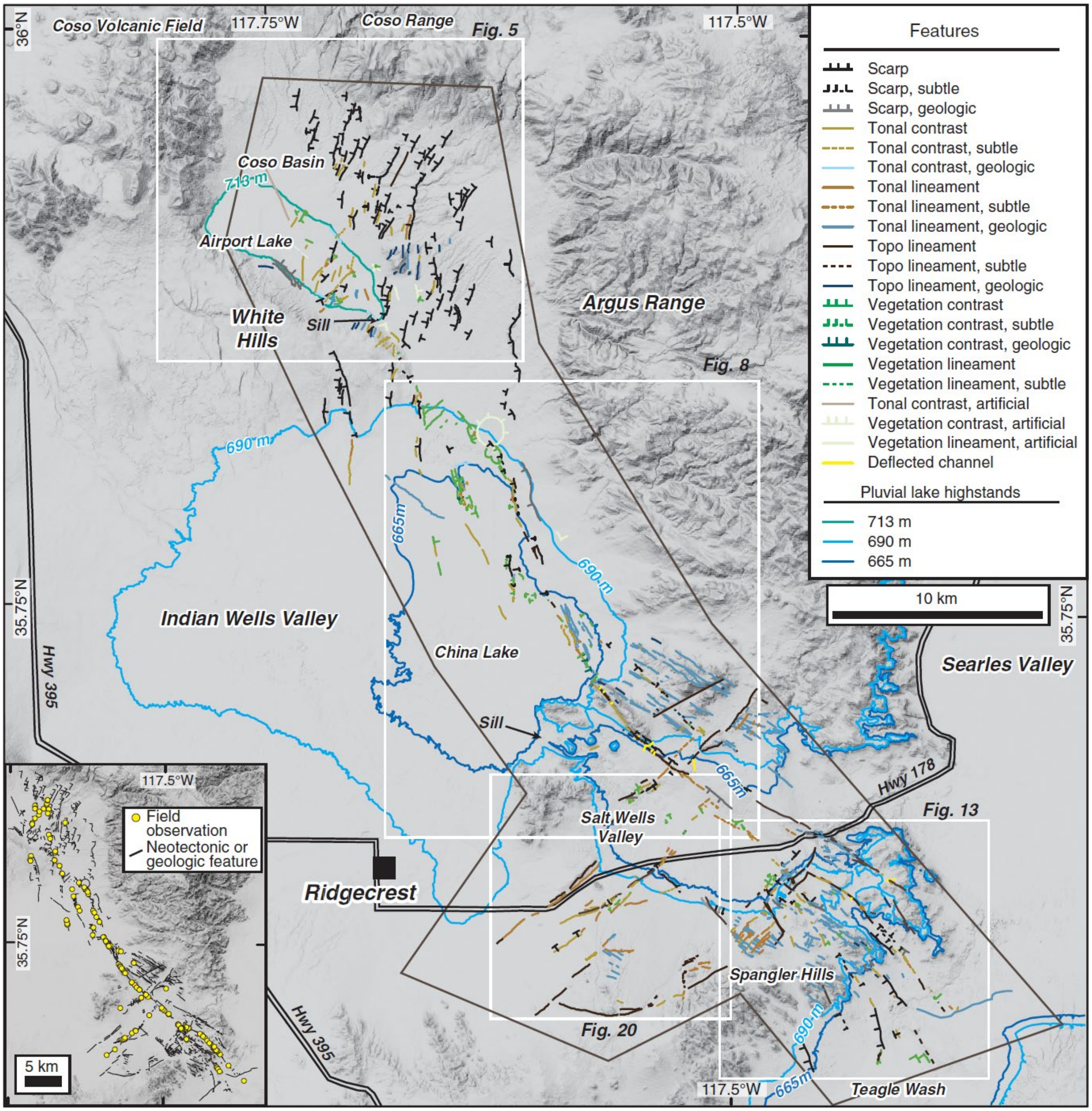

Figure 2-1C-1 Overview of preexisting neotectonic features identified in this paper.

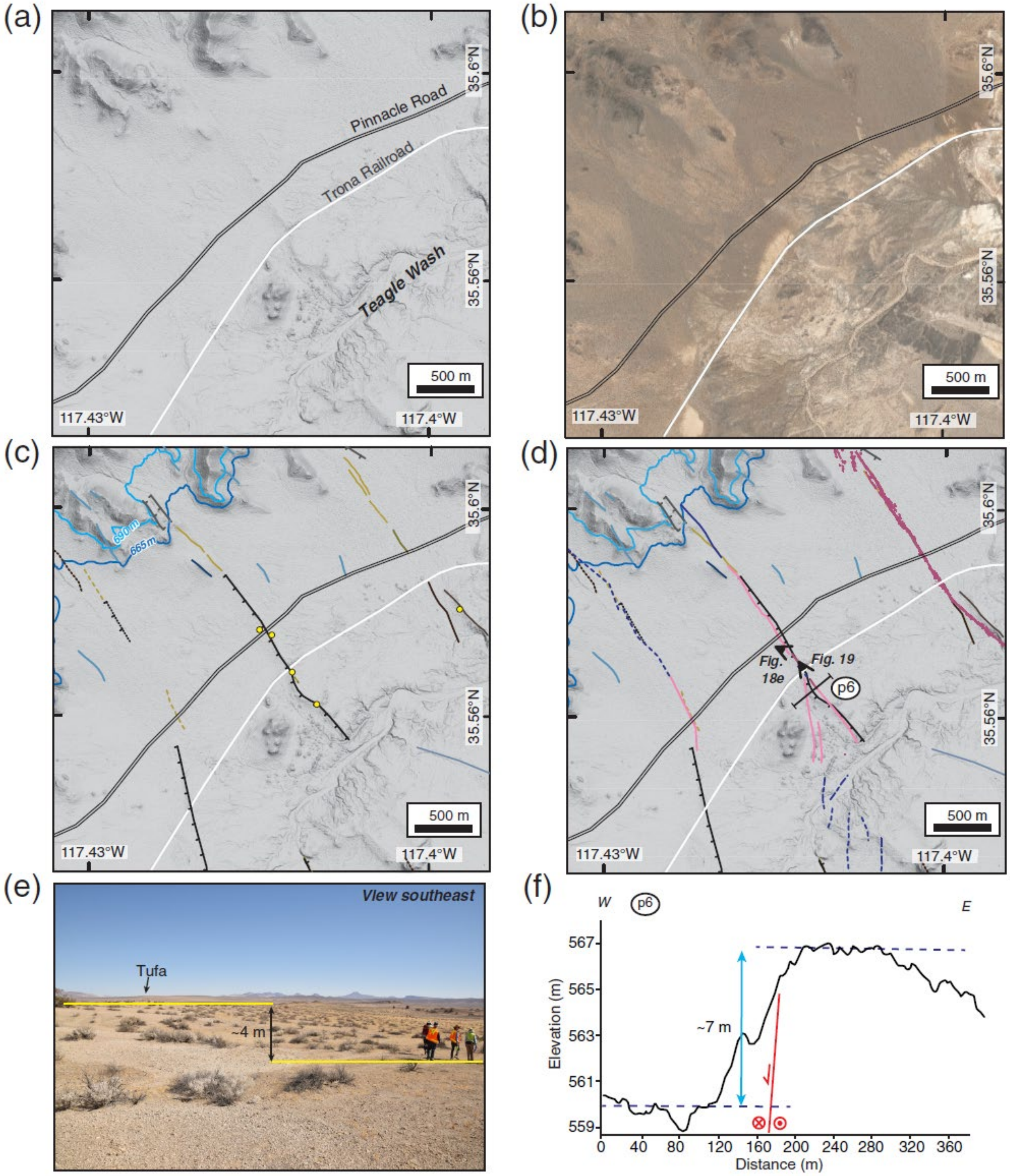

Figure 2-1C-2 Overview of preexisting neotectonic features at the Railroad cut site.

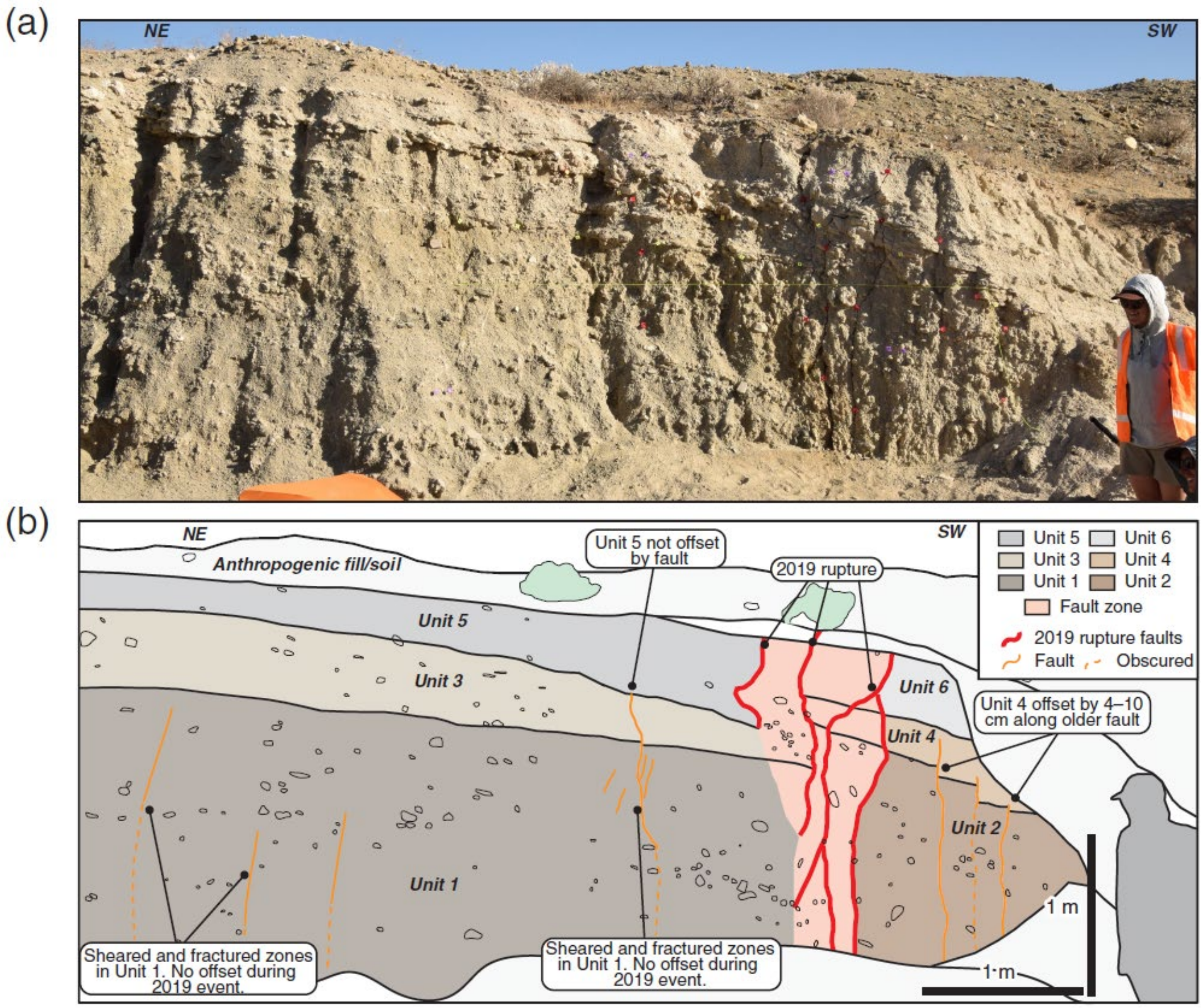

Figure 2-1C-3 Log and photo of the railroad cut natural exposure.

Day 2 Stop 2: Trona Pinnacles

Trona Pinnacles and Ridgecrest Earthquake Sequence shaking: fragile geologic features as ground motion constraints

USGS Peer Review DISCLAIMER: This draft manuscript is distributed solely for purposes of scientific peer review. Its content is deliberative and predecisional, so it must not be disclosed or released by reviewers. Because the manuscript has not yet been approved for publication by the U.S. Geological Survey (USGS), it does not represent any official USGS finding or policy.

Devin McPhillips, U.S. Geological Survey, Pasadena, California

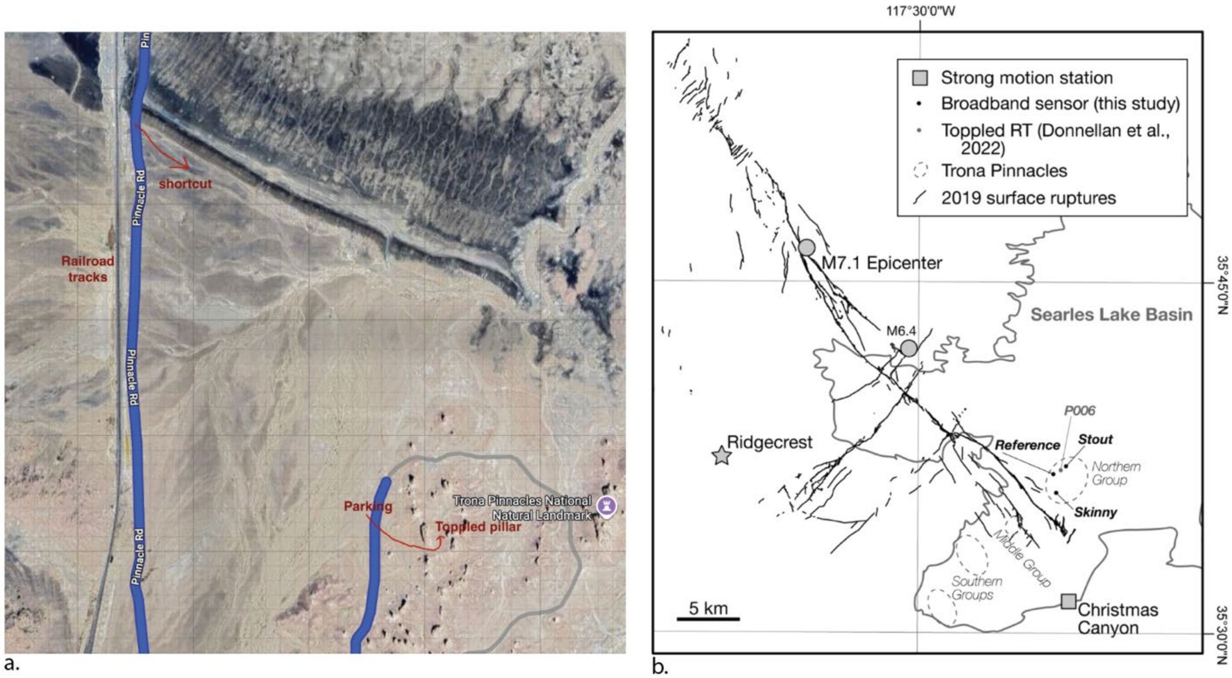

Figure 2-2-1. Maps. (a.) Driving directions. Meet at the area marked Parking at the end of the blue Google Maps route trace (Google Maps, 2025). Pinnacles extend far beyond the location of our stop, but the roads become quite rough. (b.) The Pinnacles in the context of the Ridgecrest Earthquake Sequence surface ruptures and the Pleistocence Searles Lake shoreline (Figure from García Suárez et al., 2025; rupture trace from DuRoss et al., 2019). The rupture passed within 5 km and Modified Mercalli shaking intensity was Severe to Violent intensity (Center for Engineering Strong Motion Data, 2022). Previous work has conceptualized the Pinnacles in three groups (dashed lines), and this stop is at the Northern Group. Pinnacle P006 toppled during an aftershock and is discussed below.

Conditions: We will begin the discussion at the parked cars and then walk several hundred feet on uneven ground. Vault toilets are available, but there is no running water. There is no natural shade.

Stop 2.2 Key Observations

1. Morphology and facies characteristics of tufa rock towers (i.e., Pinnacles)
2. Fragments of rock tower P006, which was likely toppled by earthquake shaking
3. At distance: Searles Lake paleoshoreline and termination of the 2019 M 7.1 Ridgecrest earthquake surface rupture

Stop 2.2 Discussion

Geologic Background: Pinnacles formation in Pleistocene Searles Lake

Biologically assisted carbonate precipitation led to underwater formation of tufa rock structures beneath the at least two lakes that filled the Searles Basin between approximately 10 and 25 ka and 32 and 100 ka (Lin et al., 1998). The Northern Group Pinnacles in particular is thought to have formed in the more recent Tioga glacial stage, when the maximum lake depth exceeded 130 m (Scholl, 1960). Tufa is a form of porous travertine, and the Trona Pinnacles generally consist of concentric, overgrown deposits with heterogeneous character (Figure 2-2-2). The tufa generally lacks pervasive, planar discontinuities, such as bedding planes or foliation. The Pinnacles were exposed following the lake desiccation around 10,000 years ago.

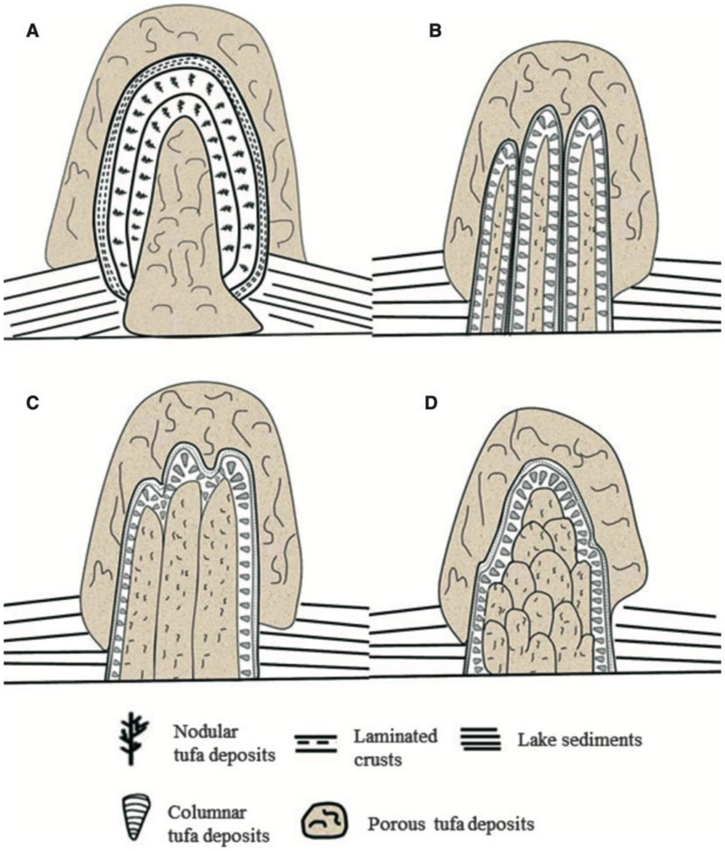

Figure 2-2-2. Schematic illustration of tufa composition from Guo and Chaffetz (2012). (a.) Pinnacles in the Northern Group (see Figure 1b) may have had initially formed with this facies composition, but the inner "porous deposit" facies is typically exposed at present. (b.-d.) Composition of Pinnacles typical of the Middle and Southern Groups. In all groups, the inner "porous deposit" facies is typically well lithified compared to the outer porous facies. Both "porous deposit" facies preserve microstructures consistent bacterially mediated carbonate precipitation, akin to stromatolites.

Geologic Background: 2019 Ridgecrest Earthquake Sequence Shaking

The surface rupture of the 2019 earthquake sequence passed with 5 km of the Northern Group Pinnacles (Figure 2-2-1; DuRoss et al., 2019). This section of the rupture very likely occurred during the M 7.1 mainshock. The Christmas Canyon China Lake seismic station nearby recorded peak horizontal accelerations during the mainshock of 0.57 g and spectral accelerations at 0.2 s exceeded 1 g (Figure 2-2-3). Goulet et al. (2019) observed damage to the Pinnacles in the following days and weeks. Aftershocks continued for years, including a M 5.5 aftershock in 2020, which caused additional damage at the Pinnacles (Donnellan et al., 2022).

Motivation for study: Validate hazard models with Fragile Geologic Features

The U.S. National Seismic Hazard Model (NSHM) describes the probability of earthquake shaking intensity exceeding a threshold value over a relevant time interval (Petersen et al., 2024). For example, many building codes are established for the strongest shaking likely in a ~2500 yr interval. You may be interested in the probability of damaging shaking over the duration of a 30 yr mortgage. For a single family home, “damaging shaking” is often measured in terms of short period shaking, such as spectral acceleration at 0.2 s, but taller buildings typically use measures that describe longer period shaking (~1 s or more). Spectral acceleration is an estimate of the acceleration felt by a structure due dynamic amplification. The NSHM includes tools to calculate site-specific hazard everywhere in the U.S. (https://earthquake.usgs.gov/nshmp/). Hazard models predict that shaking intensities similar to the maximum intensities of the 2019 Ridgecrest Earthquake Sequence recur every few thousand years (Figure 2-2-3).

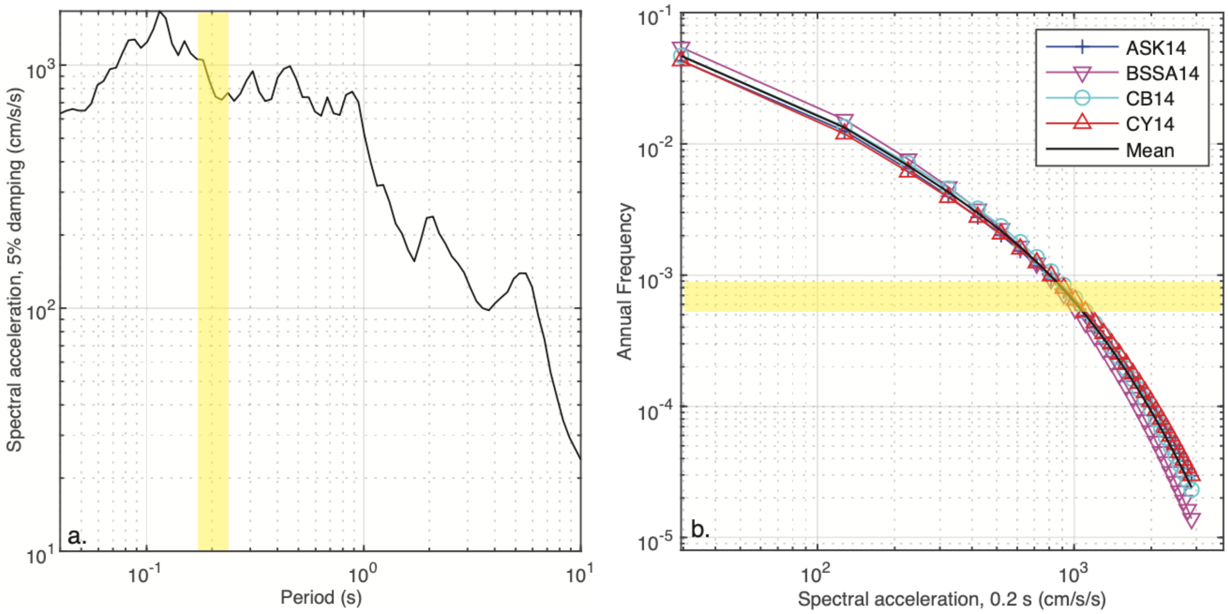

Figure 2-2-3. Comparison of Ridgecrest mainshock shaking intensity and the hazard curve for the Northern Group, Trona Pinnacles (Figure from García Suárez et al., 2025). (a.) Spectral acceleration for the 2019 M 7.1 Ridgecrest Earthquake Sequence mainshock (Center for Engineering Strong Motion Data, 2022). Yellow bar highlights the natural period of slender rock towers at the Pinnacles (about 0.2 s). (b.) Hazard curve for the Northern Group site determined by disaggregation of the Unified California Earthquake Rupture Forecast Version 3 (Biasi and Andersen, 2016). The 2023 U.S. National Seismic Hazard Model yields a similar result. Yellow bar highlights the expected frequency of recurrence of shaking at the level observed during the Ridgecrest mainshock. Lines show predictions from various ground motion models and their mean (see García Suárez et al., 2025).

All hazard models are limited by sparse data. The plots in Figure 3 mean values, and the uncertainties routinely span an order of magnitude at 95% confidence. A major source of uncertainty is that damaging earthquakes recur at timescales of hundreds or thousands of years, but seismic catalogs rarely extend longer than ~100 yr. There are only a handful of seismic recordings of shaking near ruptures during the largest earthquakes anywhere. As a result, it is challenging to validate hazard models such as the NSHM (Field et al., 2015).

Fragile geologic features (FGFs), including precariously balanced rocks and rock towers, provide rare empirical constraints on the intensity of past shaking over timescales exceeding the recurrence intervals of damaging earthquakes. If a FGF exists today, we infer that shaking during its lifetime has not been strong enough to destroy it. We must quantify the age and fragility of FGFs to validate hazard models (Stirling et al., 2021). The 2019 Ridgecrest Earthquake Sequence created an opportunity to observe the seismic response of a large group of rock towers.

Seismic response and damage accumulation

Theory suggests that geometry controls how rock towers deform in response to seismic shaking (Figure 2-2-4a). In elastic beam theory, slender beams, which are much taller than wide, deform principally by swaying about their bases. Beams with a more uniform aspect ratio deform differently, notably by distributed internal shearing. In addition, slender beams have longer natural periods, within the range of earthquake shaking. García Suárez et al. (2025) developed observations and models to test how well the seismic response of rock towers is explained by beam theory.

Seismic data confirm a geometry dependent response. Seismometers were placed on the top of two rock towers with different aspect ratios (“Skinny” and “Stout”, Figure 2-2-1b) and their response to nearby aftershocks was recorded. The response of the high-aspect-ratio rock tower was amplified compared to a reference station nearby (Figure 2-2-5). In contrast, the response of the low-aspect-ratio rock tower was not.

Rebound hammer measurements show evidence for damage accumulation over multiple seismic cycles. Rebound hammers are widely used to characterize rock and concrete in geotechnical applications, and rebound number correlates with unconfined compressive strength. At the Pinnacles, rebound numbers were measured systematically at different elevations on rock towers of various aspect ratios. The ratio of the rebound number near the middle of a rock tower to the rebound number near its base correlates with aspect ratio (Figure 2-2-4b). This correlation indicates that higher aspect ratio rock towers have relatively weaker bases than lower aspect ratio rock towers. This result is consistent with the hypothesis that high aspect ratio rock towers accumulate basal damage over time. The seismic response of these rock towers has a strong swaying mode, which is amplified around the natural period. This deformation likely creates large tractions and forms tension cracks.

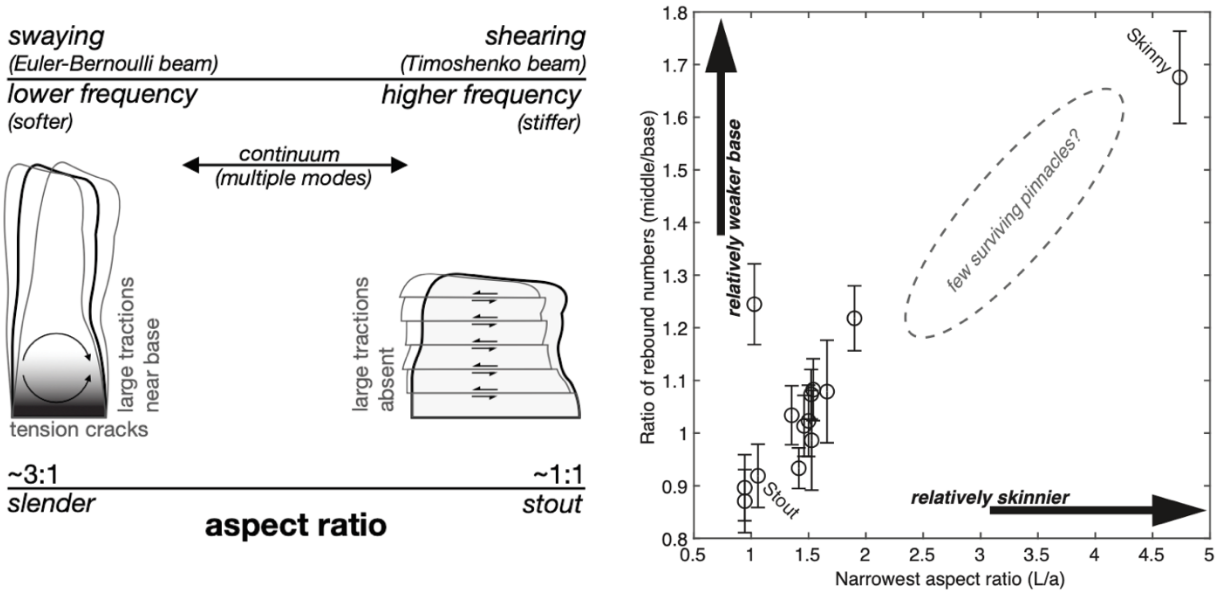

Figure 2-2-4. (Left) Schematic illustration of the role of geometric aspect ratio on the seismic response of rock towers. (Right) Plot of rebound hammer ratio data as a function of aspect ratio. Higher aspect ratio rock towers have relatively weaker bases, consistent with damage by earthquake shaking. Figures from García Suárez et al. (2025).

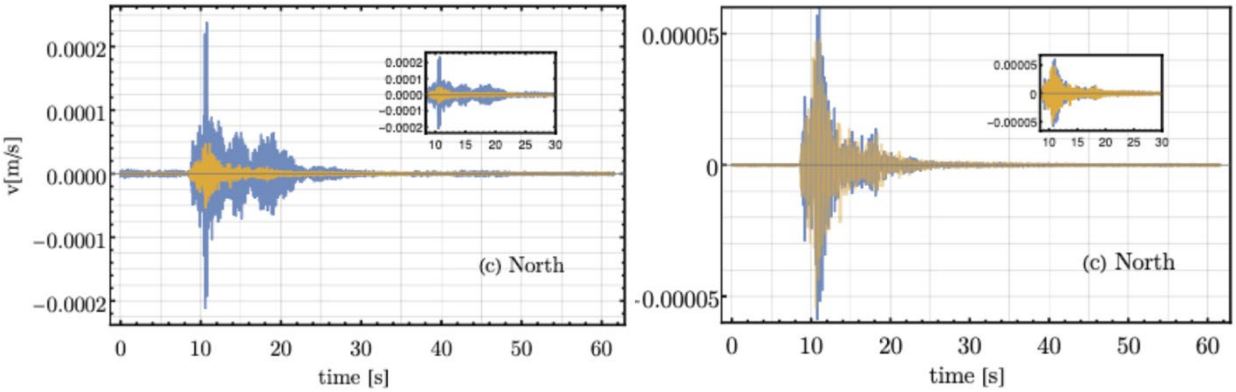

Figure 2-2-5. Seismic response of rock towers (blue) and reference station (orange) observed at the Pinnacles during a nearby M 1.9 earthquake (See Figure 2-2-1b). (Left) High-aspect-ratio rock tower ("Skinny") shows obvious amplification. (Right) Low-aspect-ratio rock tower ("Stout") shows little or none. Figures after García Suárez et al. (2025).

Case study: P006

On 3 June 2020, a M 5.5 aftershock occurred within ~5 km the Pinnacles, at a depth of 8.6 km, causing shaking of about half the intensity of the 2019 M 7.1 mainshock (Donnellan et al., 2020). At least one rock tower (P006 in Divine et al., 2019) was observed to have failed on 10 June 2020, and its failure is inferred to have occurred as a result of the 3 June aftershock (Figure 2-2-6). Aerial imagery was acquired before and after the aftershock, and photogrammetric tools were used to build 3D point clouds and meshes with ~3 cm resolution. A finite element method model was then developed to explore the response of this rock tower to seismic shaking recorded at the Christmas Canyon seismic station (Donnellan et al., 2022). The modeling approach was validated by subsequent comparison to observations (García Suárez et al., 2025)

Figure 2-2-6. Photos of the rock tower P006 from before and after the 3 June 2020 M 5.5 aftershock. Figure from Donnellan et al. (2022).

Results from the finite-element method model show that the rock tower likely deformed but did not topple with a swaying mode in response to the M 7.1 mainshock (Figure 2-2-7; Donnellan et al., 2022). Furthermore, tensile stresses developed along the outer perimeter of the rock tower's base approached or exceeded the tensile strength of the intact tufa.

Why did the rock tower P006 fail during an aftershock rather than the mainshock? Donnellan et al. (2022) suggest that mainshock shaking damaged the base of the rock tower but was marginally too weak to topple it. When the aftershock occurred, the rock tower was effectively disconnected from the tufa pedestal below it and behaved as an independent rigid body, rather than an elastic beam. This case study suggests that the fragilities of FGFs may need to be considered time dependent for hazard applications.

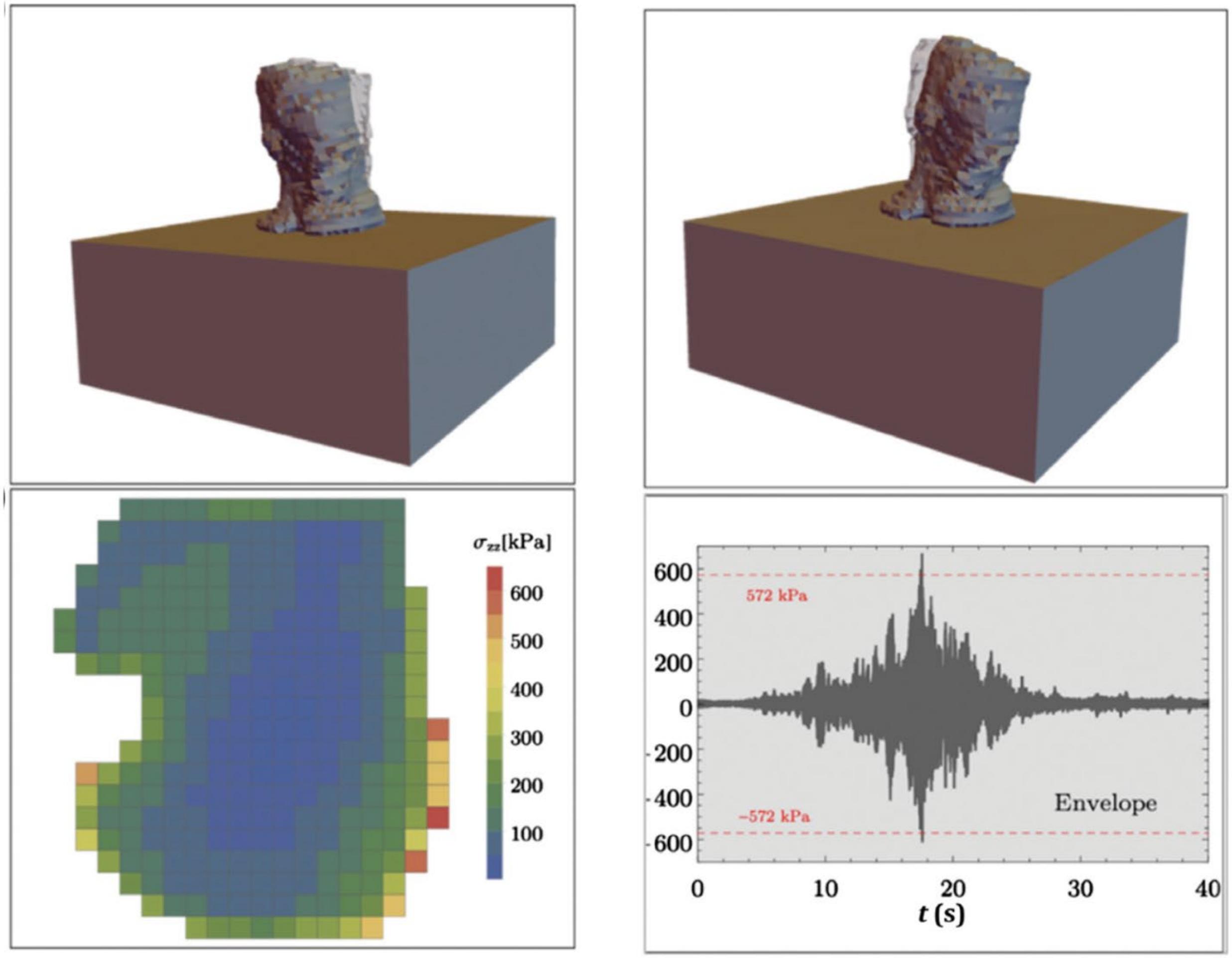

Figure 2-2-7. Finite element method model results for rock tower P006 at the Pinnacles. (Top row) The mesh deforming in response to shaking, illustrating the swaying mode. (Bottom left) Map of simulated tensile stresses in a cross-section through the base of the rock tower. (Bottom right) Time series of tensile stress in the model element with the maximum peak tensile stress. At about 18 s, the stresses exceed the estimated tensile strength envelope of the tufa rock. Figure after García Suárez et al. (2025).

References

Biasi, G. and J. G. Anderson (2016). Disaggregating UCERF3 for Site-Specific Applications. Earthquake Spectra 32(4), 2009–2026.

Center for Engineering Strong Motion Data (2022). https://www.strongmotioncenter.org/. Accessed: May 2022

Devine, S. C., X. Meng, C. A. Goulet, A. Donnellan, D. McPhillips, and G. A. Lyzenga (2020). Developing a database for the fragile geologic features at the Trona Pinnacles national monument, 2020 SCEC Annual Meeting, 14–17 September 2020.

Donnellan, A., J. Garcia-Suarez, D. Asimaki, C. Goulet, D. McPhillips, X. Meng, S. Devine, and G. Lyzenga (2022). Toppling of trona pinnacles in the 2019 Ridgecrest Earthquake Sequence and subsequent M 5.6 aftershock of June 2021. Seismological Research Letters.

DuRoss, C.B., Gold, R.D., Dawson, T.E., Scharer, K.M., Kendrick, K.J., Akciz, S.O., Angster, S.J., Bachhuber, J., Bacon, S., Bennett, S.E. and Blair, L. (2020). Surface displacement distributions for the July 2019 Ridgecrest, California, earthquake ruptures. Bulletin of the Seismological Society of America, 110(4), pp.1400-1418

Field, E. (2015). All models are wrong, but some are useful. Seismological Research Letters. doi: 10.1785/02201401213

García Suárez, J., D. McPhillips, and D. Asimaki, In Press. Seismic response of rock towers at the Trona Pinnacles (USA) to the 2019 Ridgecrest earthquake sequence: Theory, observations, and models. Bull. Seis. Soc. Am.

Google Maps (2025). https://maps.google.com. Accessed: September 2025.

Goulet, C., X. Meng, A. Donnellan, and G. Lyzenga (2019). Survey of damaged Tufa Pinnacles in Trona following the 2019 M7.1 Ridgecrest earthquake, 2019. SCEC Annual Meeting, Palm Springs, California, 7–11 September 2019.

Guo, X. and H. S. Chafetz (2012). Large tufa mounds, searles lake, california. Sedimentology 59(5), 1509–1535.

Lin, J.C., Broecker, W.S., Hemming, S.R., Hajdas, I., Anderson, R.F., Smith, G.I., Kelley, M. and Bonani, G., 1998. A reassessment of U-Th and14C ages for late-glacial high-frequency hydrological events at Searles Lake, California. Quaternary Research, 49(1), pp.11-23.

Petersen, M.D., Shumway, A.M., Powers, P.M., Field, E.H., Moschetti, M.P., Jaiswal, K.S., Milner, K.R., Rezaeian, S., Frankel, A.D., Llenos, A.L. and Michael, A.J. (2024). The 2023 US 50-state national seismic hazard model: Overview and implications. Earthquake Spectra, 40(1), pp.5-88.

Scholl, D. W. (1960). Pleistocene algal pinnacles at Searles Lake, California. Journal of Sedimentary Research 30(3), 414–431.

Stirling, M. W., M. E. Oskin, J. R. Arrowsmith, A. H. Rood, C. A. Goulet, L. Grant Ludwig, T. R. King, A. Kottke, J. C. Lozos, C. M. Madugo, D. McPhillips, D. H. Rood, N. H. Sleep, and C. E. Wittich (2021). Evaluation of Seismic Hazard Models with Fragile Geologic Features. Seismological Research Letters 92(1), 314–324.

Day 2 Stop 3: M7.1 Trench Sites

Ian Pierce University of Nevada, Reno, now at PG&E
Alana Williams Arizona State University
Rich Koehler Nevada Bureau of Mines and Geology, University of Nevada Reno
Ramon Arrowsmith Arizona State University
Kathleen Rodrigues Division of Earth and Ecosystem Sciences, Desert Research Institute

Rich Koehler walked most of the publicly accessible ruptures in July temperatures.

Morning of July 6, 2019

Start at the road, will give overview and description of the site. Less mobile folks can drive back towards Pinnacles and access the site directly to skip the hike (see directions section of this guide). The road requires medium clearance, but should not need 4x4.

Things to see along the route:

Now-repaired train tracks (these were heavily deflected following the earthquake).

Rupture morphology: look for evidence of longer term fault morphology while we walk.

Lacustrine geomorphology: younger and reworked Pleistocene exposures.

Train tracks deflected by the M7.1 rupture.

Tufa displaced by surface rupture.

Discussion (A) Paxton Ranch Spangler Hills Trenches (Pierce et al.)

Paxton Ranch Fault Trenches: Spangler Hills

Discussion from Pinnacles Road, the trench site is several miles north up the sandy wash approaching the summit of the Spangler Hills.

In the Spangler Hills, two trenches were excavated in a low transport surface adjacent to a ~0.5-m-high fault scarp (SH-1/2 on Figure I-1b). The first trench was positioned along the margin of an active channel to capture finer-grained deposits, while the second crossed a low fan-pediment surface a few meters away. Both trenches revealed clear evidence of the 2019 rupture as well as fractures and faults consistent with older events. However, correlation of specific event horizons was difficult due to thin Holocene stratigraphy. Moreover, low tufa platforms at higher elevations indicate this site was submerged under Searles Lake highstands in the late Pleistocene, but the sedimentary record was not sufficiently continuous to bracket distinct events. These trench logs and oblique aerial photos of the site are included below.

Thin stratigraphy and low sedimentation rates at this site further complicate paleoseismic interpretation. When earthquakes occur more frequently than new layers are deposited, deformation features from multiple ruptures accumulate within the same units, creating a “saturated” record. This overprinting obscures evidence of separate events and can produce composite horizons that represent several earthquakes rather than one. Such conditions often reflect slow geomorphic processes or limited sediment supply, meaning the stratigraphic record cannot keep pace with tectonic activity. As a result, we decided to open another trench in a different area to search for a more complete event record.

An alternative approach in settings like this is to target areas where faulting is distributed across a broader zone, such as a complex stepover, relay ramp, or splay fault (like at Day 2 Stop 1). These zones might be less likely to rupture in the same way during each earthquake, so a longer trench across multiple strands may capture evidence of older events that did not rupture in the most recent earthquake. This strategy might provide a more complete paleoseismic record when single-strand sites are limited by thin stratigraphy or repeated overprinting.

Takeaway: make sure your “fan surface” isn’t a thin transport surface (e.g., pediment) before you trench it.

SH-T1 is along the channel margin, while SH-T2 is on the low surface (SH-T2 is the upper trench in upper photo, right trench in lower photo).

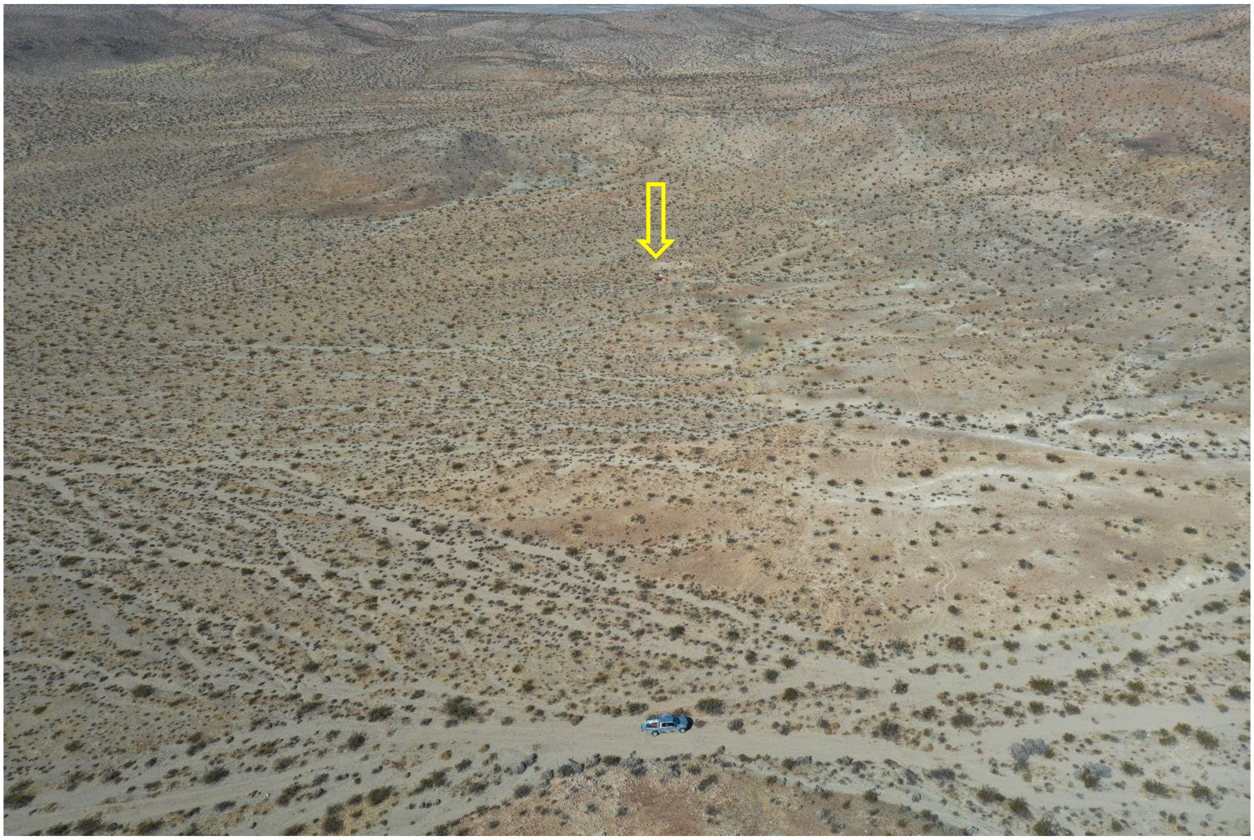

Yellow arrow indicates approximate trench location, photo looking NW along the fault trace.

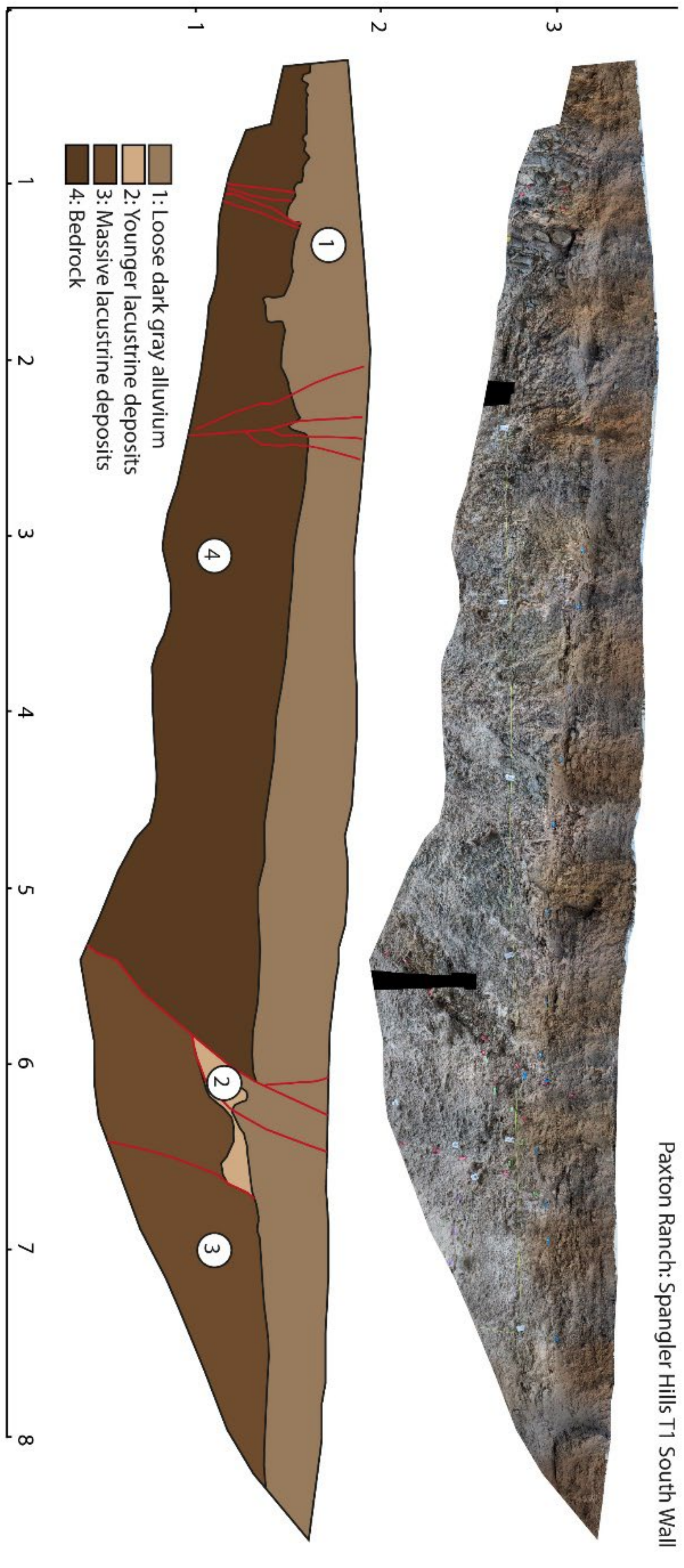

SH-T1 (Previous page): Thin Holocene stratigraphy precluded discerning individual events, and two primary shear zones are present here both rupturing in the 2019 M7.1 earthquake.

SH-T2 (Following page): Thin Holocene stratigraphy precluded discerning younger events. A wide heavily sheared zone provides evidence of multiple late Quaternary events. The cemented lacustrine deposits in this trench behave as a pediment surface for the Holocene.

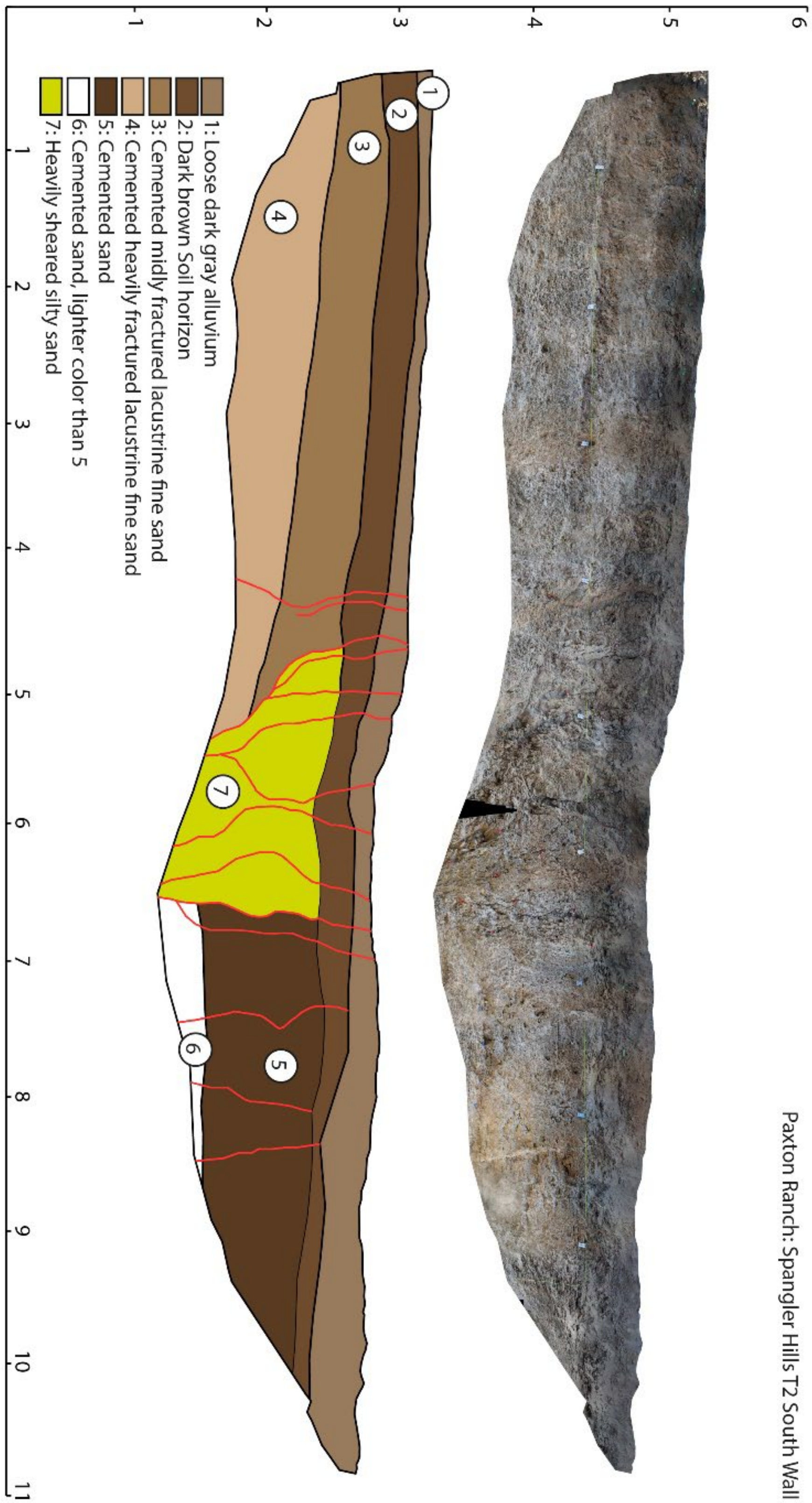
Paxton Ranch: Spangler Hills T2 South Wall
1: Loose dark gray alluvium
2: Dark brown Soil horizon
3: Cemented midly fractured lacustrine fine sand
4: Cemented heavily fractured lacustrine fine sand
5: Cemented sand
6: Cemented sand, lighter color than 5
7: Heavily sheared silty sand
1
2
3
4
5
6
7
1
2
3
4
5
6
7
8
9
10
11
1
2
3
4
5
6

Discussion (B) Paxton Ranch – Searles Valley Trench (Pierce et al.)

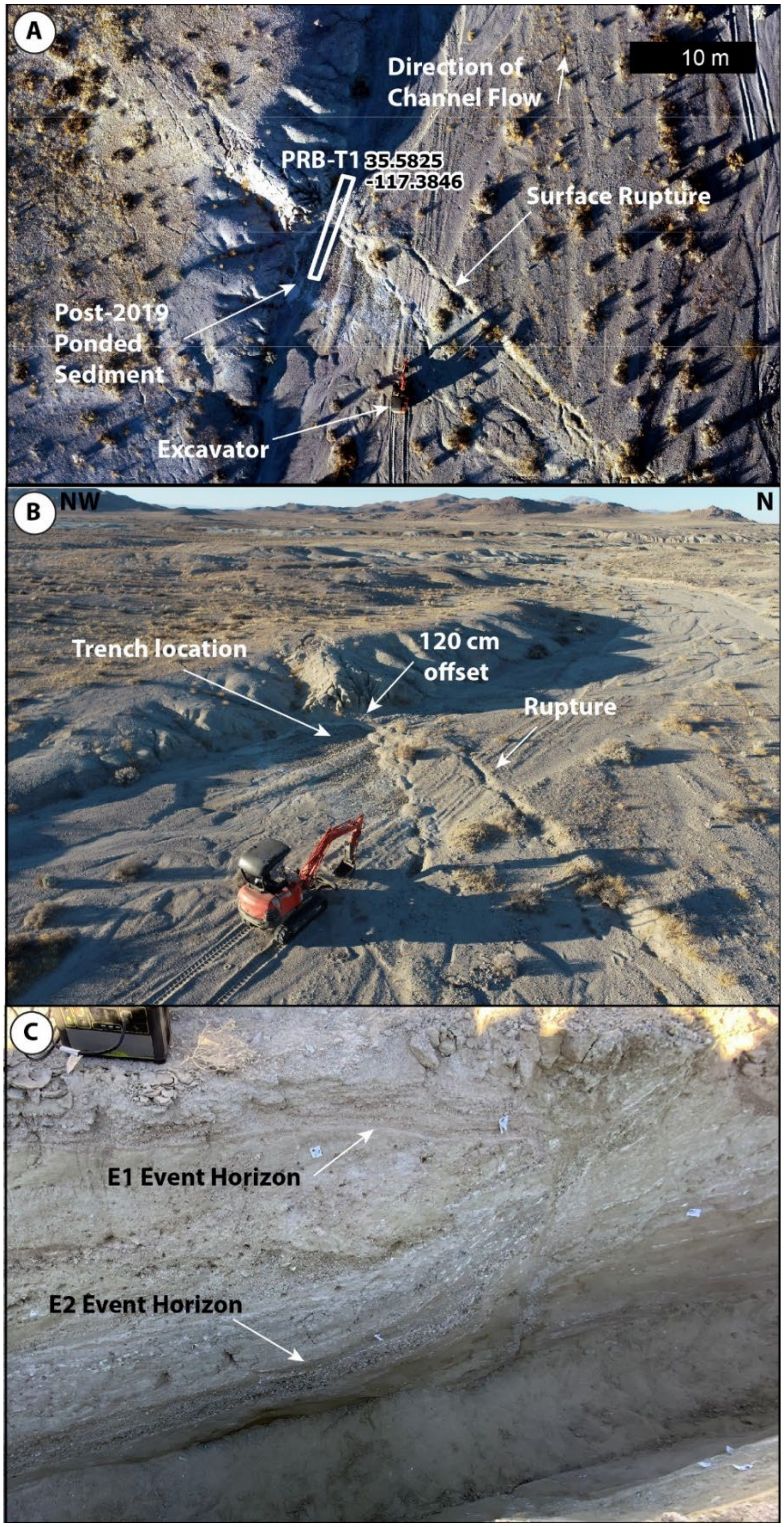

Figure 2-3-B1 A: Orthophotomosaic showing the Paxton Ranch (M7.1) Basin trench location on edge of wash. Wash flows from south to north. Note the ponded materials deposited behind the scarp. **B**: Oblique drone image of site before excavation showing echelon faulting and small mole-track. C: Field photo of northwest trench wall showing event horizons and fault zone.

Paxton Ranch Fault Basin Trench (PRB-T1)

A single 21-m-long, 2-m-deep trench was excavated across an uphill-facing scarp formed by the 2019 earthquake in a wash south of Pinnacle Road at ~579 m elevation (117.3845°W, 35.5825°N; **Figure 2-3-B1**). The trench is oriented N20°E, roughly perpendicular to the scarp, and was selected because post-earthquake ponding behind the scarp had begun depositing a thin silt/clay layer behind the scarp, suggesting potential for well-preserved event horizons. Right-lateral displacement of ~120 cm was measured in this area following the 2019 event (Ponti et al., 2020).

Stratigraphy in the trench comprises fluvial deposits capping late Pleistocene lacustrine sequences, with a prominent fault zone uplifting the downstream (northeast) reach (**Figure 2-3-B2**).

Units 3-9 are interpreted as nearshore lacustrine deposits. Units 2–7 warp upward toward the fault zone from the southwest, dipping ~5° NE at a distance but locally up to 25° SW near the fault zone, forming a gentle syncline geometry.

- Unit 9 is exposed only on the northeast side of the fault zone and is >1.2 m thick. Most of Unit 9 is a light gray massive fine sand with several coarser sand interbeds in the lower part, and several thin, intermittent white silty-clay stringers.
- Unit 8 is also only exposed on the northeast side of the fault zone, is ~50 cm thick, and is an interbedded sequence of well sorted medium sands, coarse sands, fine pebbles, and a ~3-cm-thick light-brown clay bed. It conformably overlies Unit 9 on the northeast side of the fault zone, and is interpreted to be a nearshore/beach deposit.
- Unit 7 is only on the southwest side of the fault zone on the northwest wall, but on the southeast wall it conformably caps Unit 8 on the northeast side of the fault zone. Unit 7 is a massive light-gray fine sand with thin, white silty-clay stringers, similar to Unit 9, and is >50 cm thick.
- Unit 6 is a light-gray massive fine sand, ~20 cm thick, conformably overlying Unit 7, and also restricted to the southwest side of the fault.

- Units 4 and 5 consist of cross-laminated coarse sand (Unit 4) to fine pebble layers (Unit 5) that conformably overlie Unit 6. Their backset laminations and well-sorted coarse texture suggest a beach or nearshore environment. Unit 5 extends only ~2 m from the fault zone and pinches out, while Unit 4 is ~35 cm thick near the fault but pinches out ~14 m to the southwest.
- Unit 3 is a well-bedded sequence of silt, clay, sand, and thin pebble layers. It conformably overlies Unit 4 and likely represents a back-beach playette environment where small, closed basins accumulated clay (possibly a result of faulting).
- Unit 2 forms a sharp, wavy erosional boundary above Unit 3. It is ~80 cm thick, composed of moderately sorted sands, pebbles, and occasional cobbles in cross-bedded lenses. This fluvial deposit transitions abruptly from the underlying lacustrine facies. Near the top of Unit 2 is a thin (2–3 cm) clay layer.
- Unit 1 is a loose, gray, laminated sand capping the exposure on both sides of the fault. It forms an angular unconformity above Units 2 and 8 and has a maximum thickness away from the fault of ~10 cm. Unit 1 represents modern fluvial wash deposition.

Stratigraphy in this trench is consistent with the regional climatic history of repeating Pleistocene lacustrine sequences followed by a drier mid-Holocene climate. Unit 9 is a nearshore lacustrine deposit, capped by Unit 8, a beach deposit, left behind as the pluvial lake receded. Units 6/7 are a younger sequence of pluvial nearshore deposits, subsequently capped by another beach sequence comprised of Units 4/5. Unit 3 is the result of deposition within a small, closed basin that possibly formed behind a fault scarp. Following regional Holocene desiccation, fluvial units 1 and 2 eroded into the lacustrine sequence and formed the channel we see today.

Figure 2-3-B2 (following page). *Northwest Wall (upper) and mirrored southeast wall (lower) of Paxton Ranch fault Basin trench (PRB-T1). Western 10-m of trench is omitted from the figure for space requirements. Fluvial sediments cap two late Pleistocene lacustrine sequences. A positive flower structure has uplifted sediments to the northeast and two vertical fault terminations provide clear event horizons for the most recent two E1 and E2 events. Third, fourth, and fifth possible events (E3, E4, E5) are based on terminations and deformation within and above Units 8 and 9.*

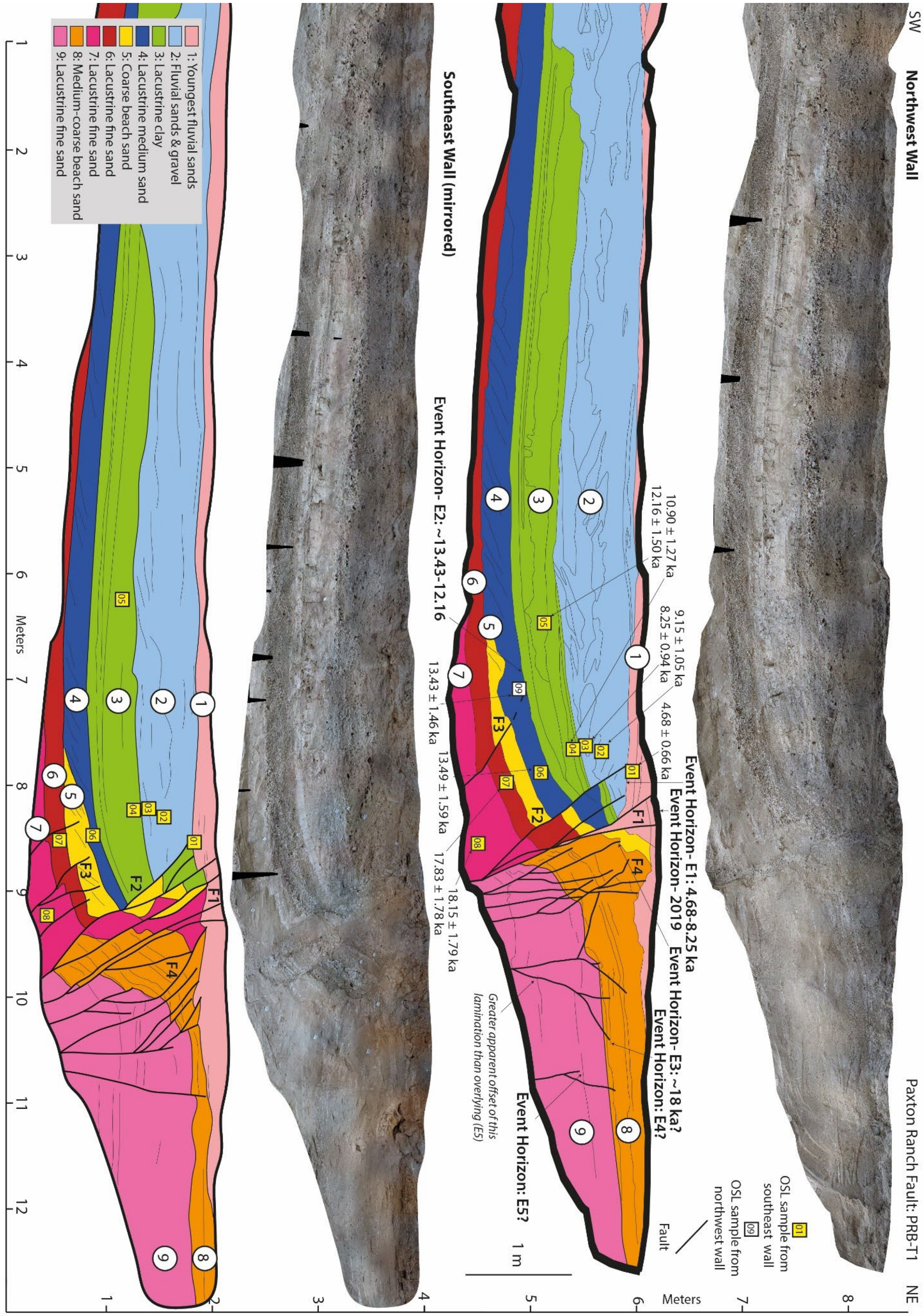

Day 2 Stop 3: M7.1 Trench Sites

Faulting at this site is dominated by a 60° NE-dipping primary strand (F1), creating an asymmetric (NE-side up) positive flower structure with multiple splays. Near the surface, F1 forms a ~90 cm-wide mole track that tapers to ~10–15 cm width at ~35 cm depth. To the northeast of the fault zone sediments are permeated by a network of cross-cutting fractures. To the southwest of F1 are two additional faults, F2 (52° NE dip) and F3 (32° NE dip), each producing apparent vertical offsets of 8–30 cm on various unit contacts. F2 terminates at the Unit 2–3 boundary, while F3 dies out in Unit 4. Overall, Units 2–7 are warped upward, thinning or pinching out across the fault zone, and units 8 and 9 warp downward across the fault, disappearing to the southwest of F1. Units 8 and 9 are likely older lacustrine units that are being faulted into the channel from beneath the adjacent terrace (**Figure 2-3-B1**).

Paleoearthquake evidence reveals as many as five events preceding the 2019 rupture:

E1 (Penultimate): Breaks F1 and F2, postdating Unit 2 but predating Unit 1.

E2 (Antepenultimate): Breaks F1 and F3, postdating/within upper Unit 4 and predating Unit 3.

While some thin clay layers in Units 1, 2, and 3 could reflect additional intervening scarp-derived ponding events, we do not interpret them as discrete paleoearthquake horizons due to limited diagnostic features.

A possible earlier event (E3): Breaks F4 (on the northwest wall), postdating Unit 8 and predating Unit 5. On the southeast wall this event is less clear, but it possibly terminates below Unit 7. The timing of upward terminations on the northeast side of the F1 fault zone is uncertain due to Unit 1 fluvial sediments unconformably eroding Units 5, 7, and 8. As the Unit 5 sediments on the northeast side of the fault zone are close to the main F1 fault zone, it is unclear if they are capping F4 or are faulted, and it is also possible this fault is part of the E1 or E2 ruptures.

Trench Interpretations on the Paxton Ranch Fault (M7.1 2019 earthquake)

In the Paxton Ranch Basin trench (PRB-T1, **Figure 2-3-B2**), two paleoearthquakes (E2, E1) clearly predate the 2019 M7.1 rupture. Fault terminations bracket E2 between ~13–12 ka, while E1 lies between ~8–4 ka. A possible E3 occurred ~18 ka, and older E4 and E5 events may have occurred during regional lacustrine highstands (~23-28 ka, Bacon et al., 2020). Our findings confirm at least two, and possibly five late Pleistocene–Holocene ruptures on the Paxton Ranch fault prior to 2019. This record suggests that the Paxton Ranch fault has a regular behavior with events every ~6 ka.

The following additional pieces of evidence support E3 and other possible earlier events (E4, E5): (1) the apparent vertical offset of Units 8 and 9 is more than double the apparent vertical offset of Units 1-5 (though this could be a result of laterally discontinuous units being laterally faulted together), (2) Units 6, 8, and 9 cannot be traced across the fault zone, (3) Units 8 and 9 have significantly more tilting and deformation near the fault zone than younger units, (4) upward terminations of faults within Units 8 and 9. The lack of age control in Units 8 and 9 precludes estimating ages for E4 and E5.

Nine luminescence sample (OV001–OV008) from Units 1–7 provide temporal constraints (Table 1). Ages range from 4.68 ± 0.66 (OV001 in Unit 1) to 18.15 ± 1.79 ka (OV008 in Unit 7). Lacustrine units 3, 4, and 5 date to ~11–13 ka, while Units 6–7 cluster around ~17–18 ka, consistent with documented spillovers of Owens Lake that would have generated lakes in Searles Valley (Bacon et al., 2020). The overall sequence is in chronological order. Thus:

- 2019 Ridgecrest M7.1 earthquake
- E1 is bracketed between 4.68 ± 0.66 ka (Unit 1) and 8.25 ± 0.94 ka (Unit 2).
- E2 is constrained by 12.16 ± 1.50 ka (Unit 3) and 13.43 ± 1.46 ka (Unit 4).
- Possible E3 ~18 ka (faulting Unit 8 and capped by Units 5 or 7).
- Older E4 and E5, possibly occurring during ~23-28 ka or other older Owens Lake spill-over events (Bacon et al., 2020).

Combined, these ages place two to five late Pleistocene–Holocene surface ruptures on this section of the Paxton Ranch fault prior to the 2019 event.

Slip Rates from Paleoseismology

Accurate slip-rate estimation from paleoseismic data is often challenging due to the large effect that temporal clustering or gaps in earthquake cycles can have on measured deformation rates (Styron, 2019).

Paxton Ranch Fault

Our data document two closed seismic cycles between E2 and 2019 in the last ∼13 ka. If we use the 1.2-1.7 m mean and 4.3-7.0 m max slip distributions measured in the field following the 2019 earthquakes (DuRoss et al., 2020), then a total of ∼2.4-3.4 m mean slip and 8.6-14.0 m max slip have accumulated over these two seismic cycles, implying a mean right-lateral rate of ∼0.2-0.3 mm/yr and max rate of 0.7-1.2 mm/yr. The max slip measurements in 2019 were measured on a farther north section of the fault, near China

Lake, and might not be representative of the slip rate at our trench site. Hence, the Paxton Ranch fault's slip rate could reasonably lie between ~0.2-1.2 mm/yr, a range that aligns with known strike-slip rates elsewhere in the Walker Lane (e.g., Pierce et al., 2021). This is roughly an order of magnitude higher than that of the Salt Wells Valley fault (mean rate of 0.01-0.02 mm/yr, and a max rate of 0.03-0.07 mm/yr.).

Day 3 Stop 1 Summit Range West slip-rate site and other incremental slip rate estimates on the central Garlock fault

Incised channel offset, at Summit Range West site. (N35.479006°, W 117.560351°)

Field Stop Leaders: James Dolan, University of Southern California (USC), Sally McGill, California State University, San Bernardino, Danielle Fougere (USC [now at WSP]) and Ed Rhodes (University of Sheffield).

LOGISTICS

From Trona Road, we will drive east along the Garlock fault for about 1.8 miles on a decent dirt road (Figure 3.1.1). When we reach the site, park on both sides of the dirt road (without blocking the road). Round trip walking will be < 100 meters.

The goals of this stop are to observe a deeply incised channel that has been left-laterally offset by the Garlock fault, and to discuss other slip-rate and paleoseismic data that have been used to build an incremental slip-rate record for the central Garlock fault.

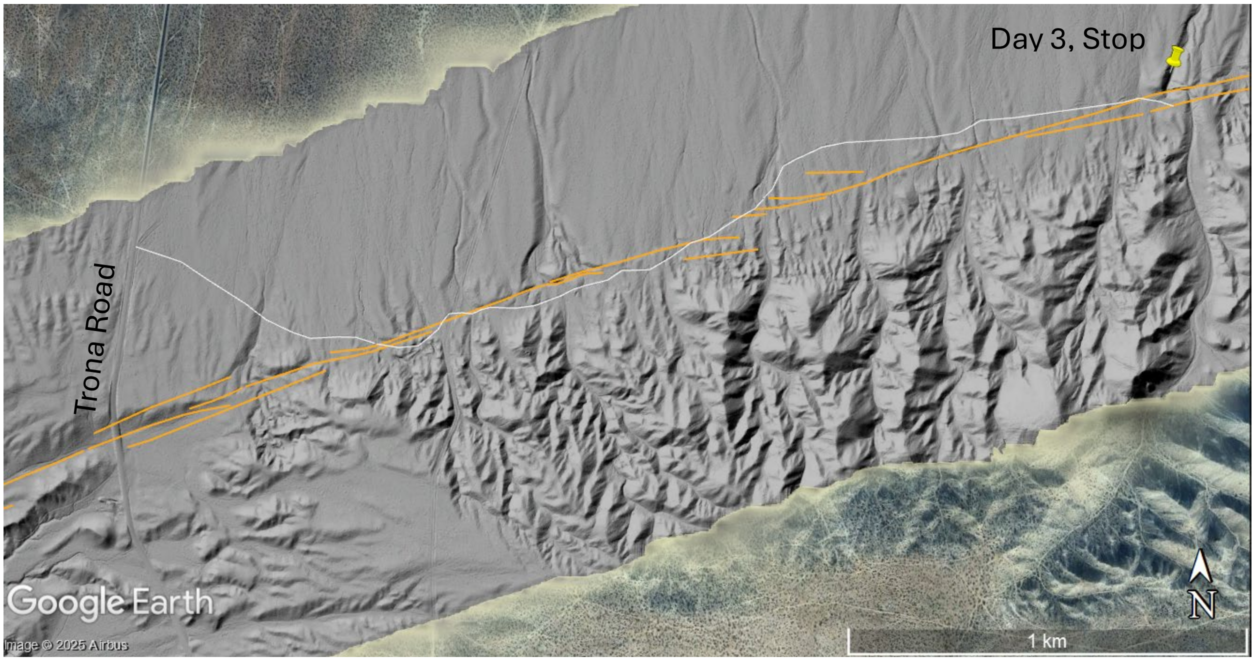

Figure 3.1.1: Lidar image and USGS Quaternary Fault and Fold mapping of the Garlock fault (orange lines), for a ~ 2 km stretch east of Trona Road. White line shows the dirt-road access to Day 3, Stop 1.

DISCUSSION

We discuss here two slip-rate sites on central GF (Figure 3.1.2): the Summit Range West (SRW) and Summit Range East sites (Fougere et al., 2024), although the trip will most likely only visit the SRW site. Summit Range West slip-rate site

The offset channel at the Summit Range West (SRW) site was first identified by Clark (1973) and was studied in detail by Ganev et al. (2012) and again by Fougere et al. (2024). This site is located along the coalescing alluvial fans that drain the northern side of the Summit Range along the central section of the Garlock fault. At this site, a channel that flows northwards across the fault and has deeply incised into two alluvial fans, Qf1 and Qf2, both of which emanated from this same source drainage (Figure 3.1.3). The alluvial fan of interest (Qf2) was deposited atop the older and more laterally extensive Qf1 fan surface (Ganev et al., 2012; Fougere et al., 2024). The deeply incised channel has been sharply offset left-laterally by the Garlock fault Figure 3.1.3).

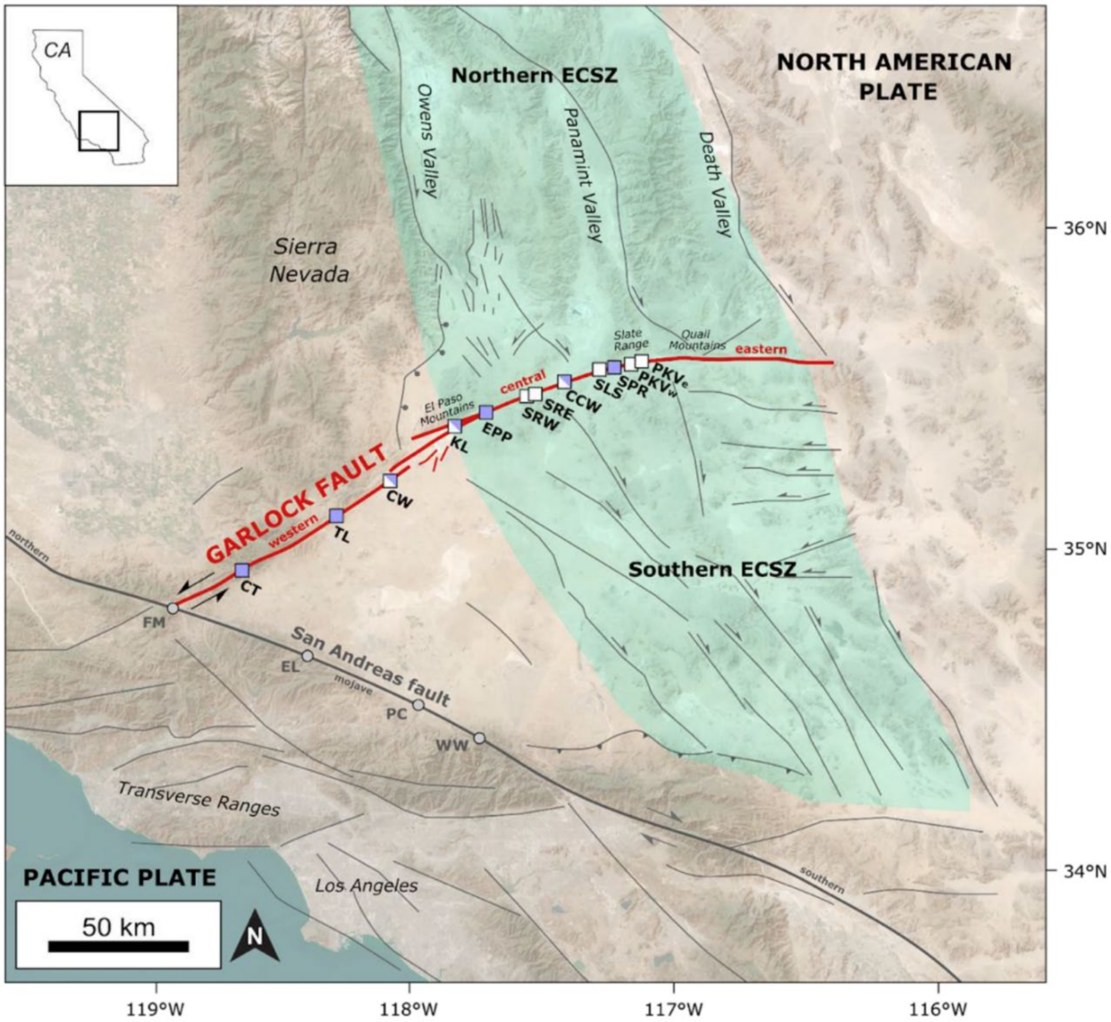

Figure 3.1.2. Map, from Fougere (2025), of the Garlock fault (red) and other active faults around the Mojave region of southern California (gray), including the Mojave section of the San Andreas fault. Squares along the Garlock fault are slip rate (white squares) and paleoseismic (purple squares) study sites. Sites that have both slip rate and paleoseismic studies are shown with half white-half purple squares. CT – Campo Teresa (Gath and Rockwell, 2018), TL – Twin Lakes (Madden and Dolan, 2008; Madden Madugo et al., 2012), CW – Clark Wash (McGill et al., 2009; Fougere et al., 2024), KL – Koehn Lake (Clark & Lajoie, 1974; Madden and Dawson, 2006, Fougere et al., in review, Seismica), EPP – El Paso Peaks (Dawson et al., 2003), SRW – Summit Range West (Ganev et al., 2012; Fougere et al., 2024), SRE – Summit Range East (Fougere et al., 2024), CCW – Christmas Canyon West (Dolan et al., 2016; Peña, 2019; Peña et al, in prep), SLS - Searles Lake Shoreline (McGill and Sieh, 1993, Fougere, 2025), SPR – Straw Peak Road (Fougere, 2025), PKVw – Pilot Knob Valley West (Crane, 2014; Rittase et al., 2014, Fougere, 2025), PKVe – Pilot Knob Valley East (Crane, 2014, Fougere, 2025). Quaternary fault traces sourced from US Geological Survey & California Geological Survey (2023).

Ganev et al. (2012) measured a preferred fault offset of 70 ± 7 m based on the restoration of the easternmost incised edge of the Qf2 fan surface on the western margins of the offset channel segments (Figure 3.1.4). They suggested that this feature most closely records the timing of fan abandonment during initial incision of the channel into the Qf2 fan surface. The thalweg of the channel is offset 58 ± 4 m, but Ganev et al. (2012) noted that progressive incision of the channel in this configuration will narrow the offset, with erosion during incision focused in particular on the downstream northeastern corner and the upstream southwestern corner of the channel. Thus, the thalweg likely does not record the full amount of fault slip that occurred since the time of abandonment of Qf2 at initial incision. Figure 3.1.5 shows reconstructions of the geologic map of the site with 55, 60, 65 and 75 meters left-lateral slip restored.

Using a ^{10}Be depth profile, Ganev et al. (2012) dated the deposits in the upper 2 m of the Qf2 fan as 13.3 (+5.9/-1.0) ka (Figure 3.1.6). Subsequently, however, Fougere et al. (2024) used the post-IR IRSL225 single-grain potassium feldspar luminescence dating method of Rhodes (2015) to date three samples from the uppermost meter of the Qf2 fan Qf2 fan. Combining these three ages yields a preferred age range of 8.0 ± 0.9 ka for the youngest Qf2 fan deposits, which they suggest most accurately dates the age of the Qf2 fan abandonment during initial channel incision (Figure 3.1.7; Fougere et al., 2024). The preferred offset value of 70 ± 7 m (Figure 3.1.5) and the 8.0 ± 0.9 ka post-IR IRSL225 age of the Qf2 fan yield a slip rate of 8.8 ± 1.0 mm/yr at the SRW site, with errors calculated in quadrature and 2-σ uncertainty (Fougere et al., 2024).

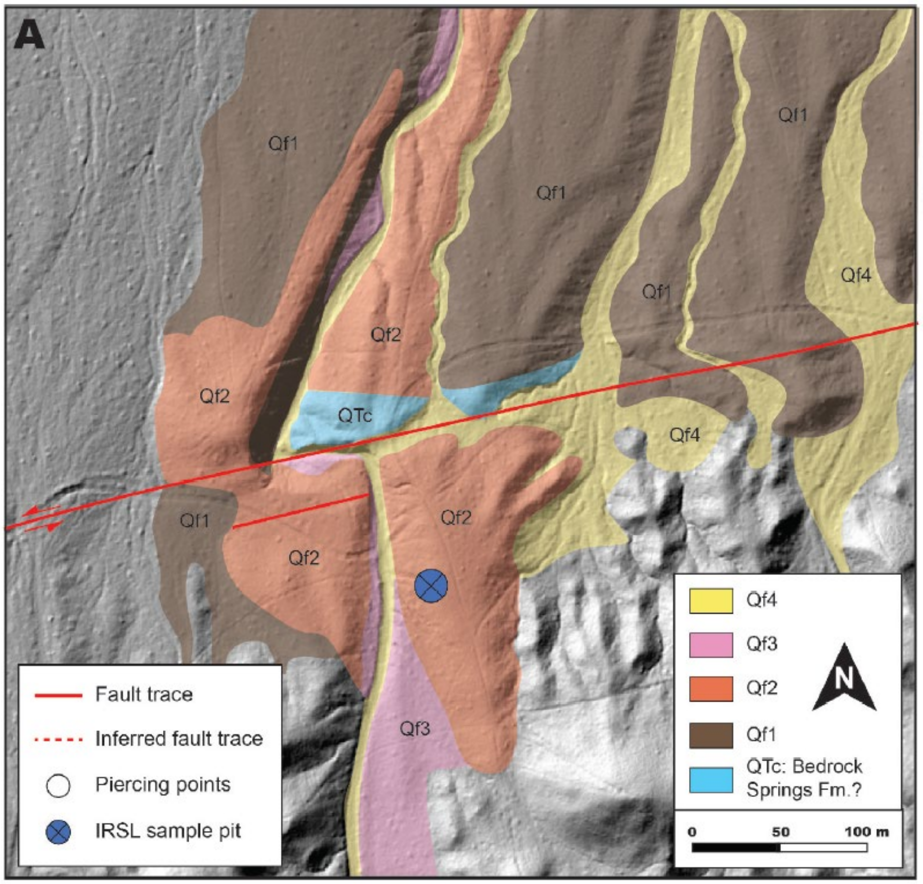

Figure 3.1.3: Geologic map of the Summit Range West slip-rate site, from Fougere et al. (2024), modified from Ganev et al.

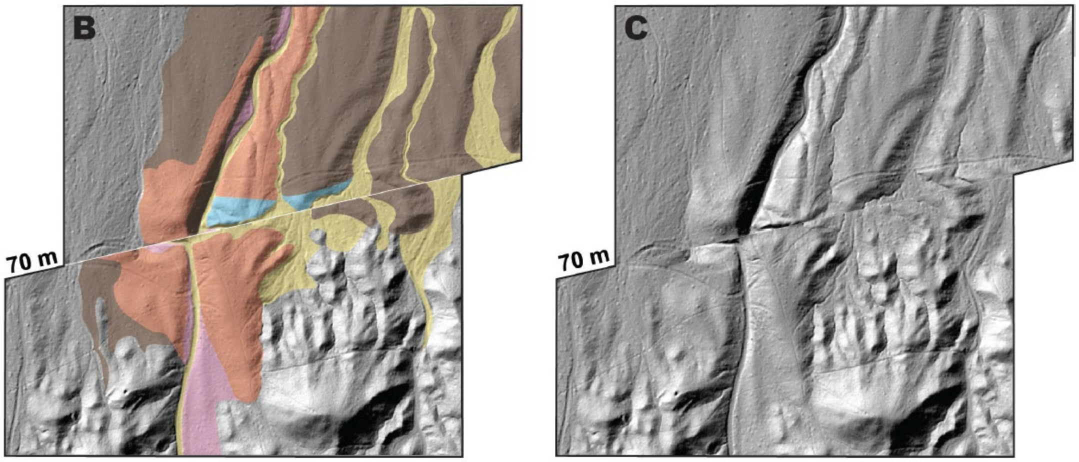

Figure 3.1.4: Restoration of 70 m at the Summit Range West site (from Fougere et al., 2024), which realigns the top west margin of the deep channel incised into Qf2 (orange deposits). This is our preferred restoration for the time of initial incision of the channel into Qf2.

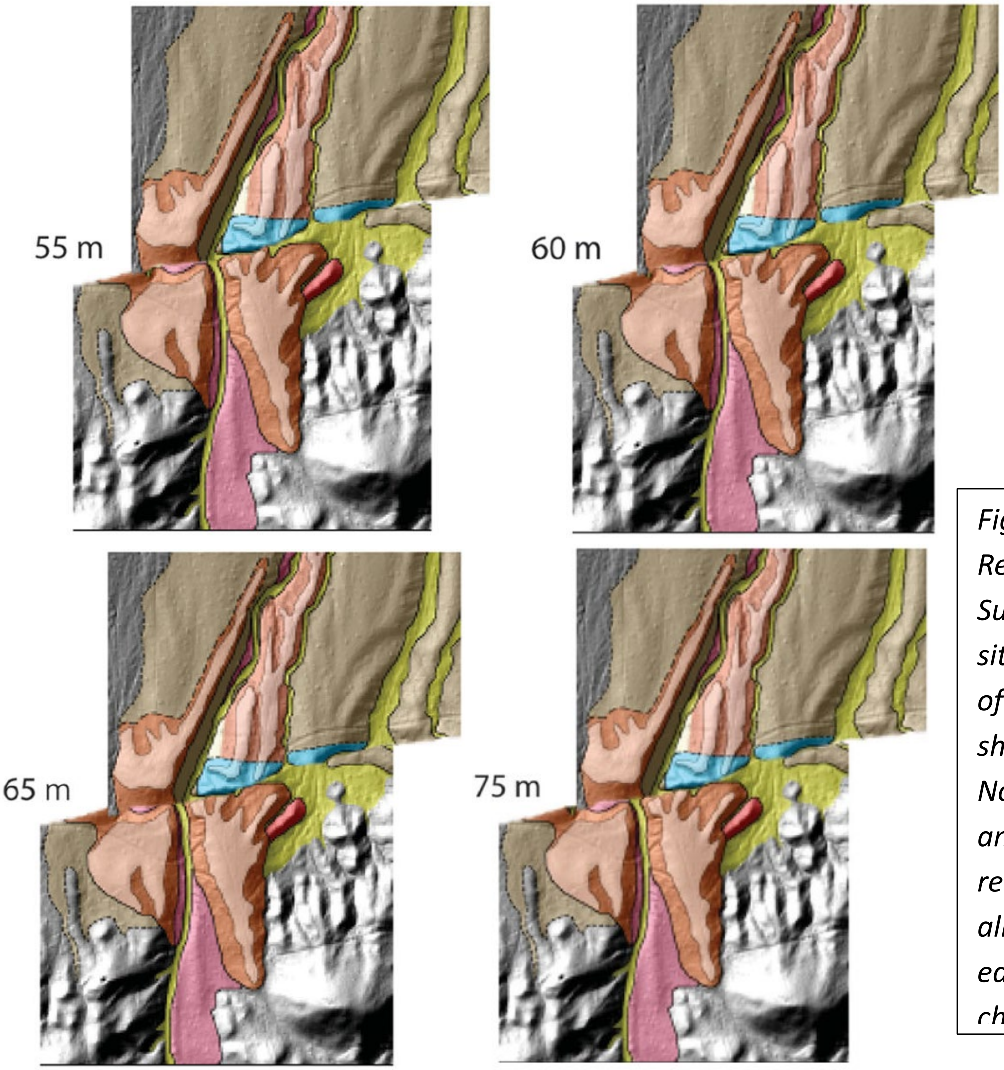

Figure 3.1.5: Reconstructions of the Summit Range West site with 55 m to 75 m of left-lateral slip shown for reference. Note that the 55 m and 60 m reconstructions do not align the top west edge of the incised channel as well as the

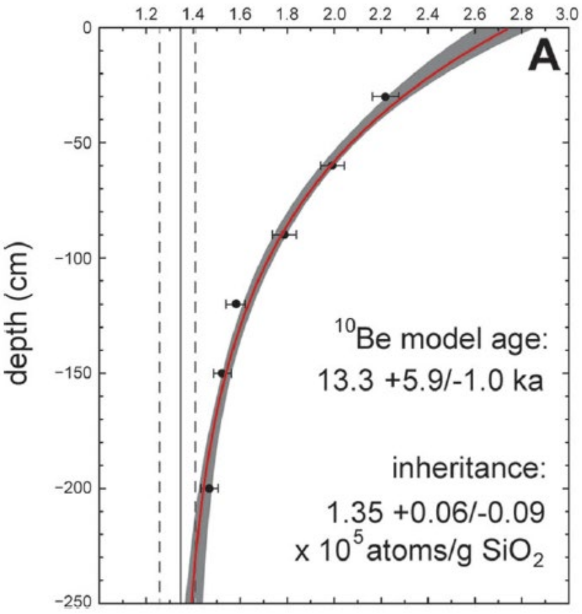

Figure 3.1.6: ^{10}Be depth profile within Qf2 at the Summit Range West site, from Ganev et al. (2012).

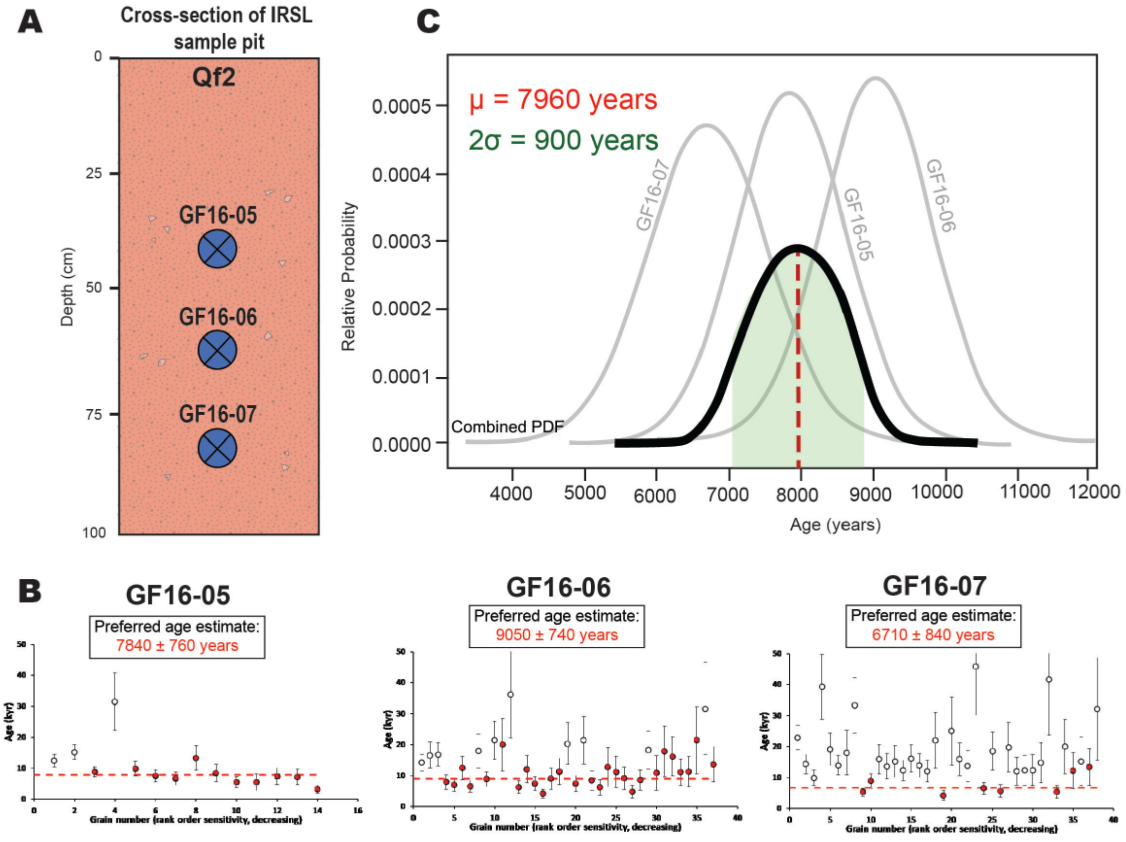

Figure 3.1.7: Post-IR IRSL223 ages of three samples from a 1-m deep pit on Qf2 at the Summit Range West site, from Fougere et al. (2024). The IRSL pit was located within a few meters of the Ganev's (2012) ^{10}Be pit.

The Summit Range East (SRE) slip-rate site

Just 3 km farther east along the central Garlock fault is another well-constrained slip-rate site. Unfortunately, the road quality makes access to that site more difficult. At the SRE site, the alluvial fan of interest, Qfc2, and its associated distributary fan channels have been offset left-laterally by the Garlock fault (Figure 3.1.8). The fault offset at the SRE site is based on the restoration of (1) a prominent distributary channel incised into the Qfc2 surface (Ch-1 in Figure 3.1.8), and (2) one of the northeastward-flowing offset drainages incised into the southeastern edge of Qfc2 (Ch-2 in Figure 3.1.8). Ch-1 yielded a preferred offset measurement of 38 ± 1 m (Figure 3b and c). Ch-2 yielded an offset measurement of 40 ± 3 m (Fougere et al., 2024). The latter measurement includes the full range of the former, and we use the more tightly constrained offset of Ch-1 for the slip-rate measurement. Fougere et al. (2024) used the post-IR IRSL225 single-grain potassium feldspar luminescence dating method of Rhodes (2015) to determine the age of Qfc2 alluvial fan deposition. Four luminescence samples were collected from a pit excavated into Qfc2. The single-grain age plots reveal two distinct age populations within the two uppermost samples, with the older age populations yielding values of 5,560 ± 370 yb2020 and 5,390 ± 410 years yb2020 (Figure 3.1.9; yb2020 notation indicates calendar years before the year the samples was dated, in this case, 2020 C.E.), similar to the underlying sample age of 5,640 ± 260 yb2020. We used the very similar older age populations of the upper two samples (SRE14-01 and SRE14-02) together with the third lowest sample (SRE14-03) to calculate an average age of deposition for the Qfc2 fan of 5,570 ± 190 yb2020 (2-σ uncertainties). Combining our preferred offset value of 38 ± 1 m based on the prominent distributary channel (Ch-1) and the 5.57 ± 0.19 ka age as an estimate of Qfc2 fan deposition yields a slip rate at the SRE site of 6.8 ± 0.3 mm/yr, with 2-σ uncertainties calculated in quadrature.

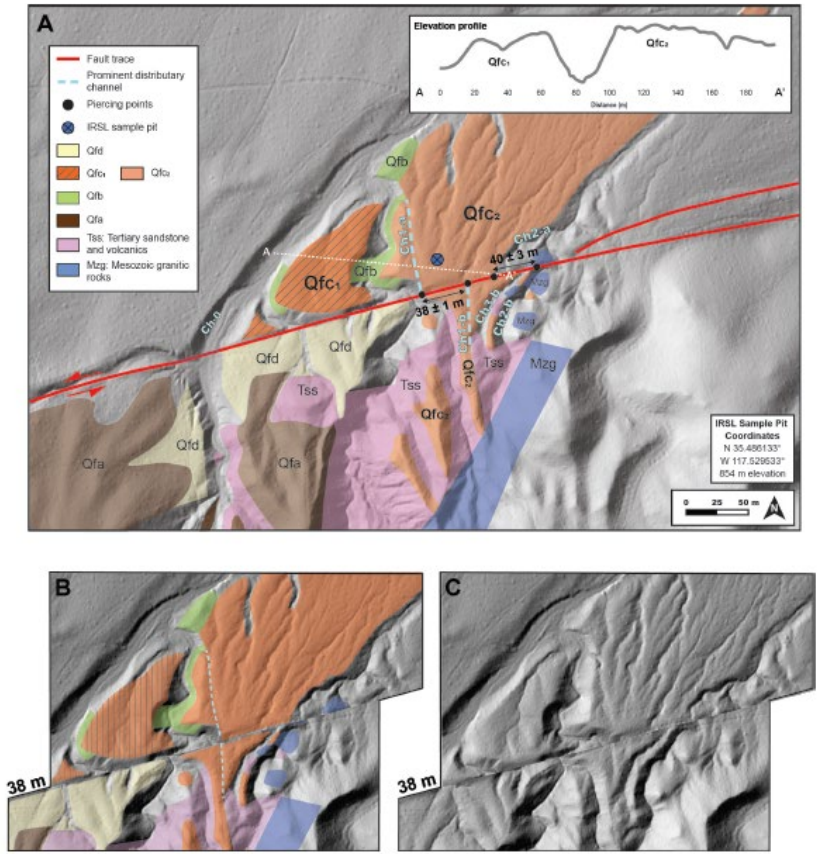

Figure 3.1.8: Geologic map of the Summit Range East site (A), along with restorations of 38 m of left-lateral slip for the geologic map (B), and Lidar image (C). Figure from Fougere et al. (2024).

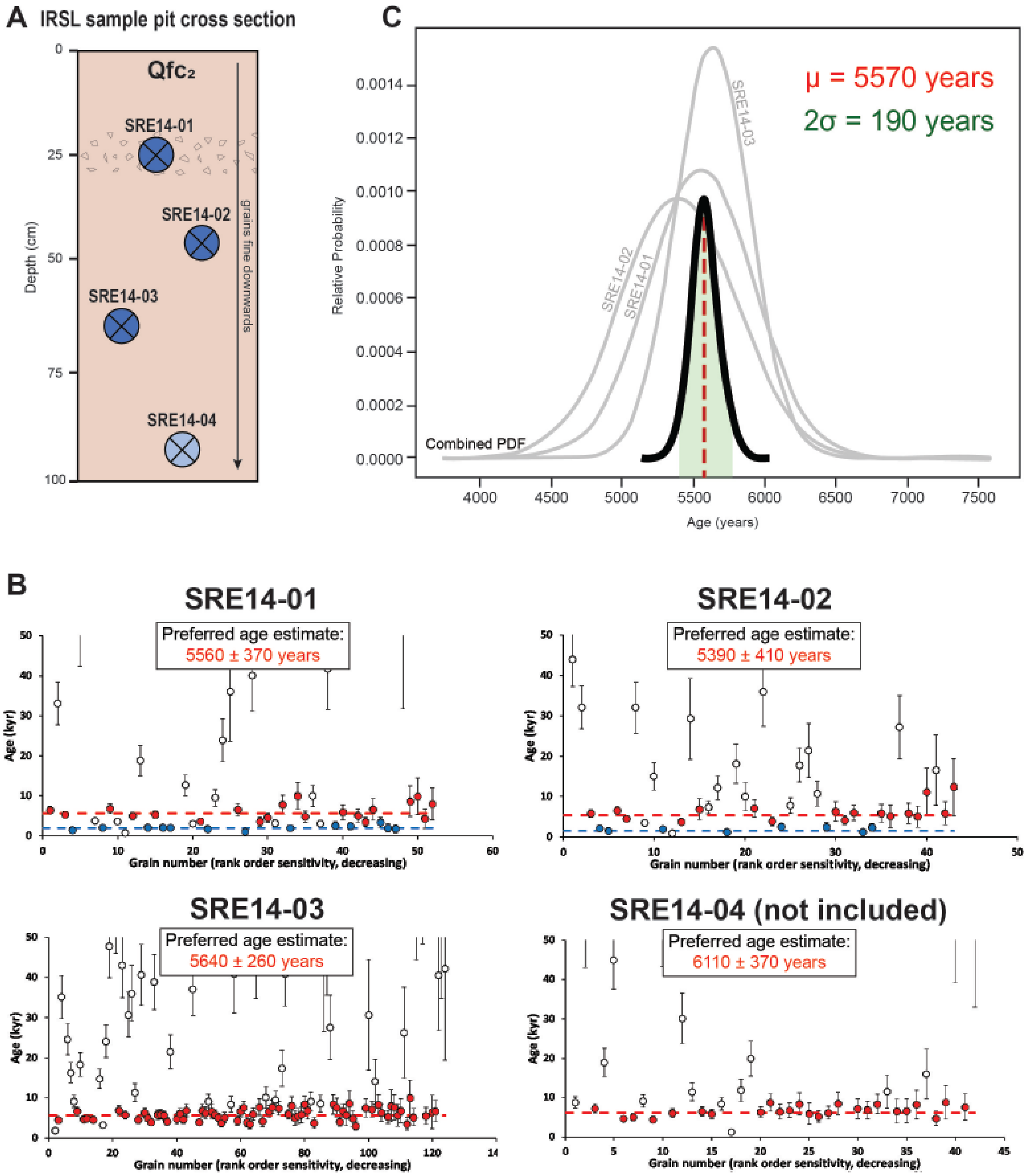

Figure 3.1.9: Post-IR IRSL225 results from the Summit Range East site.

Holocene displacement history of the central Garlock fault from the SRW, SRE and CCW sites

The two slip rates we discuss at this stop (SRW and SRE) add to a growing number of slip rates that define the incremental slip-rate record of the central Garlock fault. In figure 3.1.10B, we show the SRE and SRW slip rates, together with the 2.0 ka slip rate documented by Dolan et al. (2016) based on a 26 m offset at the Christmas Canyon West (CCW) site 13 km to the east of the SRE site and the displacement and age of the most recent event (MRE) at the El Paso Peaks trench site (McGill & Sieh, 1991; Dawson et al., 2003).

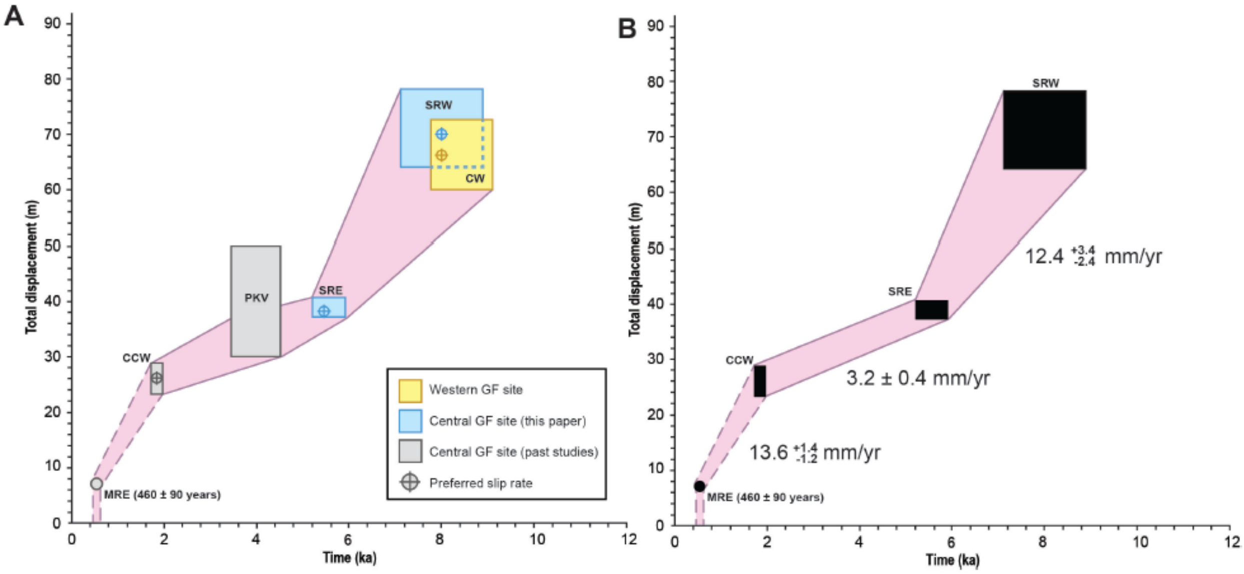

Figure 3.1.10 (a) Incremental slip history for the central and western Garlock fault including sites: CCW - Christmas Canyon West slip rate site (Dolan et al., 2016), CW - Clark Wash (this paper, building on McGill et al., 2009), MRE - most recent earthquake recorded by Dawson et al. (2003), SR - Slate Range slip rate site (Rittase et al., 2014), SRE - Summit Range East slip rate site (Fougere et al., 2024), SRW - Summit Range West slip rate site (Fougere et al., 2024, building on Ganev et al., 2012). (b) Incremental slip rates for the central Garlock fault calculated using RISeR (Zinke et al., 2017, 2019) using only the most tightly constrained rates from a 16-km-long section of the central part of the fault.

These data reveal highly irregular slip rate through time for the central Garlock fault during mid- and late Holocene time. Specifically, the data demonstrate that the fault was slipping at ~13 mm/yr – approximately double its long-term average rate – between 0.5-2.0 ka. Interestingly, this fast period corresponds to the 4-event earthquake cluster documented by Dawson et al. (2003) at the El Paso Peaks site 12 km to the west of the SRW site (Figure

3.1.2). This fast period was preceded by a period of very slow slip between 2.0 ka and ca. 5.8 ka. Paleoseismic data that we will discuss at stop 2 later today suggest that this almost 3,000-year-long lull encompassed only one or two surface ruptures (Peña, 2019; Peña et al., in preparation). In turn, the 2.0-5.8 ka slow period was preceded by an earlier period of very fast slip at ~12.5 mm/yr between ca. 5.8 ka and 8 ka (Fougere et al., 2024). This record facilitates testing for possible correlations between periods of earthquake clustering and seismic lulls with potential accelerations and decelerations of fault slip rate spanning multiple earthquake cycles, as has been suggested in previous studies (e.g., Dawson et al., 2003; Dolan et al., 2007, 2016; Ganev et al., 2012; Rittase et al., 2014). We will discuss this issue further at the second stop today.

References Cited

Clark, M., Map showing recently active breaks along the Garlock and associated faults, California. United States Geologic Survey Report, (741), 1973. doi: 10.3133/i741.

Clark, M.M. and Lajoie, K.R., 1974. Holocene behavior of the Garlock fault. In *Geological Society of America Abstracts with Programs* (Vol. 6, No. 7, pp. 156-157).

Crane, T.M., 2014. *Qualitative comparison of offset surfaces between the central and eastern Garlock fault*. M.S. Thesis, California State University, San Bernardino.

Dawson, T.E., McGill, S.F. and Rockwell, T.K., 2003. Irregular recurrence of paleoearthquakes along the central Garlock fault near El Paso Peaks, California. *Journal of Geophysical Research: Solid Earth*, *108*(B7).

Dolan, J.F., Bowman, D.D. and Sammis, C.G., 2007. Long-range and long-term fault interactions in Southern California. *Geology*, *35*(9), pp.855-858.

Dolan, J.F., McAuliffe, L.J., Rhodes, E.J., McGill, S.F. and Zinke, R., 2016. Extreme multi-millennial slip rate variations on the Garlock fault, California: Strain super-cycles, potentially time-variable fault strength, and implications for system-level earthquake occurrence. *Earth and Planetary Science Letters*, *446*, pp.123-136.

Fougere, Dannielle, 2025, *Revealing spatiotemporal patterns in fault-system behavior: Insights from multi-millennial earthquake clustering and slip-rate variability on the Garlock fault*, unpublished PhD dissertation, University of Southern California, May 2025, 183 pages.

Fougere, D., Dolan, J., Rhodes, E., & McGill, S., Refined Holocene slip rate for the western and central segments of the Garlock fault: record of alternating millennial-scale periods of fast and flow fault slip. *Seismica*, *3*(2), 2024. doi:10.26443/seismica.v3i2.1202.

Ganev, P. N., Dolan, J. F., McGill, S. F., and Frankel, K. L., Constancy of geologic slip rate along the central Garlock fault: Implications for strain accumulation and release in southern California. Geophysical Journal International, 190(2):745–760, May 2012. doi: 10.1111/j.1365-246x.2012.05494.x.

Gath, E. and Rockwell, T., 2018, Paleoseismology of the Western Garlock Fault at Campo Teresa, Tejon Ranch, Southern California, 9th International INQUA Meeting on Paleoseismology, Active Tectonics and Archeoseismology (PATA), 25 – 27 June 2018, Possidi, Greece.

Madden, C., and Dawson, T. (2006). High-resolution dating of a complete Holocene earthquake record for the central Garlock fault: Toward an understanding of earthquake recurrence, fault segment interaction and regional earthquake clustering in southern California. *SCEC Report*.

Madden Madugo, C., Dolan, J.F. and Hartleb, R.D., 2012. New paleoearthquake ages from the western Garlock fault: Implications for regional earthquake occurrence in southern California. *Bulletin of the Seismological Society of America*, *102*(6), pp.2282-2299.

McGill, S.F. and Sieh, K., 1991. Surficial offsets on the central and eastern Garlock fault associated with prehistoric earthquakes. *Journal of Geophysical Research: Solid Earth*, *96*(B13), pp.21597-21621.

McGill, S. and Sieh, K., 1993. Holocene slip rate of the central Garlock fault in southeastern Searles Valley, California. *Journal of Geophysical Research: Solid Earth*, *98*(B8), pp.14217-14231.

McGill, S.F., Wells, S.G., Fortner, S.K., Kuzma, H.A. and McGill, J.D., 2009. Slip rate of the western Garlock fault, at Clark Wash, near Lone Tree Canyon, Mojave Desert, California. *Geological Society of America Bulletin*, *121*(3-4), pp.536-554.

Peña, K., 2019. *Paleoseismology of the central Garlock fault in Searles Valley*, California. M.S. Thesis, California State University, San Bernardino.

Rhodes, E. J. Dating sediments using potassium feldspar single-grain IRSL: Initial methodological considerations. Quaternary International, 362:14–22, Mar. 2015. doi: 10.1016/j.quaint.2014.12.012.

Rittase, W.M., Kirby, E., McDonald, E., Walker, J.D., Gosse, J., Spencer, J.Q. and Herrs, A.J., 2014. Temporal variations in Holocene slip rate along the central Garlock fault, Pilot Knob Valley, California. *Lithosphere*, *6*(1), pp.48-58.

Zinke, R., Dolan, J. F., Rhodes, E. J., Van Dissen, R., & McGuire, C. P. (2017). Highly variable latest Pleistocene-Holocene incremental slip rates on the Awatere fault at Saxton River, South Island, New Zealand, revealed by lidar mapping and luminescence dating. Geophysical Research Letters, 44, 11,301–11,310. doi: 10.1002/2017GL075048

Zinke, R., Dolan, J. F., Rhodes, E. J., Van Dissen, R., McGuire, C. P., Hatem, A. E., Brown, N.D., and Langridge, R. M. (2019). Multimillennial incremental slip rate variability of the Clarence fault at the Tophouse Road site, Marlborough fault system, New Zealand. Geophysical Research Letters, 46(2), 717-725. doi: 10.1029/2018GL080688

Day 3 Stop 2: Iron Canyon

Discussion (A) Dated Late Holocene offsets and discussion of El Paso Peaks and Koehn Lake Paleoseismic Records, Garlock fault

Palesoseismic data combined with dated geomorphic offsets (N35.44404°, W 117.68179°)

Field Stop Leaders: Sally McGill, California State University, San Bernardino (CSUSB), James Dolan, University of Southern California (USC), James Burns (CSUSB), Danielle Fougere (USC [now at WSP]) and Ed Rhodes (University of Sheffield).

LOGISTICS

From Garlock Road, we will drive north along BLM route EP21. Moderately high clearance is recommended. A Subaru Forester can make it; 4WD is generally not needed as long as you don't stop in loose sand. Route EP21 eventually drops into and follows a wash within a deeply incised canyon carved into mid-Quaternary(?) alluvial fan deposits. At 1.2 miles from Garlock road, route EP21 makes a sharp left turn where the incised canyon is left-laterally offset along the Garlock fault (Figure 3.2.1). About 0.1 miles after that turn (1.3 miles from Garlock road), we continue straight (WSW) on a dirt road that is parallel to and just north of route EP 253, where EP21 bends to the north and continues up the canyon. After another 0.1 miles, park on the small playa north of the Garlock fault shutter ridge.

The goals of this stop (in addition to marveling at the large left-lateral offset of the deeply incised channel) are (1) to discuss the paleoseismic record of the central Garlock fault at this and other nearby sites, and (2) to compare that record with dated offsets of geomorphic features that record the amount of lateral slip in those earthquakes. Although the best of the dated small offsets are not easily accessible for a group this large, we can walk to one dated offset from this stop. Round trip walking will be 600 meters (0.2 miles).

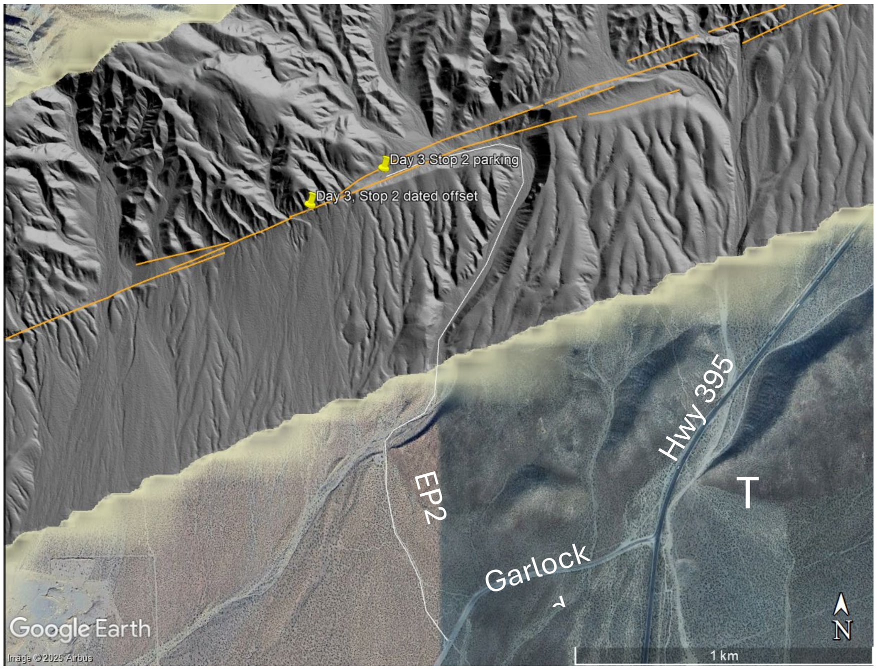

Figure 3.2A.1: *Route to Day 3, Stop 2 in the El Paso Mountains. Lidar imagery was funded by GeoEarthScope and is available at OpenTopography.org. Orange lines show faults with Holocene activity from the USGS Quaternary Fault and Fold data base. Letter "T" marks location of a published detrital sanidine age (Maguire et al., 2024; see below).*

DISCUSSION

The incised canyon we drove up has been left-laterally offset about 230-330 m, and an abandoned channel (with a fault-parallel segment) has been offset about 860-1050 m from the same source channel(s) (Figure 3.2A.2). These canyons are incised into alluvial fan deposits that have not been directly dated (to our knowledge), but they appear to be younger than, and to buttress against, older, uplifted alluvial fan sediments to the southeast that are derived from Goler Gulch and have a detrital sanidine age of 767 ± 23 ka from location "T" in Figure 3.2A.1 (Maguire et al., 2024).

Our focus at this site is on the Holocene record of earthquakes and their slip amounts. McGill and Sieh (1991) used a tape measure to measure the left-lateral offsets of 23 geomorphic features along the Garlock fault south of the El Paso Mountains (Figure 3.2A.3) and interpreted the common slip amounts of ~ 7 m, ~14 m, and ~18 m to represent the cumulative amount of slip in the past one, two and three earthquakes combined. This suggested that the two most recent earthquakes each had about 7 m of left-lateral slip and that the third event back had about 4 m of left-lateral slip.

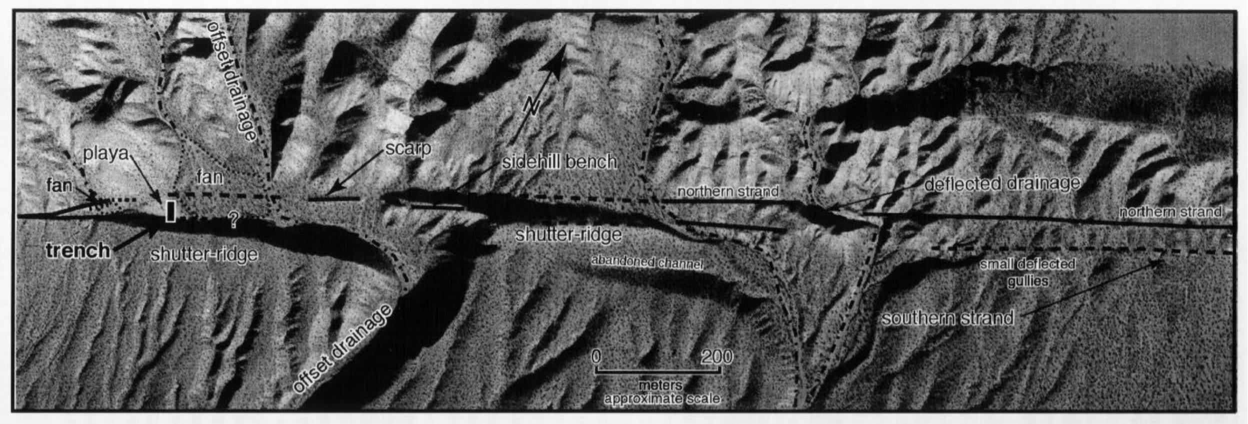

Figure 3.2.2: *Tectonic geomorphology surrounding the El Paso Peaks paleoseismic site (from Dawson et al., 2003).*

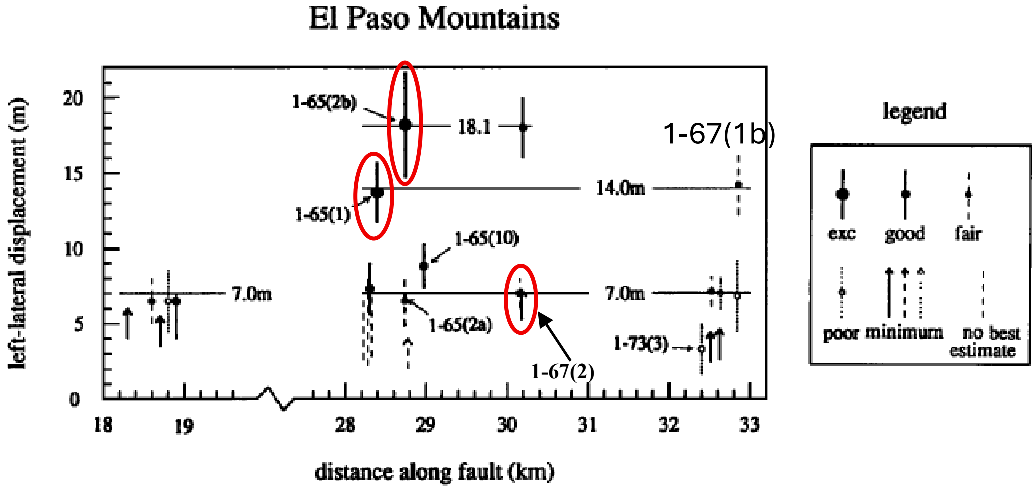

Figure 3.2.3: Measurements of offset geomorphic features along the central Garlock fault south of the El Paso Mountains (from McGill and Sieh, 1991).

Using the post-IR-IRSL225 single-grain dating method on potassium feldspar of Rhodes (2015), we have dated three of McGill and Sieh's (1991) offset features in the El Paso Mountains (circled in red in Figure 3.2A.3). We have also used drone-based aerial photography and Agisoft photogrammetric software to construct digital elevation models, hillshade images and contour lines to aid in remeasuring these three offset features (Burns, 2023). Results are shown in Table 3.2.1.

Table 3.2A.1: Dated offset features in the El Paso Mountains

McGill & Sieh label #	feature	McGill & Sieh offset (m)	Burns (2023) offset (m)	Burns (2023) Age (ka)	Burns (2023) Label
1-65(1)	Beheaded terrace and riser	13.7 ± 2.0	18 (range: 16-23)		EPM-A
1-65(2b)	Small alluvial fan	18.2 ± 3.5	23 (range: 19-25)	3.21 ± 4.4 (average of 3 samples)	EPM-B
1-67(2)	Beheaded riser	7.0 ± 1.0	9.2 ± 1.0 (max: 13.5)		EPM-C

The most conclusive results from the El Paso Mountains are from a small alluvial fan (Qal3) at EPM-B (Figure 3.2A.4) that has been offset about 23 m (range (19-25 m) from its source channel (Figure 3.2A.5). Unfortunately, this site is not easily accessible by a large group. Our preferred restoration of 23 m for this fan aligns the fan axis south of the fault with the center of the source channel north of the fault. This is larger than McGill and Sieh's (1991) measurement of 18.2 ± 3.5 m, but the uncertainties in offset overlap between the two studies. The Lidar imagery that is available today enables us to examine 0.5-m topographic contours over a broader area than was surveyed by McGill and Sieh (1991) and suggests that the eastern edge of the fan lies beyond the eastern edge of McGill and Sieh's (1991) map (Figure 3.2A.6). Our minimum possible offset restoration of 19 m pushes the east edge of the fan at the fault slightly beyond the east wall of the source channel, so any offset smaller than this is unlikely, given that the axial valley into which the fan is being deposited slopes to the southwest. The ages of three post-IR-IRSL samples from a 1-m-deep pit excavated near the apex of the offset fan range from 3460 ± 230 to 2760 ± 310 years before CE 2020. The average age of the three samples is 3210 ± 440 yrs b2020 (with one-sigma uncertainties added in quadrature).

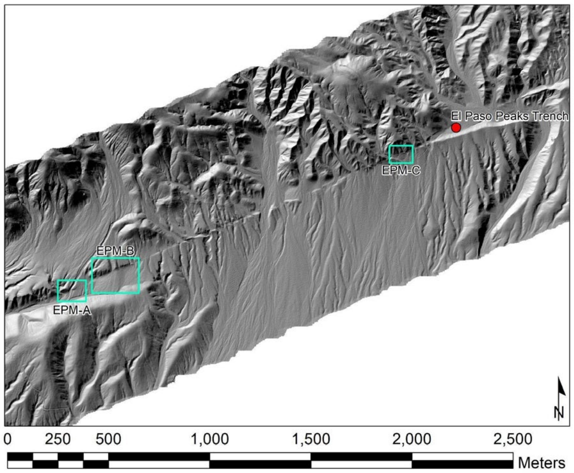

Figure 3.2A.4: *Blue rectangles show location of dated offsets along the El Paso Mountains section of the central Garlock fault (from Burns, 2023).*

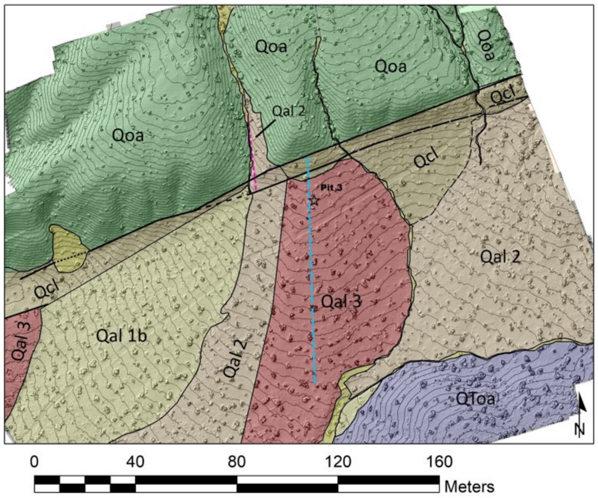

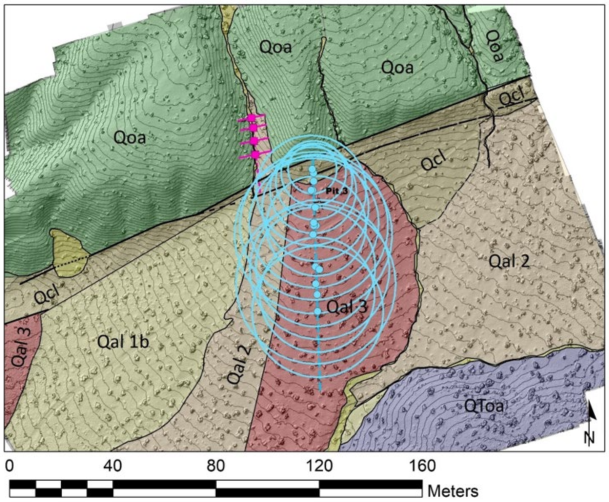

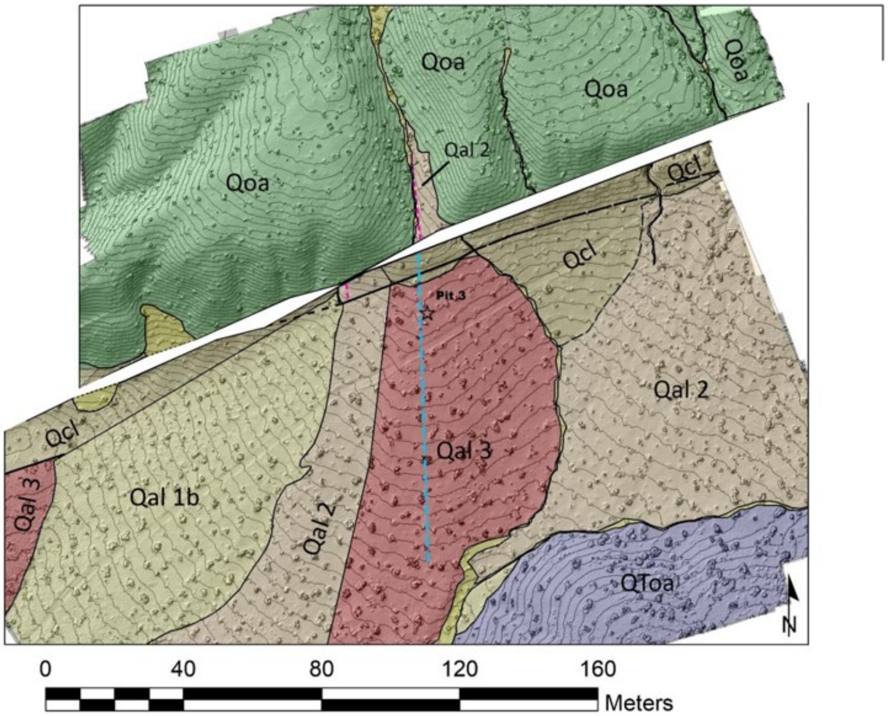

Figure 3.2A.5: Upper left, *geololgic map of a small alluvial fan at EPM-B. Contour interval is 0.5 m. Blue line shows axis of fan and pink line shows center of source channel, both of which are derived from the upper right figure.* ***Upper right,*** *same geologic map showing blue circles fit (by eye) to 0.5-m contour lines, with circle centers defining the axis of the fan (similar to method used by Gold et al., 2015, except that we fit circles by eye instead of using MatLab). North of the fault, pink lines connect contours of equal elevation on either side of the source channel, and pink dots mark the centers of those connecting lines, and, thus, the center of the source channel.* ***Lower,*** *same geologic map as in upper left, but with 23 m of left-lateral slip restored. (Figure modified from Burns, 2023).*

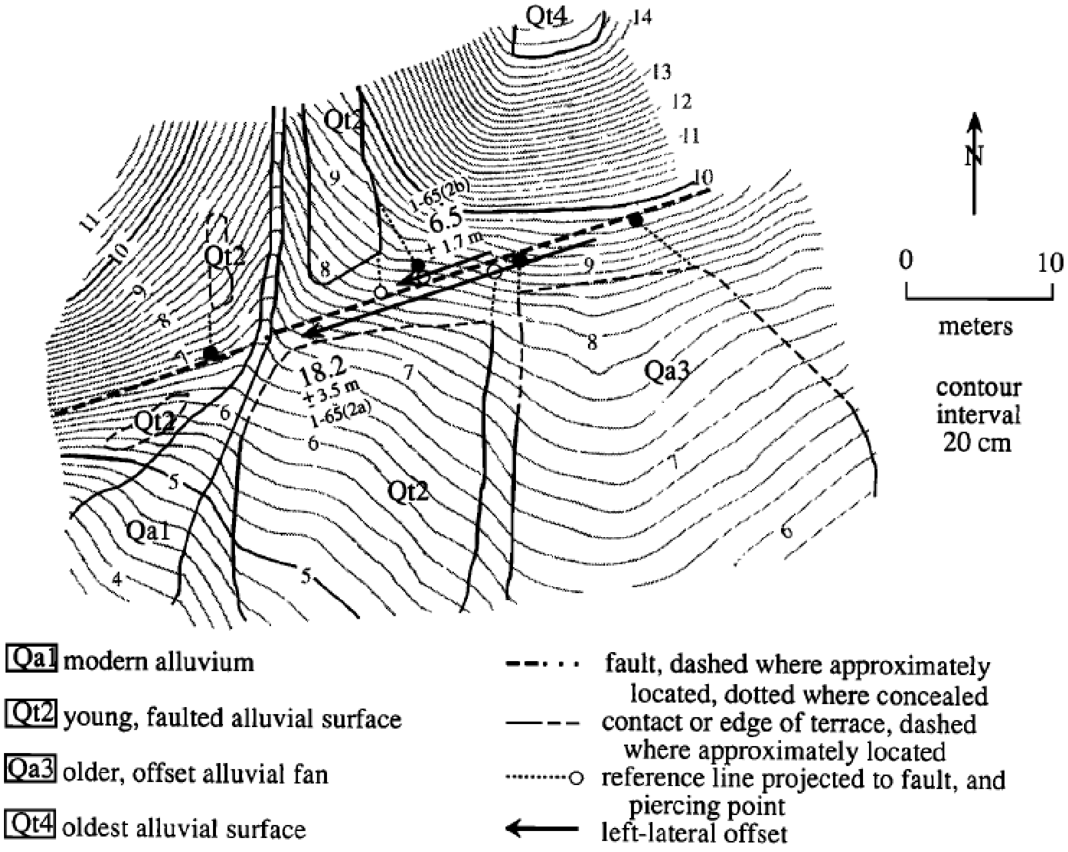

Figure 3.2A.6: *Original measurement of offset alluvial fan by McGill and Sieh (1991), which is now superseded by the 23-m restoration shown in Figure 3.2.4.*

Dawson et al.'s (2003) El Paso Peaks paleoseismic site is within a few km east of the offsets listed in Table 3.2.1, and it records four prehistoric earthquakes in the past 1.9 ka, with the next older earthquake being ~ 5 ka (Figure 3.2A.7). Thus, the 23-m offset of the small alluvial fan at EPM-B was accomplished in four earthquakes, suggesting an average slip per event of 5.75 m. Figures 3.2A.4 and 3.2A.5 show a subtle terrace riser incised into the west side of Qal3 (Fig. 3.2A.5) / Qa3 (Fig. 3.2A.6), stepping down to Qal2/Qa2. The base of this terrace riser (east edge of Qal2/Qa2) appears to be left-laterally separated about 6.5 to 8 m. This may represent the amount of slip in the most recent earthquake.

A slip rate for the time period spanned by the four most recent events (Q, R, U, and W) at the El Paso Peaks site, may now be calculated by dividing the ~23 m of slip that accumulated in those four earthquakes, by the average interval between the earthquakes. Three complete earthquake cycles occurred between the date of event Q (1860 b2020) and event W (480 b2020) (Dawson et al., 2003; Figure 3.2A.7), yielding an average recurrence interval of 460 years during this series. The current open interval between Event W and the present is 485 years, which is close to the average of the three intervals between events Q and W. Dividing the ~23 m offset of the Qal 3 fan at EPM-B, by four times the average recurrence interval during this series of earthquakes yields a slip rate of 12.5 mm/yr (range 10.3 - 13.6 mm/yr) during this series of earthquakes. This late Holocene slip rate is faster than the average slip rate during the Holocene of ~ 8 mm/yr (Fougere et al., 2024).

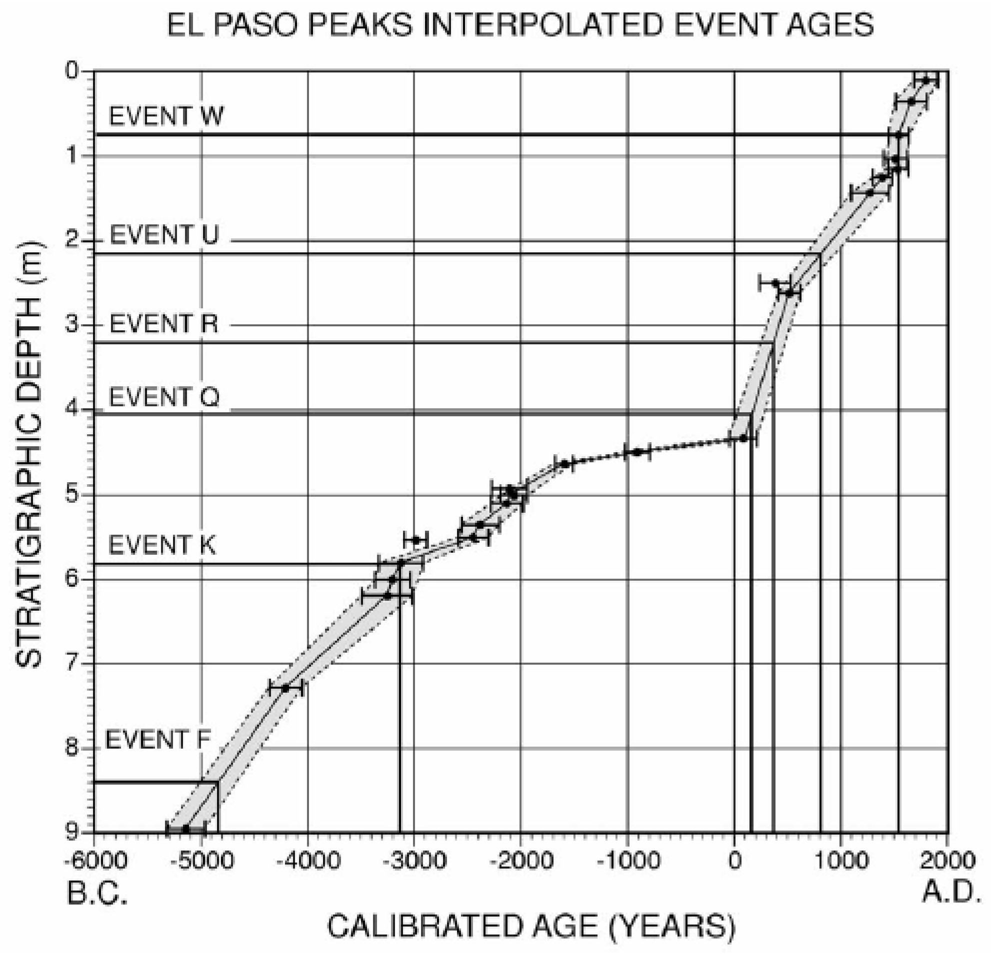

Figure 3.2.7: *Dates of prehistoric earthquakes documented at the El Paso Peaks paleoseismic site. Figure from Dawson et al., 2003).*

The results from EPM-C, which *is* accessible on this trip, are less comprehensive, but are consistent with those from EPM-B. At EPM-C a terrace riser between Qal2 and Qal3 south of the fault has been offset from its source channel north of the fault (Figure 3.2A.8). Two pits were excavated at this location for the purpose of constraining the age of this offset terrace riser. The first (Pit 4) was dug into the Qal3 terrace above the offset riser and the other (Pit 5) was dug into the alluvial terrace (Qal2) below the riser. The terrace riser is 0.5 m in height south of the fault. North of the fault the locations of points that are 0.5 m above Qal2 on the east wall of the upstream channel are marked (Figure 3.2A.9). Three possible projection lines were drawn through these points to obtain three possible piercing points on the north side of the southern fault strand, corresponding to the maximum, preferred and minimum offsets (Figure 3.2A.6 and 3.2.7), yielding a preferred reconstruction of 9.2 m 2 ± 1.0 m (Figure 3.2A.10-left). Although 10.2 m is the maximum separation between the terrace riser south of the fault and the east edge of the source channel north of the fault, if the source channel was narrower when the riser was first incised, then up to 13.5 m of left-lateral slip may have occurred since the sediments in pit 5 were deposited (Figure 3.2A.10-right).

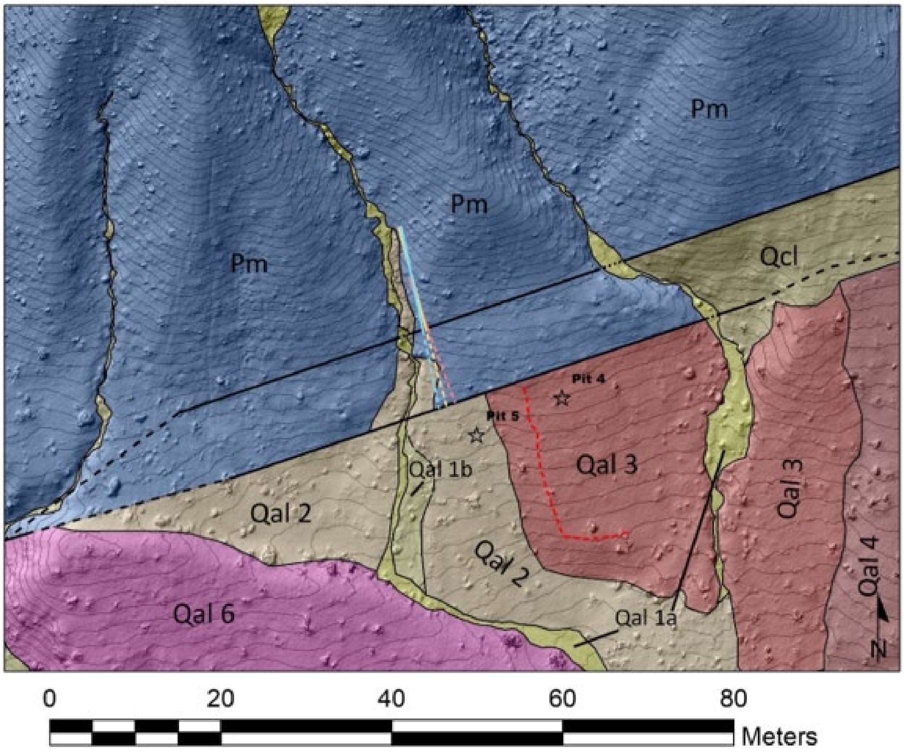

Figure 3.2A.8: *Geologic map of a terrace riser between Qal3 and Qal2 left-laterally offset from its source channel north of the fault. Figure from Burns, 2023.*

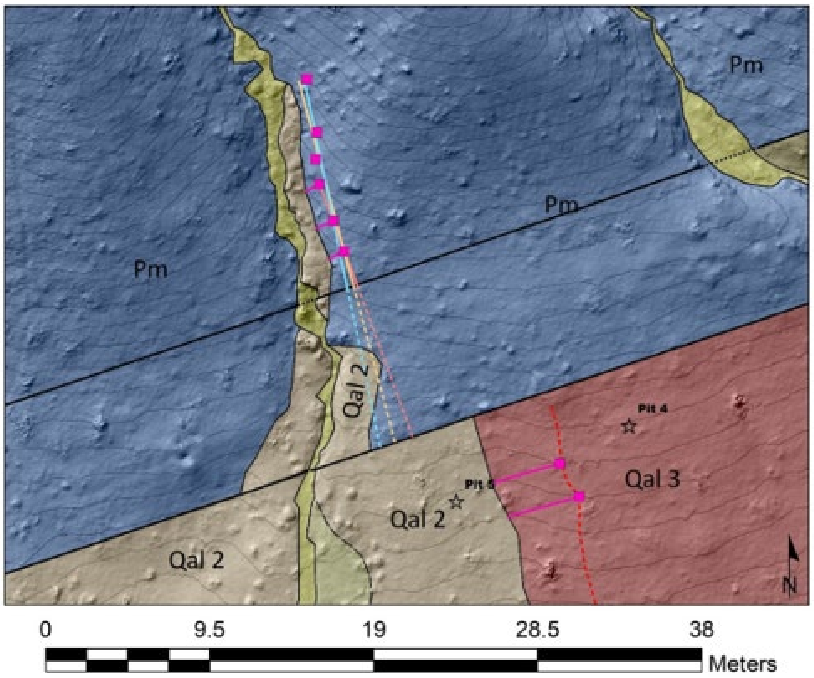

Figure 3.2A.9: *An enlarged portion of Figure 3.2A.6 showing how piercing points were determined. Figure from Burns (2023).*

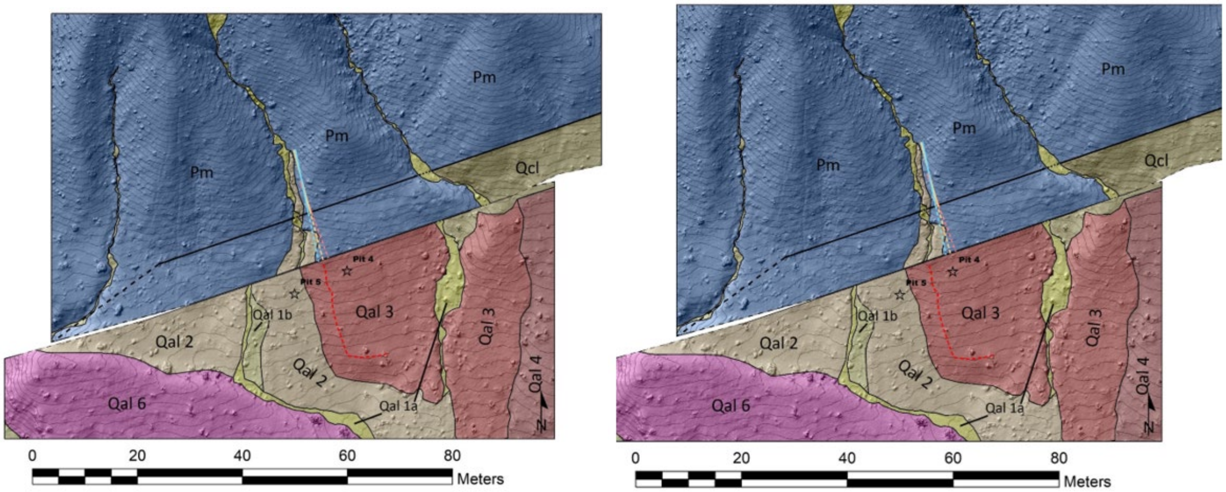

Figure 3.2A.10: Left*, preferred restoration of 9.2 m at site EPM-C.* ***Right,*** *restoration of 13.5 m of slip, which is the maximum possible offset and is only possible if the source channel was narrower at the time of initial incision than it is today. Figures from Burns (2023).*

The riser between Qal3 and Qal2 incised after sample EPM19-03 from Pit 4 in Qal3 was deposited (3690 ± 240 b2020) and before samples EPM19-04 and EPM19-05 from Pit 5 in Qal2 (1590 ± 150 b2020 and 1480 ± 180, respectively) were deposited. Comparing these ages with dates from Dawson et al.'s (2003) paleoseismic trench (located 300 m to the east) indicates that the terrace *below* the riser offset 8.2-13.5 m is old enough to have experienced the two most recent earthquakes (Events U and W) and is not old enough to have experienced the third earthquake in that trench. This is consistent with our previously determined average slip per event of about 5.75 m. Although the riser between Qal3 and Qal2 is only offset 8.2 - 13.5 m (in the two most recent earthquakes combined), the Qal3 deposit, into which the riser incised, is old enough to have experienced the most recent four earthquakes in the El Paso Peaks paleoseismic trench. In fact, the Qal3 riser at site EPM-C is comparable in age to the Qal3 alluvial fan at site EPM-B. Restoring a similar amount of slip (23 m) at EPM-C places the Qal3 deposit downstream from the nearest possible source channel (Figure 3.2A.10-right). Although there are large uncertainties in how much slip should be restored to best align the Qal3 deposit at EPM-C with its source, it is clear that 23 m provides a reasonable restoration, which is consistent with the 3.4 -3.7 ka Qal3 deposits at both EPM-B and EPM-C experiencing ~23 m of slip in the four most recent earthquakes.

Koehn Lake paleoseismic trench site

In addition to the El Paso Peaks trench record described above, a second high-resolution paleoseismic record for the western part of the central Garlock fault was recently documented at Koehn Lake by Fougere et al. (2025 in review *Seismica*). Unfortunately, access to this site would be problemative for a large group, so we take the opportunity to discuss these new paleoseismic results at this stop. Koehn Lake is an ephemeral lake that is at present largely dry, occupying an area of oblique extension caused by a left-releasing stepover in the Garlock fault that varies in width from 2 to 4 km, forming a pull-apart basin between the western and central segments of the Garlock fault (Figure 3.2A.11). The area of the pull-apart basin, Fremont Valley, exhibits a flat-floored central basin bounded by the El Paso Mountains to the north and to the south by the Rand Mountains (Dibblee and Minch, 2008). Primarily coarse-grained Quaternary alluvial sediments derived from the Mesozoic granitic rocks of the El Paso Mountains and the Mesozoic granitic rocks and the Cretaceous Rand schist exposed in the Rand Mountains are deposited along the northern and southern margins of the Fremont Valley (Figure 3.2A.11).

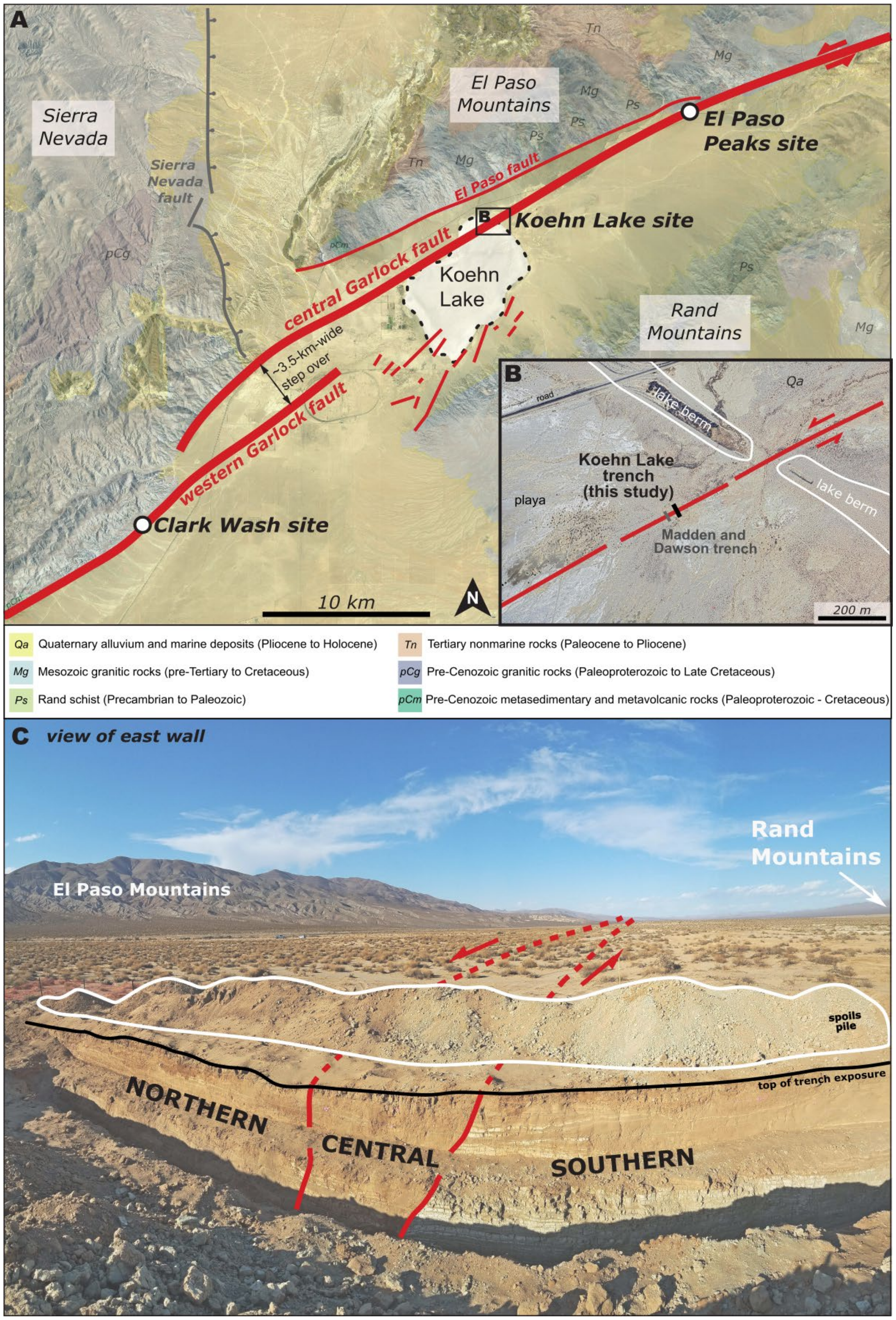

Figure 3.2A.11. *(a) Fremont Valley map with geology sourced from Macrostrat (Peters et al., 2018), (b) Annotated satellite image of the Koehn Lake paleoseismic and slip rate site (Google Earth, accessed December 2024), and (c) Annotated photograph of the Koehn Lake trench looking eastwards.*

At the Koehn Lake site, the westernmost part of the central segment of the Garlock fault cuts through the northeastern corner of the dry lake bed (Figure 3.2A.11). To the north of

Koehn Lake and the central Garlock fault segment, the El Paso fault extends sub-parallel to the active Garlock fault for 26 km along the southern front of the El Paso Mountains. This fault, however, does not show any geomorphic evidence of Holocene displacement (USGS Quaternary Fault and Fold Database, accessed December 2024). In contrast, the central Garlock fault strand that extends along the northwestern corner of the Koehn Lake basin displays abundant geomorphic evidence of Holocene displacements (Clark, 1973; McGill and Rockwell, 1998; Madden and Dawson, 2006).

Burke (1979) excavated a trench across the Garlock fault at a site near the northeastern corner of the dry lake bed, where the playa sediments interfinger with the distal portions of alluvial fans derived from the north and northeast. He reported evidence for 9-17 earthquakes constrained by a single radiocarbon age, recalibrated in this study using Oxcal version 4.4 and the most up-to-date calibration curve (IntCal20, Bronk Ramsey, 2009; Reimer et al., 2020), of 17,530-18,250 cal. years B.P. Madden and Dawson (2006) re-excavated the Burke (1979) trench and documented seven to nine surface ruptures at the site since 10 ka, with three to five of these earthquakes occurring since 4150 years ago.

More recently, Fougere et al. (2025 in review *Seismica*) excavated a 37-m-long, 2.5-m-deep trench across the Garlock fault ~20 m to the east of the paleoseismic trenches of Burke (1979) and Madden and Dawson (2006). The main fault zone exposed in this trench is expressed as two major fault strands that bound a 5- to 6-m-wide central graben (Figure 3.2A.11). Complete stratigraphic mismatches between the sections bounded by these faults indicate that they have accommodated most of the left-lateral displacement through the trench site. Additionally, minor faulting occurs throughout the northern and southern sections of the trench, which are less densely faulted than the central section. Although stratigraphy throughout the trench was generally well defined at the cm to dm scale, the extremely friable nature of the upper 0.5-1 m of the trench made identification of event horizons within these sediments difficult, resulting in a high likelihood of missing a few latest Holocene events at this site.

Detailed mapping of the trench walls revealed numerous well-defined surface rupture event horizons, which were identified by a variety of event indicators, including upward fault terminations, filled fissures, angular unconformities, growth stratigraphy, collapse features, and soft-sediment deformation features. The ages of these event horizons were constrained with 51 Infrared Stimulated Luminescence (IRSL) ages and 47 ^{14}C analyses. The resulting paleo-earthquake ages, when combined with paleo-earthquake ages from the nearby El Paso Peaks trench of Dawson et al. (2003), reveal a detailed chronology of paleo-earthquake occurrence along the central Garlock fault since ca. 12 ka (Figure 3.2A.12). This 14-event record demonstrates that earthquake recurrence on the Garlock fault has been characterized by temporal clusters of closely timed earthquakes separated by millennia-long periods of relative seismic quiescence. Specifically, the data reveal three temporal clusters of four earthquakes each at 0.5-2.0 ka (previously identified by Dawson et al., 2003), 5.0-7.1 ka, and 8.2-10.1 ka.

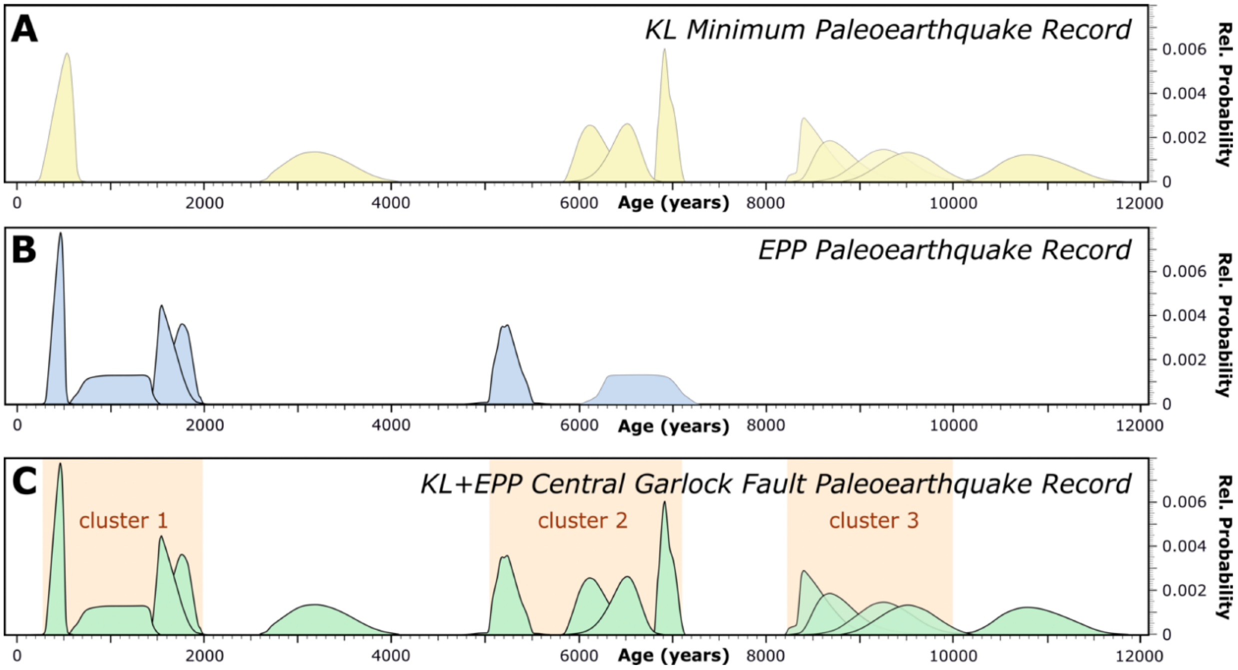

Figure 3.2A.12: A. Minimum paleo-earthquake record for the Koehn Lake site (record is incomplete during the past 2 ka). B. Minimum paleo-earthquake record for the El Paso Peaks site (Dawson et al., 2003). C. Combined record for the Koehn Lake and El Paso Peaks sites (from Fougere, 2025; See also Fougere et al., in review, Seismica). Ages of each event are shown as probability density functions and temporal clusters of earthquakes (cluster 1, 2, and 3) are highlighted in orange in part C.

Holocene to latest Pleistocene displacement history of the central Garlock fault

Over the past several decades, multiple researchers have documented both paleo-earthquake age data and fault slip rates at different displacement scales for the Garlock fault spanning Holocene and latest Pleistocene time (McGill & Sieh, 1991; 1993; McGill et al., 2009; Madden Madugo et al., 2012; Rittasse et al., 2013; Dolan et al., 2016; Fougere, 2025; Fougere et al., 2024; 2025 in review; 2025 in preparation). Taken together, the resulting paired paleo-earthquake age + incremental slip-rate record for the central Garlock fault represents one of the most detailed records of its kind for any fault in the world over Holocene-latest Pelistocene time scales. Specifically, we have documented thirteen different slip-rates along the central Garlock fault over a wide range of different Holocene and latest Pleistocene time-scales sapping 0.5 ka to ca. 14 ka and displacements from <10 m to >100 m (McGill et al., 2009; Dolan et al., 2016; Fougere et al., 2024; 2025 in preparation). In addition to the late Holocene slip rate of Rittasse et al. (2014) from Pilot Knob Valley, this exceptionally detailed incremental slip-rate record facilitates comparison with the detailed paleo-earthquake age records from the El Paso peaks site of Dawson et al. (2003) and the new record from the Koehn Lake site of Fougere et al. (2025, in review).

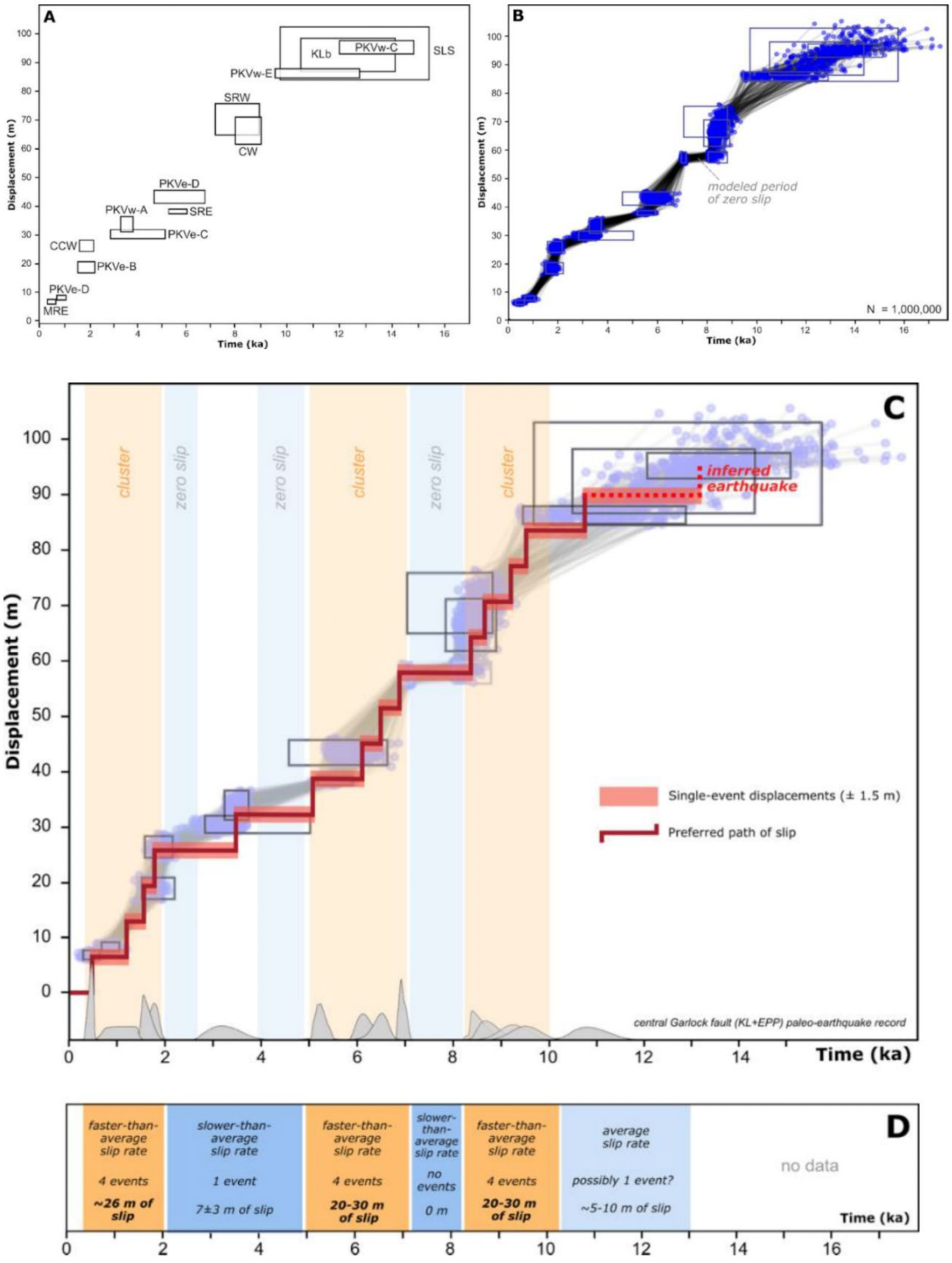

Fig. 3.2A.13: Figure 5.10 (A) Age-displacement measurements used in incremental slip rate record for the western and central Garlock fault, (B) updated in incremental slip rate record

calculated using RISer (Zinke et al., 2017; 2019), (C) combined records showing earthquake-by-earthquake slip, and (D) summary of periods of fault behavior.

Preliminary compilation of all of these results (Figure 3.2A.13; Fougere, 2025; Fougere et al., manuscript in preparation 2025) reveals periods of much-faster-than-average slip rate spanning ~25 m of fault slip that occurred during temporal clusters consisting of four earthquakes each (0.5-2.0 ka; 5.0-7.1 ka; 8.1-10.1 ka) that are separated by millennia-long periods of much slower (2.0-5.0 ka; 10.1-13.0 ka) or no (7.1-8.1 ka) slip during Holocene and latest Pleistocene time; slip rates during the fast periods are ~13 mm/yr relative to the long-term average slip rate of the central Garlock fault of ~7.5-8.5 mm/yr. These fast-slow alternations in slip rate may be a result of fault interactions amongst the Garlock and San Andreas faults and the faults of the eastern California shear zone (ECSZ), as suggested by Dolan et al. (2007; 2016) and Hatem et al. (2018). These models suggest that the Pacific-North America plate boundary fault system in this part of southern California comprises two sub-systems, in which the sub-system consisting of the Garlock fault and Mojave segment of the San Andreas fault (SAFm) alternates periods of faster-than-average slip with its mechanically complementary sub-system encompassing the faults of the ECSZ. In this model, the Garlock fault and SAFm are currently in a relatively “slow” mode, whereas the ECSZ is currently in a “fast” mode, perhaps accounting for the numerous historical earthquakes that have occurred in the ECSZ (1872 Owens Valley; 1992 Landers; 1999 Hector Mine; 2019 Ridgecrest) relative to the dearth of large-magnitude earthquakes and apparent relatively slow rates of elastic strain accumulation observed on the Garlock fault and SAFm. An emerging incremental slip-rate record for the for the Mojave section of the SAFm supports this possibility, at least as far back as the current ca. 4 ka limit of the overlapping SAFm and Garlock fault incremental slip-rate records, in which the SAFm and Garlock fault appear to exhibit similar timing in terms of switches between fast and slow modes (Gordon et al., 2025 in prep).

References Cited

Burns, James, 2023, *Late Holoene slip history of the central Garlock fault, Mojave Desert*, *California*, M.S. Thesis, California State University, San Bernardino, 137 pp.

Clark, M. M., 1973, Map showing recently active breaks along the Garlock and associated faults, Californian: U.S. Geological Survey Map I-741.

Dawson, T. E., McGill, S. F., and Rockwell, T. K., 2003, Irregular recurrence of paleoearthquakes along the central Garlock fault near El Paso Peaks, California. *Journal of Geophysical Research*, 108(B7), 2356, 2003. doi:10.1029/2001JB001744.

Dibblee, T. W. and Minch, J.A. (2008). Geologic Map of the Cross Mountain & Saltdale 15 Minute Quadrangles: Kern County, California. Santa Barbara Museum of Natural History.

Dolan, J.F., Bowman, D.D. and Sammis, C.G., 2007. Long-range and long-term fault interactions in Southern California. *Geology*, *35*(9), pp.855-858.

Dolan, J.F., McAuliffe, L.J., Rhodes, E.J., McGill, S.F. and Zinke, R., 2016. Extreme multi-millennial slip rate variations on the Garlock fault, California: Strain super-cycles, potentially time-variable fault strength, and implications for system-level earthquake occurrence. *Earth and Planetary Science Letters*, *446*, pp.123-136.

Fougere, Dannielle, 2025, *Revealing spatiotemporal patterns in fault-system behavior: Insights from multi-millennial earthquake clustering and slip-rate variability on the Garlock fault*, unpublished PhD dissertation, University of Southern California, May 2025, 183 pages.

Fougere, D., Dolan, J., Rhodes, E. and McGill, S., 2024, Refined Holocene slip rate for the western and central segments of the Garlock fault: Record of alternating millennial-scale periods of fast and flow fault slip. *Seismica,* 3(2), 21 pp. doi: 10.26443/seismica.v3i2.1202.

Fougere, D. M., J. F. Dolan, A. H. Ivester, S. F. McGill, E. J. Rhodes, C. J. Anthonissen, and J. Gauriau, in review, A 12,000-year-long record of paleo-earthquakes on the Garlock Fault at Koehn Lake: Implications for multi-millennial earthquake clustering, regional fault interactions, and seismic hazard analysis, submitted to *Seismica*, September 2025.

Gold, P.O., Behr, W.M., Rood, D., Sharp, W.D., Rockwell, T.K., Kendrick, K., and Salin, A., 2015, Holocene geologic slip rate for the Banning strand of the southern San Andreas Fault, southern California: *Journal of Geophysical Research, Solid Earth*, v. 120, 25 pp., doi:10.1002/2015JB012004.

Hatem, A.E. and Dolan, J.F., 2018. A model for the initiation, evolution, and controls on seismic behavior of the Garlock fault, California. *Geochemistry, Geophysics, Geosystems*, *19*(7), pp.2166-2178.

Madden, C., and Dawson, T. (2006). High-resolution dating of a complete Holocene earthquake record for the central Garlock fault: Toward an understanding of earthquake recurrence, fault segment interaction and regional earthquake clustering in southern California. *SCEC Report.*

Maguire, S., E. Kirby, D. Walker, M. Heizler, E. McDonald, Y. Asmerom, and V. Polyak, 2024, Evaluations slip along the Garlock fault zone, eastern California, at timescales of 10^4 to 10^6 years, *Geological Society of America Abstracts with Programs*, Vol. 56, No. 5, 2024. doi: 10.1130/abs/2024AM-405056.

McGill, S. F., Sieh, K. Surficial offsets on the central and eastern Garlock Fault associated with prehistoric earthquakes. *Journal of Geophysical Research*, 96, 21,597-21,621, 1991.

McGill, S., & Rockwell, T. (1998). Ages of late Holocene earthquakes on the central Garlock fault near El Paso Peaks, California. Journal of Geophysical Research: Solid Earth, 103(B4), 7265-7279. doi: 10.1029/97JB02129

McGill, S.F., Wells, S.G., Fortner, S.K., Kuzma, H.A. and McGill, J.D., 2009. Slip rate of the western Garlock fault, at Clark Wash, near Lone Tree Canyon, Mojave Desert, California. *Geological Society of America Bulletin*, *121*(3-4), pp.536-554.

Rhodes, E. J. Dating sediments using potassium feldspar single-grain IRSL: Initial methodological considerations. Quaternary International, 362:14–22, Mar. 2015. doi: 10.1016/j.quaint.2014.12.012.

Rittase, W.M., Kirby, E., McDonald, E., Walker, J.D., Gosse, J., Spencer, J.Q. and Herrs, A.J., 2014. Temporal variations in Holocene slip rate along the central Garlock fault, Pilot Knob Valley, California. *Lithosphere*, *6*(1), pp.48-58.

Zinke, R., Dolan, J. F., Rhodes, E. J., Van Dissen, R., & McGuire, C. P. (2017). Highly variable latest Pleistocene-Holocene incremental slip rates on the Awatere fault at Saxton River, South Island, New Zealand, revealed by lidar mapping and luminescence dating. *Geophysical Research Letters*, 44, 11,301–11,310. doi: 10.1002/2017GL075048

Zinke, R., Dolan, J. F., Rhodes, E. J., Van Dissen, R., McGuire, C. P., Hatem, A. E., Brown, N.D., and Langridge, R. M. (2019). Multimillennial incremental slip rate variability of the Clarence fault at the Tophouse Road site, Marlborough fault system, New Zealand. *Geophysical Research Letters*, 46(2), 717-725. doi: 10.1029/2018GL080688

Discussion (B) Pleistocene slip rates along the Garlock fault determined from displaced fanglomerates

Sydney Maguire, Columbia University/Lamont Doherty Earth Observatory, NY
Eric Kirby, Penn State University, PA

LOGISTICS

From Stop 2A, you have the option to drive from stop 2A or walk to stop 2B by either southward down the alluvial fan or following the dirt road we drove in on through the canyon.

Stop 2B Coordinates: 35°26'23.13"N, 117°40'47.71"W

The goals of this stop are to observe the provenance of fanglomerate deposits that have been displaced eastward relative to unique source watersheds in the El Paso Mountains (Carter, 1994). We will discuss (1) new mapping of these fanglomerate deposits that reveals stratigraphic patterns consistent with translation of deposits along the El Paso Range, (2) new maximum depositional ages of the deposits determined using $^{40}Ar/^{39}Ar$ dating of detrital volcanic sanidine, and (3) implications for slip-rates along the Garlock fault during the past 2 Myr.

Stop 2B Discussion

The Garlock fault zone presents an enigmatic example of how interseismic strain accumulation interacts with an active fault. Dextral shear along the ECSZ passes continuously across the Garlock fault (Savage et al., 1990; Peltzer et al., 2001) without any apparent signal of elastic strain accumulation along the fault (Meade and Hager, 2005). The absence of cross-cutting relationships between ECSZ faults and the Garlock fault zone (GFZ) further suggests the fault may have passively rotated with distributed shear across eastern California (Gan et al., 2003; Guest et al., 2003), leading to abandonment of prior fault

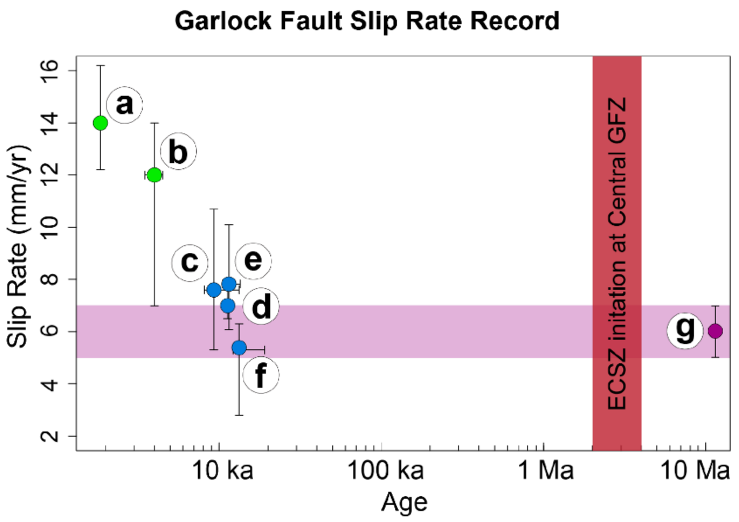

Figure 3-2B-1: Garlock fault slip rate record. Sources are as follows: a - Dolan et al., 2016; b - Rittase et al., 2014; c - McGill et al., 2009; d - Clark and Lajoie, 1974; e - McGill and Sieh, 1993; f - Ganev et al., 2012; Slip rate "g", denotes the 5-7 km/Myr rate of the Garlock since the Miocene (see review by Andrew et al., 2015).

strands (e.g., Marine Gate fault, Andrew et al., 2023). The pace of slip along the Garlock fault during this interaction, however, is poorly known. The Garlock fault is thought to have initiated around ~11 Ma (Burbank and Whistler, 1987; Loomis and Burbank, 1988; Blythe and Longinotti, 2013; Andrew et al., 2015; Ludwig, 2022) and to have accumulated ~65 km of displacement since that time (Smith, 1962; Dibblee, 1967; Smith et al., 1968; Smith and Ketner, 1970; Jahns et al., 1971; Davis and Burchfiel, 1973; Carr et al., 1997). Despite abundant markers of displacement along the GFZ during the Late Pleistocene and Holocene (e.g. Clark and Lajoie, 1974; McGill and Sieh, 1991; McGill and Sieh, 1993; McGill et al., 2009; Ganev et al., 2012; Rittase et al., 2014; Dolan et al., 2016; Fougere et al., 2024), there are no data that constrain slip rates in time intervals between ~15 ka and ~11 Ma (Figure 3-2B-1). To fill this gap, we examine the timing and magnitude of displacement of several geologic and geomorphic features along the southern flank of the El Paso Mountains.

Displacement of fanglomerate deposits along the southern flank of the range provide a unique record of fault displacement ranging from ~800 m to 18 km along the combined El Paso and Garlock faults (Carter, 1980; 1994). Bedrock strata within the El Paso Mountains are subvertical and strike NNW, nearly orthogonal to the Garlock fault zone (Figure 2). This fortuitous orientation leads to alluvial fan lithologies with distinct provenance that are sourced from distinct watersheds along the range front (Carter, 1994).

Modern alluvial fans exhibit unique provenance at Mesquite Canyon and Goler Gulch (Carter, 1980; 1994). At Mesquite Canyon, abundant angular clasts of Mesquite Schist, a distinctive porphyroblastic, fine-grained, quartz-sericite-albite schist (Christiansen, 1961) comprise the majority of modern clasts; this watershed is the only location along the El Paso range front where this unit is found in modern fans (Carter, 1980; 1994). At Goler Gulch, modern alluvium contain a unique pairing of quartzite cobbles derived from the Paleocene Goler Formation, a conglomerate located near the crest of the range, and massive, unfractured boulders of the Miocene Black Mountain Basalt (Carter, 1994). Although there are locations along the range front where each of these units provides sediment to modern fans, Goler Gulch is the only watershed where they are being actively eroded together (Carter, 1994).

Fanglomerate deposits south of the Garlock fault with similar provenance are found many kilometers east of their source area, suggesting that these fanglomerate deposits have been laterally displaced along the fault system (Carter, 1980; 1994). These deposits comprise a prominent shutter ridge east of Goler Gulch (referred to as the Powerline shutter ridge), alluvial fans between Iron Canyon and US-395, and topographically prominent outcrops east of US-395 in the Summit Diggings area (Dibblee, 1952; Carter 1980; 1994; Andrew et al. 2014; 2015).

New mapping of the fault-displaced fanglomerates (Figure 3-2B-2) reveal a system of alluvial fan deposition across the Garlock and subsequent translation eastward with burial by more eastward fan sources. Stratigraphy of fanglomerate units at the Powerline shutter ridge, alluvial fans between Iron Canyon and US-395, and topographically prominent outcrops east of US-395 in the Summit Diggings area demonstrate identical stacking order of fanglomerate packages with distinct lithologies.

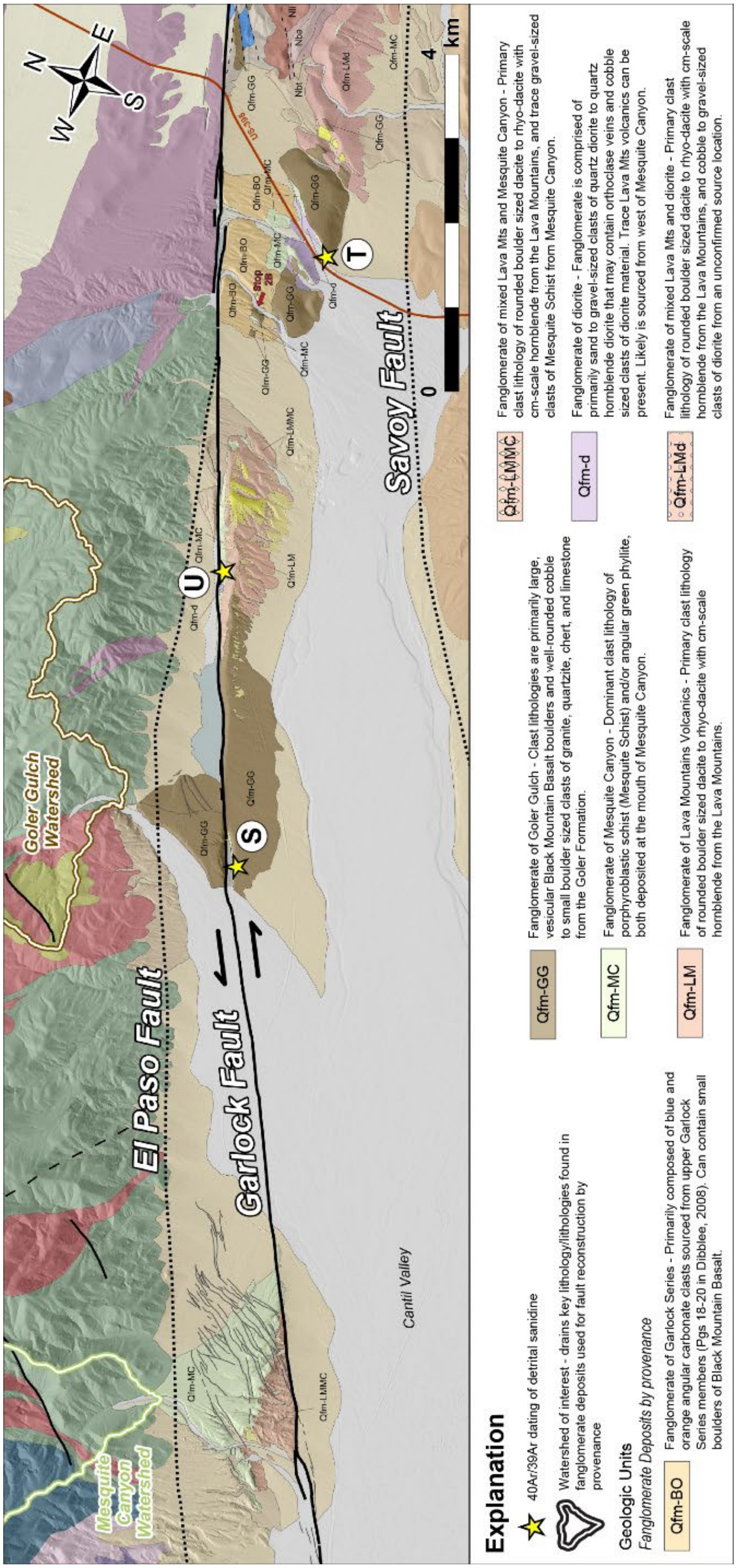

Figure 3-2B-2: Geologic map of fanglomerate deposits by provenance. See explanation for descriptions. 40Ar/39Ar Detrital Sanidine sample locations noted with a symbol and label in a white circle.

Here at the Iron Canyon Stop 2B, we stand before three alluvial fanglomerate packages. To the west, sediment sourced from Goler Gulch is preserved in pedogenic carbonate overlaying sediment sourced from Mesquite Canyon. Sediment derived from the Paleozoic Garlock Series onlaps these basalt-mantled hillslopes and can be found stratigraphically above in some places along the eastward wall of the canyon.

To establish a chronologic sequence of fanglomerate deposition, we employ a relatively new approach to establishing the maximum deposition age (MDA) of deposits through $^{40}Ar/^{39}Ar$ dating of detrital sanidine (DS) grains (e.g., Heizler et al., 2021). This method has been shown to place maximum bounds on the ages of Plio-Pleistocene terrestrial sedimentary deposits throughout western North America (e.g., Hereford et al., 2016; Aslan et al., 2018; Heizler et al., 2021) and Oligocene strata along the Gulf Coast (Yancey et al., 2018). MDAs for an alluvial deposit rely on determining the age of >100 sanidine crystals in a given sample using the ^{40}Ar/^{39}Ar geochronologic system (Heizler et al., 2017) and are generally derived by calculating the weighted inverse variance mean age of the youngest population of ages in the sample (Figure 3-2B-3). In cases where a population cannot be defined, the age of the youngest 2 or 3 grains provide a bound on the age of the deposit (Heizler et al., 2021). In this field guide, we present three new MDAs from ^{40}Ar/^{39}Ar ages of detrital sanidine. These ages provide maximum constraints for the timing of deposits with known provenance that we use to estimate minimum slip rates along the Garlock fault.

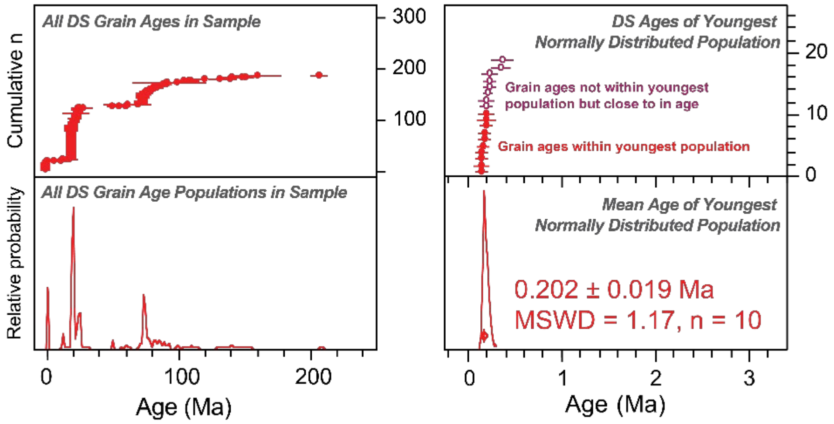

Figure 3-2B-3: Example of ^{40}Ar/^{39}Ar detrital sanidine age distributions for sample S. Full sample age distribution (left) and youngest normally distributed population (right). For youngest population, solid symbols indicate analyses used to define weighted mean ages, and open symbols show analyses excluded from calculation. All age uncertainties are reported at 2σ. MSWD—mean square of weighted deviates.

Slip Rates Since 200 Ka – Goler Heights Alluvial Fan

The distal portions of a distinct alluvial fan at Goler Gulch has been displaced by the main strand of the Garlock fault zone by ~800 meters (Figure 3-2B-4). This fan, located immediately east of Goler Gulch, is home to the unincorporated community of Goler Heights and is referred to as the Goler Heights Fan (GHF). The GHF is made up of at least two generations of fan development; an older surface preserved east of the primary axis of the fan that is cut by secondary normal faults trending NE, oblique to the Garlock fault, and a

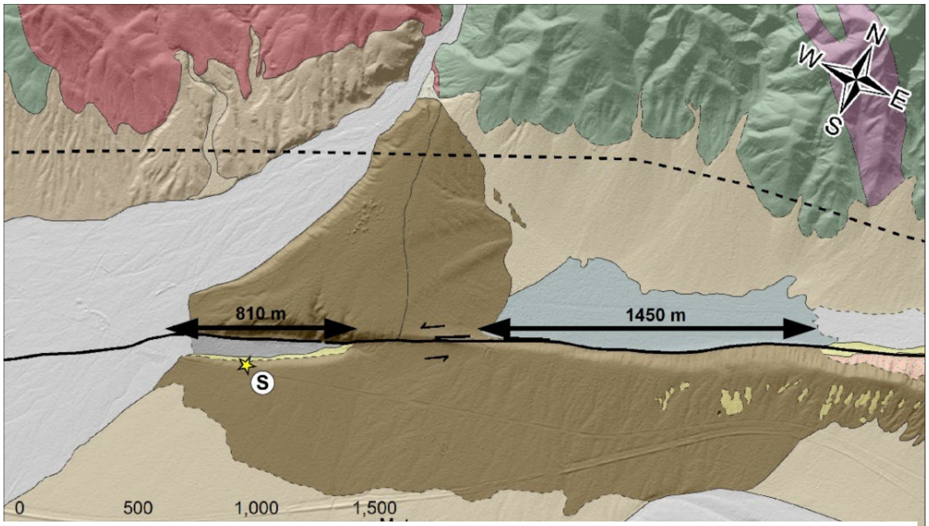

Figure 3-2B-4: Back-slip end-member scenarios for slip reconstructions of the Goler Heights Fan. Left end-member shows reconstruction of fan riser geomorphology. Right end-member shows reconstruction based on the relative age difference in alluvial fanglomerate deposits. Geology corresponds to mapped units in Figure 3-2B-2. Sample location noted with a yellow younger fan surface with no obvious scarps. Both surfaces are elevated by 15-20 m relative to the modern wash. The deposit contains large (up to 1 m) Black Mountain Basalt boulders and cobbles from the Goler Formation. This edge forms a topographic riser between the GHF surface and the active wash. A similar riser is present south of the Garlock fault, that separates the alluvial fan surface ~800-meter-long, 100-meter-wide fault-parallel depression that closes eastward along the fault. Boulders of Black Mountain Basalt and Goler Formation conglomerate clasts are exposed in colluvium and gullies along the riser, indicating Goler Gulch provenance as well. Carter (1994) suggested that the two risers are the same feature, offset a minimum of 800 meters by the Garlock. Our observations suggest that the surface morphology, relative degree of soil development, and sediment provenance are similar to the fan north of the Garlock fault, and therefore we agree with the interpretation that this is a displaced fan-terrace riser.

To determine the age of the fan surface, we sampled sand from a 10-20 cm thick lens exposed in a shallow borrow pit along the north-facing fan-terrace riser south of the Garlock, 1-1.5 meters below the depositional surface of the fan. The sample yielded 187 DS grains ranging in age from ~180 ka to >200 Ma, with 18 grains yielding individual ages <300 ka (Figure 3-2B-3). Of these, 10 grains define the youngest normally distributed population with a mean age of 202 ± 19 ka and an MSWD near 1. Following Heizler et al. (2021), we consider this to be a reasonable estimate of the maximum depositional age (MDA) from these data. Notably, this is a time period of numerous small silicic volcanic centers in the Coso Volcanic Field (Mantley and Bacon, 2000), and we believe this is a likely source for the sanidine.

We reconstruct the offset between the two risers by aligning geologic observations. Piercing points are obscured by both erosion and slope modification but are better estimated for the SGF where the riser terminates against the Garlock fault scarp. We assume a minimum offset of 810 meters by restoring this point to the western edge of the present day GHF. The maximum allowable offset is limited by the characteristics of mapped fanglomerate sediment along the Powerline shutter ridge. Because the fault acts a conveyor belt with continuous eastward sliding of deposits, we can only reconstruct a maximum amount of slip by aligning the eastern edge of the fan to where an obvious discrepancy in relative age exists between the GHF and the fanglomerate deposits with Goler Gulch provenance (Qfm-GG) within the Powerline shutter ridge. The eastern edge of the GHF aligns with the geologic contact between first-order Qfm-GG fanglomerate sediment and a second-order colluvial apron of Qfm-GG fanglomerate sediment at approximately 1450 meters east of the modern wash. The source fanglomerate of this apron is markedly more incised than the fanglomerate to the west. We interpret this contact as the eastern-most possible extent of the GHF surface south of the Garlock. Together, our interpretation implies that the minimum slip rate at this site ranges from *3.6 to 7.9 mm/yr since ~200 ka*.

Slip Rates Since 1-2 Ma

To estimate slip rates along the Garlock for the last 1-2 Ma, we reconstruct two different packages of fanglomerate sediment to their associated watersheds by their clast provenance.

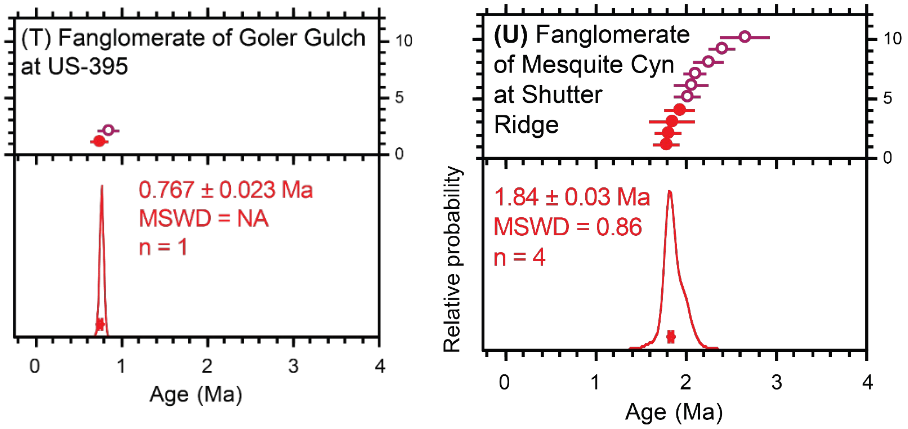

Figure 3-2B-5: Youngest age population of detrital sanidine grains for Sample T and U. "n" defines the number of grains used to constrain the MDA. Solid symbols indicate analyses used to define weighted mean ages, and open symbols show analyses excluded from calculation. All age uncertainties are reported at 2σ. MSWD—mean square of weighted deviates.

Immediately east of US-395, a two-meter-thick package of Qfm-GG sediment mantles the south side of the hill approximately ~7 km from its source at Goler Gulch. Of the 275 detrital sanidine grains we dated, the youngest single grain defines an MDA of 767 ± 23 ka (Figure 3-2B-5). A second grain with an age of 874 ± 23 ka confirms the presence of young grains in this sample, but these two ages do not define a normal distribution. Rather, we use the age of the single youngest grain to define the MDA from this sample, following Heizler et al. (2021). To assess the distance this section of fanglomerate was translated along the Garlock, we assume a historic maximum width for the source alluvial fan before displacement. The historic width of the alluvial fan at Goler Gulch is estimated using the shape of the present-day mapped fan north of the Garlock plus the restoration of the SGF fan riser for a maximum allowable width of 2.5 km (Figure 3-2B-6). This yields a total offset of 7.25 ± 1.25 km from the sample area to its historic source. Based on the maximum depositional age of 0.767 ± 0.023 Ma, this requires a minimum slip rate of *7.6 - 11.4 mm/yr*.

Along the north side of the Powerline Shutter Ridge, an exposed section of fanglomerate with Mesquite Canyon provenance restores ~10 km to Mesquite Canyon. Sand from a shallow (~0.5-m deep) soil pit yields a distribution of ages from 169 total grains ranging from 1.8 Ma to > 200 Ma (Figure 3-2B-5). The four youngest DS grains from this sample yield an MDA of 1.84 ± 0.033 Ma with an MSWD of 0.9. To estimate the historic width of the Mesquite Canyon Fan, we observe the westernmost extent of mapped fan sediment and curl the contact eastward across younger alluvial surfaces (Figure 3-2B-6). Based on the symmetric appearance of the present-day fan, we believe that deposition of sediment was not skewed in either direction and therefore do not believe that historic fan would project further east than today's fan shape. We estimate a 3.0 km width of the historic fan across the Garlock at Mesquite Canyon. The distance between the sample at the Powerline Shutter Ridge and the historic fan yields a total offset of 9.8 ± 1.5 km. We resolve a minimum slip rate of *4.4 to 6.2 mm/yr* since 1.84 ± 0.033 Ma.

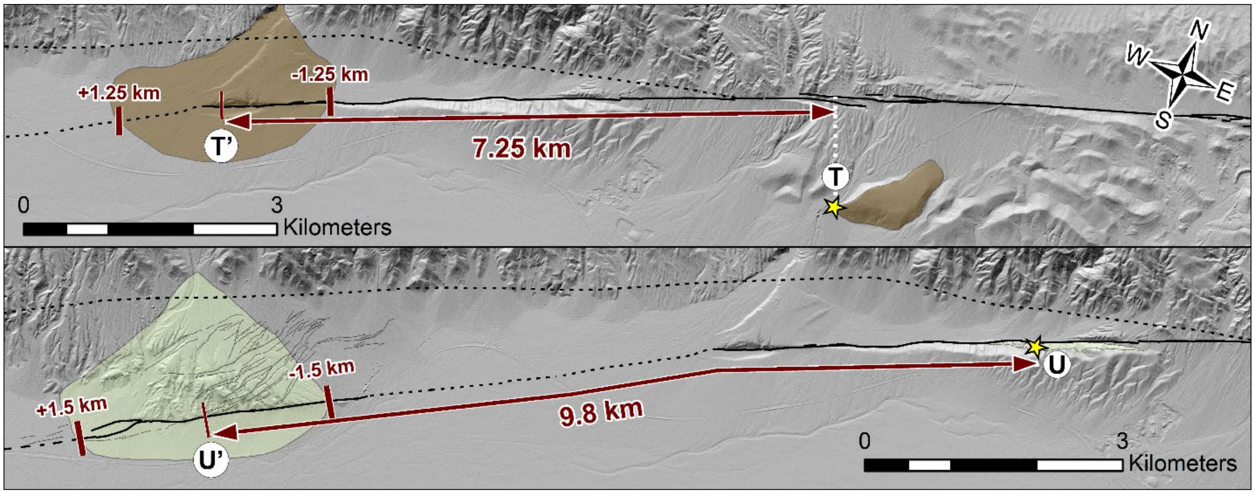

Figure 3-2B-6: Reconstruction of slip for T-T' (top) and U-U' (bottom). Estimated historic width of source fans shown in corresponding colors with the sampled deposit. Red arrow shows displacement to center of fan. Thicker red lines at ends of historic fan are the minimum and maximum bounds for the deposits' original depositional location based on the proposed width.

A Brief Discussion of Slip Rates Over the Past 2 Myr

The assessment of these four new records of slip data, presented above, suggest that slip rates over the past ~2 Myr are relatively constant through time, with perhaps an exception around 1 Mya. Because the ages used are maximum depositional ages, the true age could theoretically be younger, meaning that all slip rates presented here are minimum slip rates and could theoretically be faster. We present three new slip rates, *3.6 to 7.9 mm/yr since ~200 ka, 7.6 - 11.4 mm/yr since ~0.76 Ma, and 4.4 to 6.2 mm/yr* since *~1.8 Ma* (Figure 3-2B-7). All three slip rates are distinctly similar to the 5 – 7 mm/yr rate since the Miocene and slip rates during the late-Pleistocene (Clark and Lajoie, 1974; McGill and Sieh, 1991; McGill and Sieh, 1993; McGill et al., 2009; Ganev et al., 2012; Fougere et al., 2024) but are possibly faster within the last 1 Ma. Smaller scale perturbations, such as the period of rapid slip since 0.8 Ma, appear to average out to a consistent 5 – 7 mm/yr rate at timescales of 10^6 years, but require a period of slower slip over ~1 Myr.

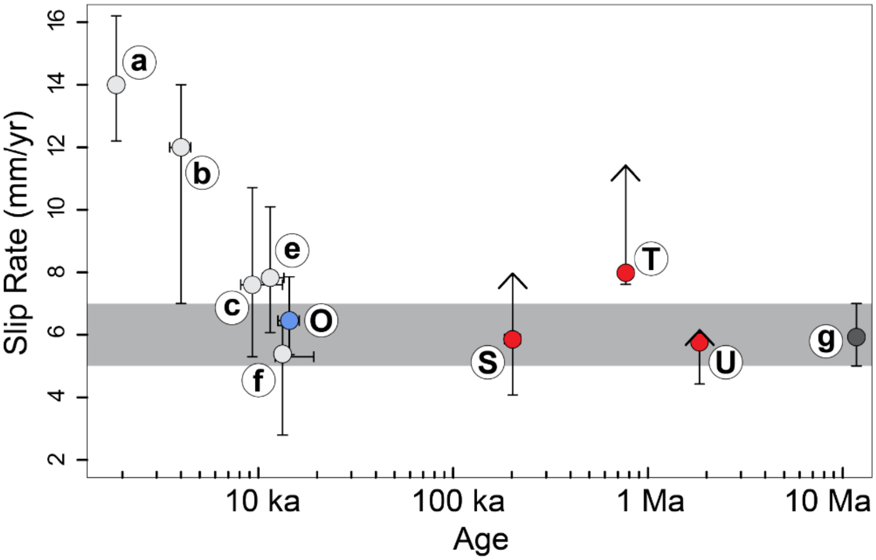

Figure 3-2B-7: New slip rates recorded from ^{40}Ar/^{39}Ar dating of detrital sanidine and provenance shown with a red circle. Sample O is not discussed in this text but is discussed by Maguire (2023). Other slip rate sources are as follows: a - Dolan et al., 2016; b - Rittase et al., 2014; c - McGill et al., 2009; e - McGill and Sieh, 1993; f - Ganev et al., 2012; Slip rate "g", denotes the 5-7 km/Myr rate of the Garlock since the Miocene (see review by Andrew et al., 2015).

References Cited

Andrew, J.E., Rittase, W.M., and Walker, J.D., 2014, Geologic Map of the Southern Slate Range and a Portion of the Central Garlock Fault, China Lake Naval Weapons Station, San Bernardino County, California: Geological Society of America Digital Map and Chart 20.

Andrew, J.E., Walker, J.D., Monastero, F.C., 2015. Evolution of the central Garlock fault zone, California: A major sinistral fault embedded in a dextral plate margin. Geological Society of America Bulletin 127, 227–249.

Andrew, J.E., Walker, J.D., Rittase, W.M., 2023. Evolution of slip partitioning in a major continental margin strike-slip fault system during a transition to oblique plate-margin tectonics: Insight into the evolution of the Garlock fault zone, California (USA). Geosphere.

Aslan, A., Boraas-Connors, M., Sprinkel, D.A., Becker, T.P., Lynds, R., Karlstrom, K.E., and Heizler, M., 2018, Cenozoic collapse of the eastern Uinta Mountains and drainage evolution of the Uinta Mountains region: Geosphere, v. 14, no. 1, p. 115– 140.

Blythe, A.E., Longinotti, N., 2013. Exhumation of the southern Sierra Nevada–eastern Tehachapi Mountains constrained by low-temperature thermochronology: Implications for the initiation of the Garlock fault. Lithosphere 5, 321–327.

Burbank, D.W., and Whistler, D.P., 1987, Temporally constrained rotations derived from magnetostratigraphic data: Implications for the initiation of the Garlock fault: Geology, v. 15, p. 1172–1175.

Carr, M.D., Christiansen, R.L., Poole, F.G., and Goodge, J.W., 1997, Bedrock geologic map of the El Paso Mountains in the Garlock and El Paso Peaks .5' quadrangles, Kern County, California: U.S. Geological Survey Miscellaneous Investigations Map I-2389, scale 1:24,000 with pamphlet.

Carter, B., 1980, Quaternary displacement on the Garlock fault, California, in: Fyfe, D. L., and Brown, A. R., ed., Geology and mineral wealth of the California desert: South Coast Geol. Soc., p 457-466.

Carter, B., 1994, Neogene offsets and displacement rates, central Garlock fault, California, in McGill, S.F., and Ross, T.M., eds., Geological Investigations of an active Margin: Redlands, California, San Bernardino County Museum Association, p. 348–356.

Christiansen, R. L., 1961, Structure, metamorphism and plutonism in the El Paso Mountains, Mojave desert, California: Stanford University, Ph.D. Thesis, p. 1-180.

Clark, M. M., and Lajoie, K. R., 1974, Holocene behavior of the Garlock fault: Geological Society of America, Abstracts with Programs, v. 6, p. 156-157.

Davis, G.A., and Burchfiel, B.C., 1973, Garlock fault: An intracontinental transform structure, southern California: Geological Society of America Bulletin, v. 84, p. 1407–1422.

Dibblee, T.W., Jr., 1952, Geology of the Saltdale quadrangle, California: California Division of Mines and Geology Bulletin 160, 66 p.

Dibblee, T.W., Jr., 1967, Areal geology of the western Mojave Desert, California: U.S. Geological Survey Professional Paper 522, 153 p.

Dolan, J.F., McAuliffe, L.J., Rhodes, E.J., McGill, S.F., Zinke, R., 2016. Extreme multi-millennial slip rate variations on the Garlock fault, California: Strain super-cycles, potentially time-variable fault strength, and implications for system-level earthquake occurrence. Earth and Planetary Science Letters 446, 123–136.

Fougere, D., Dolan, J., Rhodes, E. and McGill, S., 2024, Refined Holocene slip rate for the western and central segments of the Garlock fault: record of alternating millennial-scale periods of fast and flow fault slip, *Seismica*, *3*(2)

Gan, W., Zhang, P., Shen, Z.-K., Prescott, W.H., Svarc, J.L., 2003. Initiation of deformation of the Eastern California Shear Zone: Constraints from Garlock fault geometry and GPS observations: INITIATION OF DEFORMATION OF THE EASTERN CALIFORNIA SHEAR ZONE. Geophys. Res. Lett. 30.

Ganev, P.N., Dolan, J.F., McGill, S.F., Frankel, K.L., 2012. Constancy of geologic slip rate along the central Garlock fault: implications for strain accumulation and release in southern California: Geologic slip rates from central Garlock fault. Geophysical Journal International 190, 745–760.

Guest, B., Pavlis, T.L., Golding, H., Serpa, L., 2003, Chasing the Garlock: A study of tectonic response to vertical axis rotation. Geol 31, 553.

Heizler, M.T., Karlstrom, K., Zimmerer, M., Ross, J., Crossey, L., McIntosh, W., 2017, Detrital Sanidine 40AR/39AR Dating: Transforming Sedimentary Rock Geochronology: New Mexico GSA Spring Meeting Abstract.

Heizler, M.T., Karlstrom, K.E., Albonico, M., Hereford, R., Beard, L.S., Cather, S.M., Crossey, L.J., Sundell, K.E., 2021. Detrital sanidine 40Ar/39Ar dating confirms <2 Ma age of Crooked Ridge paleoriver and subsequent deep denudation of the southwestern Colorado Plateau. Geosphere 17, 438–454.

Hereford, R., Beard, L.S., Dickinson, W.R., Karlstrom, K.E., Heizler, M.T., Crossey, L.J., Amoroso, L., House, P.K., and Pecha, M., 2016, Reevaluation of the Crooked Ridge river—Early Pleistocene (ca. 2 Ma) age and origin of the White Mesa alluvium, northeastern Arizona: Geosphere, v. 12, p. 768–789.

Jahns, R.H., Troxel, B.W., and Wright, L.A., 1971, Some structural implications of a late Precambrian–Cambrian section in the Avawatz Mountains, California: Geological Society of America Abstracts with Programs, v. 3, p. 140.

Loomis, D.P., and Burbank, D.W., 1988, The stratigraphic evolution of the El Paso Basin, southern California: Implications for Miocene development of the Garlock fault and uplift of the Sierra Nevada: Geological Society of America Bulletin, v. 100, p. 12–28.

Ludwig, K.G.., 2022, Geochronologic and thermochronologic constraints on the Mesozoic to Cenozoic deformation history of southeastern California [M.S. thesis abstract]: Columbia, University of Missouri.

Maguire, S., 2023, A 2-Myr History of Slip Along the Garlock Fault Zone, Eastern California, Master's thesis, The University of North Carolina at Chapel Hill.

Manley, C.R., Bacon, C.R., 2000. Rhyolite Thermobarometry and the Shallowing of the Magma Reservoir, Coso Volcanic Field, California. Journal of Petrology 41, 149–174.

McGill, S.F., Sieh, K., 1991. Surficial offsets on the Central and Eastern Garlock Fault associated with prehistoric earthquakes. J. Geophys. Res. 96, 21597–21621.

McGill, S., Sieh, K., 1993. Holocene slip rate of the Central Garlock Fault in southeastern Searles Valley, California. J. Geophys. Res. 98, 14217–14231.

McGill, S.F., Wells, S.G., Fortner, S.K., Kuzma, H.A., McGill, J.D., 2009. Slip rate of the western Garlock fault, at Clark Wash, near Lone Tree Canyon, Mojave Desert, California. Geological Society of America Bulletin 121, 536–554.

Meade, B.J., Hager, B.H., 2005. Block models of crustal motion in southern California constrained by GPS measurements. J. Geophys. Res.110, B03403.

Peltzer, G., Crampé, F., Hensley, S., Rosen, P., 2001. Transient strain accumulation and fault interaction in the Eastern California shear zone. Geol 29, 975.

Rittase, W.M., Kirby, E., McDonald, E., Walker, J.D., Gosse, J., Spencer, J.Q.G., Herrs, A.J., 2014. Temporal variations in Holocene slip rate along the central Garlock fault, Pilot Knob Valley, California. Lithosphere 6, 48–58.

Savage, M.K., Fischer, K.M., Hall, C.E., 2004. Strain modelling, seismic anisotropy and coupling at strike-slip boundaries: applications in New Zealand and the San Andreas fault. SP 227, 9–39.

Smith, G.I., 1962. Large Lateral Displacement on Garlock Fault, Califonia, as Measured from Offset Dike Swarm. Bulletin 46.

Smith, G.I., Troxel, B.W., Gray, C.H., Jr., and von Huene, R., 1968, Geologic reconnaissance of the Slate Range, San Bernardino and Inyo counties, California: California Division of Mines and Geology Special Report 96, 33 p.

Smith, G.I., and Ketner, K.B., 1970, Lateral displacement on the Garlock fault, southeastern California, suggested by offset sections of similar metasedimentary rocks: U.S. Geological Survey Professional Paper 700- D, p. D1– D9.

Yancey, T. E., Heizler, M. T., Miller, B. V., & Guillemette, R. N., 2018, Eocene–Oligocene chronostratigraphy of ignimbrite flareup volcanic ash beds on the Gulf of Mexico coastal plains. Geosphere, 14(3), 1232-1252.

References for Pierce et al. contributions (Day 1, Day 2, Introduction)

Aitken, M. J. (1985). Thermoluminescence dating. Academic Press.

Auclair, M., Lamothe, M., & Huot, S. (2003). Measurement of anomalous fading for feldspar IRSL using SAR. *Radiation Measurements*, *37*(4–5), 487–492.

Brennan, B. J., Lyons, R. G., & Phillips, S. W. (1991). Attenuation of alpha particle track dose for spherical grains. *International Journal of Radiation Applications and Instrumentation. Part D. Nuclear Tracks and Radiation Measurements*, *18*(1–2), 249–253.

Durcan, J. A., King, G. E., & Duller, G. A. T. (2015). DRAC: Dose Rate and Age Calculator for trapped charge dating. *Quaternary Geochronology*, *28*, 54–61.

Galbraith, R. F., & Green, P. F. (1990). Estimating the component ages in a finite mixture. International Journal of Radiation Applications and Instrumentation. Part D. Nuclear Tracks and Radiation Measurements, 17(3), 197–206.

Galbraith, R. F., Roberts, R. G., Laslett, G. M., Yoshida, H., & Olley, J. M. (1999). Optical dating of single and multiple grains of quartz from Jinmium rock shelter, northern Australia: Part I, experimental design and statistical models. *Archaeometry*, *41*(2), 339–364.

Guérin, G., Mercier, N., Nathan, R., Adamiec, G., & Lefrais, Y. (2012). On the use of the infinite matrix assumption and associated concepts: a critical review. Radiation Measurements, 47(9), 778–785.

Huntley, D. J., & Lamothe, M. (2001). Ubiquity of anomalous fading in K-feldspars and the measurement and correction for it in optical dating. *Canadian Journal of Earth Sciences*, *38*(7), 1093–1106.

Liritzis, I., Stamoulis, K., Papachristodoulou, C., & Ioannides, K. (2013). A re-evaluation of radiation dose-rate conversion factors. *Mediterranean Archaeology and Archaeometry*, *13*(3), 1–15.

Murray, A. S., & Wintle, A. G. (2000). Luminescence dating of quartz using an improved single-aliquot regenerative-dose protocol. *Radiation Measurements*, *32*(1), 57–73.

Murray, A. S., & Wintle, A. G. (2003). The single aliquot regenerative dose protocol: potential for improvements in reliability. *Radiation Measurements*, *37*(4–5), 377–381.

Prescott, J. R., & Hutton, J. T. (1994). Cosmic ray contributions to dose rates for luminescence and ESR dating: large depths and long-term time variations. *Radiation Measurements*, *23*(2–3), 497–500.

Smedley, R. K., Duller, G. A. T., Pearce, N. J. G., & Roberts, H. M. (2012). Determining the K-content of single-grains of feldspar for luminescence dating. *Radiation Measurements*, *47*(9), 790–796.

Amos, C.B., Brownlee, S.J., Rood, D.H., Fisher, G.B., Burgmann, R., Renne, P.R., Jayko, A.S., 2013. Chronology of tectonic, geomorphic, and volcanic interactions and the tempo of fault slip near Little Lake, California. Geol. Soc. Am. Bull. 125, 1187–1202. https://doi.org/10.1130/B30803.1

Bacon, S.N., Jayko, A.S., Owen, L.A., Lindvall, S.C., Rhodes, E.J., Schumer, R.A., Decker, D.L., 2020. A 50,000-year record of lake-level variations and overflow from Owens Lake, eastern California, USA. Quat. Sci. Rev. 238, 106312. https://doi.org/10.1016/j.quascirev.2020.106312

Bacon, S.N., Pezzopane, S.K., 2007. A 25,000-year record of earthquakes on the Owens Valley fault near Lone Pine, California: Implications for recurrence intervals, slip rates, and segmentation models. Geol. Soc. Am. Bull. 119, 823–847. https://doi.org/10.1130/B25879.1

Barnhart, W.D., Hayes, G.P., Gold, R.D., 2019. The July 2019 Ridgecrest, California, Earthquake Sequence: Kinematics of Slip and Stressing in Cross-Fault Ruptures. Geophys. Res. Lett. 46, 11859–11867. https://doi.org/10.1029/2019GL084741

Beanland, S., Clark, M.M., 1994. The Owens Valley Fault Zone, Eastern California, and Surface Faulting Associated with the 1872 Earthquake (U.S. Geological Survey Bulletin No. 1982). U.S. Geological Survey.

Bell, J.W., Caskey, S.J., Ramelli, A.R., Guerrieri, L., 2004. Pattern and Rates of Faulting in the Central Nevada Seismic Belt, and Paleoseismic Evidence for Prior Beltlike Behavior. Bull. Seismol. Soc. Am. 94, 1229–1254. https://doi.org/10.1785/012003226

Bell, J.W., dePolo, C.M., Ramelli, A.R., Sarna-Wojcicki, A.M., Meyer, C.E., 1999. Surface faulting and paleoseismic history of the 1932 Cedar Mountain earthquake area, west-central Nevada, and implications for modern tectonics of the Walker Lane. Geol. Soc. Am. Bull. 111, 791–807. https://doi.org/10.1130/0016-7606(1999)111<0791:SFAPHO>2.3.CO;2

Cadena, A., 2013. Paleoseismologic Evidence for Holocene Activity on the Pinto Mountain Fault, Twentynine Palms, California. Central Washington University.

Choi, N.H., 2016. Late Pleistocene Slip Rate along the Panamint Valley Fault System, Eastern California (Masters Thesis). Oregon State University.

Dawson, T.E., McGill, S.F., Rockwell, T.K., 2003. Irregular recurrence of paleoearthquakes along the central Garlock fault near El Paso Peaks, California. J. Geophys. Res. Solid Earth 108. https://doi.org/10.1029/2001JB001744

Dee, S., Koehler, R.D., Elliott, A.J., Hatem, A., Pickering, A., Pierce, I., Seitz, G., Collett, C., Dawson, T., De Masi, C., dePolo, C., Hartshorn, E., Madugo, C., Trexler, C.C., Verdugo, D.M., Wesnousky, S., Zachariasen, J., 2021. Surface Rupture Map of the 2020 M6.5 Monte Cristo Range Earthquake. Nevada Bureau of Mines and Geology Map 190.

Dixon, T.H., Miller, M., Farina, F., Wang, H., Johnson, D., 2000. Present-day motion of the Sierra Nevada block and some tectonic implications for the Basin and Range province, North American Cordillera. Tectonics 19, 1–24.

Dokka, R.K., Travis, C.J., 1990. Role of the eastern California shear zone in accommodating Pacific-North American plate motion. Geophys. Res. Lett. 17, 1323–1326.

Dolan, J.F., McAuliffe, L.J., Rhodes, E.J., McGill, S.F., Zinke, R., 2016. Extreme multi-millennial slip rate variations on the Garlock fault, California: Strain super-cycles, potentially time-variable fault strength, and implications for system-level earthquake occurrence. Earth Planet. Sci. Lett. 446, 123–136. https://doi.org/10.1016/j.epsl.2016.04.011

DuRoss, C.B., Gold, R.D., Dawson, T.E., Scharer, K.M., Kendrick, K.J., Akciz, S.O., Angster, S.J., Bachhuber, J., Bacon, S., Bennett, S.E.K., Blair, L., Brooks, B.A., Bullard, T., Burgess, W.P., Chupik, C., DeFrisco, M., Delano, J., Dolan, J.F., Frost, E., Graehl, N., Haddon, E.K., Hatem, A.E., Hernandez, J.L., Hitchcock, C., Hudnut, K., Thompson Jobe, J., Koehler, R., Kozaci, O., Ladinsky, T., Madugo, C., McPhillips, D.S., Milliner, C., Morelan, A., Olson, B., Patton, J., Philibosian, B., Pickering, A.J., Pierce, I., Ponti, D.J., Seitz, G., Spangler, E., Swanson, B., Thomas, K., Treiman, J., Valencia, F., Williams, A., Zinke, R., 2020. Surface Displacement Distributions for the July 2019 Ridgecrest, California, Earthquake Ruptures. Bull. Seismol. Soc. Am. 110, 1400–1418. https://doi.org/10.1785/0120200058

Fialko, Y., Simons, M., Agnew, D., 2001. The complete (3-D) surface displacement field in the epicentral area of the 1999 MW7.1 Hector Mine Earthquake, California, from space geodetic observations. Geophys. Res. Lett. 28, 3063–3066. https://doi.org/10.1029/2001GL013174

Fougere, D., Dolan, J., Rhodes, E., McGill, S., 2024. Refined Holocene Slip Rate for the Western and Central Segments of the Garlock Fault: Record of Alternating Millennial-Scale Periods of Fast and Slow Fault Slip. Seismica 3. https://doi.org/10.26443/seismica.v3i2.1202

Ganev, P.N., Dolan, J.F., Blisniuk, K., Oskin, M., Owen, L.A., 2010. Paleoseismologic evidence for multiple Holocene earthquakes on the Calico fault: Implications for earthquake clustering in the Eastern California shear zone. Lithosphere 2, 287–298. https://doi.org/10.1130/L82.1

Gold, R.D., DuRoss, C.B., Barnhart, W.D., 2021. Coseismic Surface Displacement in the 2019 Ridgecrest Earthquakes: Comparison of Field Measurements and Optical Image Correlation Results. Geochem. Geophys. Geosystems 22, e2020GC009326. https://doi.org/10.1029/2020GC009326

Haddon, E.K., Amos, C.B., Zielke, O., Jayko, A.S., Bürgmann, R., 2016. Surface slip during large Owens Valley earthquakes. Geochem. Geophys. Geosystems 17, 2239–2269. https://doi.org/10.1002/2015GC006033

Hatch, R., Smith, K., Abercrombie, R., Ruhl, C., Hammond, W., Pierce, I., 2019. Relocations and Tectonic Implications of the Nine Mile Ranch Sequence from 2016-2018: 3 Mw 5.4-5.6 Near Hawthorne, Nevada, in: Program with Abstracts. Presented at the Annual Meeting of the Seismological Society of America, Seismological Research Letters, Seattle, Washington, p. 1069.

Hill, D.P., Reasenberg, P.A., Michael, A., Arabaz, W.J., Beroza, G., Brumbaugh, D., Brune, J.N., Castro, R., Davis, S., dePolo, D., Ellsworth, W.L., Gomberg, J., Harmsen, S., House, L., Jackson, S.M., Johnston, M.J.S., Jones, L., Keller, R., Malone, S., Munguia, L., Nava, S., Pechmann, J.C., Sanford, A., Simpson, R.W., Smith, R.B., Stark, M., Stickney, M., Vidal, A., Walter, S., Wong, V., Zollweg, J., 1993. Seismicity Remotely Triggered by the Magnitude 7.3 Landers, California, Earthquake. Science 260, 1617–1623. https://doi.org/10.1126/science.260.5114.1617

Hoffman, W.R., 2009. LATE PLEISTOCENE SLIP RATES ALONG THE PANAMINT VALLEY FAULT ZONE, EASTERN CALIFORNIA. Pennsylvania State University.

Hudnut, K.W., Seeber, L., Pacheco, J., 1989. Cross-fault triggering in the November 1987 Superstition Hills Earthquake Sequence, southern California. Geophys. Res. Lett. 16, 199–202. https://doi.org/10.1029/GL016i002p00199

Kirby, E., Anandakrishnan, S., Phillips, F., Marrero, S., 2008. Late Pleistocene slip rate along the Owens Valley fault, eastern California. Geophys. Res. Lett. 35. https://doi.org/10.1029/2007GL031970

Madden, C.L., Rubin, C.M., Streig, A., 2006. Holocene and Latest Pleistocene Activity on the Mesquite Lake Fault near Twentynine Palms, Eastern California Shear Zone: Implications for Fault Interaction. Bull. Seismol. Soc. Am. 96, 1305–1320. https://doi.org/10.1785/0120020120

Magen, Y., Ziv, A., Inbal, A., Baer, G., Hollingsworth, J., 2020. Fault Rerupture during the July 2019 Ridgecrest Earthquake Pair from Joint Slip Inversion of InSAR, Optical Imagery, and GPS. Bull. Seismol. Soc. Am. 110, 1627–1643. https://doi.org/10.1785/0120200024

Marchandon, M., Vergnolle, M., Cavalié, O., 2020. Fault interactions in a complex fault system: insight from the 1936–1997 NE Lut earthquake sequence. Geophys. J. Int. 224, 1157–1173. https://doi.org/10.1093/gji/ggaa451

McAuliffe, L.J., Dolan, J.F., Kirby, E., Rollins, C., Haravitch, B., Alm, S., Rittenour, T.M., 2013. Paleoseismology of the southern Panamint Valley fault: Implications for regional earthquake occurrence and seismic hazard in southern California. J. Geophys. Res. Solid Earth 118, 5126–5146. https://doi.org/10.1002/jgrb.50359

McCalpin, J., 2009. Paleoseismology, 2nd ed. Academic Press.

Numelin, T., Kirby, E., Walker, J.D., Didericksen, B., 2007. Late Pleistocene slip on a low-angle normal fault, Searles Valley, California. Geosphere 3, 163–176. https://doi.org/10.1130/GES00052.1

Peña, K.A., 2019. PALEOSEISMOLOGY OF THE CENTRAL GARLOCK FAULT IN SEARLES VALLEY, CALIFORNIA. California State University, San Bernardino.

Pierce, I., Guliyev, I., Yetirmishli, G., Muradov, R., Kazimova, S., Javanshir, R., De Pascale, G.P., Johnson, B., Marshall, N., Walker, R., Wordsworth, P., 2024. Surface Rupturing Earthquakes of the Greater Caucasus Frontal Thrusts, Azerbaijan. Tectonics 43, e2023TC007758. https://doi.org/10.1029/2023TC007758

Pierce, I., Koehler, R., 2023. 3D Paleoseismology from iOS Lidar and Structure from Motion Photogrammetry: a case study on the Dog Valley fault, California. Seismica 2. https://doi.org/10.26443/seismica.v2i1.208

Pierce, I., Williams, A., Koehler, R.D., Chupik, C., 2020. High-Resolution Structure-From-Motion Models and Orthophotos of the Southern Sections of the 2019 Mw 7.1 and

6.4 Ridgecrest Earthquakes Surface Ruptures. Seismol. Res. Lett. 91, 2124–2126. https://doi.org/10.1785/0220190289

Pierce, I.K.D., 2022. Spatiotemporal Clustering of Paleoseismicity in the Walker Lane, USA: An Extensional Supercycle? Geophys. Res. Lett. 49, e2022GL099078. https://doi.org/10.1029/2022GL099078

Pierce, I.K.D., Green, L., Talebian, M., Walker, R.T., Johnson, B., 2024. Satellite Mapping of Fault Rupture From the 1968 and 1979 Dasht-e Bayaz and Khuli-Buniabad Earthquakes, Northeast Iran: Rupture Complexities and Evidence of Rupture Arrest and re-Rupture in Successive Earthquakes 2.

Pierce, I.K.D., Wesnousky, S.G., Owen, L.A., Bormann, J.M., Li, X., Caffee, M., 2021. Accommodation of Plate Motion in an Incipient Strike-Slip System: The Central Walker Lane. Tectonics 40, e2019TC005612. https://doi.org/10.1029/2019TC005612

Ponti, D.J., Blair, J.L., Rosa, C.M., Thomas, K., Pickering, A.J., Akciz, S., Angster, S., Avouac, J., Bachhuber, J., Bacon, S., Barth, N., Bennett, S., Blake, K., Bork, S., Brooks, B., Bullard, T., Burgess, P., Chupik, C., Dawson, T., DeFrisco, M., Delano, J., DeLong, S., Dolan, J., Donnellan, A., DuRoss, C., Ericksen, T., Frost, E., Funning, G., Gold, R., Graehl, N., Gutierrez, C., Haddon, E., Hatem, A., Helms, J., Hernandez, J., Hitchcock, C., Holland, P., Hudnut, K., Kendrick, K., Koehler, R., Kozaci, O., Ladinsky, T., Leeper, R., Madugo, C., Mareschal, M., McDonald, J., McPhillips, D., Milliner, C., Mongovin, D., Morelan, A., Nale, S., Nevitt, J., O'Neal, M., Olson, B., Oskin, M., Padilla, S., Patton, J., Philibosian, B., Pierce, I., Pridmore, C., Roth, N., Sandwell, D., Scharer, K., Seitz, G., Singleton, D., Smith-Konter, B., Spangler, E., Swanson, B., Jobe, J.T., Treiman, J., Valencia, F., Vanderwal, J., Williams, A., Xu, X., Zachariasen, J., Zimmerman, J., Zinke, R., 2020. Documentation of Surface Fault Rupture and Ground-Deformation Features Produced by the 4 and 5 July 2019 Mw 6.4 and Mw 7.1 Ridgecrest Earthquake Sequence. Seismol. Res. Lett. 91, 2942–2959. https://doi.org/10.1785/0220190322

Ramos, M., Neo, J.C., Thakur, P., Huang, Y., Wei, S., 2020. Stress Changes on the Garlock Fault during and after the 2019 Ridgecrest Earthquake Sequence. Bull. Seismol. Soc. Am. 110. https://doi.org/10.1785/0120200027

Reitman, N.G., Briggs, R.W., Barnhart, W.D., Hatem, A.E., Thompson Jobe, J.A., DuRoss, C.B., Gold, R.D., Mejstrik, J.D., Collett, C., Koehler, R.D., Akçiz, S., 2023. Rapid Surface Rupture Mapping from Satellite Data: The 2023 Kahramanmaraş, Turkey (Türkiye), Earthquake Sequence. Seism. Rec. 3, 289–298. https://doi.org/10.1785/0320230029

Rittase, W.M., Kirby, E., McDonald, E., Walker, J.D., Gosse, J., Spencer, J.Q.G., Herrs, A.J., 2014. Temporal variations in Holocene slip rate along the central Garlock fault, Pilot Knob Valley, California. Lithosphere 6, 48–58. https://doi.org/10.1130/L286.1

Rockwell, T.K., 2000. Paleoseismology of the Johnson Valley, Kickapoo, and Homestead Valley Faults: Clustering of Earthquakes in the Eastern California Shear Zone. Bull. Seismol. Soc. Am. 90, 1200–1236. https://doi.org/10.1785/0119990023

Rockwell, T.K., Lindvall, S., Herzberg, M., Murbach, D., Dawson, T.E., Berger, G., 2000. Paleoseismology of the Johnson Valley, Kickapoo, and Homestead Valley Faults: Clustering of Earthquakes in the Eastern California Shear Zone. Bull. Seismol. Soc. Am. 90, 1200–1236. https://doi.org/10.1785/0119990023

Rodriguez Padilla, A.M., Quintana, M.A., Prado, R.M., Aguilar, B.J., Shea, T.A., Oskin, M.E., Garcia, L., 2021. Near-Field High-Resolution Maps of the Ridgecrest Earthquakes from Aerial Imagery. Seismol. Res. Lett. 93, 494–499. https://doi.org/10.1785/0220210234

Rosenthal, J.S., Meyer, J., Palacios-Fest, M.R., Young, D.C., Ugan, A., Byrd, B.F., Gobalet, K., Giacomo, J., 2017. Paleohydrology of China Lake basin and the context of early human occupation in the northwestern Mojave Desert, USA. Quat. Sci. Rev. 167, 112–139. https://doi.org/10.1016/j.quascirev.2017.04.023

Ross, Z.E., Idini, B., Jia, Z., Stephenson, O.L., Zhong, M., Wang, X., Zhan, Z., Simons, M., Fielding, E.J., Yun, S.-H., Hauksson, E., Moore, A.W., Liu, Z., Jung, J., 2019. Hierarchical interlocked orthogonal faulting in the 2019 Ridgecrest earthquake sequence 7.

Rymer, M.J., Seitz, G.G., Weaver, K.D., Orgil, A., Faneros, G., Hamilton, J.C., Goetz, C., 2002. Geologic and Paleoseismic Study of the Lavic Lake Fault at Lavic Lake Playa, Mojave Desert, Southern California. Bull. Seismol. Soc. Am. 92, 1577–1591. https://doi.org/10.1785/0120000936

Sawyer, T.L., 1988. Late Holocene Paleoseismicity of the Northern Death Valley Fault System, Fish Lake Valley, Nevada, in: OF1989-01: Late Cenozoic Evolution of the Southern Great Basin. University of Nevada, Reno, p. 63.

Scharer, K.M., Yule, D., 2020. A Maximum Rupture Model for the Southern San Andreas and San Jacinto Faults, California, Derived From Paleoseismic Earthquake Ages: Observations and Limitations. Geophys. Res. Lett. 47, e2020GL088532. https://doi.org/10.1029/2020GL088532

Sieh, K., Jones, L., Hauksson, E., Hudnut, K., Eberhart-Phillips, D., Heaton, T., Hough, S., Hutton, K., Kanamori, H., Lilje, A., Lindvall, S., McGill, S.F., Mori, J., Rubin, C., Spotila, J.A., Stock, J., Thio, H.K., Treiman, J., Wernicke, B., Zachariasen, J., 1993. Near-Field Investigations of the Landers Earthquake Sequence, April to July 1992. Science 260, 171–176. https://doi.org/10.1126/science.260.5105.171

Stirling, M.W., Litchfield, N., Villamor, P., Dissen, R., Nicol, A., Pettinga, J., Barnes, P., Langridge, R., Little, T., Barreil, D.J.A., Mountjoy, J., Ries, W., Rowland, J., Fenton, C., Hamling, I., Asher, C., Barrier, A., Benson, A., Bischoff, A., Zinke, R., 2017. The Mw7.8 2016 Kaikōura earthquake: Surface fault rupture and seismic hazard context. Bull. N. Z. Soc. Earthq. Eng. 50, 73–84.

Styron, R., 2019. The impact of earthquake cycle variability on neotectonic and paleoseismic slip rate estimates. Solid Earth 10, 15–25. https://doi.org/10.5194/se-10-15-2019

Thompson Jobe, J.A., Philibosian, B., Chupik, C., Dawson, T., K. Bennett, S.E., Gold, R., DuRoss, C., Ladinsky, T., Kendrick, K., Haddon, E., Pierce, I., Swanson, B., Seitz, G., 2020. Evidence of Previous Faulting along the 2019 Ridgecrest, California, Earthquake Ruptures. Bull. Seismol. Soc. Am. 110, 1427–1456. https://doi.org/10.1785/0120200041

Unruh, J., Humphrey, J., Barron, A., 2003. Transtensional model for the Sierra Nevada frontal fault system, eastern California. Geology 31, 327–330.

Vadman, M.J., Garvue, M.M., Spotila, J.A., Bemis, S.P., Stamps, D.S., Owen, L.A., Figueiredo, P.M., 2023. Evidence for a prehistoric multifault rupture along the southern Calico fault system, Eastern California Shear Zone, USA. Geosphere 19, 1589–1615. https://doi.org/10.1130/GES02653.1

Wesnousky, S.G., 2005a. Active faulting in the Walker Lane. Tectonics 24, 35 pp. https://doi.org/10.1029/2004TC001645

Wesnousky, S.G., 2005b. The San Andreas and Walker Lane fault systems, western North America: transpression, transtension, cumulative slip and the structural evolution of a major transform plate boundary. J. Struct. Geol. 27, 1505–1512. https://doi.org/10.1016/j.jsg.2005.01.015

Wesnousky, S.G., Bormann, J.M., Kreemer, C., Hammond, W.C., Brune, J.N., 2012. Neotectonics, geodesy, and seismic hazard in the Northern Walker Lane of Western North America: Thirty kilometers of crustal shear and no strike-slip? Earth Planet. Sci. Lett. 329–330, 133–140. https://doi.org/10.1016/j.epsl.2012.02.018

Xu, X., Sandwell, D.T., Smith-Konter, B., 2020. Coseismic Displacements and Surface Fractures from Sentinel-1 InSAR: 2019 Ridgecrest Earthquakes. Seismol. Res. Lett. 91, 1979–1985. https://doi.org/10.1785/0220190275

Yang, J., Zhu, H., Lay, T., Niu, Y., Ye, L., Lu, Z., Luo, B., Kanamori, H., Huang, J., Li, Z., 2021. Multifault Opposing-Dip Strike-Slip and Normal-Fault Rupture During the 2020 Mw 6.5 Stanley, Idaho Earthquake. Geophys. Res. Lett. 48, 13. https://doi.org/10.1029/2021GL092510